Universidad Autónoma de Madrid

Programa de Doctorado en Biociencias Moleculares

Role of stromal Caveolin-1 (CAV1) levels in breast cancer angiogenesis

Alberto Díez Sánchez

Madrid, 2018

Departamento de Bioquímica

Facultad de Medicina

Universidad Autónoma de Madrid

Role of stromal Caveolin-1 (CAV1) levels in breast cancer angiogenesis

Doctorando: Alberto Díez Sánchez, Licenciado en Biotecnología

Director: Miguel Ángel del Pozo Barriuso, MD, PhD.

Fundación Centro Nacional de Investigaciones Cardiovasculares Carlos III (CNIC)

Madrid, 2018

CERTIFICADO DEL DIRECTOR DE TESIS

El doctor Miguel Ángel del Pozo Barriuso CERTIFICA que el doctorando Alberto Díez Sánchez ha desarrollado y concluido su trabajo de tesis doctoral “Role of stromal Caveolin-1 (CAV1) levels in breast cancer angiogenesis” bajo su supervisión, en el Centro Nacional de Investigaciones Cardiovasculares (CNIC).

Y para que así conste lo firma en Madrid, a 10 de Julio de 2018,

Fdo. Dr. Miguel Ángel del Pozo Barriuso

Centro Nacional de Investigaciones Cardiovasculares (CNIC)

ACKNOWLEDGMENTS

It is said that scientific knowledge is built on top of the shoulder of giants, in more practical terms, I consider all these people below my personal giants.

First ones I encountered, were my parents and grandparents, everything I have achieved has been done on top of their previous efforts, to them I dedicate my most sincere gratitude for teaching this once lazy kid the value of effort.

Next, I have to thank all those high-school teachers and university professors that during my education have been able to spark in me the sense of amazement derived from understanding how nature works. Special acknowledgments to my high school biology teacher Charo Díaz, who was able to amazingly convey and share her enthusiasm for her teachings, you are guilty of my choice for biological sciences.

While instigating this interest was crucial in my career, a very different scenario was maintaining and nurturing it. Here I would like to thank all those good mentors I have come across during my short lab years: Luis Ángel Fernández (CNB), Marilyn G. Farquhar (UCSD), Mehul Shah (UCSD), Geir Bjørkøy (NTNU)... In this regard, I am especially grateful to my thesis director, Miguel Ángel del Pozo (CNIC), for giving me enough freedom to seek my own questions, make my own mistakes and having the patience of, afterward, dealing with them.

On a day to day basis, I am grateful for the people that I have been sharing my bench floor with (both in Spain and in Norway); talking about, most usually, the disappointment of failing experiments and, less commonly, the excitement for a major breakthrough has made my passage through these thesis years much easier and funnier than anticipated. Finishing this period with a good feeling is because of you.

In terms of heavy-lifting work, I am grateful for having Mauro, Inés, and Miguel by my side. All the work presented here today would not have been possible without your key contributions. I do not forget my collaborators, in image analysis (Xenia, Daniel, and Laura), high-content screening (Irene and Mariano) and bioinformatics analysis, your abilities do not cease to amaze me.

On a personal level, I feel blessed with my lifelong neighborhood friends, not only because of the countless hours of fun that have made easier dealing with lab stress, but also for their continuous support. Without deserving it, they have been calling me “doctor” even before starting my degree. This one is for you.

Last but not least, a very special thanks to Mara, my life partner, who has been lately dealing with my stress-related mood swings using an infinite amount of patience and unconditional love. You have made this possible and I cannot wait to have more of yourself for the years to come.

This doctoral thesis was made possible with the funding of Obra Social "la Caixa"

SUMMARY

Tumors have been described as “wounds that never heal”; and non-tumoral surrounding cell populations involved in angiogenesis and response to injury, such as endothelial cells, immune cells and fibroblasts are actively engaged to support the aberrant growth and remodeling of the tumor mass, which conversely determine tumor architecture and behavior. These cells, along with extracellular matrix (ECM) components, define the tumor microenvironment or tumor stroma.

While breast cancer progression was conceived for a long time to be largely dependent on aberrant mutations in tumor cells, stromal Cancer-Associated Fibroblasts (CAFs) have been demonstrated to modulate breast cancer growth, invasion, metastasis and therapeutic resistance.

Caveolin-1 (CAV1), a prominent organizer of plasma membrane properties and function, exhibits extensive ties with many events defining tumor onset and progression. Although previous studies have shown CAV1 expression levels in CAFs to influence breast cancer growth and metastasis, the underlying driving mechanisms remain incompletely characterized. In this regard, ECM modification and metabolic reprogramming have been proposed as key aspects of a stromal CAV1-dependent role in tumor biology.

This thesis research report aims to contribute to our understanding as to how CAV1 expression in stromal CAFs impact tumor angiogenesis, and thus tumor hypoxia, cancer aggressiveness and metastasis.

The present work showcases evidence supporting a positive reciprocal feedback relationship between stromal CAV1 downregulation and endoplasmic reticulum (ER) stress, which can drive exacerbated proangiogenic signaling, causative of the generation of an aberrant and dysfunctional tumor vasculature.

This report proposes defective angiogenesis and consequent hypoxia as major driving causes for increased aggressiveness of breast cancer in low stromal CAV1 tumors.

RESUMEN

Los tumores podrían describirse como heridas que nunca terminan de curarse. En respuesta a esta agresión, se puede observar el reclutamiento de células del sistema inmune, de fibroblastos que intentan cerrar la lesión y de células endoteliales implicadas en la formación de nuevos vasos sanguíneos y linfáticos. Estas células, en conjunto con la matriz extracelular (ECM, *Extracellular Matrix*, por sus siglas en inglés) que las rodea, conforman lo que se conoce como microambiente o estroma tumoral.

Durante décadas, la progresión y el comportamiento del cáncer de mama se concebían como procesos dependientes de las mutaciones que acaecían en las células tumorales. Sin embargo, recientemente varios estudios han demostrado que el microambiente tumoral en general, y los fibroblastos estromales asociados al tumor (CAFs, *Cancer-Associated Fibroblasts*, por sus siglas en inglés) en particular, son capaces de modular el crecimiento tumoral, la capacidad invasiva y el proceso metastático del cáncer de mama, así como la resistencia a determinadas terapias.

Aunque estudios previos han demostrado que los niveles de la proteína Caveolina-1 (CAV1) que presentan los fibroblastos estromales (CAFs) tienen una influencia sobre la capacidad metastática y de crecimiento del cáncer de mama, el mecanismo responsable de esta habilidad moduladora está por resolver. Procesos como la modificación ejercida por estos CAFs sobre la ECM y su potencial para reprogramar el metabolismo tumoral se han postulado como piezas de este rompecabezas.

Este trabajo describe como una bajada en la expresión de CAV1 en CAFs estromales orquestra la formación de una vasculatura tumoral disfuncional y aberrante que resulta en un incremento de la hipoxia, la agresividad y la capacidad metastática de estos tumores con bajos niveles de CAV1 estromal. Además, establece un círculo vicioso de retroalimentación positiva entre la menor expresión de CAV1 y la inducción de estrés reticular, que en última instancia es responsable de la activación de una señalización proangiogénica exacerbada que deriva en la formación de la vasculatura aberrante arriba mencionada.

INDEX

NON-STANDARD ABBREVIATIONS AND ACRONYMS

2-DG	2-Deoxyglucose
ACTA2	Smooth Muscle Actin (aka αSMA)
ADAMTS	A Disintegrin and Metalloproteinase with Thrombospondin Motifs
Ag	Antigen
aka	Also Known As
ANG	Angiogenin
ANGP1/2	Angiopoietin-1/2 (Protein) *ANGPT1/2* (Gene/Transcript)
ANOVA	Analysis of Variance
AR	Androgen Receptor
ATF4 / 6	Activating Transcription Factor 4 / 6
AVCs	Angiogenic Vascular Cells
BLBC	Basal-Like Breast Cancer
BM	Basement Membrane
BMPs	Bone Morphogenetic Proteins
brCAN	Breast cancer cell lines
CAFs	Cancer-Associated Fibroblasts (aka TAFs)
CAFscr	Breast CAFs transduced with a non-targeting lentivirus
CAFshCAV1	Breast CAFs transduced with a CAV1 mRNA-targeting lentivirus
CAV1	Caveolin-1 (protein/*gene*/*transcript)*
CCDN1	Cyclin D1
CCL2	C-C Motif Chemokine Ligand 2 (aka MCP-1)
CCL5	Chemokine (C-C motif) ligand 5
CD31	Platelet Endothelial Cell Adhesion Molecule (aka PECAM-1)
CherryFP	Cherry Fluorescent Protein (aka ChFP)
CHOP	C/EBP-Homologous Protein (aka DDIT3)
CK	Cytokeratin
c-Met	Tyrosine-protein kinase Met (aka HGFR)
CMV	Cytomegalovirus
cPPT	Central Polypurine Tract
CSCs	Cancer Stem Cells
CSD	Caveolin Scaffolding Domain
CSF-1	Colony Stimulating Factor 1
CTLA-4	Cytotoxic T-Lymphocyte Antigen 4
CXCL10	C-X-C Motif Chemokine Ligand 10
CXCL12	Stromal Derived Growth Factor 1 (aka SDF1)
CXCL8	Interleukin-8 (*gene/transcript*)
CXCR1/2	C-X-C Motif Chemokine Receptor 1/2
DCA	Dichloroacetic Acid
DCIS	Ductal Carcinoma In Situ
DCs	Dendritic Cells
DPP4	Dipeptidyl Peptidase 4
ECAR	Extracellular Acidification Ratio
ECGM	Endothelial Cell Growth Medium
ECM	Extracellular Matrix
ECs	Endothelial Cells
EdU	5-ethynyl-2'-deoxyuridine
EGF	Epidermal Growth Factor

EGFR	Epidermal Growth Factor Receptor
eIF2α	Eukaryotic Translation Initiation Factor 2A
ELISA	Enzyme-linked Immunosorbant Assay
EMT	Epithelial to Mesenchymal Transition
EndMT	Endothelial to Mesenchymal Transition
EPCs	Endothelial Progenitor Cells
ER	Estrogen Receptor (appears in breast cancer introduction)
ER	Endoplasmic Reticulum (rest of the text)
FACS	Fluorescence Activated Cell Sorting
FAP	Fibroblast Activation Protein
FBS	Fetal Bovine Serum
FGFs	Fibroblast Growth Factors
FSP1	Fibroblast Specific Protein 1 (aka S100A4)
GFP	Green Fluorescent Protein
GLUT1	Glucose Transporter Type 1 (aka SLC2A1)
GSH	Glutathione
GSH-EE	Glutathione Ethyl Ester
H&E	Hematoxylin and Eosin
HCS	High Content Screening
HER2	Human Epidermal Growth Factor Receptor 2
HG	High Glucose
HGF	Hepatocyte Growth Factor
HIFs	Hypoxia Inducible Factors
HIF1A	Hypoxia Inducible Factor 1 Alpha (aka HIF-1α)
HK	Hexokinase
HR	Hormone Receptor status in breast cancer
HRAS	Harvey Rat Sarcoma Viral Oncoprotein
HRE	Hypoxia Response Elements
HUVEC	Human Umbilical Vein Endothelial Cells
IDC	Invasive Ductal Carcinoma
IFNγ	Interferon Gamma
IFP	Interstitial Fluid Pressure
IGF-1	Insulin-like Growth Factor 1
IHC	Immunohistochemistry
IICs	Immune Infiltrating Cells
IL-1β	Interleukin-1 Beta (protein), *IL1B* (*gene/transcript*)
IL-6	Interleukin-6 (protein), *IL6* (*gene/transcript*)
IL-8	Interleukin-8 (protein), *CXCL8* (*gene/transcript*)
ILC	Invasive Lobular Carcinoma
IMG	Intussusceptive microvascular growth
IPA	Ingenuity Pathway Analysis
IRE1α	Inositol-Requiring Enzyme 1 Alpha
ISR	Integrated Stress Response
ITGA11	Integrin Subunit Alpha 11
Ki67	Marker Of Proliferation Ki-67
kDa	Kilodalton
LC3	Autophagy-Related Ubiquitin-Like Modifier LC3
LCIS	Lobular Carcinoma In Situ

LG	Low Glucose
logFC	Log_2 fold-change
LTRs	Long Terminal Repeats
LYVE1	Lymphatic Vessel Endothelial Hyaluronan Receptor 1
mAb	Monoclonal Antibody (aka MAB)
MCP-1	Monocyte Chemoattractant Protein-1 (aka CCL2)
MCS	Multi Cloning Site
MCT1	Monocarboxylate Transporter 1
MDSCs	Myeloid-Derived Suppressor Cells
MEK	Mitogen-Activated Protein Kinase Kinase 1 (aka MAP2K1)
miR	microRNA (aka miRNA)
MMPs	Matrix Metalloproteinases
MOI	Multiplicity of Infection
MSCs	Mesenchymal Stem Cells
MT	Prefix for genes encoded by the mitochondrial genome
mTOR	Mechanistic Target Of Rapamycin Kinase
MW	Molecular Weight
NAFs	Normal Activated Fibroblasts
NDUFS1/2	NADH:Ubiquinone Oxidoreductase Core Subunit S1/2
NFs	Normal Fibroblasts
NFκB	Nuclear Factor Kappa B Subunit 1
NK	Natural Killer cell
NSG	NOD.Cg-Prkdc^{scid} Il2rg^{tm1Wjl}/SzJ mice
OCR	Oxygen Consumption Rate
OXPHOS	Oxidative Phosphorylation
P2A	Porcine Teschovirus "self-cleaving" 2A peptide
P62	Sequestosome 1 (aka SQSTM1)
pAb	Polyclonal Antibody
PARP	Poly(ADP-Ribose) Polymerase
PBS	Phosphate Buffered Saline
P_{CMV}	Cytomegalovirus promoter (aka CMV)
pCR	Pathological Complete Response
PD-1	Programmed Cell Death 1
PDGFRβ	Platelet-Derived Growth Factor Receptor Beta
PDGFs	Platelet-Derived Growth Factors
PD-L1	Programmed Cell Death 1 Ligand 1
PECAM1	Platelet And Endothelial Cell Adhesion Molecule 1 (aka CD31)
PERK	Pancreatic EIF2-Alpha Kinase
PERKi	Pancreatic EIF2-Alpha Kinase inhibitor
PET-CT	Positron Emission Tomography - Computed Tomography
PFA	Paraformaldehyde
PFKFB3	6-Phosphofructo-2-Kinase/Fructose-2,6-biphosphatase 3
PGK1	Phosphoglycerate Kinase 1
PI3K	Phosphatidylinositol-4,5-Bisphosphate 3-Kinase
PIGF	Phosphatidylinositol Glycan Anchor Biosynthesis Class F
pO_2	Partial Oxygen (O_2) pressure
PR	Progesterone Receptor
Puro^R	Puromycin resistance

qPCR	Quantitative Polymerase Chain Reaction
RAF	Raf-1 Proto-Oncogene, Serine/Threonine Kinase
RAS	Kirsten Rat Sarcoma Viral Oncogene Homolog (aka K-RAS)
RE	Restriction Enzyme
RE8luc	Far Red light emitting luciferase
RER	Rough Endoplasmic Reticulum
RLUs	Relative Luminescent Units
RNASeq	RNA sequencing
ROBO	Roundabout Guidance Receptor
ROS	Reactive Oxygen Species
RPL / RPS	Ribosomal Protein L family / Ribosomal Protein S family
RRE	Rev Response Elements
sCAV1high	Tumor xenografts with high levels of stromal CAV1 (from CAFscr)
sCAV1low	Tumor xenografts with low levels of stromal CAV1 (from CAFshCAV1)
SD	Standard Deviation
SDF-1	Stromal Derived Growth Factor 1 (aka CXCL12)
SDHA/B	Succinate Dehydrogenase Complex Flavoprotein Subunit A/B
SEM	Standard Error Mean
SERCA	ATPase Sarcoplasmic/Endoplasmic Reticulum Ca2+ Transporting 2
SHG	Second Harmonic Generation
SLIT	Slit Guidance Ligand
SPARC	Secreted Protein Acidic And Rich In Cysteine (aka Osteonectin)
SRC	SRC Proto-Oncogene, Non-Receptor Tyrosine Kinase
SREs	Steroid Response Elements
STAT3	Signal Transducer And Activator Of Transcription 3
TAFs	Tumor-Associated Fibroblasts (aka CAFs)
TAMs	Tumor-Associated Macrophages
TCs	Tumor Cells (TNBC breast cancer cell lines in this case)
TCs^{luc}	TNBC Cell Lines transduced with a luciferase-expressing lentivirus
TGF-β	Transforming Growth Factor Beta
THBS1/2	Thrombospondin 1/2
TIE2	TEK Receptor Tyrosine Kinase
TIMPs	Tissue Inhibitor Of Metalloproteinases
TKIs	Tyrosine Kinase Inhibitors
TKs	Tyrosine Kinases
TME	Tumor Microenvironment
TNBC	Triple Negative Breast Cancer
TNF	Tumor Necrosis Factor
TPI1	Triosephosphate Isomerase 1
T_{reg}	Regulatory T cells
TSS	Transcription Start Site
UPR	Unfolded Protein Response
VASH1	Vasohibin 1
VEGFA	Vascular Endothelial Growth Factor (*gene*/*transcript*) VEGF-A (protein)
VEGFR2	Vascular Endothelial Growth Factor Receptor 2 (protein/*gene)*
WPRE	Woodchuck Hepatitis Virus Posttranscriptional Regulatory Element
XBP1	X-Box Binding Protein 1

GLOSSARY OF MEDICAL TERMS

Adapted from NCI Dictionary of Cancer Terms

(These medical terms are highlighted in **bold** in the main text)

Adjuvant therapy: Additional cancer treatment given after the primary treatment to lower the relapse occurrence. Adjuvant therapy may include chemotherapy, radiation therapy, hormone therapy, targeted therapy, or biological therapy.

BRCAness: Used to define tumors with loss-of-function mutations in either BRCA1 or BRCA2 or tumors that share molecular features of BRCA-mutant tumors such as a defect in double-strand break repair (DSBR) by homologous recombination repair (HRR).

Cancer Stage: Stage refers to the extent of cancer in an individual patient, such as how large the tumor is, and if it has spread. The TNM system is the most widely used cancer staging system: (i) T refers to the size and extent of the main primary tumor, (ii) N refers to the number of nearby lymph nodes that have cancer and (iii) M refers to presence of metastases in a secondary site.

Disease-free survival: The length of time between first-line therapy and relapse, thus survival time without any signs or symptoms of disease. In clinical practice, measuring the disease-free survival is a useful tool to evaluate treatment efficacy. Also known as DFS or relapse-free survival (RFS).

Immune-checkpoint inhibitors: Drugs that block certain proteins made by some immune system cells, such as T cells, and some cancer cells. These proteins help keep immune responses in check and can keep T cells from killing cancer cells. When these proteins are blocked, the “brakes” on the immune system are released and T cells are able to kill cancer cells more efficiently. Examples of checkpoint proteins found on T cells or cancer cells include PD-1/PD-L1 and CTLA-4/B7-1/B7-2. Some immune checkpoint inhibitors are used to treat cancer.

Incidence: The number of new cases of a disease diagnosed each year.

Metronomic: Treatment in which low doses of drugs are given on a continuous or frequent, regular schedule (such as daily or weekly), usually over a long time. Metronomic chemotherapy causes less severe side effects than standard chemotherapy. Giving low doses of chemotherapy may stop the growth of new blood vessels that tumors need to grow.

Neoadjuvant therapy: Treatment given as a first step to shrink a tumor before the main treatment, which is usually surgery, is given. Examples of neoadjuvant therapy include chemotherapy, antiangiogenic therapy, radiation therapy, and hormone therapy.

Overall survival: The length of time from either the date of diagnosis or the start of treatment for a disease, such as cancer, that patients diagnosed with the disease are still alive. In a clinical trial, measuring the overall survival is one way to see how well a new treatment works. Also called OS.

Pathologic complete response (pCR): The lack of all signs of cancer in tissue samples removed during surgery or biopsy after treatment with radiation or chemotherapy. To find out if there is a pathologic complete response, a pathologist checks the tissue samples under a microscope to see if there are still cancer cells left after the anticancer treatment. Knowing if the cancer is in pathologic complete response may help show how well treatment is working or if cancer will relapse. Also called pathologic complete remission.

Tumor Grade: Tumor grade is the description of a tumor based on how abnormal the tumor cells and the tumor tissue look under a microscope. It is an indicator of how quickly a tumor is likely to grow and spread. If the cells of the tumor and the organization of the tumor's tissue are close to those of normal cells and tissue, the tumor is called "well-differentiated" These tumors tend to grow and spread at a slower rate than tumors that are "undifferentiated" or "poorly differentiated," which have abnormal-looking cells and may lack normal tissue structures.

Predictive factor: A condition or finding that can be used to help predict whether a patient's cancer will respond to a specific treatment. Predictive factor may also describe something that increases an individual's risk of developing a condition or disease.

Prevalence: Total number of people in a specific group who have (or had) a certain disease, condition, or risk factor (such as smoking or obesity) at a specific time point or during a given period of time. For example, the prevalence of breast cancer may show how many women in the U.S. were diagnosed with breast cancer within the past 10 years, including those who are receiving treatment and those who are considered cured and are still alive on a certain date.

Prognosis: The likely outcome or course of a disease; the chance of recovery or recurrence.

Relapse: The return of a disease or the signs and symptoms of a disease after a period of improvement.

Sentinel lymph node: The first lymph node to which cancer is likely to spread from the primary tumor. When cancer spreads, the cancer cells may appear first in the sentinel node before spreading to other lymph nodes.

Sentinel lymph node mapping: The use of dyes or radioactive substances to identify the first lymph node to which cancer is likely to spread from the primary tumor.

1A. INTRODUCTION

1. INTRODUCTION

1.1 Breast Cancer: an overview

More than 1.5 million women worldwide are diagnosed with breast cancer each year, making it the most common form of cancer in women[1]. It does not only show the highest **incidence**, but it is also the first cause of cancer death in women, both worldwide and in Spain[2,3].

Breast cancer **prevalence**, together with awareness-raising efforts, has given breast cancer a high public profile. Therefore, research into breast cancer's treatments, early detection, and improved screening campaigns have been well funded. As a result, the survival rates for breast cancer have improved markedly over the decades[4].

However not all breast tumors are the same, and for some there are still not effective treatments, so nearly half-a-million women worldwide still die from this disease each year[2]. Recognizing breast cancer multiple subtypes by understanding the different phenotypic and molecular differences allow health professionals to stratify patients with distinct clinical implications[5]. An accurate classification turns out to be an efficient **prognostic** and **predictive** factor, both in terms of estimating the disease outcome (**disease-free** and **overall survival**) and the likelihood/lack of response to a specific treatment, respectively.

Strikingly, once distant dissemination (metastasis) has developed, breast cancer remains largely incurable with a median survival of patients with metastatic breast cancer ranging from 2 to 3 years[6]. One subtype with a particularly poor prognosis is Triple Negative Breast Cancer (TNBC). Here, the tumor cells lack the three receptors often leveraged for targeted treatment in breast cancer, leaving drug developers with little to aim at[7,8].

1.1.1 Breast Anatomy and Physiology

The breast is a highly complex and plastic tissue subject to cyclical and sequential changes, mainly related to hormonal variations, happening at different stages in a woman's life.

It is composed of glandular and adipose tissue held together by a framework of fibers called Cooper's ligaments. Each mammary gland located in the breast, termed lobe, is made of a series of milk-producing lobules. These lobes consist of clusters of lobules lined by an inner layer of milk-producing luminal epithelial cells, an intermediate layer of myoepithelial cells that provide structural support and assist in milk ejection during lactation, and an outer basement membrane[9]. The lobules continue into small ducts, showing the same structural and cellular organization, that finally merge into a unique duct draining each lobe. These ducts form a tree-branch-like network that converges at the base of the nipple and are responsible for delivering the milk to the surface of the skin through tiny pores in the nipple[10] **(Fig. 1)**.

Breast cancer usually begins in the ducts that carry milk to the nipple or within the lobules[11,12]. During metastasis, cancer cells escape the primary tumor through the tumor vasculature and, preferentially, via the breast lymphatic system which is in charge of excess fluid drainage and white blood cell transport[13,14]. As many cancers do, breast cancer possesses an organ-specific pattern of dissemination, metastasizing to the lung, liver, bones, and brain[15], which is enriched in one target organ or another depending on breast cancer subtype[16]. Ducts, lobules, and lymph nodes are key structures when determining the **stage** of a patient's breast cancer.

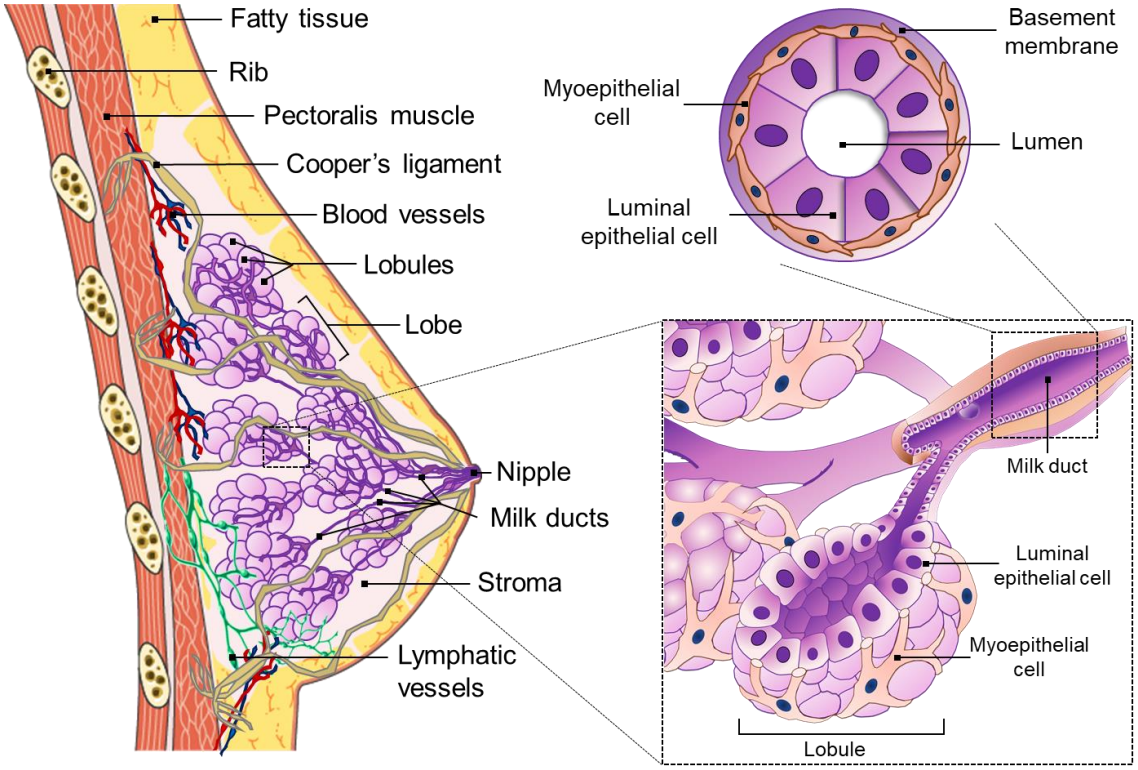

Figure 1. Breast anatomy and histology. Breast is composed of glandular and stromal tissue. Glandular tissue consists of lobes and ducts and the stroma includes the area in between lobes. Breast structures are presented at the macroscopic, lobular and cellular levels.

1.1.2 Classification of Breast Cancers

Breast cancer classification divides breast cancer into subtypes according to different criteria with the purpose of estimating the disease outcome (prognosis) or selecting the best treatment. Major criteria for classification include: histological type, tumor **grade**, tumor **stage**, receptor status and gene expression profile.

1.1.2.1 Histopathological Features

Histological type refers to the growth pattern of tumors, and whether they stay *in situ* (in its place of origin) or invade the surrounding tissues **(Fig. 2)**. Among these non-invasive *in situ* lesions, we find: (i) Ductal Carcinoma In Situ (DCIS), a precancerous lesion that starts in the milk ducts and has not spread into any normal surrounding tissue, and (ii) Lobular Carcinoma

In Situ (LCIS), a collection of abnormal cells (neoplasia), that starts growing in the milk-producing lobules at the end of breast ducts. Both, DCIS and LCIS are precancerous non-invasive neoplasia, and thus are not considered malignant cancer[17,18]. Around 1 out of every 5 new breast "cancer" cases are diagnosed as DCIS[12] .

Approximately 80% of breast carcinomas are Invasive Ductal Carcinoma (IDC), followed by Invasive Lobular Carcinomas (ILC) which account for approximately 10-15% of cases[19]. IDC and ILC are cancers that originated in the milk ducts or the lobules, respectively, but have broken through the basement membrane and spread into the surrounding tissues of the breast.

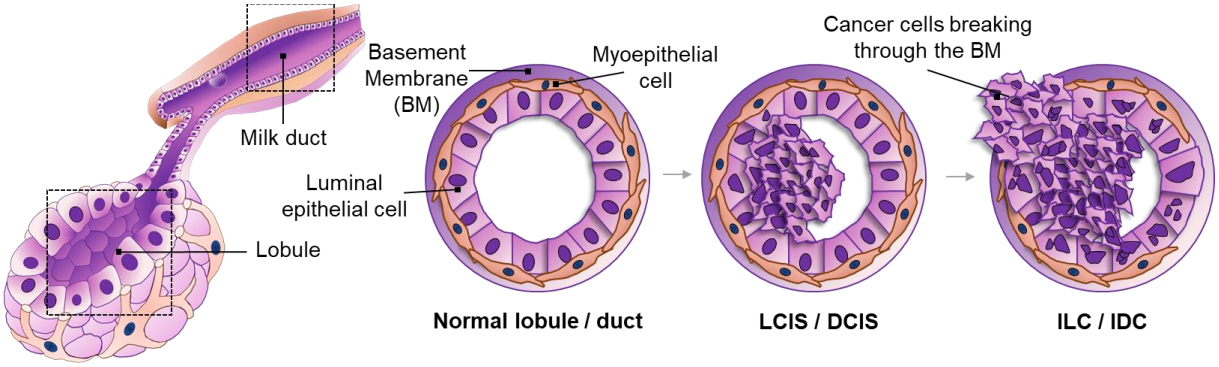

Figure 2. Histopathological classification of lobular and ductal breast cancer. Invasion of cancer cells through the basement membrane marks the transformation from *in situ* lesions (LCIS/DCIS) into invasive carcinomas (ILC / IDC).

1.1.2.2 Immunohistochemical Evaluation: Receptor Status

Breast cancer prognosis and treatment protocols still rely primarily on receptor status assessment by immunohistochemistry (IHC) of three markers: estrogen receptor (ER), progesterone receptor (PR) and human epidermal growth factor receptor 2 (HER2)[20,21].

The presence of one or more of these receptors suggests that a treatment targeting these pathways might be effective. Targeted proliferation-inhibition therapies for $HER2^+$ breast cancers include monoclonal antibodies (Trastuzumab and Pertuzumab) aimed at the HER2 receptor and tyrosine kinase inhibitors (Lapatinib) that interrupt the EGFR and HER2 signaling pathways[22]. Hormone receptor (HR) positive breast tumors (ER^+ and/or PR^+) are treated with endocrine therapy, which slows or stops the growth of hormone-sensitive tumors by: (i) blocking the body's ability to produce hormones or (ii) interfering with effects of hormones on breast cancer cells using estrogen receptor modulators (i.e. Tamoxifen) or antiestrogen drugs (i.e. Fulvestrant)[23,24].

Meanwhile, the absence of, or in the case of HER2, lack of overexpression of, all of these receptors (ER^- PR^- $HER2^-$), termed Triple Negative Breast Cancer (TNBC), indicates a need for the more toxic, non-targeted, classical chemotherapy[7,8].

Receptor status designation and Ki67 proliferation index (+ for high an - for low) largely correspond, but do not completely overlap, with more recent determinations of intrinsic molecular subtypes based on patterns of gene expression[25,26].

1.1.2.3 Gene Expression Profiling: Intrinsic Molecular Subtype

Pivotal studies of gene expression, made possible by high-throughput analysis platforms (i.e. microarrays), have resulted in the classification of breast cancer according to intrinsic molecular subtypes: luminal A, luminal B, HER2-enriched, normal-like, and basal-like breast cancer (BLBC)[25,26].

These five intrinsic subtypes have been validated by other studies with varying numbers of genes included in the signature[27]. Among these studies, PAM50, a 50-gene classifier mostly based in hormone receptor, proliferative and myoepithelial/basal-related genes[28], has been shown to be a significant **prognostic** and **predictive** factor for breast tumors in a clinical setting[29–31]. However these "gene signatures" are yet to be fully incorporated into clinical practice[32–34].

Table 1. Summary of breast cancer molecular intrinsic subtypes and IHC receptor status approximate equivalence with associated disease outcomes and prevalence. Slash (/) in between receptor status represents and/or (presence of both receptors/or just one of them).

Intrinsic subtype	IHC Receptor Status	Outcome	Prevalence[35]
Luminal A	ER^+ / PR^+ $HER2^-$ $Ki67^-$	Good	38.5%
Luminal B	ER^+ / PR^+ $HER2^-$ $Ki67^+$	Intermediate	19.8%
	ER^+ / PR^+ $HER2^+$ $Ki67^+$	Poor	
HER2-enriched	ER^- PR^- $HER2^+$	Poor	11.6%
Basal-like (BLBC)	ER^- PR^- $HER2^-$, basal $marker^+$	Poor	25.4%
Normal-like	ER^+ / PR^+ $HER2^-$ $Ki67^-$	Intermediate	4.7%

These subtypes have been associated with different prognoses, with patients harboring luminal A tumors having the best prognosis, and patients with HER2-enriched and BLBC having the worst[21]. The poor prognosis of these two subtypes derives from a higher risk of early **relapse** among those patients with an incomplete eradication of tumor cells (or **pathological complete response, pCR**) after treatment[36]. Furthermore, patients can be separated by treatment protocols based on these subtypes[25,26], since luminal and HER2 enriched subtypes are amenable to targeted therapies, while patients with BLBC currently have only chemotherapy as an option[28,37].

1.1.3 Triple Negative Breast Cancer (TNBC)

The majority of TNBCs (95%) are classified histologically as Invasive Ductal Carcinomas (IDCs)[38]. Although it has been discussed that TNBC and BLBC are the same subtypes, not all TNBC express basal cells markers[39]. It is true that most TNBCs are classified as BLBCs (80.6%), but some also fall into HER2-enriched (10.2%), normal-like (4.7%), luminal B (3.5%) and luminal A (1.1%) categories[40] **(Fig. 3A)**.

Behind its homogeneous nomenclature, TNBC is comprised of many different disease entities. Based on genetic expression profiling, TNBC has been categorized into six "TNBCtypes" associated with different potential treatments[41]: Basal-like 1 and 2 (BL-1, BL-2), Immunomodulatory (IM), a rare, histologically distinct form of TNBC associated with a favorable prognosis[42], Mesenchymal (M) and Mesenchymal stem-like (MSL) showing signatures related to epithelial to mesenchymal transition (EMT), and Luminal Androgen Receptor (LAR), characterized by androgen receptor (AR) signaling and *in vitro* sensitiveness to AR antagonists **(Fig. 3B)**.

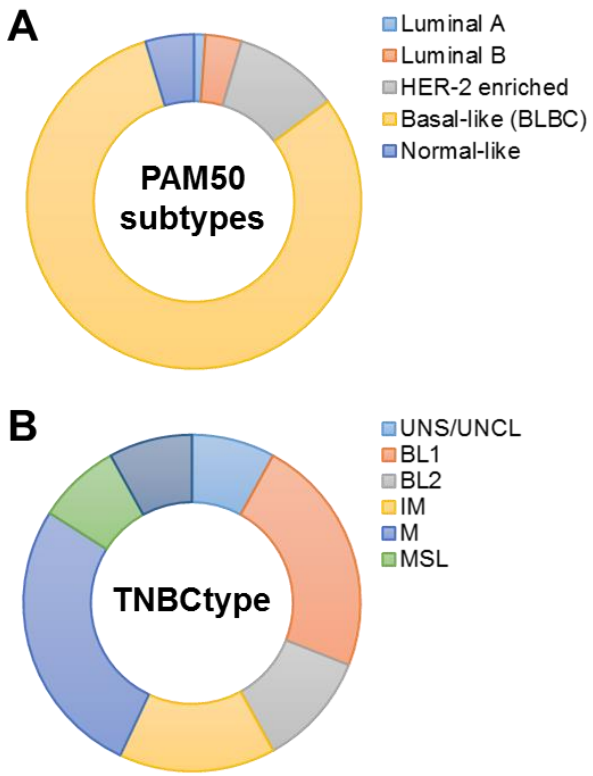

Figure 3. TNBC molecular subtypes according to (A) PAM50 classification or (B) TNBCtype; UNS, unstable; UNCL, unclassified.

In regard to treatment options, TNBC patients with mutations in BRCA1/2 or other genes related to homologous recombination-mediated DNA repair ("**BRCAness**") may benefit from treatment with platinum compounds and PARP inhibitors aimed at inhibiting DNA repair mechanisms[8]. The majority of actionable genomic alterations, related to PI3K/mTOR or RAS/RAF/MEK pathways, tend to be rare in TNBC[8]. Still, **immune-checkpoint inhibitors** are a very promising therapeutic option in **adjuvant** and **neoadjuvant** therapy of early-stage and metastatic TNBC[8,43].

However, the only proven current method for systemic management of triple-negative breast cancer, for both early-stage and metastatic settings, is cytotoxic chemotherapy[7,8]. In patients who receive **neoadjuvant** chemotherapy and show **pathological complete response (pCR)** on resection, **prognosis** is very good. However, patients who do not show complete pCR have a worse prognosis with a higher incidence of recurrences[8].

Despite optimal systemic chemotherapy, fewer than 30% of women with metastatic breast cancer survive 5 years after diagnosis, and virtually all women with metastatic TNBC will ultimately die of their disease[44]. Thus, there is an urgent need to find targeted therapies and stratify TNBC patients by treatment options.

1.2 Tumor Microenvironment (TME) / Tumor Stroma

Cancer progression was long conceived to be largely dependent on aberrant mutations in tumor cells. Therefore, a substantial share of cancer research has been focused on unveiling the dominant oncogenes and tumor suppressor genes whose respective malfunction serves to impart aberrant properties on normal cells[45].

However, a new understanding of tumor biology, where cancer cells are not the only active elements determining tumor progression, has emerged during the past decade[46,47]. Tumors develop within complex tissue environments, which they depend on for sustained growth, invasion, and metastasis. This environment, referred as tumor stroma or tumor microenvironment (TME), is supported by an extracellular matrix (ECM) where stromal cells, blood, and lymphatic vessels coexist and interact with tumor cells[45–48] **(Fig. 4)**.

Due to the non-physiological nature of the tumor cells it harbors, TME exhibits altered homeostasis and aberrant immune responses, actively contributing to tumor behavior and progression[49–51]. Tumor onset is characterized by an unresolved inflammatory response[52,53], where stromal cells accumulate and become activated in an attempt to normalize the situation. Nevertheless, their normal role in homeostasis maintenance turns dysfunctional and finally evolves to accommodate and support the growing tumor[54]. In this sense, tumors have been described as “wounds that never heal”[55], thus cells involved in angiogenesis and the response to injury, such as angiogenic vascular cells (AVCs), infiltrating immune cells (IICs), and fibroblasts will be on-site constituting the stromal cell compartment of the TME.

Cancer therapy is incorporating this paradigm and moving towards more integrative approaches, where personalized diagnostics and combinatorial therapeutics will target not only cancer cells but also stromal cells and pathways of the TME[56,57]. Furthermore, according to the key role of the TME in disease progression, stromal gene expression can provide valuable biomarkers able to predict clinical outcome in breast cancer patients[58–61].

Given the scope of this work and the fact that an immunodeficient NSG mice model[62] has been used in the presented results, illustrative but not comprehensive examples of the roles that the immune system plays in the TME are presented. Consequently, even though the TME also influences pre-metastatic niche formation and metastatic colonization of distant organs[46], the focus is presented in the influence the TME has over primary tumor growth, invasion, and dissemination.

1.2.1 Immune Suppression and Tumor-Associated Macrophages (TAMs)

A decisive step for the malignant progression of developing tumors is evasion and suppression of the host immune system[45,46]. Myeloid-Derived Suppressor Cells (MDSCs) and regulatory T cells (T_{reg}) have the ability to modulate the immune response in cancer **(Fig. 4)**:

- MDSCs are mobilized during tumorigenesis and infiltrate growing tumors, where they disrupt immunosurveillance mechanisms, including T cell activation[63], inhibition of natural killer (NK) cell cytotoxicity[64] and antigen presentation by dendritic cells (DCs)[65].
- T_{reg} cells also suppress tumor-associated antigen presentation and interfere with cytolytic granule release by NK cells[66,67]. In breast cancer, increased numbers of T_{reg} cells are associated with reduced overall survival[68].

These "brakes" on the immune system have been recently targeted in a variety of cancers, including HR^+ [69] and TNBC[8,43] breast cancers, using **immune checkpoint inhibitors** (i.e. PD-1/PD-L1 and CTLA-4 targeting antibodies), in an attempt to restore immune system function and allow T cells to attack the tumor[69,70].

Tumor-Associated Macrophages (TAMs) are another important IIC regulator of tumorigenesis, facilitating cancer cell invasion at the leading edge of tumors, by secreting matrix-degrading metalloproteinases (MMPs), promoting angiogenesis (discussed later) and, particularly in breast cancer, promoting tumor cell growth via paracrine EGF – CSF-1 signalling[71] **(Fig. 4)**.

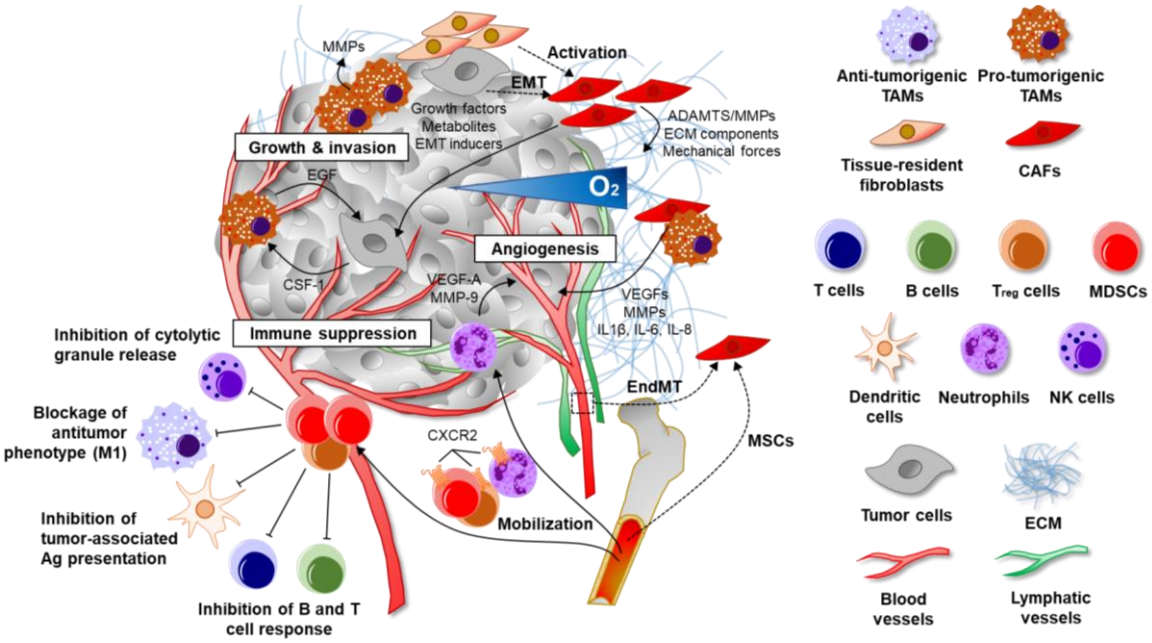

Figure 4. Tumor microenvironment (TME) - derived effects (solid arrows) over tumor progression and possible origins (dashed arrows) of Cancer-Associated Fibroblasts (CAFs). TME-associated cells play diverse roles in tumor growth, invasion, angiogenesis and immune suppression. Figure adapted from[46].

1.2.2 Cancer-Associated Fibroblasts (CAFs)

Consistent with the idea of tumors as “wounds that do not heal”[55], a predominant portion of the breast tumor stroma is occupied by specific fibroblasts termed Cancer-Associated Fibroblasts (CAFs)[72,73], which through the secretion of metabolites, growth factors and chemokines, as well as the production and modification of ECM, have been demonstrated to contribute to the core and emergent hallmarks of cancer[45,74] **(Fig. 5)**. Among these hallmarks, CAFs have been reported to sustain proliferative signaling, activate invasion and metastasis, reprogram energy metabolism, help to evade tumor immune destruction and induce angiogenesis[45,73,75–77].

Although CAF influx into the tumor is hypothesized to be mediated by growth factors secretion (FGFs, PDGFs, and TGF-β) derived from cancer and immune infiltrating cells (IICs)[78–80], a detailed model for CAFs recruitment and origin is still being unraveled[75,81,82].

In order to sustain proliferative signaling of cancer cells, CAFs express and secrete mitogenic growth factors, such as hepatocyte growth factor (HGF), insulin-like growth factor-1 (IGF-1), stromal derived growth factor (SDF-1), EGF-family members, as well as various fibroblast growth factors (FGFs) with the ability of stimulating cancer cell proliferation[72,77,83–86].

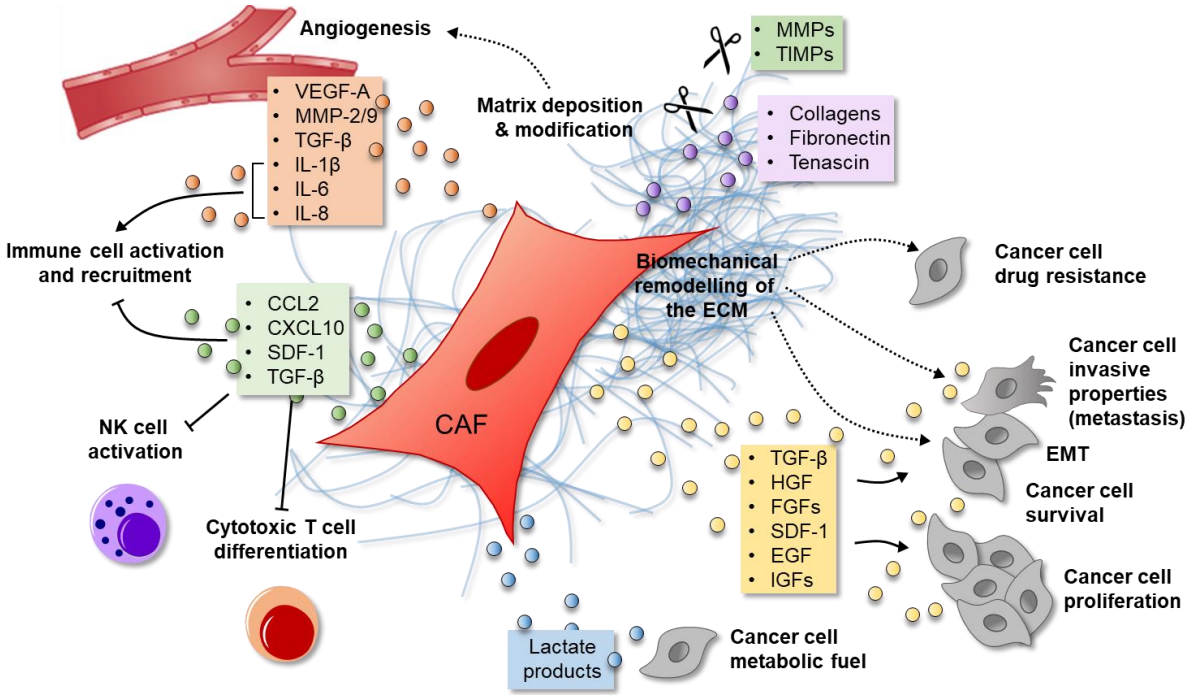

Figure 5. Cancer-Associated Fibroblasts (CAFs) display key contributions to the hallmarks of cancer. Figure adapted from[75].

In addition to producing growth factors and other ECM cues, CAFs also favor cancer cell proliferation and survival by metabolically reprogramming the TME[87]. A series of studies suggest that CAFs are induced by cancer cells to switch on aerobic glycolysis, thereby secreting lactate and pyruvate, which in turn serves as fuel for cancer cell proliferation[87,88].

This metabolic support phenotype, termed “Reverse Warburg effect”, is displayed by CAFs in which the scaffold protein Caveolin-1 (CAV1; see below) is downregulated, resulting in an activated TME that drives early tumor recurrence, metastasis and poor clinical outcome in breast cancer[89,90].

Beyond MDSCs and T_{regs}, CAFs also help the tumor avoid immune destruction by inhibiting cytotoxic T and NK cells, partly by secreting transforming growth factor-β (TGF-β), thus promoting an anti-inflammatory response that allows tumor growth and progression[91]. Once the primary tumor acquires the ability to evade host immune responses and cancer cells enter the circulation, metastatic dissemination is underway[46]. Prior to this event, cancer cells have to locally invade the surrounding tissues.

One of the initiating steps of primary tumor invasion is epithelial to mesenchymal transition (EMT), during which tumor cells lose epithelial markers and acquire mesenchymal features that confer stem-like properties and a migratory phenotype[92–94]. In breast cancer, CAFs modulate the capability of tumors to invade locally: (i) by activating EMT programs in cancer cells via secretion of TGF-β[95], (ii) by stimulating c-Met signaling via HGF production, which promotes both invasiveness and proliferation[96] and (iii) by modifying the surrounding ECM both by exerting physical forces[97–101], and by secreting matrix components[72] and matrix modifying proteases[102–105], a function also partially carried out by TAMs[106,107].

In addition to the aforementioned mechanism, CAFs also influence tumor growth, metastatic behavior, and immune cell infiltration via regulation of angiogenesis[45,75,77], as discussed later.

1.2.2.1 CAFs and the Extracellular Matrix (ECM)

The importance of ECM properties for cancer progression is such that it affects the clinical prognosis and response to therapy of breast tumors[58–60]. In breast cancer, tumors can be stratified across four subclasses (ECM 1-4) based strictly on ECM composition, which is predictive of patient outcome[108]. Furthermore, increased breast density and fibrosis have been long linked with an increased predisposition to breast tumors[109–111].

As tumors grow and become invasive, the stromal content also increases. Periostin and tenascin C, produced in part by CAFs, are generally absent in normal adult mammary tissue, but they become expressed in breast tumors[112–116].

By exerting physical forces[97–101] and secreting ECM proteins[72] and ECM-remodeling enzymes[102–105], CAFs can profoundly alter the architecture and physical properties of the ECM. The resulting increased stiffness and fibrosis have been proposed to: (i) induce a rise in interstitial fluid pressure (IFP), associated with an impaired delivery of therapeutics[117] and (ii) facilitate tumor cell migration and dissemination[97–101]. Consequently, reducing interstitial

pressure in some tumors results in improved tumor hemodynamics and a more favorable distribution of cytotoxic drugs[118–121].

1.2.2.2 Cancer-Associated Fibroblasts (CAFs): Origin and Markers

Despite being described as early as 1858 by Virchow[122], fibroblasts remain a mysterious and heterogeneous cell population that is classified by what it is not rather than by what it is. They are the non-vascular, non-epithelial and non-inflammatory cells of the connective tissue[123] with a likely mesenchymal lineage origin[75].

Fibroblasts within healthy tissues most often exhibit spindle morphologies and are generally considered to have negligible metabolic and transcriptomic activity. Thus, they are speculated to be in a quiescent or resting state. Upon physical damage or acute/chronic inflammation of the functional organ parenchyma, these quiescent fibroblasts become "activated" as part of a coordinated wound healing response aimed at achieving tissue regeneration and repair[124,125].

Fibroblast activation in response to tissue injury results in a robust induction of protein synthesis activity or "secretory phenotype" producing[72,81,125]:

- Inflammatory cytokines, such as TNF, IFNγ, IL-6, CCL5, and CXCL10, which results in the recruitment of immune cells in charge of removing damaged cell and debris by phagocytosis. In addition, some of these proinflammatory cytokines, along with CAF-derived VEGF-A play a role in tissue neo-vascularization (angiogenesis).
- Growth factors, such as TGFβ, HGF, FGF, EGF, and PDGF, which induce fibroblast and epithelial proliferation, associated with the scarring and re-epithelization processes aimed at tissue repair.
- ECM components, such as fibronectin and collagens (I, III, IV, and V), aimed at repairing the damaged ECM scaffold. Accumulation of fibronectin and collagen I, along with fibroblast- and IICs-derived VEGF-A production also promote angiogenesis.
- Matrix metalloproteinases (MMPs) and tissue inhibitors of metalloproteinases (TIMPs) involved in ECM remodeling.

These normal activated fibroblasts (NAFs) also acquire contractile capabilities, which together with ECM deposition and modification, enable wound closure and production of connective tissue. This newly acquired contractility requires the induction of expression of the cytoskeletal smooth muscle actin protein α (αSMA, also known as ACTA2), which along with that of vimentin, is acquired through TGFβ-mediated signaling[81,126].

Altogether, the acquired synthetic and contractile abilities result in the aforementioned increased secretory and migratory functions that amplify NAFs activation, recruitment, and proliferation. Once the wound healing process is complete, the number of activated fibroblasts

decreases significantly owing to apoptosis or reprogramming, and the quiescent phenotype is restored[127].

In the case of persisting and sustained damaging stimuli, such as the development of cancer lesions, a chronic wound healing response, also known as tissue fibrosis, is triggered. As stated before, tumors can be considered as "wounds that never complete the healing process"[55], exhibiting continuous repair activation.

Fibroblast associated with this cancer scenario, are termed Cancer-Associated Fibroblasts (CAFs) or Tumor-Associated Fibroblasts (TAFs). They are present within the tumor stroma or TME in aberrantly high numbers as compared to normal tissue, and in addition to the functions associated with NAFs, they display distinct traits which significantly impact cancer progression (see above).

It is unclear from where CAFs arise from during disease progression[75,81,82,128]. Studies have reported CAFs to arise from bone-marrow-derived precursors[129], mesenchymal stem cells (MSCs)[75,128], endothelial cells undergoing endothelial to mesenchymal transition (EndMT)[130], resting tissue fibroblasts and possibly from epithelial tumor cells following EMT[131,132] **(Fig. 4)**. In line with this heterogeneity of possible origins, although many different markers can identify activated fibroblasts, none of them is specific for fibroblasts[133]. Such markers include fibroblast-specific protein 1 (FSP1; also known as S100A4), αSMA, vimentin, platelet-derived growth factor receptor β (PDGFRβ), ITGA11 and fibroblast activation protein α (FAP)[72,81,134].

In this case, regression of CAFs to a quiescent state is hypothesized to be limited by epigenetic regulation[135]. In fact, breast tumor stromal cells (presumably CAFs) display unique epigenetic changes not observed in fibroblasts from normal mammary tissue[136,137].

1.3 Tumor Angiogenesis

Although an oncogenic event may allow tumor cells to evade immune surveillance or may enhance their survival, the large-scale growth of a solid tumor ultimately requires a blood supply, a hypothesis dating back to 1971[138]. This blood is provided to the tumor through the formation of new blood vessels from preexisting ones, a process called angiogenesis.

Angiogenesis, now accepted as a hallmark of cancer[74], constitutes the response to a growing need for oxygen and nutrients from the bloodstream, without which tumors would succumb to dormancy[46]. Once a tumor lesion exceeds a few millimeters in diameter, hypoxia (inadequate oxygen supply) and nutrient deprivation, triggers the formation of an actively growing and infiltrative vascular network, a phenomenon known as "angiogenic switch"[139,140]. This switch is associated with the progression of pre-malignant stages of epithelial tumors (i.e. breast DCIS), where a basal lamina isolates the tumor from the vascularized surroundings to a malignant stage (i.e. breast IDC)[141].

According to the revised model of sprouting angiogenesis[142], in response to a proangiogenic stimulus, the endothelial cells (ECs), that constitute the blood vessel inner layer, become activated and induce both the remodeling of EC cell-to-cell junctions and the surrounding vascular basement membrane (BM), along with the detachment of pericytes (outer layer of perivascular support cells) **(Fig. 6)**. These coordinated functions allow ECs at the leading edge of the sprout to form filopodia and migrate in the direction of the angiogenic stimulus. These migrating ECs, known as tip cells, are followed by endothelial stalk cells, which proliferate to elongate the vessel sprout, form a lumen and recruit pericytes for stabilization. In order to generate a perfused vessel, the tip cells of two migrating EC fronts contact and fuse (anastomose). Upon perfusion, blood vessel maturation ensues; ECs become quiescent phalanx cells, which deposit BM, and pericytes cover the newly formed vessel.

In adults, most blood vessels are quiescent, and angiogenesis only occurs under specific conditions such as during the female reproductive cycle, after an exercise-induced increase in muscle mass[143] or as a response to pathophysiological conditions, such as ischemia and wound healing[144].

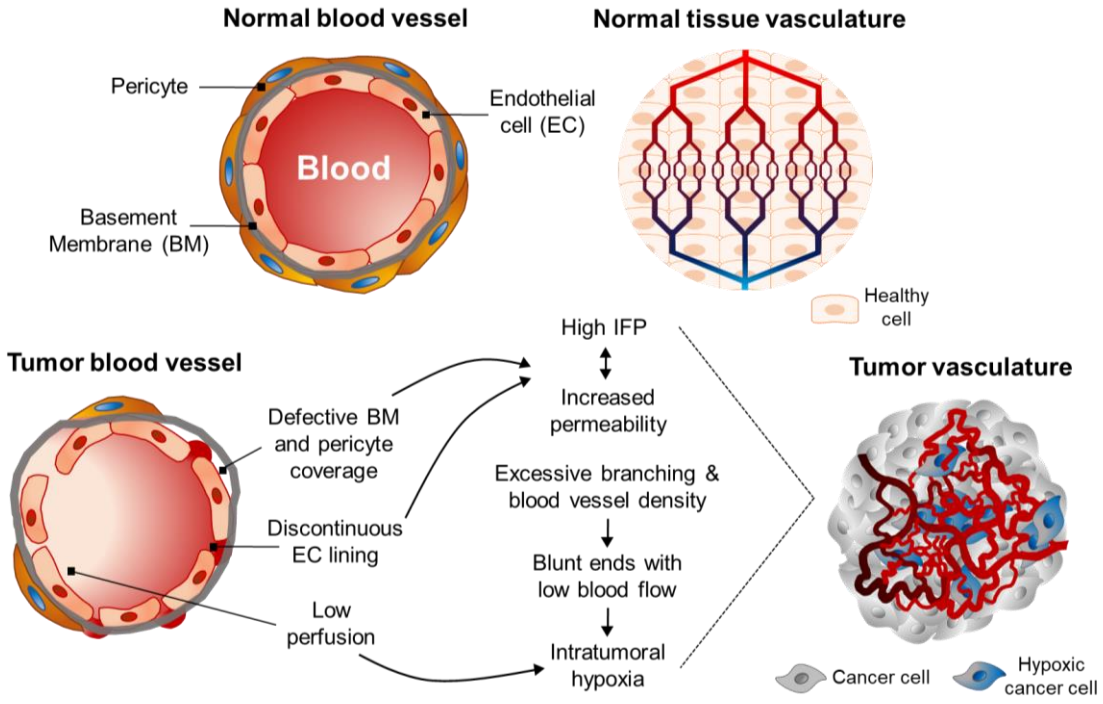

Figure 6. Structural and dysfunctional blood vessel features present in tumor vasculature.

In the case of tumor angiogenesis, owing to excessive and sustained proangiogenic signaling[145–147], tumor vasculature very often acquires an aberrant morphology, characterized by excessive branching and blood vessel density, abundant and abnormal binges and blind ends, discontinuous EC lining, and defective BM and pericyte coverage[148,149]. These structural features, associated with impaired vascular maturation, are all indicative of poor vessel functionality, both in terms of low perfusion and increased permeability[148,150] **(Fig. 6)**.

As a consequence of the generation of this impaired vascular network, the tumor continues to be deprived of an adequate oxygen and nutrient supply, factors which along the non-resolved wound healing response contribute to aggravate vascular dysfunctionality by further promoting an aberrant proangiogenic signaling[151–155]. Subsequent intratumoral hypoxia, besides being a driver of tumor angiogenesis, contributes to cancer cell escape and metastasis by providing an aggressive selection pressure for resilient stem-like tumor cells that subsequently migrate away from the primary tumor[46,73].

1.3.1 Alternative Modes of Tumor Vascularization

Although tumor vascularization has traditionally been defined as the sprouting of new vessels from pre-existing vessels (angiogenesis), new findings show that the blood vessels that support tumor growth or tumor rebound after therapy can also originate from:

- Intussusceptive microvascular growth (IMG)[156], a nonsprouting angiogenesis where the capillary wall extends into the lumen to split a single vessel in two has been reported in various tumor types, including breast cancer[157–160].
- Vascular co-option[161], the process by which cancer cells surround and hijack host tissue vessels resulting in their incorporation by the tumor. This mechanism mainly occurs in highly vascularized tissues such as liver, lungs, and brain[162] and is also observed in metastatic growth in those organs[163–167].
- Postnatal vasculogenesis[168], where endothelial progenitor cells (EPCs) are recruited from the bone marrow to sites of vascular damage present in the tumor[169]. EPC mobilization is mediated by various cytokines (VEGF-A and CXCL12/SDF-1) and proteolytic enzymes (MMP9) released from the tumor microenvironment[170–172].
- Cancer cells themselves, which either constitute vascular channels mimicking blood vessels (via vasculogenic mimicry[173]) or differentiate from cancer stem cells (CSCs) into functional ECs[174,175] or pericytes[176].

1.3.2 Microenvironmental Regulation of Tumor Angiogenesis

Given that tumor vascularization is critical for tumor growth and metastasis, understanding the tumor microenvironment pathways, cells and factors controlling this process is key to develop new tactics aimed at limiting cancer progression.

1.3.2.1 Extracellular Matrix, Secreted Factors, and Metabolism

Since its discovery and characterization[177,178], mechanistic and inhibitor studies of tumor angiogenesis have largely focused on vascular endothelial growth factor (VEGF-A) by showing its role in the induction of sprouting (EC tip formation)[179,180], vasodilation and increased vessel permeability[150,181]. However new concepts and insights in the angiogenesis field have emerged over the past years and original paradigms are being revisited[182–185].

Despite the focus on VEGF-A, the role of various growth factors (i.e. PDGF-B[120,186], TGF-β[187], FGFs[188,189], VEGF-B/C[190], and ANGP1/2[191]), cytokines (i.e. IL-1β[192], IL-6[193], IL-8[194–196], MCP-1/CCL2[197,198], and SDF-1[170,199,200]), and proteases (MMP2/9, ADAMTS1/5/8)[201] in the tumor faulty vascularization process has also been acknowledged.

In addition, the tumor stroma is made of multiple ECM components that regulate the angiogenic process[201,202]. In this setting, integrins constitute the main cell-matrix adhesion molecules that integrate signals among the ECM and specific activated cytokine or growth factors receptors. This crosstalk can determine whether a cell is in the correct environment and will accordingly instruct it to survive, migrate or invade; in this regard optimal, angiogenic growth factor stimulation relies on integrin-mediated adhesion to an appropriate ECM protein[203,204].

On this subject, ECM composition, remodeling and physical properties have been reported to control tumor angiogenic potential and invasiveness by showing both pro-angiogenic and vascular stabilizing roles[183]. In tumors, the vascular BM, remodeled by MMP2/9 and MT1-MMP, is frequently discontinuous and loosely associated with ECs and pericytes[149,150], which contributes to increased vascular leakiness and facilitates tumor extravasation and metastasis[205]. Besides the BM that surrounds the vessels, tumor stromal ECM regulates angiogenesis by: (i) acting as a depot for VEGF-A, FGFs, PDFGB and TGF-β, proangiogenic sequestered factors that are released in their bioactive form upon proteolytic processing of the ECM by proteases (i.e. MMPs)[202,206], (ii) direct proangiogenic (fibronectin, periostin, tenascin C, and perlecan)[207–210] or angiostatic (SPARC and THBS1)[211,212] functions exerted by ECM components and (iii) changing its biophysical and mechanical properties through matrix deposition, crosslinking and degradation, processes enhancing ECs migration and increasing tumor interstitial pressure (promoting inefficient drug delivery)[117,120].

Moreover, several new classes of angiogenesis regulators affecting various aspects of EC biology have been recently described, including: (i) Bone Morphogenetic Proteins (BMPs), with enhancing[213,214] and suppresing[215] roles in tumor angiogenesis depending on the family members involved, (ii) axonal guidance molecules (SLITs[216], Semaphorins[217] and Ephrins[218,219]), a group of signaling families regulating endothelial sprouting navigation, and (iii) miRNAs, also called angiomiRs[220], short non-coding RNAs that negatively regulate the expression of angiogenesis-related genes at the post-transcriptional level[221].

Lastly, EC metabolism has lately been put forward as a determinant angiogenesis regulator, a recent concept indicating that angiogenesis is not only controlled by the balance between pro- and antiangiogenic factors[222]. Despite their proximity to blood oxygen, ECs from tumor vessels rely primarily on aerobic glycolysis to generate energy, in particular tips cells[223]. In this regard, glucose transporter (GLUT1) and glycolytic enzymes (PFKFB3) have been shown to be

regulated by proangiogenic factors (VEGF-A and FGF2) and to be involved in tip cell migration and stalk proliferation[224,225].

1.3.2.2 TME-Associated Cells in Angiogenesis

Although hypoxic and nutrient-deprived cancer cells can be an important source of pro-angiogenic factors, many signals originating from different tumor stromal cells sustain and regulate tumor vascularization; mainly IICs and CAFs.

In the case of TAMs, high macrophage numbers are associated with increased vascular density and reduced survival in human tumors[226–228]. Its recruitment into the tumor, where they produce a series of proangiogenic factors (VEGF-A, PIGF, IL-1β, IL-6 and IL-8)[229–231] and proteases (MMP2/9)[232], is mediated by hypoxia-induced expression of CXCL-12/SDF-1 and Angiopoietin-2, which interact with CXCR4 and TIE2 TAMs receptors respectively[233].

Other angiogenesis-regulating IICs include: (i) neutrophils, recruited by CXCL chemokines, which play an important role during the early stages of tumor progression[230,234] by producing VEGF-A, FGF2 and MMP9 in a STAT3-dependent manner[235] and (ii) platelets, which are activated at sites of vascular hyperpermeability by contact with ECM and cancer cells[236], where they become activated and secrete VEGF-A, FGF2, and PDGFs[237]. Besides directly promoting angiogenesis, platelets initiate a wound-healing response that recruits other IICs and CAFs, further fostering tumor vascularization[238]. The function of other IICs is reviewed elsewhere[183].

Aside from IICs, CAFs have a well-established proangiogenic function in tumors, where co-implantation in xenografts enhances vascularization and accelerates growth[72,239]. Besides being a major source of tumor VEGF-A[240], CAFs also support tumor angiogenesis by producing PDGF-C[241], FGFs[188,189], IL-8[196] and recruiting ECs precursors and macrophages through CXCL12/SDF-1 secretion[77]. As promoters of the wound healing response in solid tumors[75], CAFs also enhance and regulate angiogenesis by altering the composition[207–210] and biomechanical properties[242] of the ECM, as well as releasing latent factors during its modification[202,206] **(Fig. 4 and 5)**.

1.3.3 Emergent Pathways Governing Tumor Vascularization

Under intratumoral hypoxic conditions, hypoxia-inducible factors (HIFs) activate, translocate to the nucleus and bind to hypoxia response elements (HRE), resulting in the transcription of various genes involved in angiogenesis, metastasis, apoptosis, and glycolysis[243]. Besides HIFs activation, the highly evolutionarily conserved unfolded protein response (UPR), has recently been linked to the modulation of physiological and tumor vascularization[244].

Originally described as a consequence of misfolded protein accumulation, UPR can be triggered under stress conditions for the endoplasmic reticulum (ER), such as nutrient deprivation and hypoxia[245–247], or independently. In the context of tumor angiogenesis, these

stressors can be alleviated by vascularization of the affected tissue. In this regard, activation of the three branches of the UPR, PERK-ATF4, IRE1α/XBP1 and ATF6, has been linked with proangiogenic signaling[244] **(Fig. 7)**.

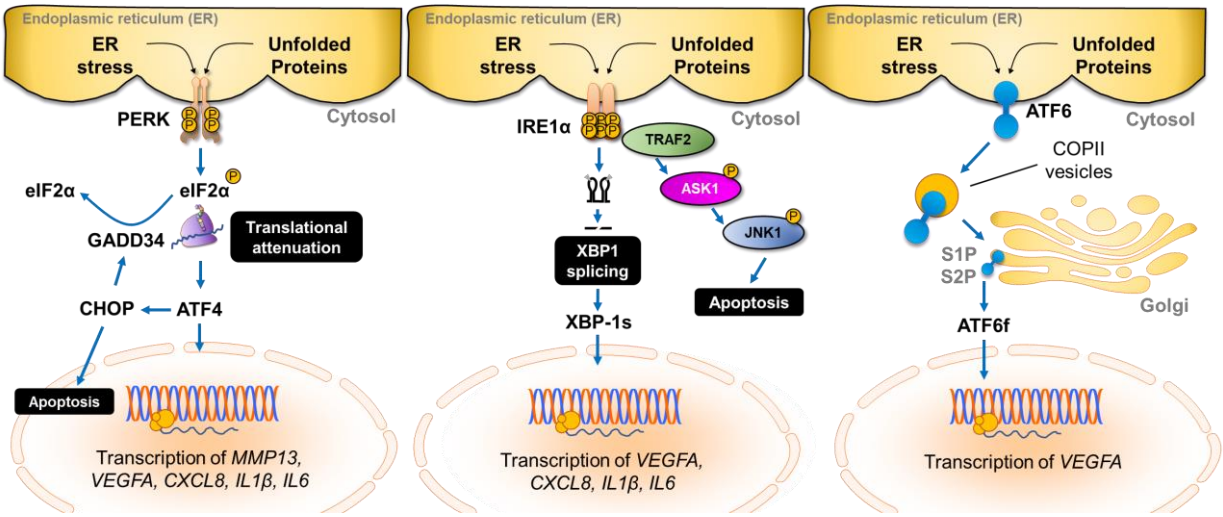

Figure 7. Unfolded protein response axes involved in proangiogenic factor production. From left to right, upon accumulation of misfolded proteins, hypoxia, low nutrient concentrations or other ER stressors: (A) PERK activates via dimerization/autophosphorylation, provoking a global translational attenuation by phosphorylating eIF2α; and favoring the translation of alternative open reading frames, such as active ATF4. ATF4 expression leads to CHOP induction, which reverses translation arrest by activating GADD34, or upon sustained stress leads to apoptosis. (B) IRE1α oligomerizes and autophosphorylates, triggering the splicing of an XBP1 intron, resulting in the production of an active XBP-1s. Alternatively, upon severe stress, a pro-apoptotic TRAF2-ASK1-JNK1 cascade is activated. (C) Post-activation, ATF6 translocates to the Golgi where is cleaved by S1P and S2P proteases and the resulting active ATF6f is shuttled to the nucleus. Upon axis activation (A) ATF4, (B) XBP-1s or (C) ATF6f transcription factors, respectively, are shuttled into the nucleus where they induce the transcription of various angiogenic cues. Figure adapted from[244].

Transcription factors from all three branches of the UPR have consensus sites in the VEGF-A promoter and have been shown to bind and drive its transcription[248]. In addition to VEGF-A production, *in vitro* ER stress induction, and consequent UPR activation have also been shown to increase production of other proangiogenic factors such as IL-8, FGF2, and angiogenin (ANG)[247,249,250].

Both PERK-ATF4[251–253] and IRE1α/XBP1[254,255] axes, have been linked to tumor vascularization *in vivo* through the induction of VEGF-A, IL-1β, IL-6, and IL-8. Modulating ER stress thus results in an attractive target for alternative antiangiogenic therapies, for instance, preclinical studies have demonstrated the anti-angiogenic/-tumoral potential of targeting PERK[256,257] and XBP1[258] axes in TNBC and pancreatic cancer models, respectively. Other approved, and undergoing clinical trials, anti-angiogenic therapies are discussed in the next section.

1.3.4 Antiangiogenic Therapies

Approval of the first antiangiogenic agent dates back to 2004; it was a humanized monoclonal antibody (mAb) targeting VEGF-A (Avastin®) prescribed for patients with metastatic colorectal cancer[259]. Since then, new **adjuvant** and **neoadjuvant** mono- and, generally combination therapies[260,261], targeting VEGFs, FGFs, PDGFs, and angiopoietin-2 (ANGP2) or its receptors (VEGFRs, FGFRs, PDGFRs, and TIE2, respectively) have been developed, including mAbs, ligand traps, vascular disrupting agents, and tyrosine kinase inhibitors (TKIs)[45,182,261,262]. Nonetheless, clinical trials in breast cancer have offered mixed results, thus it currently lacks an approved antiangiogenic therapy[263].

Based on the assumption that tumors deprived of their blood supply would succumb due to a lack of oxygen and nutrients, high hopes were placed on antiangiogenic therapy. However, the clinical application of antiangiogenic therapies targeting VEGF/VEGFR has demonstrated that the anticancer potential of these drugs is limited and associated with tumor resistance[264,265] and, in some cases, with an increase in cancer aggressiveness and metastasis[266–269].

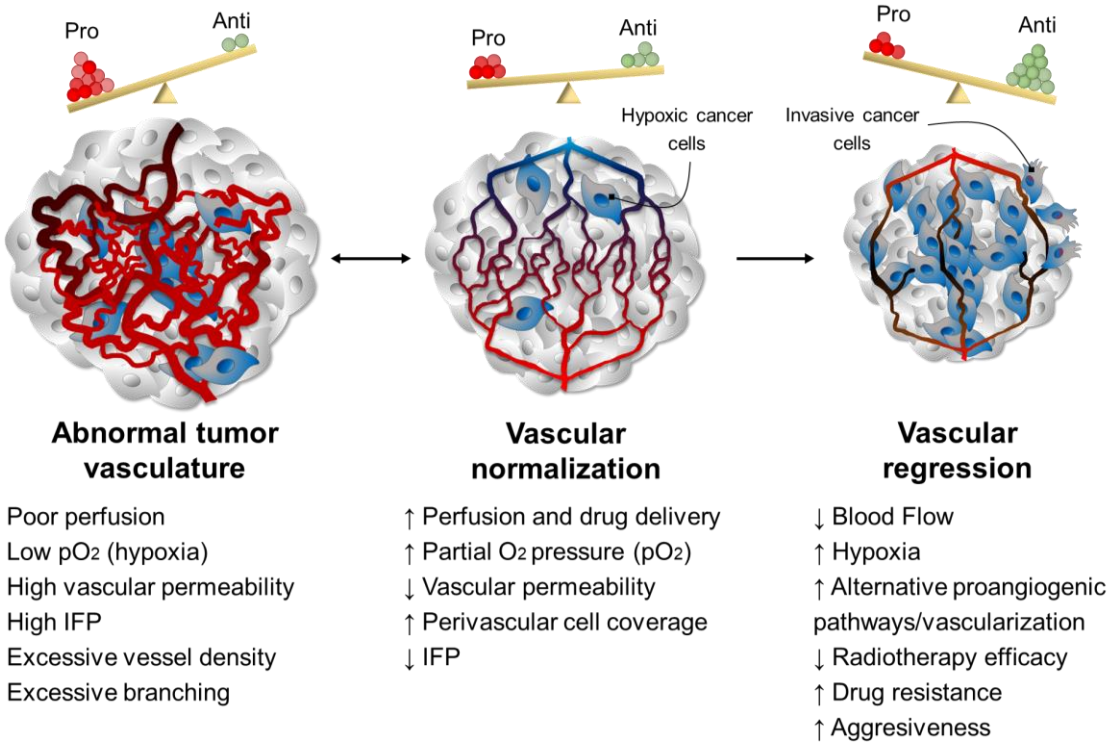

Figure 8. Tumor vascular normalization versus regression depends on a fine equilibrium between pro- (in red) and anti- (in green) angiogenic cues.

In this regard, tumors undergo a number of adaptations to survive the initial vascular regression and consequent acute hypoxia that follows angiogenesis blockade[270]. Therefore, these changes are aimed at either regenerating the tumor vasculature through alternative signaling pathways and cell effectors, or surviving in its absence, for instance: (i) metabolic reprogramming[271–273], (ii) enforcement of compensatory alternative pro-angiogenic signals

(IL-8, PIGF, FGF2, CXCL12/SDF-1, and ANGP2)[274–276], (iii) recruitment of myeloid-derived angiogenesis inducers (i.e. TAMs and neutrophils)[277–279], (iv) activation of CAFs[241] and (v) usage of angiogenesis-independent modes of tumor growth, such as IMG or vascular co-option[159,161,164].

Besides being behind the induction of the adaptive changes already mentioned, tumor hypoxia is also responsible for the increase in cancer aggressiveness, chemo-/radiotherapy resistance, and metastasis[46,73,280–284]. Overall, hypoxia induces an imbalance in the production of pro- and anti-angiogenic factors, which leads to the enhanced, fast and chaotic blood vessel formation[145–147,155]. This results in the generation of a hypoxic/faulty angiogenesis loop, where dysfunctional tumor vascularization and consequent hypoxia feed on one another[152].

In an attempt to tackle these issues and improve the efficacy of antiangiogenic therapies, the concept of vascular normalization versus vascular regression arose[146,285]. Vascular normalization advocates for the restoration of the balance between pro- and anti-angiogenic signals in the tumors, via low dose or **metronomic** antiangiogenic therapies, thus prompting selective pruning of immature dysfunctional vessels and stabilization of perfused ones[266,286]. Consequently, tumor blood flow improves, facilitating chemotherapy delivery, tumor oxygenation, and T-cell extravasation, which also opens new possibilities for either targeting tumor metabolism[287] or combining chemotherapy and immune checkpoint inhibitors with vascular normalization therapies[288] **(Fig. 8)**.

Lastly, even though new imaging techniques with targeted tracers to assess patient response to therapy have been developed[289–291], validated markers for appropriately selecting individuals with cancer amenable for antiangiogenic therapy are still needed[292,293].

1.4 Caveolin-1 (CAV1): A Prognostic Marker?

Given the importance of CAFs in the modulation of breast cancer growth, metastasis and response to therapy, understanding the molecular mechanisms driving CAFs behavior and finding CAFs markers for breast cancer patient stratification has been the focus of research recently[58–61].

Amidst these biomarkers, changes in the expression levels of Caveolin-1 (CAV1) in CAFs have been associated with the metabolic reprogramming of the tumor[87,88,294] and the modification of the ECM architecture[101], which in turn modulate breast cancer cell growth and metastasis.

1.4.1 Caveolae: Specialized Membrane Microdomains

CAV1 is a scaffolding protein with multiple binding partners that is a key structural component[295–297], along with cavins[298,299], of cell surface caveolae. Caveolae are non-planar lipid rafts that appear as 50-100nm plasma membrane invaginations under electron microscopy (EM) examination[300,301] **(Fig. 9)**. Caveolae are very heterogeneous both in terms

of membrane distribution[302] and abundance in different cell types[303]. While endothelial, smooth-muscle, adipocyte and fibroblast cells display a high abundance of caveolae[304], lymphocytes, neurons, and hepatocytes show low, but functionally important levels of caveolae[305–307].

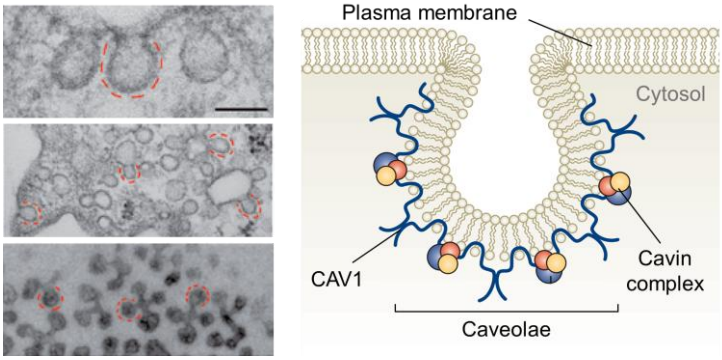

Figure 9. Caveolae structural organization. EM micrographs (left, top to bottom) showing ultrastructure of caveolae in fibroblasts and complex arrangements of caveolae in cultured adipocytes and in skeletal muscle. Scale bar: 100 nm. Caveolae schematic representation (right). Reproduced with permission from[303].

As lipid rafts, caveolae constitute specialized membrane microdomains that pre-organize, sequester and compartmentalize signaling molecules for efficient signal transduction[308]. For instance, the GTPase HRAS[309,310], SRC kinases[311] and endothelial nitric oxide synthase (eNOS)[312–314] signaling can be regulated by caveolae compartmentalization.

Besides regulating signaling cascades through compartmentalization, caveolae are involved in: (i) detecting physical stimuli like shear stress and membrane tension (mechanosensing)[303], (ii) clathrin-independent endocytosis[303], (iii) calcium signaling, through the formation of junctional complexes coupling the plasma membrane with the endoplasmic reticulum (ER)[315], and (iv) cholesterol transport[316,317].

In this regard, caveolar lipid rafts are enriched in cholesterol, along with saturated fatty acids and sphingolipids. Moreover, such is the importance of cholesterol, that not only it is essential for caveolae formation[318], but also regulates CAV1 expression (by binding to steroid regulatory elements, SREs, of its promoter)[316,319]. In addition, CAV1 is a cholesterol-binding protein[320] that shuttles cholesterol between Golgi, the plasma membrane, and mitochondria. In fact, CAV1 deficiency leads to cholesterol accumulation in mitochondrial membranes, driving mitochondrial dysfunction and aerobic glycolysis[317].

1.4.2 Caveolin-1 (CAV1): Structure Related to Function

In order to allow caveolae formation and carry out the aforementioned functions, CAV1 shows a very particular structure **(Fig. 10)**. CAV1 is a 22 kDa integral membrane protein, with a putative hairpin domain embedded within the membrane and both the amino- and carboxy-terminus facing the cytoplasm. This unique configuration is due to the presence of an intramembrane domain (102–134 aa) that prevents CAV1 from completely spanning the plasma membrane in a traditional double-pass fashion[321].

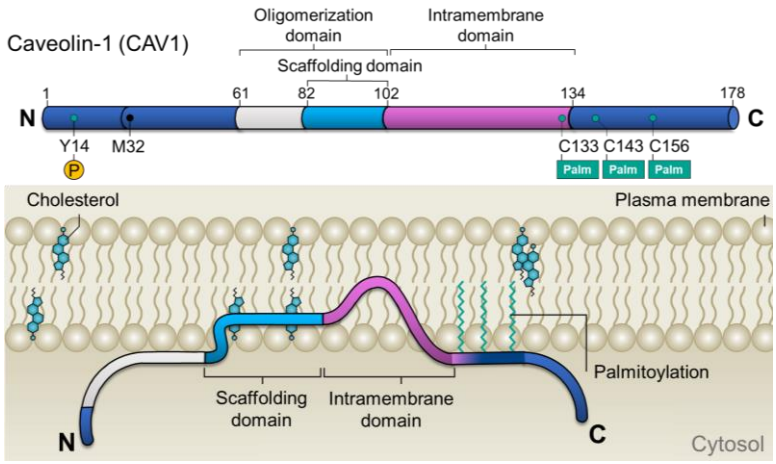

Figure 10. Domain organization of CAV1. Graphic representation of CAV1 domain organization. CAV1 palmitoylation (Palm) sites, involved in CAV1 targeting to lipid rafts are indicated in green, a Tyrosine phosphorylation (P) site (Y14) in orange, and the starting Methionine (M32) of CAV1β isoform is shown in black. Adapted from[303].

Other important domains include the oligomerization domain (61–102 aa), which mediates the homo-oligomerization of CAV1 necessary for caveolae formation[322]. The oligomerization domain also includes the Caveolin scaffolding domain (CSD), not only key for the interaction of CAV1 with caveolae-associated proteins such as eNOS, tyrosine kinases (TKs) and G-protein subunits[323], but also important for cholesterol binding[324].

Regarding its synthesis, CAV1 is produced in the rough endoplasmic reticulum (RER) as an integral membrane protein, then it traffics through the Golgi complex, where it associates with cholesterol and forms higher-order oligomers, to the cell surface via discrete carriers[303].

1.4.3 Caveolae and Caveolin-1 in Disease

Although CAV1 and caveolae are dispensable for life and mice deficient for them are viable, lack of caveolae, either as a result of mutations or gene expression changes in CAV1, results in a variety of diseases, including muscular dystrophy, lipodystrophy, cardiovascular disease and cancer[303,308,325].

Even if CAV1 is involved in cancer progression, its role is still unclear. CAV1 deficiency leads to increased proliferation, tumorigenesis[326–328] and metastasis[90]. However, a tumor-promoting role has been reported in prostate cancer[329] and melanoma[330]. These contrasting observations could be explained by differences in which specific tumor compartment is affected by the CAV1 loss (either cancer or stromal cells) and the diverse tumor stages reported.

Regarding CAV1 levels in the tumor stroma, although multiple mechanisms have been proposed to explain the deregulation of CAV1 levels in CAFs, the reason behind these changes still remains a puzzle[128,323]. While some studies have associated loss of Caveolin-1 (CAV1) in CAFs with poor clinical outcomes in breast cancer in terms of decreased survival, early tumor recurrence, lymph node metastasis and resistance to tamoxifen[89,90,331–334], exceptions have been reported[101]. CAV1 thus appears to have a complex role in tumor stroma, and further work is needed to justify the potential use of CAV1 for prognosis.

1B. AIMS & OBJECTIVES

The general aim of the research embodied in this thesis report was to explore and contribute further knowledge regarding the impact of the expression levels of stromal CAV1, on breast cancer progression, and assess potential translational opportunities for future studies.

In this regard, previous data had been obtained using mice models where either tumor cells or the stromal component were of murine origin. Precedent studies had shown how data derived from these systems offered mixed results when translated into a clinical setting.

In an attempt to overcome these problems and define with greater precision cancer cell - stromal CAV1 interactions, both the stromal compartment (CAFs) and cancer cells of the presented tumor xenograft are of human origin.

Our specific objectives were:

1. To develop and validate strategies to functionally and mechanistically dissect the specific contribution of stromal CAV1 levels to tumor biology, both *in vitro* and *in vivo*. In order to do so, different tailored strategies for the perturbation of CAV1 protein expression in a selective manner were to be deployed and tested.
2. To assess the functional impact on tumor growth and progression in vivo of such selective intervention of stromal CAV1, using state-of-the-art xenograft-based mouse models, which allow for the full characterization of established human breast cancer models, including the recapitulation of the metastatic process.
3. To gain unbiased mechanistic insight on the contribution of stromal CAV1 protein levels, both to basic stromal cell biology as well as at systems-level tumor behavior. A core component of these studies was to be founded on detailed transcriptome profiling across different contexts (*in vitro* versus *in vivo*).
4. To explore the therapeutic potential of pharmacological interventions leveraging the novel knowledge generated by our functional and molecular studies.
5. To contribute functional screens for small molecules potentially capable of intervening CAV1 protein levels on cancer-associated fibroblasts (CAFs).

2. MATERIALS & METHODS

2. MATERIALS & METHODS

2.1 Animal model

NOD.Cg-*Prkdc*^{scid} *Il2rg*^{tm1Wjl}/SzJ (NOD-SCID IL2rγnull 4; NSG) immunodeficient mice were purchased from Jackson Laboratory (Stock No: 005557; Bar Harbor, ME, USA) and housed under specific pathogen-free conditions in accordance with CNIC institutional guidelines. Experiments were performed in accordance with Spanish legislation on animal protection and were approved by the local governmental animal care committee (Protocol Proex 57/14). Breast cancer cell injections in the mammary fat pad were conducted on young female mice ranging from 8 to 10 weeks old.

2.2 Cell lines and cell culture conditions

Human breast cancer cell lines: MDA-MB-436 (ATCC® HTB-130™), MDA-MB-468 (ATCC® HTB-132™), MDA-MB-231 (ATCC® HTB-26™), HCC1937 (ATCC® CRL-2336™) and MCF7 (ATCC® HTB-22™), Breast Cancer-Associated Fibroblast (CAF) cell lines: CCD-1068Sk (ATCC® CRL-2086™) and CCD-1069Sk (ATCC® CRL-2089™), prostate cancer PC-3 (ATCC® CRL-1435™), and cervix cancer HeLa (ATCC® CCL-2™) cell lines were obtained from the American Type Culture Collection (ATCC; www.atcc.org). Human Umbilical Vein Endothelial Cells (HUVEC) were acquired from Lonza (Cat. No CC-2519) and cultured in 0.2% gelatin-coated flasks. Primary pancreatic CAFs (panCAF 1788 – 1790) were kindly provided by Dr. Manuel Hidalgo.

2.3 Isolation and culture of primary human breast Cancer-Associated Fibroblasts (CAFs)

To isolate the primary breast stromal fibroblasts used in this study, primary cancer tissues were obtained from female breast cancer patients[335] at Instituto Europeo di Oncologia (IEO, Milan) with written consent from participants and with the approval of the Institutional Review Board of IEO. The breast cancer tissue specimens used for isolation of stromal fibroblasts were diagnosed as invasive ductal carcinoma with histological grade II and classified as luminal A subtype with estrogen receptor-negative/progesterone receptor-negative/human epidermal growth factor receptor 2-negative. These patients had undergone mastectomy but had not been treated with preoperatory neoadjuvant chemotherapy. The fresh tissues were diced and digested with 160 μg ml^{-1}collagenase A (Sigma, Cat. No COLLA-RO) and 25 μg ml^{-1} hyaluronidase (Sigma, Cat. No H1136) at 37 °C for 3 h. Then the cells were collected and cultured in complete DMEM on Corning™ BioCoat™ Collagen I coated flask (Corning™ Cat. No 356485) until cells grew into a confluent monolayer. After 2–3 passages, a unique homogeneity of stromal fibroblasts was formed. Fibroblasts were then infected with pLenti-GFP (Cell Biolabs, Cat. No LTV-400) and sorted for a homogeneous positive population.

All cell types were cultured according to standard mammalian sterile tissue culture protocols and maintained in a humidified incubator at 37ºC and 5% CO_2 atmosphere.

2.4 Generation of CAFscr/CAFshCAV1 and MDA-MB-436^{luc} cell lines

All lentivirus used are described in the Lentiviral vector generation paragraph. Lentiviral infection was conducted at a Multiplicity of infection (MOI)=10 on 6-well plates containing 1x10^5 cells/well. Viral dilution was prepared in pre-warmed Opti-MEM™ (Gibco, Cat. No 11058021) containing 4 ng/ml of protamine sulfate. After removal of cell growth medium, 1 ml of the viral dilution was added per well. Primary breast Cancer-Associated Fibroblasts (CAFs), obtained as described in the previous section, were incubated for 4h and then 2ml of complete medium was added on top. After incubation for 24h post-infection, previous medium was removed and fresh pre-warmed medium was added. Luciferase-expressing MDA-MB-436 cells (MDA-MB-436^{luc}) were generated by infection with pLVX-CMV-ChFP2A-RE8luc. The expression of Cherry fluorescent protein in the infected cells allowed Fluorescence Activated Cell Sorting (FACS) of positive cells. Afterward, functional luciferase expression was assayed using a luminometer. Non-targeting control (CAFscr) and CAV1 silenced (CAFshCAV1) fibroblasts were obtained by infection with pLVX-CMV-ChFP2A-Puro^R-miR30.scr and four different CAV1 targeting pLVX-CMV-ChFP2A-Puro^R-miR30.shCAV1 lentivirus respectively. The expression of puromycin resistance gene allowed for the selection of positively infected cells using 2 µg/ml puromycin (Sigma, Cat. No P8833). Another set of CAFs used in the mitochondrial content and ROS determination assays, negative for CherryFP fluorescent protein, was generated by infection with pLVX-CMV-Puro^R-miR30.scr/shCAV1 virus.

2.5 Cell culture mediums

Human breast cancer cell lines were cultured in DMEM/F-12 (Lonza, Cat.No 12-719Q). Primary human breast Cancer-Associated Fibroblasts (CAFs), HeLa, and PC-3 cells were passaged in Dulbecco's Modified Eagle Medium, 25mM Glucose (Lonza, Cat. No BE12-604F). For experiments using different glucose concentrations, Dulbecco's Modified Eagle Medium, No Glucose (Gibco, Cat.No 11966-025) was used and glucose content was adjusted accordingly: DMEM High Glucose (HG) contains 25mM glucose and DMEM Low Glucose (LG) 2.5mM glucose. CAF cell lines (CCD-1068/69sk) were grown in IMDM (Lonza, Cat. No 12-722F) and primary panCAFs in RPMI (Lonza, BE12-702F). All DMEM, DMEM/F-12, and IMDM media were supplemented with 10% South American-sourced FBS (Gibco, 10270-106), 100 units/ml penicillin, 100 µg/ml streptomycin and 2 mM L-glutamine unless stated otherwise. For panCAFs supplementation also included 10 mM HEPES, 1 mM pyruvate and 20%FBS. HUVEC cells were grown in Endothelial Cell Growth Medium (PromoCell, Cat.No C-22010) + ECGM SupplementMix (Promocell, Cat.No C-39215). Endothelial Cell Growth Medium 2,

PromoCell (Cat.No C-22011) + ECGM-2 SupplementMix (PromoCell, Cat.No C-39216) was used for the sprouting assays.

2.6 *In vitro* drug treatments of CAFs

150,000 fibroblasts per well were seeded in 6-well plates using complete HG DMEM. 18h post-seeding, different treatments, glucose concentrations and vehicle controls were applied. After removal of seeding medium: (1) 48h treatments of 5mM 2-Deoxyglucose (2-DG, Sigma, Cat. No D6134) and 25mM Sodium dichloroacetate (DCA, Sigma Cat. No 347795) treatments were performed in complete DMEM 5mM glucose, vehicle used was dH_2O. (2) Glutathione treatments, 5mM GSH (Sigma Cat. No G4251) and 5mM GSH-EE (Sigma Cat. No G1404), were applied for 24h in complete LG DMEM, vehicle used was PBS pH 6.5 + 1mM EDTA. (3) 48h treatment of 25µM Lovastatin (Tocris, Cat. No 1530) in DMSO was carried out in complete LG DMEM, (4) 24h treatments of 1µM Thapsigargin (Tocris, Cat. No 1138) in DMSO were done in both HG DMEM and LG DMEM, (5) 2µM 24h mitoQ (kindly provided by Dr. José Antonio Enríquez) treatments dissolved in PBS were performed in HG and LG DMEM. A series of treatments were applied for 24h to fibroblasts without post-seeding medium change and using DMSO as vehicle: either (1) 10µM PERK inhibitor GSK2606414 (PERKi, Cayman, Cat. No 17376), (2) 1µg/ml Tunicamycin (Sigma, Cat. No T7765) or (3) 10µM 4µ8C (Sigma, Cat. No SML0949).

2.7 Orthotopic injection of cancer cells

Cells for mammary fat pad injection were cultured in the absence of antibiotics. Each flask was washed with PBS prior to trypsinization. After detachment cells were centrifuged for 5 min at 300rcf, the resulting pellet was washed and centrifuged twice in PBS to remove traces of FBS. Cells were finally resuspended in PBS before assessing cell concentration with a Z1 Cell Coulter (Beckman), >95% cell viability was checked by Trypan Blue exclusion. A total volume of 20µl was injected into the fat pads of 8-10-week-old female NSG mice using a 50µl Hamilton syringe (Hamilton, Cat. No 80400). Hair in the injection area was removed the day before. Each individual injection was composed of 7µl of Matrigel (Corning, Cat. No 354230, Lot. No 5173009) + 13µl PBS cell suspension containing: either $1x10^6$ breast cancer cells or $1x10^6$ breast cancer cells + $1x10^6$ CAFs. Mammary glands were harvested 4-5 weeks post-transplantation, fat adhered to the tumor was eliminated before fixation to avoid problems during vibratome cutting. Tumor volume was assessed using a precision caliper to measure the width (W) and length (L). Volume was then calculated using the spherical assumption formula $(W^2 \times L)/2$.

2.9 *In vivo* bioluminescence imaging

A dose of 150mg/kg mice body weight of D-luciferin dissolved in 100µl of PBS (Promega, Cat. No E1605) was injected intraperitoneally in the lower left abdominal quadrant in groups of 4-5 mice. 3 min after injection mice were sedated using 2% isoflurane and placed in the imaging chamber of an IVIS Lumina III Imaging system (PerkinElmer, Massachusetts, USA). 5 min post-injection a series of pictures with different exposures (0.1 to 2 seconds, Binning Small, F/Stop 1) were taken every minute for 30 min in order to obtain data from the plateau of luciferase light emission and avoid signal saturation. Average luciferase emission was quantified as Relative Luminescent Units (RLUs, proportional to photons/second) across experimental groups in comparable exposure and light production kinetics using Living Image software 4.4 (PerkinElmer).

2.10 Hypoxyprobe™, blood vessel perfusion and permeability *in vivo* assays

The following sterile saline solutions were injected into the tail vein before performing primary tumor resection (mastectomy): (1) For the hypoxia assays, 100µl of 2 mg/ml Pimonidazole-HCl (Hypoxyprobe, Cat. No HP10-200kit), 60 min before resection, (2) For the perfusion assays, 100µl of 0.5 mg/ml biotin labeled Isolectin GS-IB4 from *Griffonia simplicifolia* (Invitrogen, Cat. No I21414), 20 min prior resection, (3) For the permeability assays, 100µl of 5mg/ml 70,000MW biotynilated dextran (Invitrogen, Cat. No D1957), 30 min ahead of resection. After mastectomy, the fat adhered to the tumor was removed as its prone to cause problems during vibratome cutting, extracted tumors were cut in half and placed in cold 4% PFA for later inclusion in agarose and vibratome processing.

2.11 Tumor inclusion and vibratome cutting

Tumor fixation after mastectomy was performed in 4% PFA at 4ºC for 2h on a rocking platform. Before inclusion in agarose, three washes with cold PBS were carried out. A solution of 3% UltraPure™ Low Melting Point agarose (Invitrogen, Cat. No 16520050) was prepared in PBS and kept at 45ºC. Tumors were placed with the middle cut facing the bottom of a 24-well plate and melted agarose was poured on top. Plates were placed afterward at 4ºC to facilitate agarose polymerization and PBS was added to maintain sample hydration. After plate removal, agarose blocks containing the fixated sample were cut into 200µm thickness sections using a Vibratome® 1500. Obtained tissue slices were placed in cold PBS for further processing.

2.12 Vibratome immunofluorescence (IF) staining and imaging

Tissue slices placed in individual wells from a 24-well plate were permeabilized using PTT Buffer (PBS + 0.3% Triton X-100 + 0.1% Tween20) for 1h at 4ºC, blocked with PBT Buffer (PBS + 0.3% Triton X-100 + 4% Goat Serum (Jackson Immunoresearch, Cat. No 005-000-121)) for 2h at 4ºC and incubated overnight at 4ºC with the corresponding primary antibodies

in PBT buffer: (1) for CD31 stainings, 1:250 of Anti-PECAM 1 Armenian Hamster antibody, clone 2H8 (Merck Millipore, Cat. No MAB1398Z), (2) for hypoxic regions detection using Pimonidazole, 1:100 of biotinylated Hypoxyprobe™-1 mAb (Hypoxyprobe, Cat. No HP10-200kit), (3) for HIF1A nuclear localization, 1:250 of Anti-HIF-1-alpha Rabbit antibody (Abcam Cat. No ab51608), (4) for pericyte coverage, 1:250 of Anti-PDGFRB Rabbit antibody, clone G.290.3 (Invitrogen Antibodies, MA5-15143) or (5) for lymphatic vessel detection, 1:250 of Anti-LYVE1 Rabbit pAb (Abcam, ab14917). After incubation, six 15 min washes in cold PT2 buffer (PBS + 0.15% Tween) and a final cold PBS wash were carried out. Secondary antibody or labelled streptavidin incubations in PBT Buffer were performed at 4ºC for 6 h: (1) for CD31 stainings, 1:500 of Alexa Fluor® 647 AffiniPure Goat Anti-Armenian Hamster IgG (H+L) (Jackson Immunoresearch, Cat. No 127-605-160), (2) for pimonidazole, dextran and isolectin detection, 1:500 of BV421 Streptavidin (BD Biosciences, Cat. No 563259), (3) for HIF1A and LYVE1 stainings, 1:500 of Goat anti-Rabbit IgG (H+L) Secondary Antibody, Alexa Fluor® 647 conjugate (Thermo Fisher Scientific, A-21245), or (4) for PDGFRB detection, 1:500 of BV421 Goat Anti-Rabbit IgG (BD Biosciences Cat. No 565014). Post-secondary incubation, three 15 min washes in PT1 buffer at 25ºC (PBS + 0.3% Tween), a 4ºC overnight wash in PT2 Buffer, two 15 min washes in PT2 Buffer and a final cold PBS wash were applied. Sample staining was finished including all tissue slices in slides using Fluoromount™ (SIGMA, Cat. No F4680). Images were acquired with Zeiss LSM 700 confocal microscope at 21-23 ºC, in series of stacks separated by 10µm using a Plan-Apochromat 10x/0.45 M27 Objective. Dextran extravasation details were acquired using an LD LCI Plan-Apochromat 25x/0.8 Imm Korr DIC M27 Objective. Individual tile-scanned stacks were exported into .tiff files using ZEN 2012 Software, and maximal intensity projections were generated using ImageJ (https://imagej.nih.gov/).

2.13 Image analysis and registration of tumor xenograft vasculature

In-depth unbiased characterization of tumor xenograft vascular networks was based on a 3D automated image analysis pipeline[336]. Here, modules of the pipeline that permit the extraction of parameters regarding the morphology and physiologically meaningful features (angioarchitecture) of the tumor vasculature were used (see Table S1).

In brief, CD31 z-stacks were preprocessed by means of non-local means filtering[337] to enhance their quality. Subsequently, a rough segmentation of the tumor tissue was produced by thresholding. The tissue volume was used to assign voxels of the denoised image volumes outside of the tumoral areas to the background (i.e. with zero value). The intensity of the images was subsequently automatically adjusted.

After preprocessing, the vascular network labeled by CD31 was segmented. To achieve this, 3D Frangi filtering[338] was applied to the pre-processed image volumes to identify tubular

structures with a diameter within the range 2.5 – 10 μm. The segmentation of the vascular network was afterward used to quantify its morphological features, such as complexity (fractal dimension) and geometric/topological properties (vascular volume/surface area/breadth/Euler characteristic density and surface area per vascular volume ratio).

In order to study the angioarchitecture of the network, the skeleton of the vasculature was extracted along with the branching and ending points of the network. Furthermore, morphological characteristics of the individual vessels that comprise the vasculature were calculated. It should be noted that spur segments of CD31 that were not branching were considered as artifacts and not part of the main skeleton. Moreover, for the normalization of some of the metrics to mm^3 of tissue, a more accurate definition of the tumor tissue was required. Towards this aim, multi-level thresholding[339] was applied to all denoised images volumes following adjustment of their intensity. Only voxels of the highest intensity classes were considered as part of the tumor tissue.

Statistical analysis of the parameters was performed by means of One-way ANOVA and Bonferroni's correction for multiple comparisons. Lastly, Paraview[340] was used for the 3D visualization of the segmented volumes and skeletons. The code was written in MATLAB (Mathworks).

For image analysis of tumor-derived vibratome tissue slices obtained from *in vivo* perfusion assays, JACoP plugin (https://imagej.nih.gov/ij/plugins/track/jacop2.html), a colocalization tool for ImageJ, was used. Manders' coefficients (fraction of CD31 channel overlapping Isolectin channel, as markers of total and perfused vessels) from thresholded tumor images were represented. Higher coefficient values are indicative of an increased number of properly perfused tumor capillaries.

2.14 Second Harmonic Generation (SHG) imaging

Imaging of fibrillary collagen in vibratome sections was performed using a Zeiss LSM 780 microscope equipped with a short pulse laser (Spectra-Physics Mai Tai DS [pulse<70 ps] Laser) capable of performing two-photon microscopy. Images were acquired in series of stacks separated by 10μm using a W Plan-Apochromat 20x/1.0 DIC D=0.17 M27 75mm Objective. Individual tile-scanned stacks were exported into .tiff files using ZEN 2012 Software, and maximal intensity projections were generated using ImageJ (https://imagej.nih.gov/).

2.15 Micro-PET-CT Imaging and Processing

All PET-CT studies were performed in the Advanced Imaging Unit at CNIC, with a nanoScan PET-CT device (Mediso, Hungary). Animals were fasted overnight, and full body CT scanning was performed 1h after 18F-fluorodeoxyglucose (18F-FDG) injections (12MBq dose), followed by metabolic PET static acquisition for 15 min. Image analysis was performed in pre-fused and

pre-reconstructed images with Osirix (Aycam Medical Systems, LLC); recurrent tumors were selected and maximum standardized 18F-FDG uptake value (SUVmax) was calculated for each animal. Amide software[341] was used for image visualization and 3D rendering of tumors.

2.16 Collagen 3D *in vitro* cell culture

A solution of rat tail Collagen I High Concentration (Corning®, Cat.No 354249) was prepared at a concentration of 1.6 mg/ml according to manufacturer's protocol (NaOH neutralization) and kept on ice to avoid polymerization. Taking care of not forming bubbles, 5ml of this collagen solution was mixed with 1.2ml of supplemented DMEM containing $5x10^5$ fibroblasts. 500µl of the resulting cell suspension was plated in Ultra-Low attachment 24-well plates (Corning® Costar®, Cat.No CLS3473-24EA). Plate was placed in a cell incubator for 30 min to facilitate matrix polymerization. After gel polymerization, culture medium was added on top. Gels were cultured at 37 °C, 5% CO2 for 7 days. Fibroblasts were then extracted from the matrix using a solution of 5mg/ml of Collagenase Type 2 (Worthington, Cat.No LS004176) prepared in PBS. Collagen digestion process was carried out at 37ºC in 15 min, cells were then spun down for 2 min at 350rcf and washed once in cold PBS. The resulting cell pellet was either processed for protein or RNA extraction.

2.17 Protein extraction and Western Blot (WB) analysis

All cell cultures were approximately 80% confluent at the time of lysis. For p62 and LC3 WBs cells were lysed in a buffer containing 8 M Urea, 0.5% (v/v) Triton X-100, 100 mM DTT, 1xComplete® protease inhibitor (PI), and 8% phosphatase inhibitor cocktail I and III, respectively (Sigma). The rest of lysates were performed in RIPA Buffer containing the same protease and phosphatase inhibitors as the Urea buffer. Protein concentration was determined by Bradford protein assay (BioRad, Cat. No 5000006). Equal amounts of proteins were separated using NuPAGE® Novex® 12% or 4–12% Bis-Tris Gels (Invitrogen, Cat. No WG1402BOX). iBlot® 2 NitroCellulose Membranes (Invitrogen, Cat. No IB23001) were blocked and antibodies diluted in a 1:1 mixture of Odyssey blocking buffer (Li-Cor) and TBST (20 mM Tris, pH 7.6, 137 mM NaCl with 0.1% Tween 20). Bound antibodies were imaged by near-infrared fluorescence using fluorescent dye-labeled secondary antibodies and Odyssey NIR scanner (Li-Cor Biosciences). Images were processed using the Li-Cor Odyssey software image studio 3.1. Antibodies used for WB are listed in Table S3. All immunoblots displayed in main figures are cropped.

2.18 RNA purification and qPCR analysis

RNA was isolated from either primary tumor tissue or cultured cells with the Rneasy® Plus Mini Kit (Qiagen, Cat. No 74136). Representative portions of tumor tissue were first placed in lysis buffer and disrupted with sterile ceramic beads using a MagNA Lyser (Roche), with two

rounds of 6500rpm for 30 seconds each, with care taken to maintain the sample cold. RNA was quantified by spectrophotometry (ND1000 Spectrophotometer, NanoDrop, (Thermo Scientific, Wilmington, USA) and RNA integrity in samples used for RNASeq analysis was monitored by RNA 6000 Nano Kit (Agilent Cat.No 5067-1151). cDNA was synthesized from 1 µg of total RNA using the High-Capacity RNA-to-cDNA™ Kit (Applied Biosystems, Cat.No 4387406). qPCR was performed using Fast SYBR Green Master Mix (Applied Biosystems, Cat. No 4385616) in either a StepOnePlus™ Real-Time PCR System (Applied Biosystems) or a CFX384 Touch™ Real-Time PCR Detection System (BioRad). All samples were analyzed in triplicate, and RNA levels were obtained either with StepOnePlus™ Software v2.3 (Applied Biosystems) or CFX Manager™ Software (Biorad). For fold-change expression normalization hGAPDH, hHPRT and hACTIN housekeeping genes were used. See Table S2 for a list of primers used in this study.

2.19 RNASeq data processing and differential expression analysis

Next-generation sequencing experiments were performed at CNIC Genomics Unit using an Illumina HiSeq 2500 System (Illumina, USA) configured for single read (SR) sequencing. Resulting sequences were processed by the Bioinformatics Unit at CNIC. RNASeq sequencing reads were pre-processed by means of a pipeline that used FastQC[342], to assess read quality, and Cutadapt v1.3[343] to trim sequencing reads, eliminating Illumina adaptor remains, and to discard reads that were shorter than 30 bp. The resulting reads were mapped against a reference transcriptome and quantified using RSEM v1.2.25[344]. Around 80-90% of the reads participated in at least one reported alignment. Expected expression counts calculated with RSEM were then processed with an analysis pipeline that used Bioconductor package EdgeR[345] for normalization (using TMM method) and differential expression testing. Changes in gene expression were considered significant if associated to Benjamini and Hochberg adjusted p-value < 0.05. For reads derived from human cell line samples, the reference transcriptome was GRCh38.76. For reads derived from xenografts, the reference was a human/mouse combined transcriptome generated by putting together 194,353 human and 99,934 mouse transcripts associated to primary assemblies in GRCh38.76 and GRCm38.76, respectively. RSEM parameters were adjusted to minimize the number of alignment mismatches (--bowtie-e 30), to increase the number of allowed valid alignments for multimapper reads (--bowtie-m 60) and to disable sampling of alignments during bam file generation. To estimate the degree of cross-species mapping, bam files were processed with an “ad hoc” script written in Perl: about 80%, 18% and 2% aligned reads were mapped specifically to human, mouse or both types of transcripts, respectively. Differential expression testing was performed separately for human and mouse genes and a blocking variable was used to define sample pairs coming from the same animal. To estimate the effect of cross-

species mapping on differential expression analysis, an alternative test was performed after eliminating the contribution of reads that mapped to both human and mouse transcripts: 98% of the genes detected as differentially expressed in contrast xenograft transcriptome were shared. RNASeq-derived gene expression heatmaps represent normalized transcript counts for each replicate using a three-colour scale (green, black and red). For each individually represented gene, brighter green corresponds to the lowest transcript count, red to the highest and black to the median. Enrichment analysis was performed using Ingenuity Pathway Analysis (IPA, QIAGEN), Enrichr web tool[346] (http://amp.pharm.mssm.edu/Enrichr/) and STRING (https://string-db.org/).

2.20 Sprouting angiogenesis assay

Protocol was performed as previously described[347] with the following modifications: Assays were performed in a µ-Slide Angiogenesis well (Ibidi, Cat. No 81506) using 10µl of fibrinogen/bead solution, EGM-2 medium was changed by complete ECGM-2 medium (see Cell culture medium section) and CAFs were layered on top of the cloth at a concentration of 5000 cells/well. Fresh ECGM-2 was added 18h post CAFs seeding, and sprouting was allowed for 48h. Samples were fixed with 8% PFA for 30 min and stained with a solution containing 5µM Hoechst 33342 and 0.5µM Alexa Fluor™ 647 Phalloidin (Invitrogen, Cat. No A22287). Images were acquired with Zeiss LSM 700 confocal microscope at 21-23 ºC, in series of stacks separated by 4µm using a Plan-Apochromat 10x/0.45 M27 Objective.

2.21 IL-6 and IL-8 concentration determination by ELISA

Supernatants from CAFs cultured in 3D Collagen I matrices were recovered and centrifuged at 4ºC, 300rcf for 5 min prior to the assay. Human IL-6 and Human IL-8/CXCL8 Quantikine ELISA Kits (R&D Systems, Cat. No D6050 and D8000C respectively) were used to measure cytokine concentration present in 50µl of medium using four technical replicates per condition.

2.22 HUVECs and CAFs conditioned medium assays

Conditioned DMEM medium was collected from CAFs cultured in Collagen I 3D matrices. Medium was centrifuged at 4ºC, 300rcf for 5 min to remove floating debris prior to the assays. 18h post-seeding half of the ECGM was removed and substituted by conditioned DMEM. RNA extraction was performed 24h after adding the conditioned DMEM. For total cell number count and proliferation assays, 2500 HUVEC cells/well were seeded in a in a 0.2% gelatin-coated 96-well optical plate using complete ECGM medium. Once cells were attached, seeding medium was removed and 50µl ECGM + 1/10 of ECGM SupplementMix was added in each well for a period of 14h of starvation. After starvation, 50µl of conditioned DMEM was added, and HUVEC cells were allowed to grow for 32h. Afterwards, cells were fixed with 4%PFA and stained with either a 5µM solution of Hoechst 33342 for automated confocal Opera imaging or

with 1:1000 DRAQ5 for Odyssey plate imaging. For EdU incorporation assays, Click-iT™ EdU Alexa Fluor™ 647 Imaging Kit (Invitrogen, Cat. No C10340) was used according to the commercial protocol. Incorporation was allowed for 3h prior to fixating the 96-well samples, EdU was added at 6X concentration using 20µl of HBSS per well.

2.23 In vitro co-culture assay, image acquisition, and analysis

Cell seeding and staining were performed with an automated liquid handling Freedom EVO® series platform (Tecan). Seven 384-well optical plates were seeded in parallel, with 12 wells per cell combination and using starving DMEM/F12 without serum. Each well contained either 500 CAFs, 500 cancer cells or a combination of both. After 24h of starving, complete DMEM/F12 was added in a 1:1 proportion and the first plate of the assay was fixed with PFA 3% for 30 min after two consecutive warm (37 ºC) PBS washes. This fixation process was repeated every 24h until all seven plates were ready for staining with a 5µM solution of Hoechst 33342 (Thermo Scientific, Cat. No 62249). Plates were read using an automated Opera confocal microscope (Perkin Elmer) with a 20X High NA Air objective. Images were analyzed using Acapella platform (Perkin Elmer) in order to classify cells in the co-culture as CAFs (GFP+) or cancer cells (GFP-) and obtain cell numbers from each class.

2.24 SeaHorse: Oxygen consumption rate and glycolytic flux evaluation

Real-time oxygen consumption rate (OCR) and extracellular acidification rate (ECAR) in CAFs were determined with an XF-96 Extracellular Flux Analyzer (Seahorse Bioscience). 96-well SeaHorse plates were coated with 1µg/ml of fibronectin prior to cell seeding. 6 wells containing 5000 cells/well in 2.5mM glucose DMEM were used for each condition. Cells were treated were indicated with 5 mM 2-DG, 25mM DCA, 25µM Lovastatin or 5mM GSH for 18h prior to OCR/ECAR measurement. The assay was performed in Seahorse XF Assay Minimal Media supplemented with 2mM glutamine, 1mM pyruvate and 25 mM glucose. Drug treatments were also added during the assay maintaining the same concentrations. The pH was adjusted to 7.4 with KOH (herein called seahorse medium). Three consecutive measurements were performed under basal conditions and after the sequential addition of the following ETC inhibitors: 1µM oligomycin, 1 µM FCCP, 1 µM rotenone and 1 µM antimycin. Basal respiration rate (BRR) was defined as OCR in the absence of any inhibitor. Maximal respiration rate (MRR) was defined as the OCR after addition of oligomycin and FCCP. Spare respiration capacity (SRC) was defined as the difference between MRR and BRR. ECAR was measured in the absence of drug. To normalize respiration rates per well, cell counts were assayed by CyQuant Cell Proliferation Assay (Thermo Fisher) and values from respiration were referred to values of cell number for representation.

2.25 Determination of levels of angiogenesis-related proteins using Proteome Profiler

Representative frozen portions of the tumor were lysed in cold PBS + cOmplete™, Mini, EDTA-free Protease Inhibitor Cocktail (Roche, Cat.No 04693159001) with sterile ceramic beads using a MagNA Lyser (Roche), with two rounds of 6500rpm for 30 seconds each, with care taken to maintain the sample cold. After homogenization, Triton X-100 was added to a final concentration of 1%, samples were frozen at -80ºC, thawed and centrifuged at 4ºC/10,000g for 5 min. Resulting supernatants were recovered and assayed for protein concentration. Pools of supernatants from 4 biological replicate tumors representing the same experimental conditions were prepared. 200µg of protein from the tumor lysate pool was assayed using a membrane-based antibody detection Proteome Profiler™ Human Angiogenesis Array Kit (R&D Systems, Cat. No ARY007) according to the kit protocol. In order to adapt the protocol for Near Infrared (NIR) fluorescence detection using an Odyssey NIR scanner (Li-Cor Biosciences), HRP-conjugated Streptavidin provided in the kit was replaced with DyLight 800 Streptavidin (Invitrogen, Cat. No 10668484).

2.26 Mitochondrial content and ROS production analysis by flow cytometry and immunofluorescence (IF)

For flow cytometry assays 150,000 CAFs per well were seeded in a 6-well plate using DMEM HG. 18h later medium was changed to either 2ml DMEM 25 mM glucose or DMEM 2.5mM glucose, and the corresponding treatments (5mM 2-DG or 25Mm DCA). 48h post-treatments, half of the medium was removed and a 1:2000 dilution of 1mM MitoTracker DeepRed FM (Invitrogen, Cat. No M22426) and 1mM Mitotracker Orange CM-H2TMRos (Invitrogen, Cat. No M7511) in HBSS was added per well, along with single staining and negative controls. Cells were placed in the incubator for 30 min and then washed with warm PBS before trypsinization. Three subsequent wash and centrifugation, at 4ºC/300g for 5 min, steps were carried out in cytometer tubes a solution of PBS + 2%FBS. Final pellet was resuspended in 300µl of PBS + 2%FBS and analyzed in a BD™ LSR II Flow Cytometer (BD Biosciences). Data analysis was performed using FlowJo V10 software. For immunofluorescence 5000 CAFs per well were seeded in a 96-well optical plate using DMEM HG. Treatments and staining were carried out in the same way as for flow cytometry. Instead of trypsinized, these cells were fixed in PFA 4% at the end of the protocol and imaged in a Zeiss LSM 700 confocal microscope at 21-23 ºC using an EC Plan-Neofluar 40x/0.75 Objective. Samples stained for CAV1 and mitochondrial content were permeabilized and blocked for 1h/25ºC in PBS + BSA 1% + 0.2% Triton X-100 (PB Buffer), stained with a 1:1000 dilution of anti-Caveolin-1 (D46G3) XP® Rabbit mAb (Cell Signalling, Cat. No 3267) in 1:1 mix of PB buffer:PBS (SB Buffer) for 1hr/25ºC and a secondary staining mix of 1:1000 GARAB Alexa 561 and 1:2000 Hoechst 33342 in SB Buffer. Three washes of PBS + Tween 0.05% were carried after primary and secondary incubation.

2.27 High Content Screening (HCS) of potential CAV1 drug modulators in pancreatic CAFs (panCAFs)

Prior to panCAF cell seeding, designed 384-well plates were coated with corresponding siRNAs (non-targeting siCTRL, siRNA CAV1 and siRNA INCENP) according to the referenced reverse transfection protocol[348]. Afterwards, 1500 cells/well of panCAF1790 fibroblasts were seeded in 50µl of RPMI (+ supplements; see *Cell culture mediums*) using a Thermo Multidrop automated cell seeder. Cells were then left untreated inside the incubator for 20h to allow for its attachment. Following drug treatment, cell fixation and staining procedures were performed in an automated Tecan platform. Drug treatment was performed by adding an extra 50µl per well of a RPMI 20%FBS solution containing a 2X concentrated stock of each drug. 48h post-treatment assay was stopped with a 37ºC PBS wash and a posterior fixation step with 3% PFA. Samples stained for CAV1 were permeabilized and blocked for 1hr/25ºC in PBS + BSA 1% + 0.2% Triton X-100 (PB Buffer), stained with a 1:1000 dilution of anti-Caveolin-1 (D46G3) XP® Rabbit mAb (Cell Signalling, Cat. No 3267) in 1:1 mix of PB buffer:PBS (SB Buffer) for 1hr/25ºC and a secondary staining mix of 1:1000 GARAB Alexa 488, 1:200 of Wheat Germ Agglutinin-Alexa 647 (Invitrogen, Cat. No W32466) and 1:2000 Hoechst 33342 in SB Buffer. Three washes of PBS + Tween 0.05% were carried after primary and secondary incubation. Image acquisition was performed in an Opera confocal microscope (Perkin Elmer) with a 20X High NA Water objective. Image analysis for nuclei number and CAV1 intensity evaluation was performed in Acapella suite (Perkin Elmer), briefly CAV1 signal intensity was quantified in the cytoplasmic area marked by Wheat Germ Agglutinin. For a list of compounds used in this screening and a detailed toxicity analysis see the following reference[349].

2.28 NFκB nuclear/cytoplasmic localization analysis by immunofluorescence (IF)

Analyses for NFκB localization were performed by immunostaining of primary breast CAFs treated for 24h at the concentrations indicated in the section *In vitro drug treatments of CAFs* and processed for immunofluorescence as described in the HCS section above, using an anti-NFκB polyclonal antibody (Abcam, Cat. No ab16502) and counterstaining for DNA (Hoechst 33342). Image acquisition was performed in an Opera confocal microscope (Perkin Elmer) with a 20X High NA Water objective. Image analysis for NFκB localization was performed in Acapella suite (Perkin Elmer), shortly NFκB signal intensity was quantified in the cytoplasmic area marked by the CAF-derived GFP and in the nucleus stained by Hoechst, afterwards a ratio was established among the two obtained measurements.

2.29 ATF4 localization analysis by immunofluorescence (IF)

Analyses for ATF4 localization in were performed by immunostaining of primary breast CAFs treated for 24h at the concentrations indicated in the section *In vitro drug treatments of CAFs* and processed for immunofluorescence as described in the HCS section above, using an anti-

ATF4 monoclonal antibody (Santa Cruz, Cat. No sc-390063) and counterstaining for DNA (Hoechst 33342) and calreticulin (Abcam, Cat. No ab2907). Images were acquired on an SP8 Leica laser confocal microscope through a 63X/1.25NA and 40X/0.85NA objective, equipped with a DRM camera.

2.30 Histological and immunohistochemical studies

Primary tumors were collected during mastectomy and lungs were harvested after necropsy as previously described[350] and fixed with 4% PFA. After tissue processing, paraffin organ embedding was carried out using a paraffin embedding module (Leica, Cat. No EG1150) and 4µm tissue sections for study were obtained using a microtome (Leica RM2245). For metastasis determination, 10 consecutive sections of lung sections were stained with routine hematoxylin and eosin (H&E) using an automated multistainer (Leica ST5020). Immunohistochemistry detection of Ki67 for cell proliferation checking was performed using a kit (Master Diagnostica, Cat.No MAD-000310QD), for secondary staining peroxidase-conjugated EnVision Flex DAKO reagent was used (Agilent, Cat.K4003), coloration was done with 3,3′-Diaminobenzidine (DAB) substrate chromogen (Agilent, Cat. No K3468), finally nuclei were counterstained with hematoxylin. Slide preparations were produced with an automated glass coversliper (Leica CV5030). Preparations were scanned with Hamamatsu Nanozoomer 2.0 RS (Hamamatsu, Japan), with the digitalization software NDP.scan 2.5. Images were visualized using NDP.view2 software (Hamamatsu, Japan).

Registration of lung histology images for quantification of metastasis was carried out in Fiji (ImageJ 1.50e_x64) from stacks conformed by consecutive slices correspondent to the same sample. Linear stack alignment with scale-invariant feature transformation (SIFT) algorithm[351] was applied to find a rigid transformation for each slice using default parameters. Registered images, obtained by interpolation of transformed images, were later analyzed manually in Fiji to quantify metastasis-affected area.

Image processing and quantification of Ki67-based proliferation were developed as a macro in Fiji. After homogenization and background subtraction using rolling ball algorithm[352] (radius=10), color deconvolution[353] was used to separate Hematoxylin, DAB, and a third component that did not perfectly matched the stains. Foreground and background pixels were detected in each component after normalization and edge-preserving smoothing using bilateral filter [354] (radius=3, range=50), by applying a robust automatic threshold selection[355] (noise=5, lambda=3) and a posterior watershed algorithm[356]. Segmentation of cells was obtained from the iterative union of foreground pixels, hole-filling and object-split using watershed. Detection of proliferative/non-proliferative cells was carried out by geodesic reconstruction of cell segmentations from DAB/Hematoxylin foreground pixels. Noisy structures and under-

segmentations were discarded by size filtering. Proliferation readout measured the ratio of proliferative cells with respect to the total.

2.31 Electron microscopy

CAF cells were grown on 100-mm dishes, treated as indicated, and fixed with 4% paraformaldehyde and 2% glutaraldehyde for 120 min at room temperature. Upon gentle scrapping, postfixation was carried out with 1% OsO_4 and 1.0% $K_3Fe(CN)_6$ in H_2O at 4 °C for 60 min. Samples were subsequently dehydrated with ethanol and embedded in Epoxy 812 Resin (TAAB Laboratories) according to standard procedures. Ultrathin (80 nm) sections were stained with saturated uranyl acetate and lead citrate and visualized with a JEOL JEM 1010 (Tokyo, Japan) electron microscope at 80 kV. 16-bit images were recorded with a 4 k × 4 k CMOS F416 camera from TVIPS (Gauting, Germany), typically at 12000X magnification. Average intermembrane space from the smaller dimension across ER sections, mitochondria width/length and mitochondria cristae width were computed upon manual segmentation using ImageJ plugin.

2.32 Lentiviral vector generation

See Table S4 for a list of primers used for cloning and resulting lentiviral vectors. A common backbone for all lentiviral constructs, except where mentioned otherwise, was generated by cloning a PCR amplified cassette (with primers A1&A2) containing a constitutive CMV promoter driving the expression of Cherry fluorescent protein and a P2A linker peptide[357] between ClaI and MluI sites of pLVX-shRNA2 vector (Clontech, Cat. No 632179), replacing both original CMV and U6 promoters, the shRNA MCS and ZsGreen1 protein. Template plasmid for cassette amplification, pRRL-CMV-ChFP2A, was donated by the Viral Vectors unit at CNIC. The resulting plasmid was called pLVX-CMV-ChFP2A. Lentiviral construct driving the expression of PpyRE8 Far Red luciferase (pLVX-CMV-ChFP2A-RE8luc) was generated by cloning a PCR amplified cassette (with primers L1&L2) between the PacI and PmeI sites located downstream of P2A self-cleaving peptide[357] present in pLVX-CMV-ChFP2A backbone. Template plasmid, pGEX-6P-2 PpyRE8 HCO, contained a modified version of *Photinus pyralis* capable of generating light in the far red light spectrum[358], was generated and donated by Professor Bruce Branchini lab (Connecticut College, USA). Lentiviral constructs for silencing CAV1 were created by cloning a PCR amplified cassette (with primers M1&M2) containing the Puromycin resistance (pac) gene and non- targeting miR30.shRNA between PacI and MluI present in pLVX-CMV-ChFP2A plasmid. pGIPZ non-silencing shRNAmir lentiviral control vector (Dharmacon), was used as the PCR template. The resulting plasmid, pLVX-CMV-ChFP2A-Puro^R-miR30.scr, was used to clone in four different sequences targeting human CAV1 transcript. Chemically synthesized and PAGE purified oligos (Sigma), were aligned to form a dsDNA structure with flanking XhoI and EcoRI ready available sites and cloned into

pLVX-CMV-ChFP2A-Puro^{R}-miR30.scr substituting the non-targeting sequence. Three of the sequences targeting CAV1 derived from http://cancan.cshl.edu/cgi-bin/Codex/Codex.cgi and a fourth one[101] was adapted to fit the miR30.shRNA format. See non-targeting and CAV1 targeting sequences in Table S4B. A second version of the plasmid, pLVX-CMV-Puro^{R}-miR30.scr, was created by cloning a PCR amplified cassette (with primers M1.1&M2) between AgeI and MluI sites present in pLVX-CMV-ChFP2A plasmid, resulting in the removal of Cherry fluorescent protein. pGIPZ non-silencing shRNAmir lentiviral control vector (Dharmacon), was used as the PCR template.

An alternative backbone, where the CMV promoter was substituted for a MCS for the insertion of tissue-specific promoters (Table S4C) was generated by cloning a PCR amplified cassette (with primers B1&B2) containing a Cherry fluorescent protein and a P2A linker peptide between ClaI and XbaI sites of pLVX-shRNA2 vector (Clontech, Cat. No 632179), replacing both original CMV and U6 promoters, the shRNA MCS and ZsGreen1 protein. Template plasmid for cassette amplification, pRRL-CMV-ChFP2A, was donated by the Viral Vectors unit at CNIC. Subsequent Far Red luciferase cloning was performed as stated above and a MCS was included (SpeI-AscI-AgeI-NdeI) by hybridizing two 5' phosphorylated oligos (MCS1+MCS2) synthesized by Sigma and cloned upstream of CherryFP in the ClaI RE site of the pLVX backbone. The resulting plasmid was called pLVX-MCS-ChFP2A-RE8luc. Silencing miRNA backbone and non-targeting miR30.scr were amplified from pGIPZ (with primers MB1 & MB2) and cloned downstream of RE8luc in between PmeI and MluI sites. Resulting plasmid was termed pLVX-MCS-ChFP2A-RE8luc-miR30.scr Subsequent cloning of CAV1 targeting sequences was performed as described above. A region of the ITGA11 promoter[134,359] (-2123 TSS +25) was amplified (with primers I1 & I2) and cloned in between the AgeI and NdeI RE sites present in the MCS of the different non-targeting and CAV1 targeting versions of pLVX-MCS-ChFP2A-RE8luc-miR30; resulting plasmids were named pLVX-MCS-ChFP2A-RE8luc-miR30.scr/shCAV1 respectively.

Selection of infected cells was achieved either through FACS (Sinergy 4L system, SONY) or puromycin selection through two consecutive passages at 2 µg/ml.

2.33 Statistical analysis

All the statistical tests were performed using GraphPad PRISM6 software unless mentioned otherwise. Statistical significance was evaluated by the appropriate methods stated in the figure legends or in the methodology section. Means were represented as ±SEM unless stated otherwise. Differences were considered as statistically significant at *P<0.05, **P<0.01, ***P<0.001, and ****P<0.0001

3. RESULTS

3. RESULTS

3.1 Modification of CAV1 stromal levels: approaches and tool generation

One of the main research aims of this thesis was to establish effective loss-of-function experimental systems allowing for the specific dissection of stromal CAV1 contribution to tumor progression *in vivo*. In order to tackle these requirements, two different complementary approaches were devised.

3.1.1 Engineering promoter-based fibroblast selectivity in dual-reporter miRNA-based lentiviral vectors

In a first model, breast cancer biopsy fragments would have been orthotopically transplanted into immunodeficient NSG mice and transduced intratumorally with lentiviral vectors targeting the CAV1 mRNA, selectively in fibroblasts **(Fig. 11A)**. In this strategy, human breast tumor biopsies, containing both patient stroma and cancer cells, would have been engrafted onto immunodeficient NSG mice as a means to expand the small biopsies into tumor masses. Subsequently, the resulting tumors would have been subdivided and frozen to set up a small tumor biobank that would have later been used to transplant and perform *in vivo* intratumoral lentiviral injections.

In order to selectively target stromal fibroblasts, present in the tumor biopsy, a lentiviral vector expressing a CAV1-targeting microRNA-like (miRNA) under the control of a fibroblast-specific promoter, was developed **(Fig. 11B and Table S4)**. This lentiviral vector also contained a bicistronic cassette, linked by a self-cleaving P2A peptide[357], composed of a CherryFP fluorescent protein, for *in vitro* studies, and a far-red light emitting luciferase (RE8luc)[358] optimized for *in vivo* tracking. Downstream of the expression cassette, either a non-targeting scramble miRNA or four different human CAV1 targeting miRNAs were cloned.

The inclusion of the CAV1 targeting sequences into a miRNA frame, as opposed to RNApol III-based silencing systems (shRNA), allows for the simultaneous transcription of the expression cassette (CherryFP - P2A - RE8luc, aka ChFP2A-RE8luc) and the silencing element (miRNA) under the control of a unique upstream RNApol II-driven promoter[360]. Thus, the detection of *in vitro* fluorescence or *in vivo* bioluminescence would be indicative of ongoing miRNA transcription.

A first vector version was constructed to bear a constitutive cytomegalovirus promoter (P_{CMV}) to check the downregulation efficiency of all four different miRNA sequences targeting CAV1. The miR30.CAV1.2 sequence showed the highest silencing efficiency as compared with the others in a variety of model systems **(Fig. 11E and 13B)**.

Standard lentiviral vector packaging systems do not confer cell type-level selectivity for infection. Thus, adapting a fibroblast-specific promoter that would actively drive the expression of the integrated provirus selectively in stromal fibroblasts was paramount. In order to screen for fibroblast-specific transcripts and promoters, the expression of a number of published fibroblast-specific markers (FAP, FSP1, and ITGA11) was assessed both in cancer-associated and normal fibroblasts and in different breast cancer cell lines **(Fig. 11C)**.

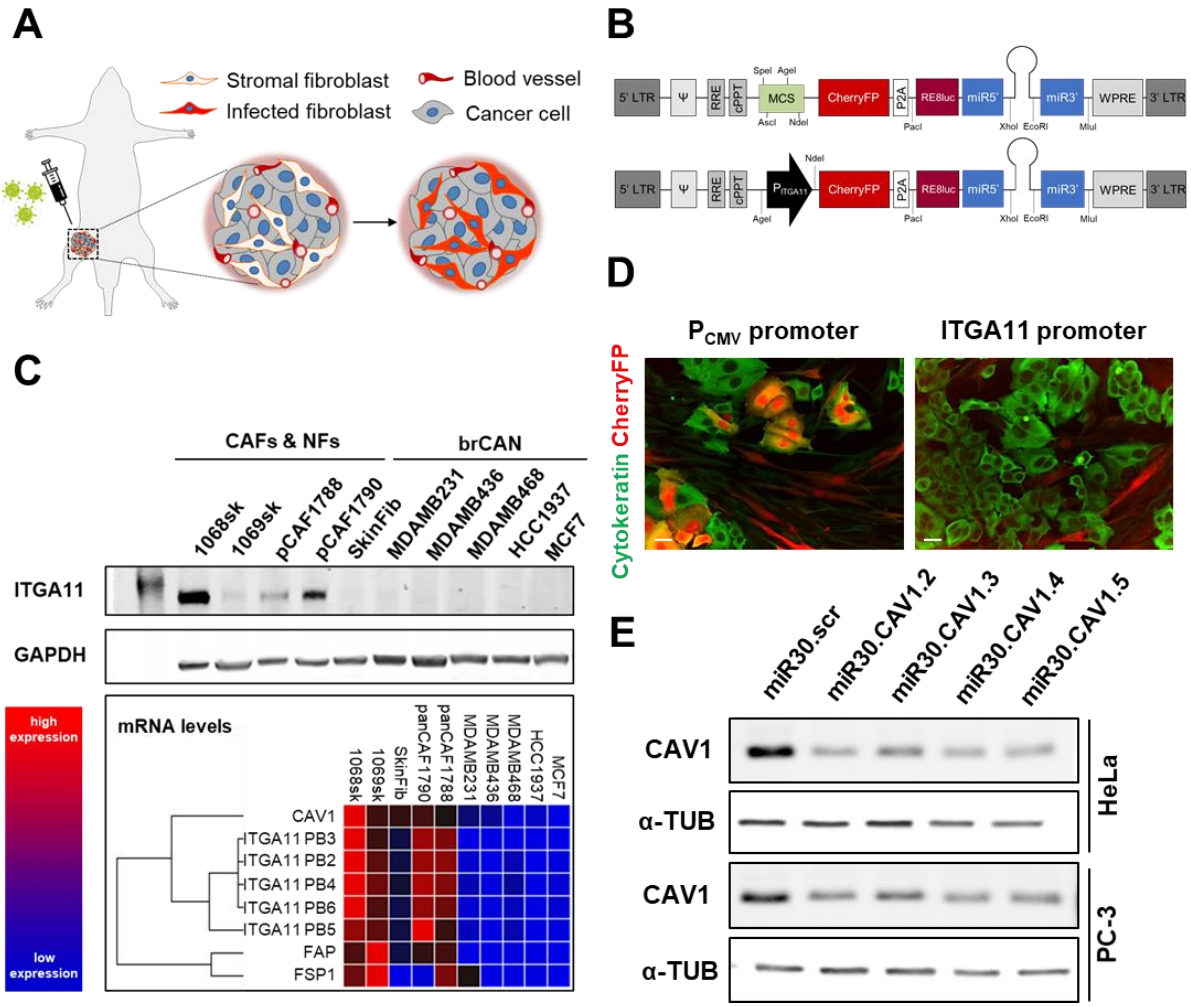

Figure 11. Engineering promoter-based fibroblast selectivity in dual-reporter miRNA-based lentiviral vectors. (A) *In vivo* targeting of breast tumor stromal fibroblasts. Depiction of immunodeficient NSG mice implanted with tumors derived from human biopsies (xenografts) and intratumorally injected with lentivirus in which fluorescent protein/luciferase and microRNA expression are controlled by a fibroblast-specific promoter. **(B)** Third generation lentivirus expressing a bicistronic cassette, containing a: (i) fluorescent protein (CherryFP, in red) and a light-emitting luciferase (RE8luc, in dark red) linked via a P2A self-cleaving peptide (in white), and (ii) a miR30-based shRNA silencing element. Expression of both elements (i and ii) is controlled either by a tissue-specific promoter (P_{ITGA11}, lower scheme) inserted into a multicloning site (MCS, in green, upper scheme) or a ubiquitous P_{CMV} promoter. Unique restriction enzyme sites are depicted below the schemes and the rest of lentiviral vector elements (LTRs, Ψ, RRE, cPPT, and WPRE) are shown in grey. **(C)** Expression levels of CAV1, ITGA11, FAP and FSP1 in different CAFs cell lines, normal (NFs) skin fibroblasts (SkinFib) and breast cancer cell lines (brCAN).

Heatmap shows high (in red) and low (in blue) expression levels of mRNA expression assayed by qPCR (ITGA11 was assayed using 5 different primers, PB2-6). Western blot depicts protein levels of ITGA11 in the aforementioned cells; GAPDH was used as loading control. **(D)** Representative fluorescence microscopy images of brCAN (MCF7) and CAFs (1068sk) co-cultures infected with a CherryFP (in red) containing lentivirus (ChFP2A-RE8luc) expressed under the control of P_{CMV} (left panel) or ITGA11 promoter (right panel). Pan-cytokeratin, an epithelial marker of brCAN is shown in green. Scale bar: 20µm. **(E)** Western blot showing CAV1 expression levels in HeLa and PC-3 cells after infection with either non-targeting (miR30.scr) or CAV1-targeting (miR30.CAV1) P_{CMV} ChFP2A-RE8luc lentivirus.

While Fibroblast Specific Protein 1 (FSP1) is a widely used fibroblast marker[361], not all isolated fibroblasts exhibited significant expression. Moreover, "mesenchymal-like" breast cancer cell lines such as MDA-MB-231 did express detectable levels **(Fig. 11C)**. Finally, ITGA11 promoter was chosen over FAP promoter given the overall higher expression of its mRNA in CAFs **(Fig. 11C)**.

The specificity of ChFP2A-RE8luc lentivirus containing the ITGA11 promoter was tested in an *in vitro* co-culture system of MCF7 breast cancer and CCD1068SK CAF cell lines, showing a lack of CherryFP expression in cancer cells and CherryFP production in fibroblasts **(Fig.11D)**.

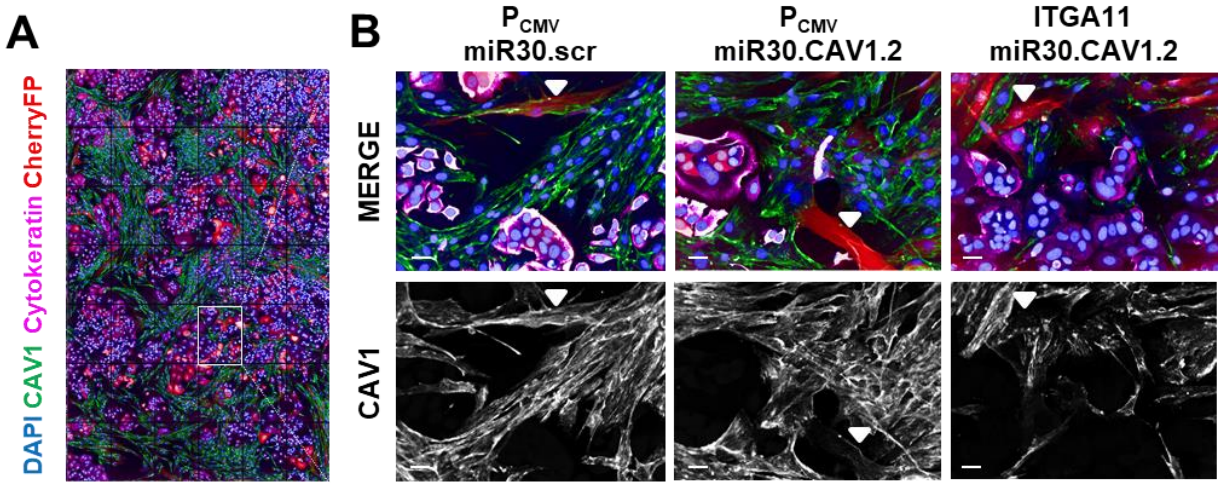

Figure 12. CAFs – CAV1 targeting in CAFs-brCAN co-culture assay. (A) Fluorescence microscopy tilescan reconstruction of brCAN/CAFs co-culture assays. CCD 1068SK CAFs show expression of CAV1 (in green) while MCF7 brCAN cells do not. MCF7 are marked with an antibody against Pan-Cytokeratin, an epithelial cell marker (in magenta). Infected cells are expressing CherryFP (in red) and nuclei are stained with DAPI (in blue). **(B)** Representative images of brCAN/CAFs co-culture assays. CAV1 levels in cells infected with non-targeting CMV miR30.scr (left panel, white arrow marked, in red) remain unaffected. CAFs expressing CAV1 targeting miRNAs under the control of a P_{CMV} promoter (central panel, white arrow, in red) downregulate CAV1 levels. Co-cultures infected with ITGA11 promoter controlled lentivirus (right panel, in red), while maintaining CAF expression specificity, showed poor CAV1 silencing efficiency.

As the objective of this lentiviral system was to achieve CAV1 silencing specifically in CAFs, while leaving brCAN cells unaffected, miRNA-expressing ChFP-P2A-RE8luc lentiviral vectors, either under the control of the ubiquitous P_{CMV} or the fibroblast-specific ITGA11 promoter were tested in the same CAF/brCAN co-culture scenario **(Fig. 12A)**. CAFs proved difficult to transduce, as seen in the infections with the P_{CMV} version of the lentivirus, and while ITGA11 remained a good promoter choice for fibroblast-specific expression, CAV1 silencing efficiency was unsatisfactory in these systems as most infected CAFs (CherryFP positive) displayed detectable residual CAV1 expression **(Fig. 12B)**.

Given the technical challenges posed by the first approach, a second strategy that overcame the hurdles of a potential suboptimal *in vivo* CAF infection and CAV1 downregulation was finally chosen.

3.1.2 Efficient CAV1 silencing *ex vivo* (pre-grafting) in CAFs for comparative xenograft studies

In this second strategy, primary breast stromal CAFs and TNBC breast cancer cell lines (TCs) were modified *ex vivo* prior to their injection into the mammary fat pad of NSG mice **(Fig. 13A)**. Two stable CAF cell lines derived from human primary breast CAFs expressing high levels of CAV1 were generated: (i) CAFscr, infected with a non-targeting lentivirus, and (ii) CAFshCAV1, where CAV1 was silenced using a lentiviral construct **(Fig. 13C)**.

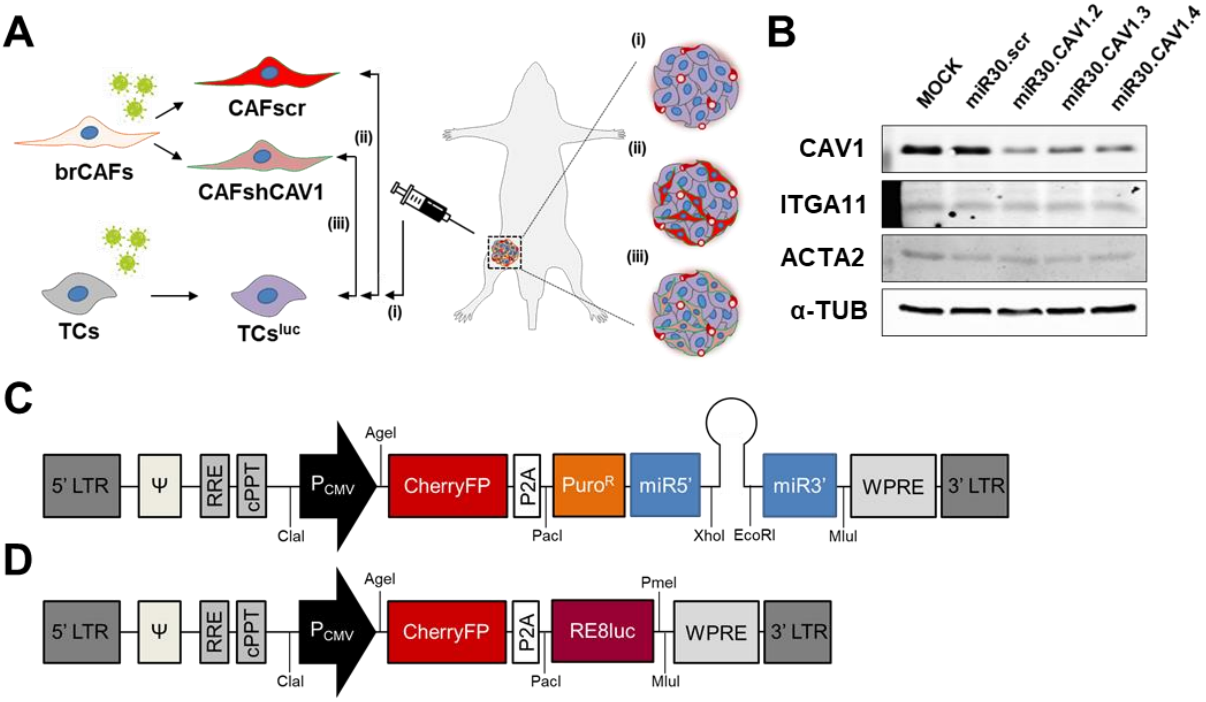

Figure 13. Efficient CAV1 silencing ex vivo (pre-grafting) in CAFs for comparative xenograft studies. (A) Experimental approach to generate mouse xenograft models of human breast cancer with high and low stromal levels of CAV1. Three different cell combinations were injected into the mammary fat pads of NSG mice: (i) isolated luciferase-labeled breast cancer cells (TCs^{luc}) without a stromal

component (CAFs), (ii) TCs^{luc} with CAFscr, constituting the high stromal CAV1 xenografts (sCAV1high), and (iii) TCs^{luc} with CAFshCAV1, as low stromal CAV1 tumors (sCAV1low). **(B)** Western blot showing CAV1, ITGA11 and ACTA2 expression levels in brCAFs cells after infection with either non-targeting (miR30.scr) or CAV1-targeting (miR30.CAV1.2-4) P_{CMV} ChFP2A-Puro^{R} lentivirus. ITGA11 (Integrin α11) and ACTA2 (Smooth muscle actin) are considered normal- and cancer-associated fibroblast markers respectively. **(C)** Lentiviral vector pLVX-CMV-ChFP2A-RE8luc, aimed at miRNA expression (non-targeting or CAV1 targeting) from Fig. 11B where the luciferase gene has been swapped with a puromycin resistance gene (Puro^{R}) allowing antibiotic-mediated selection of transduced cells. **(D)** Lentiviral vector used to generate fluorescent protein/luciferase-labeled TCs (TCs^{luc}). Its bicistronic expression cassette contains a: (i) fluorescent protein (CherryFP, in red), for FACS sorting, and a luciferase (RE8luc, in dark red) for *in vivo* tracking, linked via a P2A self-cleaving peptide (in white); all under the control of an ubiquituos P_{CMV} promoter.

Then, three different combinations of human cells were injected into the mammary fat pad of immunodeficient NSG mice: (i) either luciferase-labeled human breast cancer cell lines (TCs^{luc}: MDA-MB-436 or MDA-MB-468), (ii) breast cancer cells (TCs) plus CAFscr fibroblasts or (iii) breast cancer cells (TCs) together with CAFshCAV1 fibroblasts. Tumor xenografts containing CAFscr or CAFshCAV1 fibroblasts were considered as high (sCAV1high) or low stromal CAV1 (sCAV1low) tumors respectively **(Fig. 13A)**.

For the generation of CAFscr and CAFshCAV1 cells, a modified version of the lentivirus designed in the first approach was used **(Fig. 11B)**. In this lentivirus the luciferase cassette was substituted by a puromycin resistance gene (Puro^{R}) allowing an antibiotic-mediated selection of infected cells. In this case, as expression specificity was no longer needed (infection was performed *in vitro* in non-mixed cell populations), both the expression cassette (ChFP2A-Puro^{R}) and the miRNA-based silencing elements were under the control of an ubiquitous P_{CMV} promoter **(Fig. 13C)**.

Lentivirus-mediated CAV1 silencing in CAFs was performed using 3 different miRNA sequences (miR30.CAV1.2-4), again showing the highest CAV1 silencing levels in the case of miR30.CAV1.2 **(Fig. 13B)**. Primary human breast CAFs infected with miR30.scr were labeled CAFscr, while the ones infected with miR30.CAV1.2 were used for the rest of the study as CAFshCAV1 given they had the highest level of CAV1 silencing.

In order to track cancer cell growth *in vivo*, luciferase-labeled breast cancer cell lines were generated (TCs^{luc}) from established TNBC cell lines (MDA-MB-436 and MDA-MB-468) via lentiviral infection. The lentiviral vector used in the infection of TCs (pLVX-CMV-ChFP2A-RE8luc) expressed a CherryFP fluorescent protein, that allowed for FACS sorting of infected cells, and a far-red light emitting luciferase (RE8luc) optimized for *in vivo* tracking of labeled TCs via bioluminescence detection[358] **(Fig. 13D)**.

3.2 Stromal CAV1 levels modulate primary tumor growth

Using the aforementioned second strategy **(Fig. 13A)**, a first set of experiments with non-luciferase-labeled TNBC cells (TCs) was performed. In this set of experiments, tumor resection was carried out 30 days after cell injection (engraftment) into the mammary fat pad.

Examination of primary tumor size after mastectomy revealed that sCAV1high tumors (TCs + CAFscr) were significantly bigger **(Fig. 14B and 14D)** and showed a clear reddish pigmentation **(Fig. 14A and 14C)**, as compared with either the sCAV1low group (TCs + CAFshCAV1) or tumors generated by the injection of only cancer cells (TCs). While MDA-MB-436 cells were able to generate a visible tumor when injected alone, MDA-MB-468 cells were less penetrant, giving rise to tumor masses only in some mice **(Fig. 14C)**.

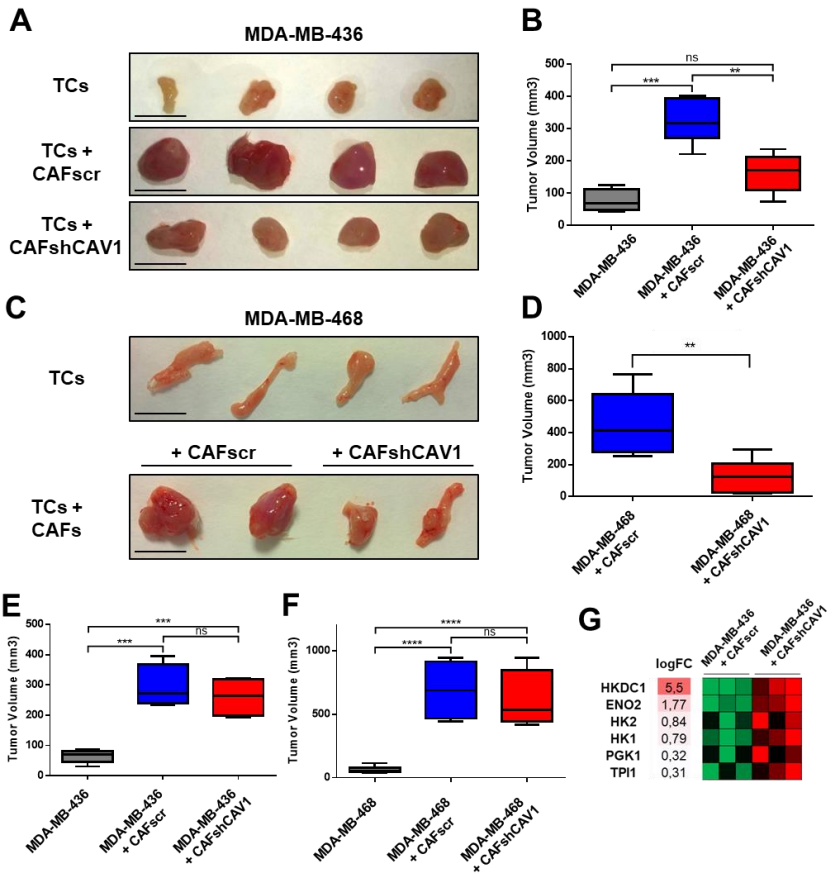

Figure 14. Stromal CAV1 levels modulate primary tumor growth. (A) Orthotopic xenograft tumors were generated by injecting MDA-MB-436 TCs alone or in combination with CAFs (expressing high or low CAV1 levels, CAFscr and CAFshCAV1 respectively). Tumors were isolated at 30 days post-cell injection. Representative tumors are shown. Scale bar: 10mm **(B)** Tumor size was calculated at 30 days post-injection of TC and CAF cells. Data are presented as boxplots (Min to Max values); n=4 mice/group, **P<0.01, ***P<0.001 (One-way ANOVA, Bonferroni's multiple comparison test). **(C)** Orthotopic xenograft tumors from isolated MDA-MB-468 breast tumor cells (TCs) or in combination with CAFs. Mice were mastectomized and tumors isolated at 30 days following injection into mammary glands. Representative tumors are shown. Of note, at this time point, no tumor was developed from MDA-MB-468 TCs when injected alone (image depicts mammary fat pads). Scale bar: 10mm. **(D)** Tumor size was calculated at 30 days post-injection of TC and CAF cells. Data are presented as boxplots (Min to Max values); n=6 mice/group, **P<0.01, (Two-tailed unpaired t-test). **(E and F)** Tumor size was calculated at 40 days post-injection of breast tumor cells (MDA-MB-436 or MDA-MB-468, respectively) and CAF cells. Difference in volume between CAFscr and CAFshCAV1 derived tumor xenografts is no longer significant although tendency remains. Data are presented as boxplots

(Min to Max values) and are representative of 2 independent experiments; n=4 mice/group, ***P<0.001 (One-way ANOVA, Bonferroni's multiple comparison test). **(G)** RNASeq heatmap of tumor xenograft lysates showing significant changes in expression levels of glycolytic enzymes. Mastectomy was performed 30 days post-cell injection. In gene expression heatmap, red denotes increased gene expression while green corresponds to downregulation. LogFC (Fold Change) of gene expression compared to the MDA-MB-436 + CAFscr control. n=3 tumor/group.

By extending the period of primary tumor growth before resection from the usual 30 to 40 days MDA-MB-468 cells generated small tumors on their own **(Fig. 14F)**. Upon extension of primary tumor growth experiments, statistical significance for the difference in size among high and low stromal CAV1 tumors was lost, although trends agreed with the previous significant differences **(Fig. 14E and 14F)**.

Low stromal CAV1 (sCAV1low) MDA-MB-436 xenografts resected 30 days post-cell injection also showed a significant upregulation of glycolysis-related genes upon RNASeq transcription analysis of whole tumor xenograft lysates **(Fig. 14G and Table S6A)**.

Analogous experiments were performed using a luciferase-expressing MDA-MB-436 cell line (MDA-MB-436^{luc}) to track cancer cell growth non-invasively at different time points **(Fig. 15A)**. Again, the presence of CAFs encouraged primary cancer cell growth **(Fig. 15B)**.

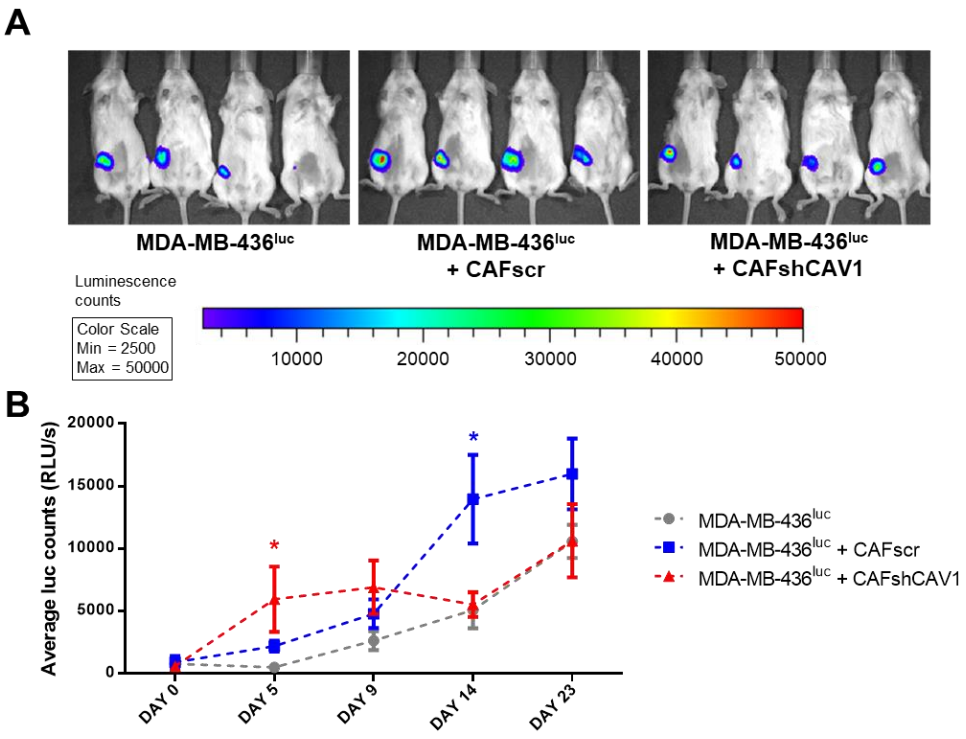

Figure 15. Tracking *in vivo* tumor cell growth. (A) Bioluminescent imaging of mice transplanted with a luciferase-expressing breast cancer cell line (MDA-MB-436^{luc}) either isolated or in combination with CAFs. Images correspond to 23 days post-cell injection time point. Color scale shows luminescence count production. **(B)** Quantification of tumor cell-derived bioluminescence during primary tumor xenograft growth. Last two data points are not shown as they are not representative of tumor size due to necrosis and tumor tissue opacity. Data are presented as mean ± SEM and are representative of 3

independent experiments; n=4 mice/group, *P<0.05 compared to MDA-MB-436 ^{luc}, (Individual time point analysis: One-way ANOVA, Tukey's multiple comparison test).

An intriguing observation was that sCAV1low tumors showed a *two-stage growth curve*. During the first stage of tumor growth, TCs^{luc} from sCAV1low tumors grew faster **(Fig. 15B)**. However, around day 10 post-cell injection in the mammary fat pad, this behavior was reversed and TCs^{luc} growth in sCAV1low tumors (red hue data) was stalled compared to sCAV1high tumors (blue hue data), which continued growing exponentially beyond that time threshold **(Fig. 15B)**. Supporting an underlying differential proliferation rate for such differences in the later phase, sCAV1high tumors exhibited increased nuclear Ki67-positive cell counts (a standard marker of cell proliferation) upon immunostaining of histological tumor sections **(Fig. 16A and 16B)**.

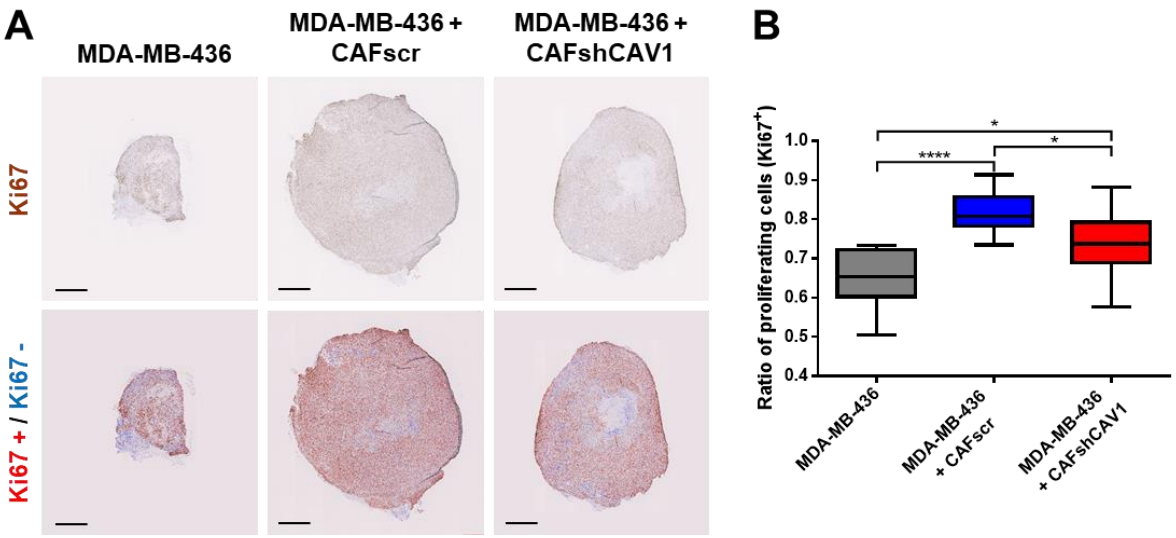

Figure 16. Proliferation assessment by Ki67 IHC. (A) Ki67 (proliferation marker, in brown) IHC of MDA-MB-436 derived primary breast xenografts removed 30 days post-cell injection. Total cell nuclei are shown upon hematoxylin staining (light blue). Automated image analysis (lower panels) allowed for classification of Ki67+ proliferating cell nuclei (red) and Ki67 – non-proliferating cell nuclei (blue). Scale bar: 1mm. **(B)** Proliferating (Ki67+) cell quantification in tumor xenograft IHC sections (see Figure S1I). Data are presented as boxplots (Min to Max values); n=4 tumor/group, *P<0.05, ****P<0.0001, (One-way ANOVA, Bonferroni's multiple comparison test).

In order to isolate these effects, a series of *in vitro* experiments, where TCs co-cultured together with CAFs of either genotype and then profiled using automated high-content image analysis were performed **(Fig. 17A)**. In accordance with the first stage of the biphasic tumor growth observed *in* vivo, these studies showed that cancer cells co-cultured with CAFshCAV1 fibroblasts multiplied faster than cancer cells cultured alone or in combination with CAFscr fibroblasts **(Fig. 17B and 17C)**. Quantification of CAFs present in the co-culture assay showed no differences in cell number for the duration of the experiment **(Fig. 17D and 17E)**.

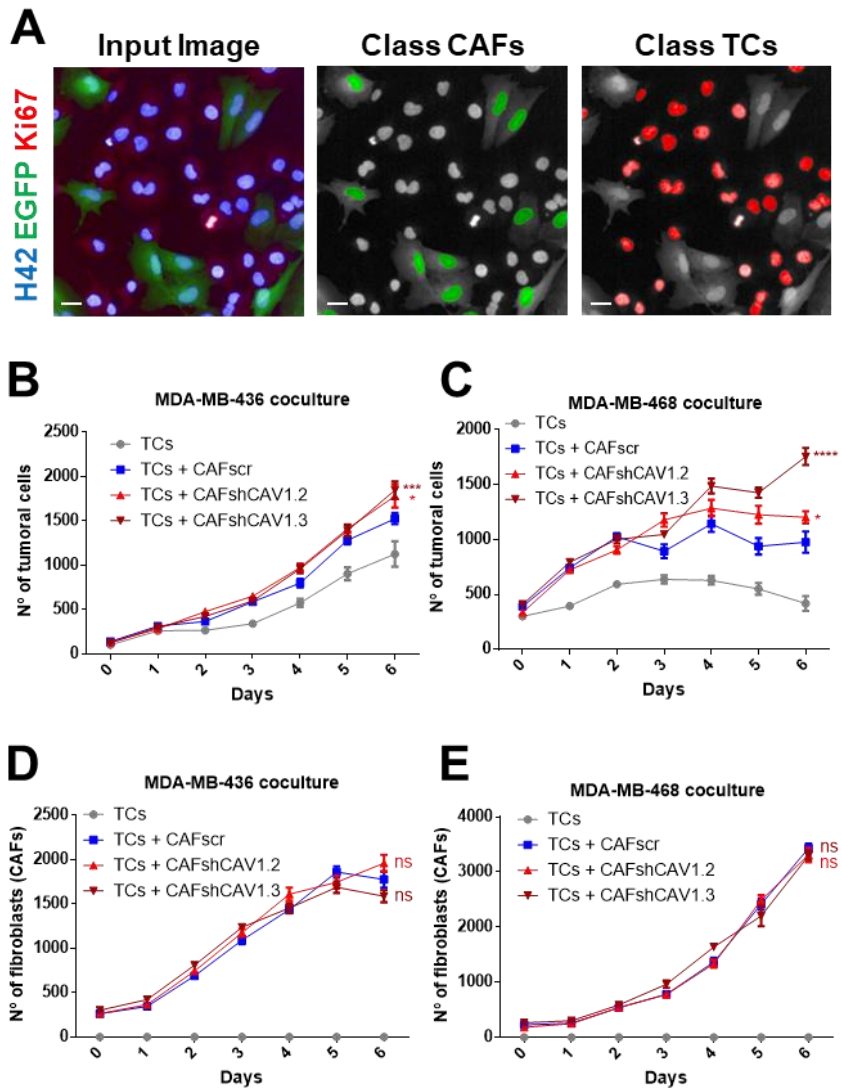

Figure 17. In vitro co-culture assay of breast CAFs and TNBC cell lines (TCs) (A) Co-culture assay of CAFs and TCs, showing an input image of GFP positive CAFs (green), total nuclei (blue) and Ki67 staining (red). Presence or absence of GFP allowed for classification of cells into class CAFs (green nuclei) or class TCs (red nuclei), respectively, for later quantification. Scale bar: 20µm. **(B and C)** Breast tumor cell (TCs) class quantification in MDA-MB-436 + CAFs and MDA-MB-468 + CAFs co-cultures, respectively, along 7 days. Presence of CAFshCAV1 encourages increased TCs numbers. Note the stalled cell growth in the case of isolated MDA-MB-468 cell line grown in absence of CAFs. Data are presented as mean ± SEM and are representative of 3 independent experiments; n=12 well/group, *P<0.05, ***P<0.001, ****P<0.0001, compared to TCs + CAFscr at Day 6 (Two-way ANOVA, Bonferroni's multiple comparison test). **(D and E)** Fibroblast (CAFs) class quantification in MDA-MB-436 and MDA-MB-468 co-cultures, respectively, along 7 days. Cell growth shows no difference among CAFscr and CAFshCAV1 fibroblasts. Note the absence of false positive classifications of fibroblasts in images derived from cancer cell-only (TCs) conditions (in grey). Data are presented as mean ± SEM and are representative of 3 independent experiments; n=12 well/group (Bonferroni's and Tukey's multiple comparison test).

Cancer-Associated Fibroblasts (CAFs) had already been described as cancer cell growth promoters[45,75–77]. With these results, it could be observed how CAV1 levels in stromal fibroblasts dynamically affect the different stages of tumor growth. While CAFshCAV1 fibroblasts promote a quick initial cancer cell proliferation *in vitro* and *in vivo*, long-term growth is better supported by CAFscr-containing sCAV1high tumors.

3.3 Aberrant proangiogenic signaling generates a dysfunctional tumor vasculature in sCAV1low tumors

The extent and functionality of tumor vasculature play a key role in blood perfusion (and thus, oxygen and nutrient delivery) determining tumor metabolism and growth kinetics[46,145,259,362]. Given the observed differences in color and growth rate among high and low stromal CAV1 tumor xenografts, the vasculature structure and functionality of these tumors was assessed as a potential factor influencing the aforementioned phenomena.

Blood vessel density was significantly increased in tumors containing CAFs compared to tumors composed of only MDA-MB-436 cancer cells, in accordance with the proposed role these CAFs have in enhancing angiogenesis[45,75–77]. Among CAF-containing xenografts, sCAV1low tumors showed a significantly higher vascular density compared to sCAV1high tumors **(Fig. 18A)**.

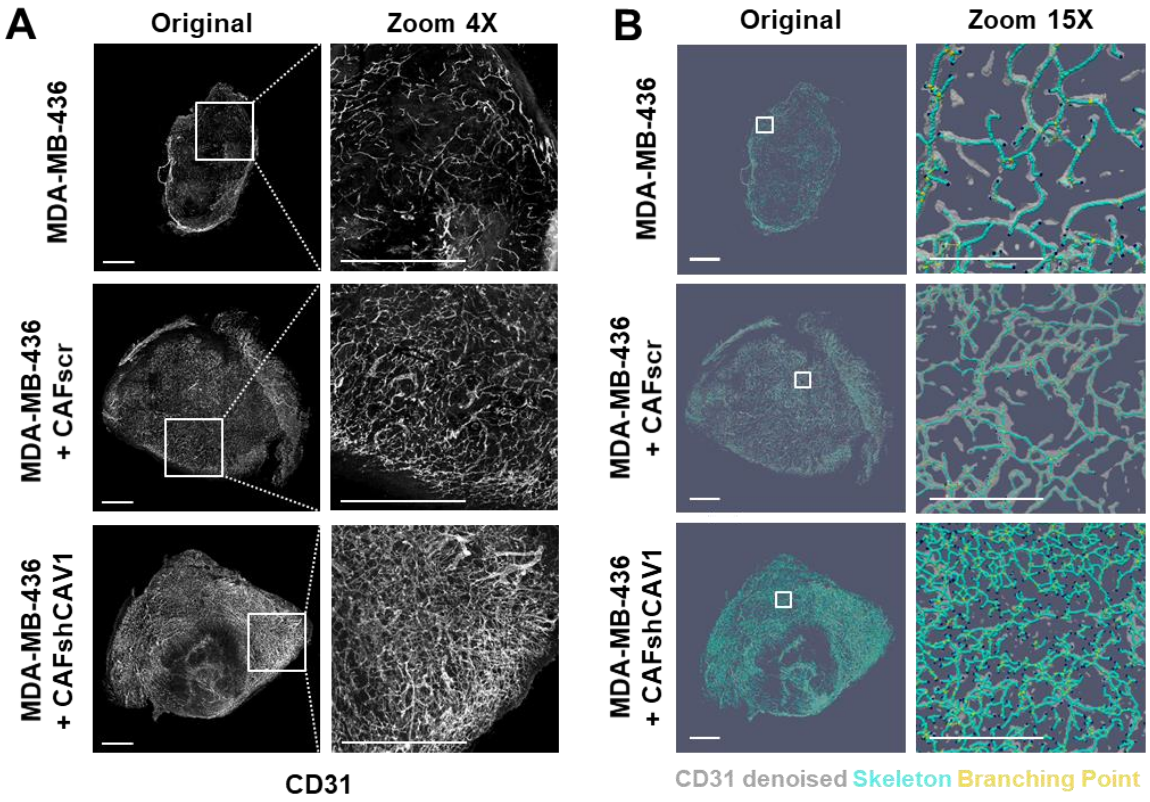

Figure 18. (A) sCAV1low tumor xenografts show the highest blood vessel density. Representative tumor xenograft sections (and insets) depicting distinctive blood vessel densities. Blood vessels are stained using CD31, an endothelial cell marker. Scale bar: 1mm. **(B)** Automated image segmentation of tumor xenograft vasculature. Vessel volume is defined by CD31 denoised Z-stack images (grey). Skeleton (cyan) and branching points (yellow) are built within the vessel volume to calculate structural properties (see Table S1). Scale bar: Original 1mm, Zoom 15X 0.25mm.

As a consequence of an excessive and sustained proangiogenic signaling[145–147], tumor vasculature acquires an aberrant morphology, characterized by: (i) disproportionate blood

vessel density, (ii) abundant branching and (iii) an increased number of blind ends. As revealed by automated image segmentation and analysis **(Fig. 18B)**, these hallmarks/signatures of vascular network aberrancy[148,149], were increased in sCAV1low tumor xenografts as compared to sCAV1high tumors **(Fig. 18B, 19A and Table S1)**.

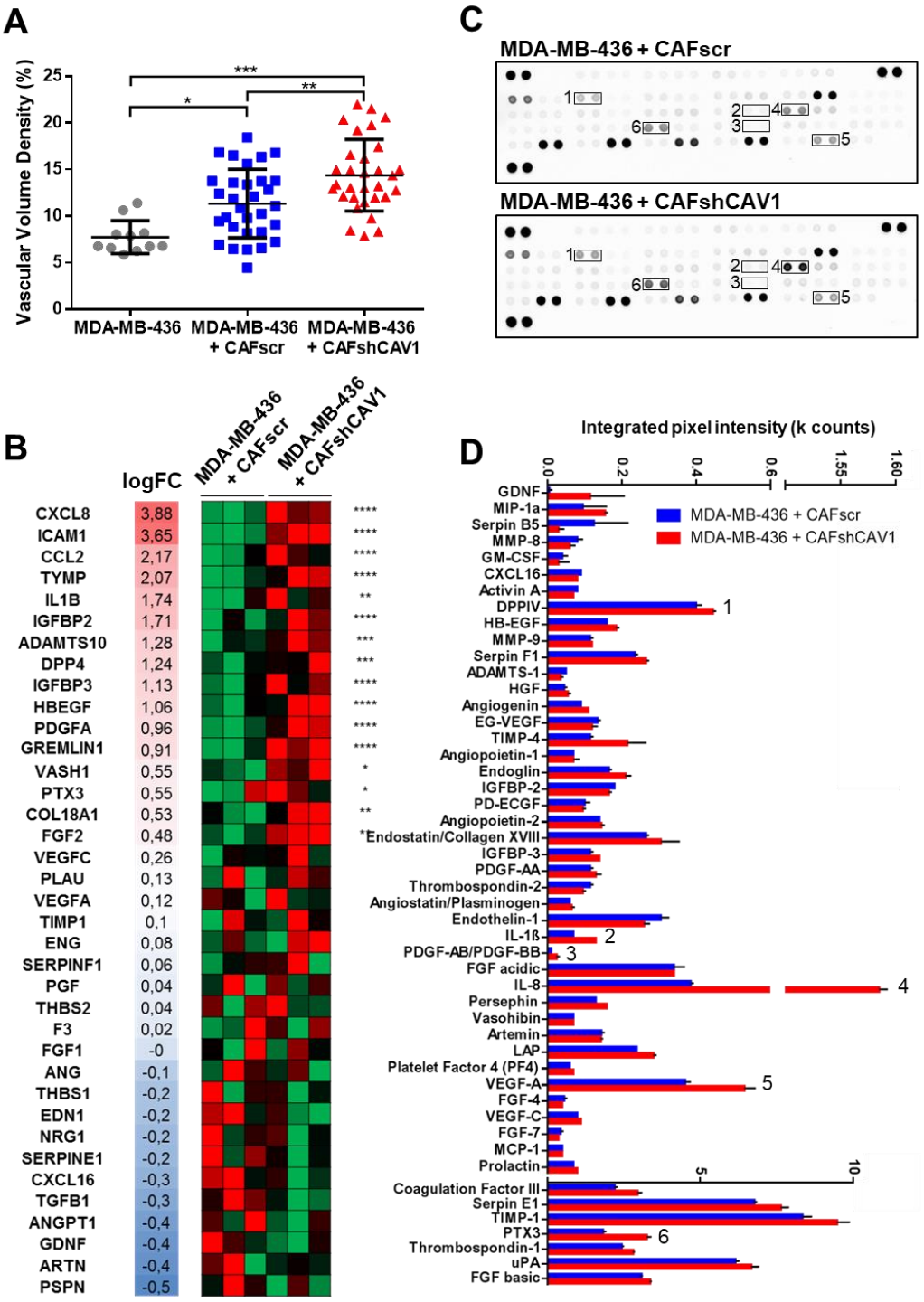

Figure 19. Increased vascular density and proangiogenic signaling in sCAV1low tumors. (A) Vascular volume density of tumor xenograft quantification. Data are presented as mean ± SD in a scatter plot; n = 11 whole tumor images/MDA-MB-436 group and n = 31 whole tumor images/MDA-MB-436 +

CAF groups, *P<0.05, **P<0.01, ***P<0.001, (One-way ANOVA, Bonferroni's multiple comparison test). **(B)** RNASeq heatmap of tumor xenograft lysates showing expression levels of angiogenesis-related factors. Mastectomy was performed 30 days post-cell injection. Significant upregulation of proangiogenic factors is noted as * P<0.05, ** P<0.01, *** P<0.001, **** P<0.0001 (Benjamini-Hochberg adjusted P-values). In gene expression heatmap red denotes increased gene expression while green corresponds to downregulation. LogFC (Fold Change) of gene expression compared to the MDA-MB-436 + CAFscr control. n=3 tumor/group. **(C)** Representative human angiogenesis proteome profiler arrays of pooled tumor xenograft lysates. Dot signal intensity correlates with protein amount captured by the membrane-immobilized antibodies. Highlighted pairs of dots (1-6) correspond to upregulated proangiogenic factors in MDA-MB-436 + CAFshCAV1 xenografts (see Figure 19D). Results are representative of 3 independent experiments. **(D)** Expression levels of angiogenesis-related proteins captured in the proteome profiler (see Fig. 19C) were measured by densitometry and expressed as mean pixel density after subtracting background.

In accordance with the structural features observed in sCAV1low tumors (increased vascular density, branching, and blind end numbers), RNASeq analysis of these tumors showed an upregulation of cytokines associated with a proangiogenic phenotype **(Fig. 19B)**. Using membranes spotted with capture antibodies, the presence of these proangiogenic factors in tumor lysates was also tested. Results showed a similar upregulation at the protein level of the following proangiogenic factors: IL-8, IL-1β, VEGF-A, PDGF-AB/BB, DPP4 and PTX3 **(Fig. 19C and 19D)**. Among these proangiogenic factors, Interleukin-8 (IL-8), a cytokine with potent proangiogenic effects[194–196,363,364], also involved in neutrophil recruitment[365,366] and recently linked with breast cancer stem cell (CSCs) maintenance[367,368], ranked as highest among these genes differentially upregulated in sCAV1low tumors, both at the transcript (*CXCL8*) and protein (IL-8) levels **(Fig. 19C and 19D)**.

The aforementioned morphological features, associated with impaired vascular maturation, are all indicative of poor vessel functionality, both in terms of low perfusion and increased permeability[148,150].

In order to analyze blood vessel functionality, perfusion capacity and permeability of the tumor capillaries were checked by injecting either biotin-labeled isolectin or a defined size dextran, in the tail vein of mice prior to performing mastectomy. Blood vessels in sCAV1low tumors showed not only a poorer perfusion, marked by the very limited isolectin staining **(Fig. 20A)**, but also increased leakiness as pointed by dextran extravasation **(Fig. 21)**. Conversely, sCAV1high tumors showed ~60% of isolectin-stained CD31-positive structures, indicating an estimated >3-fold higher perfusion as compared to sCAV1low tumors **(Fig. 20B)**.

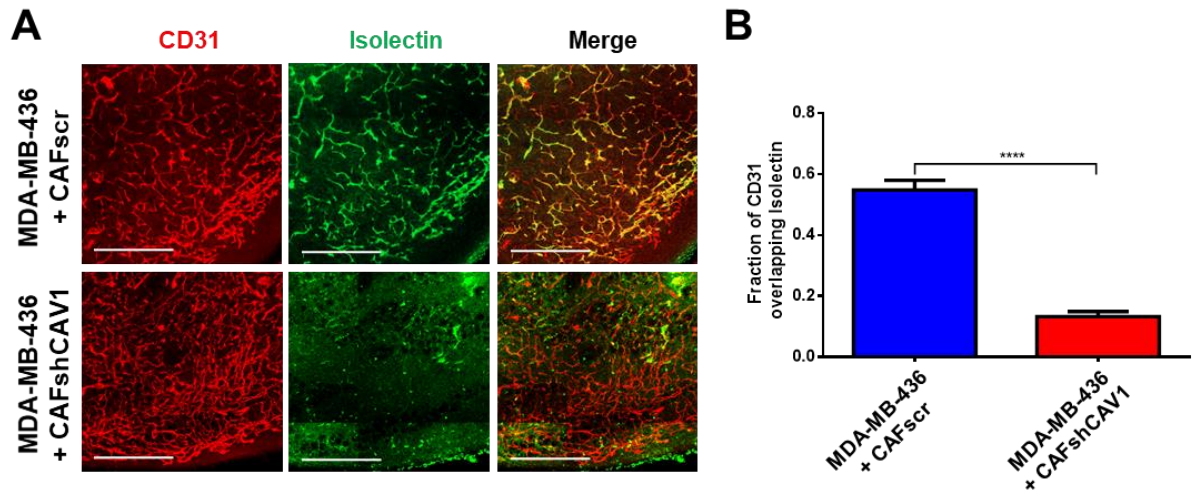

Figure 20. Perfusion of tumor vasculature is impaired in sCAV1low tumors. (A) Representative details of xenograft tumor sections showing inadequate perfusion in sCAV1low tumors. Blood vessels are revealed by CD31 (red) and isolectin staining demarks properly perfused capillaries (green). n=4 tumor/group. Scale bar: 0.5mm. **(B)** Quantification of isolectin positive tumor blood vessels (CD31+) for proper perfusion determination (see Fig. 20A). Data are presented as mean ± SEM; n=14 images/group, ****P<0.0001, (Two-tailed unpaired t-test).

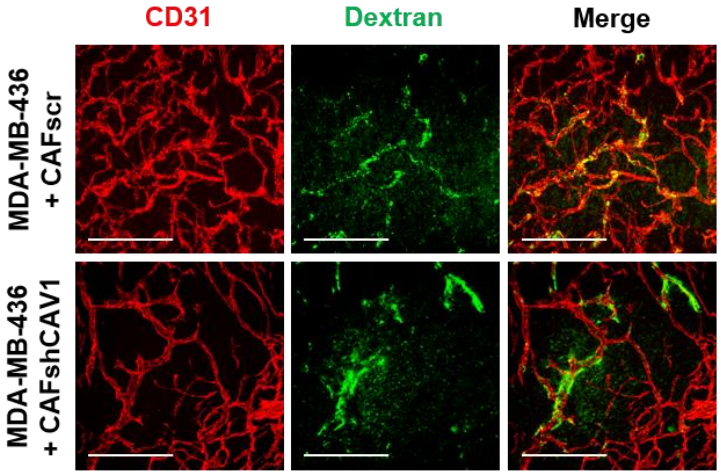

Figure 21. Permeability assessment of tumor xenograft vasculature. Blood vessels are defined by CD31 staining (red) and dextran is shown in green. Note the dextran leakage outside of the capillaries in the low sCAV1low tumors. n=4 tumor/group. Scale bar: 200µm

Capillary leakiness was also qualitatively assessed by relative interstitial signal of labeled dextran as compared to that retained within vascular structures. sCAV1low tumors exhibited substantial dextran signal in the interstitial space **(Fig. 21)**, suggesting altered permeability barrier in the vasculature of these tumor xenografts.

A balance of proangiogenic and antiangiogenic molecules maintains an organized and efficient blood supply in tissues. In the case of tumors, the exacerbated production of proangiogenic factors results in the growth of abnormal and inefficient vascular networks[145–147]. These networks show high vascular permeability and poor perfusion levels, features that the present work show to be exacerbated in sCAV1low TNBC tumor xenografts.

3.4 Inadequate blood supply in sCAV1low tumors results in increased hypoxia and fibrosis

Tumors can grow to a size of approximately 1–2 mm^3 before their metabolic demands are restricted due to a limited diffusion of oxygen and nutrients[138,259]. From that point onwards, blood vessels are required to sustain a supply of oxygen and nutrients to the tumor. The observed differences in vascular network functionality of tumors as dictated by their stromal CAV1 levels prompted to evaluate the differences in oxygen supply when comparing these conditions.

In order to study the levels of hypoxia (deprivation of an adequate oxygen supply) within the tumor, pimonidazole staining was used. Pimonidazole is a vital probe which becomes specifically activated in hypoxic cells in which its binding to protein thiol groups is greatly enhanced[369]. The resulting protein adducts can subsequently be detected through immunostaining. Upon pimonidazole immunostaining, an increased area of the tumor affected by hypoxia was observed in the case of sCAV1low tumors, even in vascularized regions **(Fig. 22A)**. The formation of lymphatic vessels, a key route for metastatic dissemination of breast cancer[13–15], was also observed both around hypoxic areas[370,371] and the outer border of tumor xenografts, although no significant differences were observed in the extent of the tumor area covered by lymphatic vasculature **(Fig. 22B)**.

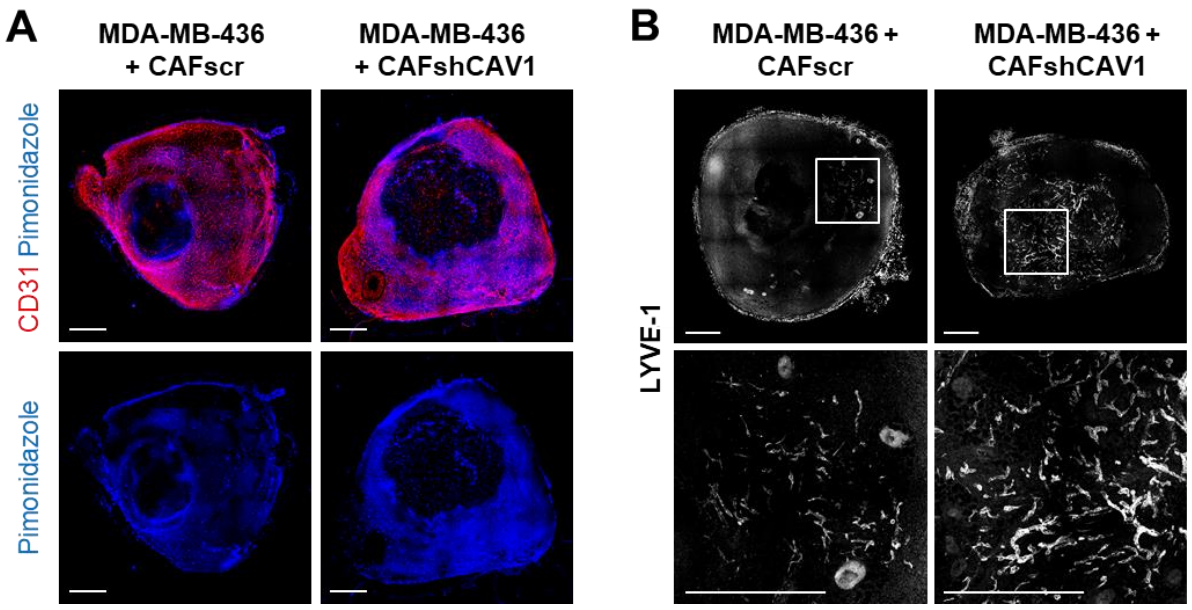

Figure 22. Hypoxia and lymphatic vessel detection in breast tumor xenografts. (A) Representative tissue sections obtained from primary breast tumor xenografts showing blood vessels stained with endothelial marker CD31 (red) and pimonidazole adducts, a marker of hypoxia (blue). Note the differential size of the necrotic core (in black, negatively stained) at inner regions of the tumors. Scale

bar: 1mm. **(B)** Breast primary tumor xenograft tissue sections showing intra- and peritumoral lymphatic blood vessels (marked by LYVE-1 staining) around the hypoxic necrotic core. Scale bar: 1mm.

In addition, Hypoxia-Inducible Factor 1 Alpha (HIF1A) nuclear localization, as a marker of hypoxia[155], correlated with pimonidazole positive areas **(Fig. 23A)** and comparative RNASeq transcriptional analysis of tumors confirmed an increased expression of hypoxia response transcript signatures in sCAV1low tumors **(Fig. 23B)**. Importantly, extending the time of primary tumor growth, from 30 to 40 days, led to an enrichment in the response to hypoxia expression profile in sCAV1low xenografts as compared to their sCAV1high counterparts **(Figure S1)**.

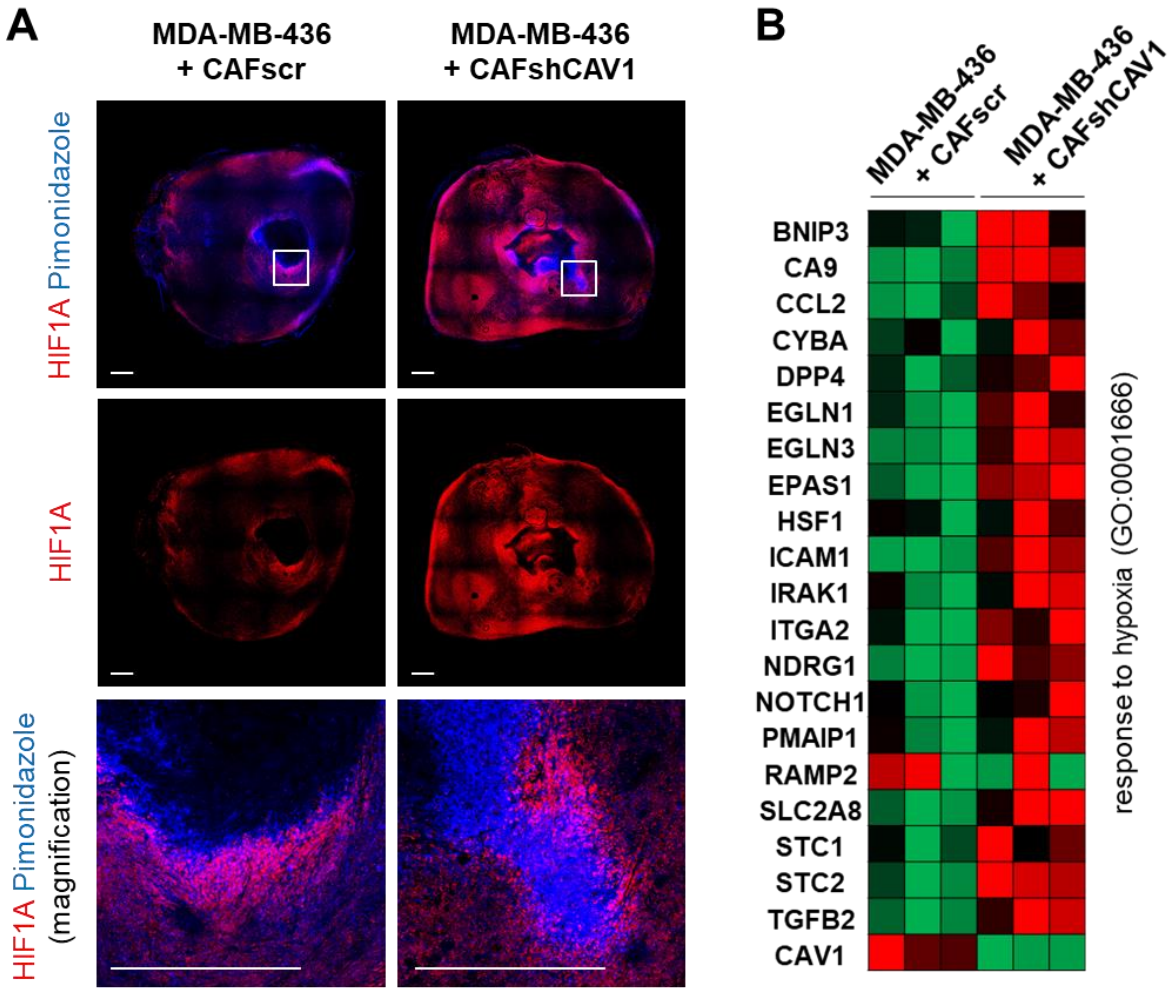

Figure 23. sCAV1low tumors suffer increased hypoxia. (A) Co-staining of pimonidazole adducts (blue) and HIF1A (red) showing hypoxic regions in primary breast tumor sections. Scale bar: 0.5mm. **(B)** Heatmaps derived from RNASeq expression profiles of primary tumor lysates showing a significant upregulation of genes related to hypoxia in sCAV1low tumors resected 30 days post-cell engraftment. n=3 tumors/group. In gene expression heatmap, red denotes increased gene expression while green corresponds to downregulation. n=3 tumor/group. See also Fig. S1.

As sustained hypoxic conditions are related to increased ECM deposition and tissue fibrosis[73,372], collagen fiber formation in tumor xenografts was evaluated by Second Harmonic Generation (SHG) imaging. In this regard, a clear increase in ECM deposition and fiber formation, aka fibrosis, a condition associated with poor prognosis and increased malignancy in breast cancer[103,373], was observed in sCAV1low tumors upon SHG microscopic examination **(Fig. 24A)**. Moreover, unbiased gene expression analysis of tumor lysates by RNASeq confirmed an increase in the expression of genes associated with ECM deposition and remodeling **(Fig. 24B)**.

Given that the amount of pimonidazole that is detected is directly proportional to the level of hypoxia within tumors[369], the co-localization of pimonidazole positive regions with nuclear HIF1A staining and the transcriptional profile of these tumors, it could be concluded that tumors with low stromal CAV1 (sCAV1low) were suffering increased hypoxia when compared to the ones with a higher stromal CAV1 expression (sCAV1high).

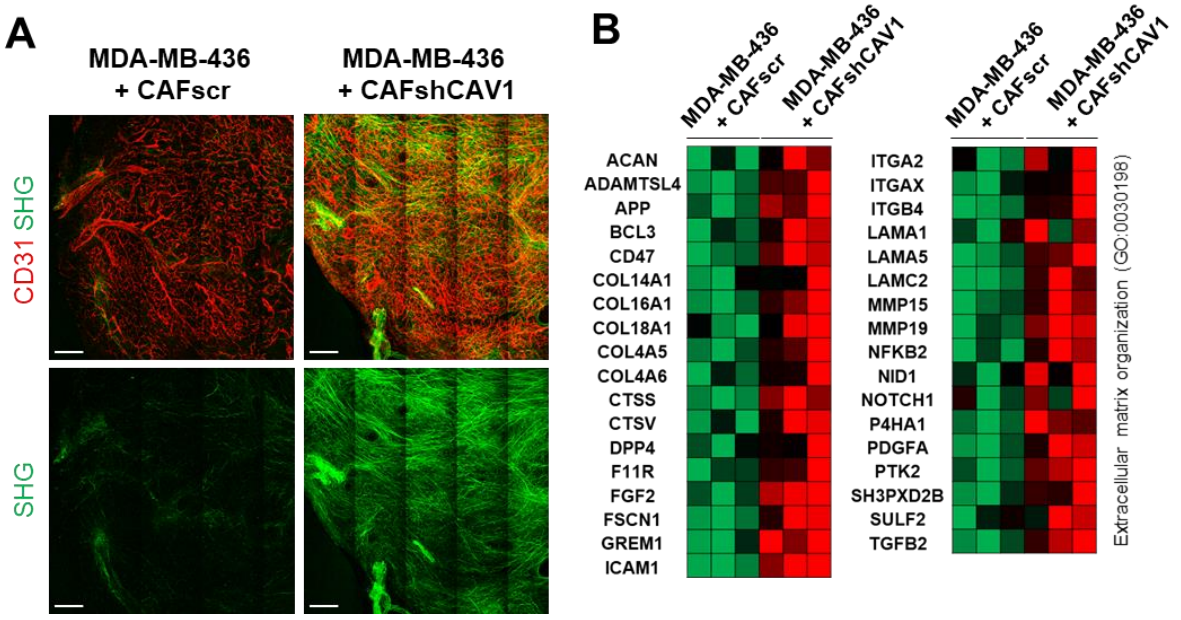

Figure 24. sCAV1low tumors show increased fibrosis. (A) Second Harmonic Generation (SHG) imaging (green) of primary breast tumors showing the increased fibrosis of tumors with low stromal CAV1 even in highly vascularized areas marked by CD31 staining (red). Scale bar: 200µm. **(B)** Heatmaps derived from RNASeq expression profiles of primary tumor lysates showing a significant upregulation of genes related to ECM organization in sCAV1low tumors resected 30 days post-cell engraftment. n=3 tumors/group. See also Fig. S1.

3.5 CAFshCAV1 proangiogenic expression profile increases endothelial cell proliferation and sprout formation

Given the changes in vascular network morphology and functionality observed in the previous tumor xenografts, where the most salient differential element was CAV1 stromal expression

levels, a decision was made to study the role that these stromal CAFs could be playing in angiogenesis induction and regulation.

First, the recapitulation of these gene signatures was corroborated *in vitro*. To do so, CAFscr and CAFshCAV1 cells were 3D-cultured in collagen I gels, and their transcriptome profiles were analyzed by RNASeq. Gene set enrichment analysis revealed that CAFshCAV1 showed an increased expression of *CXCL8* (IL-8), *IL6*, *CCL2*, *VEGFA* and *IL1B*, encoding for those cytokines associated with proangiogenic and proinflammatory processes[177,192–198] which were previously identified as relatively increased *in vivo* in sCAV1low tumors. Furthermore, the expression of negative regulators of angiogenesis, such as *EDN1*, *THBS1*, *THBS2,* and *VASH1,* was attenuated in CAFshCAV1 fibroblasts **(Fig. 25A)**. Confirmation of this RNA expression profiles was obtained by qPCR, except for *THBS1/2* downregulation, which using this approach fell below the significance threshold **(Fig. 25B)**.

In order to check if this increased expression of cytokines also correlated with a rise in secretion, conditioned medium of these 3D-cultured CAFs was assayed by ELISA. Results showed a correlation between expression of *CXCL8* and *IL6* genes and secretion levels of IL-8 and IL-6 cytokines **(Fig. 25C and 25D)**.

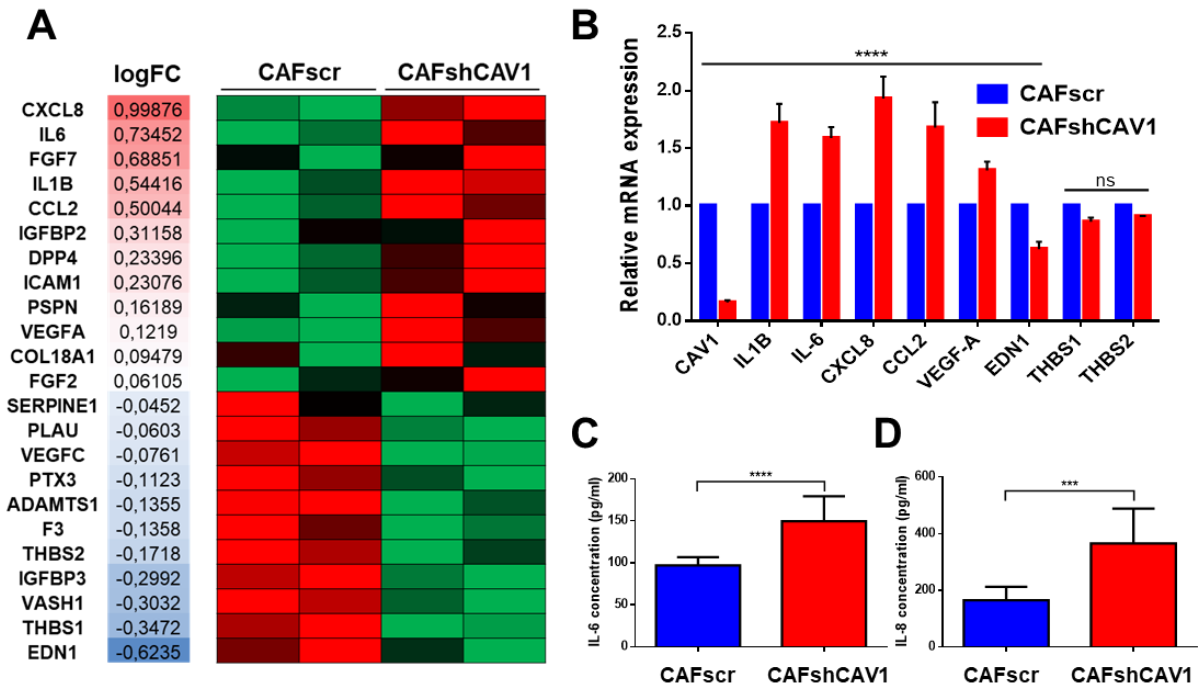

Figure 25. CAFshCAV1 fibroblasts show a proangiogenic expression profile. (A) Gene expression profile heatmaps (RNASeq-derived) from CAFs cultured for 7 days in a 3D Collagen I matrix. Upregulation of proangiogenic and downregulation of antiangiogenic factors is shown. In gene expression heatmap red denotes increased gene expression while green corresponds to downregulation. LogFC (Fold Change) of gene expression compared to the CAFscr control. n=2 group.

(B) RNASeq gene expression validation by qPCR (see Fig. 25A). Significant upregulation of proangiogenic *CXCL8, IL1B, IL6, CCL2* and *VEGFA* genes and downregulation of antiangiogenic *EDN1* gene can be observed. n=5, ****P<0.0001, (Two-way ANOVA, Bonferroni's multiple comparison test). **(C and D)** IL-6 and IL-8, respectively, concentration determination by ELISA in supernatants derived from 3D-cultured CAFs. n=4, ***P<0.001, ****P<0.0001. All quantification data are presented as mean ± SEM. Statistical significance was calculated by Two-tailed unpaired t-test when two experimental conditions were compared.

As an *in vitro* approach for testing the influence these CAFs could exert over the endothelial cells (that are part of the tumor blood vessels), Human Umbilical Vein Endothelial Cells (HUVECs) were exposed to CAF-conditioned medium as well as grown in the presence of CAFs in *in vitro* co-culture assays **(Fig. 26)**.

When culturing endothelial HUVEC cells under the exposure of CAFshCAV1-conditioned medium (CM), an increase in total endothelial cell number **(Fig. 26A and 26B)**, as well as an increase in proliferation, measured by EdU incorporation **(Fig. 26A and 26C)**, was observed when compared to HUVECs grown under the influence of CAFscr-conditioned medium.

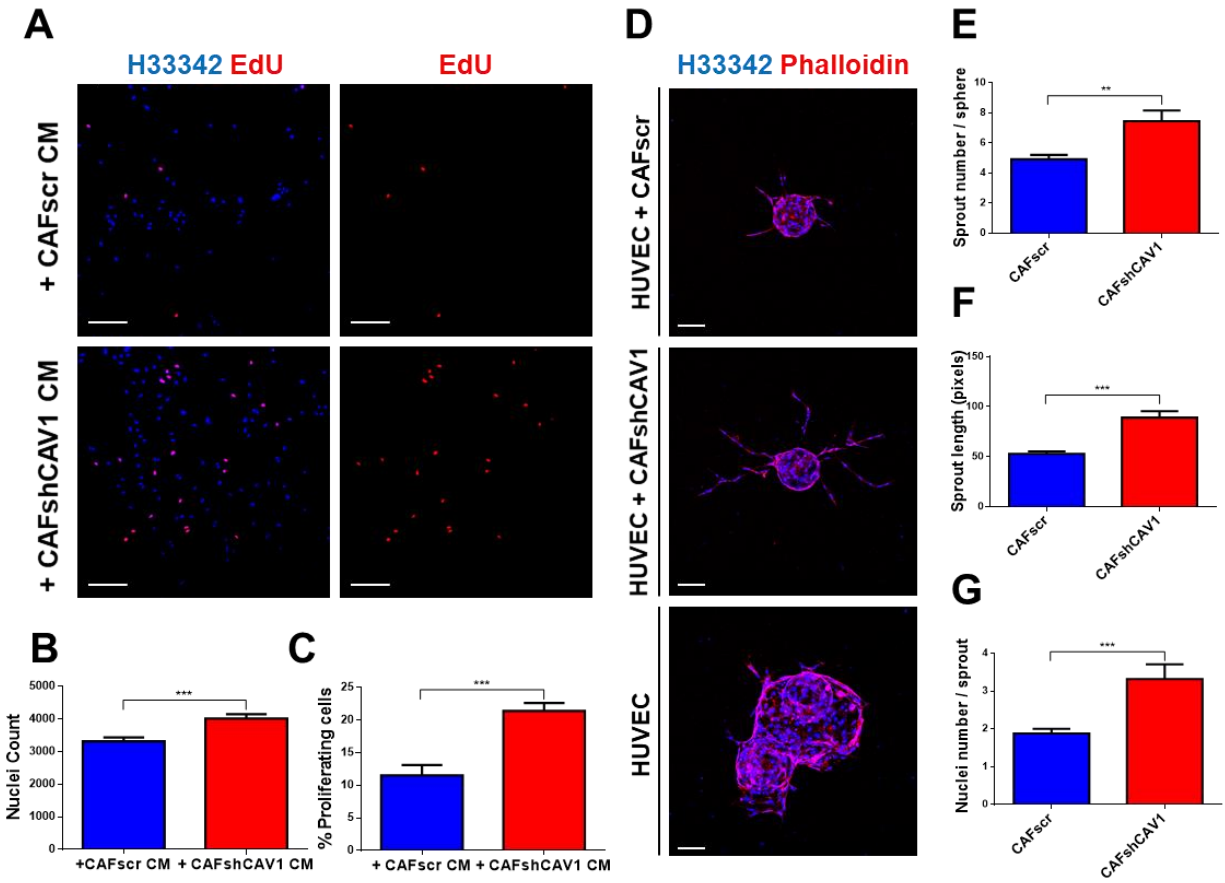

Figure 26. CAFshCAV1 display a proangiogenic effect in *in vitro* assays. (A) Representative HUVEC cell immunofluorescence depicting Edu incorporation into proliferating cells (red) and total cell nuclei number (blue, H33342 staining). HUVEC cells were grown in the presence of CAFscr or

CAFshCAV1 conditioned medium (CM). Scale bar: 200 µm. **(B)** HUVEC cell count after 32h exposure to CAF-conditioned medium. Cell count is increased when cultured under CAFshCAV1-derived medium influence. n=5, ***P<0.001. **(C)** HUVEC proliferation, measured by EdU incorporation, shows a boost when endothelial cells are cultured in CAFshCAV1 conditioned medium. n=3, ***P<0.001. **(D)** HUVEC sprouting assay shows an increase in endothelial sprout formation and length when co-cultured with CAFshCAV1 fibroblasts. Absence of fibroblasts results in sprout formation failure and disorganized growth. HUVEC cell nuclei appear in blue (H33342) and actin cytoskeleton in red (phalloidin). n=3. Scale bar: 100 µm. **(E, F, and G)** Quantification of sprout number/sphere, sprout length and nuclei number sprout, respectively. Co-culture with CAFshCAV1 fibroblasts shows an increase in all three parameters correlating with the production of proangiogenic factors. n=3, **P<0.01, ***P<0.001. All quantification data are presented as mean ± SEM. Statistical significance was calculated by Two-tailed unpaired t-test.

In order to mimic the formation of new blood vessels, an *in vitro* angiogenesis HUVEC sprouting assay in co-culture with CAFs was performed. This assay confirmed that HUVEC sprouting is only observed in the presence of a supporting layer of fibroblasts (CAFs in this case), as previously reported[347,374,375] **(Fig. 26D)**. When co-culturing these HUVEC cells with CAFshCAV1 fibroblasts an increase in the length and number of these sprouts, characteristics of an enhanced proangiogenic response[347,375], was noted when compared to the CAFscr co-culture. **(Fig. 26E and 26F)**. Increased sprout length was a result of increased cell number per sprout, rather than by endothelial cell elongation or hypertrophy **(Fig. 26G)**, in accordance with the higher proliferation rates quantified for HUVEC cells exposed to CAFshCAV1 conditioned medium **(Fig. 26C)**.

Taken together these experiments support a positive regulatory role of CAFs in the angiogenic process, which is dysregulated when CAV1 is downregulated and results in an exacerbated proangiogenic signaling that is capable of boosting endothelial cell proliferation and the disordered formation of new blood vessels.

3.6 CAV1 downregulation in CAFs leads to metabolic inflexibility and loss of organelle homeostasis resulting in increased proangiogenic cytokine production

CAV1 downregulation posed CAFs to exert an *in vivo* and *in vitro* proangiogenic effect. Still, the molecular mechanisms by which CAV1 downregulation leads to increased production of proangiogenic factors remained elusive. In order to unveil the signaling networks responsible for the production of these factors, the same RNASeq of 3D-cultured CAFscr and CAFshCAV1 cells was analyzed in a search for pathway upregulation/enrichment.

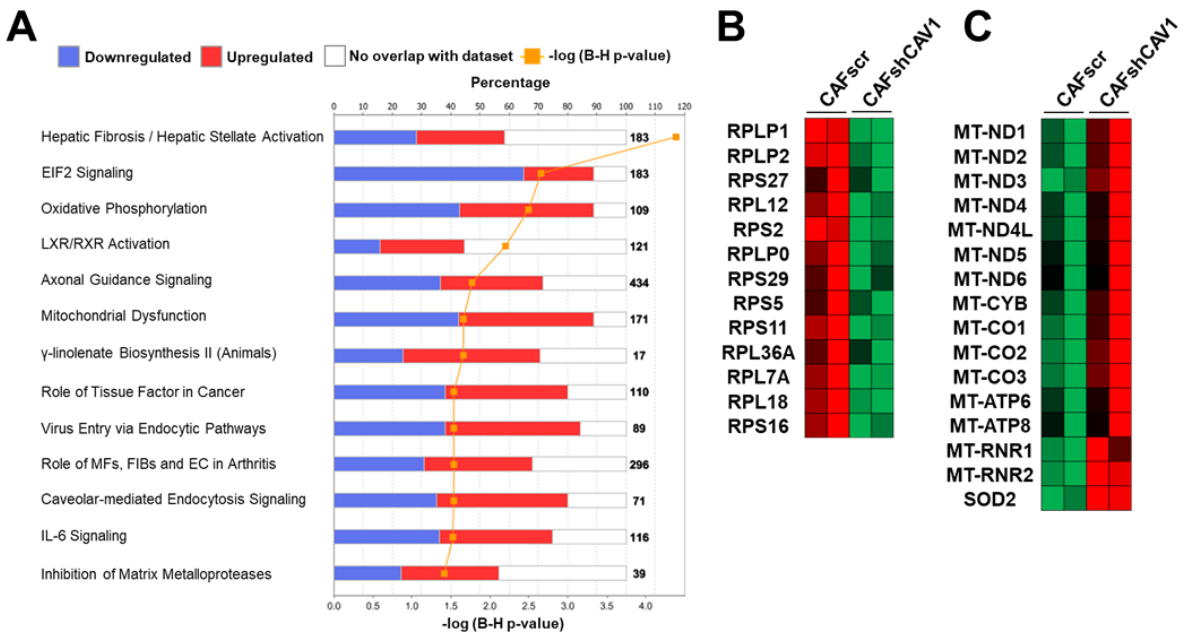

Figure 27. Transcriptional profile analysis reveals signatures compatible with the activation of an Integrated Stress Response (ISR). (A) Canonical pathway analysis using IPA (IPA; Qiagen, www.ingenuity.com) of transcriptomics data from 3D-cultured CAFs (RNASeq). Blue denotes downregulated genes in the pathway, while red upregulated. (Pathway overlap significance represented as –log Benjamini-Hochberg adjusted P-value). **(B and C)** Gene expression profile heatmaps (RNASeq-derived) from CAFs cultured for 7 days in a 3D Collagen I matrix. Significant **(B)** downregulation of ribosomal proteins (RPS/RPL) and **(C)** upregulation of mitochondrial genome-encoded (MT) OXPHOS genes and SOD2 (superoxide dismutase 2) is shown. In gene expression heatmap red denotes increased gene expression while green corresponds to downregulation. n=2 group.

This transcriptome analysis revealed signatures compatible with a robust activation of an integrated stress response (ISR)[376,377] in CAFshCAV1 fibroblasts **(Fig. 27A)**, including: (i) repression of the initiation phase of protein synthesis (eIF2α signaling downregulation) and (ii) decreased expression of ribosomal protein family genes (*RPL & RPS*) **(Fig. 27B)**; in addition to mitochondrial dysfunction-related traits[378], such as imbalanced upregulation of mitochondrial genome-encoded (MT) oxidative phosphorylation (OXPHOS) and superoxide response genes (*SOD2*) **(Fig. 27C and 28B).**

Further ultrastructural electron microscopy analyses of CAFshCAV1 cells revealed an altered mitochondrial architecture, especially when cells were exposed to low glucose levels (2.5mM) akin those found *in vivo*. Mitochondria from CAFshCAV1 fibroblasts showed reduced length, and aberrant cristae architecture (i.e. broader necks and reduced extension) **(Fig. 28A, 2SA, and 2SB)**, as previously reported in CAV1-knockout cells[379]. A deeper characterization of CAFshCAV1 cells also showed: (i) Increased mRNA levels of mitochondrially encoded (MT) oxidative phosphorylation (OXPHOS) system genes **(Fig. 27C and 28B)** and (ii) increased net

mitochondrial mass and enhanced reactive oxygen species (ROS) production as shown by fluorescence microscopy and cytometry assays **(Fig. 28C, 28D and 28E)**, pointing to a potentially compensatory behavior for mitochondrial dysfunction. These findings harmonize with previous studies reporting a lower efficiency of the OXPHOS system in mitochondria derived from Cav1-knockout mice[317,380,381].

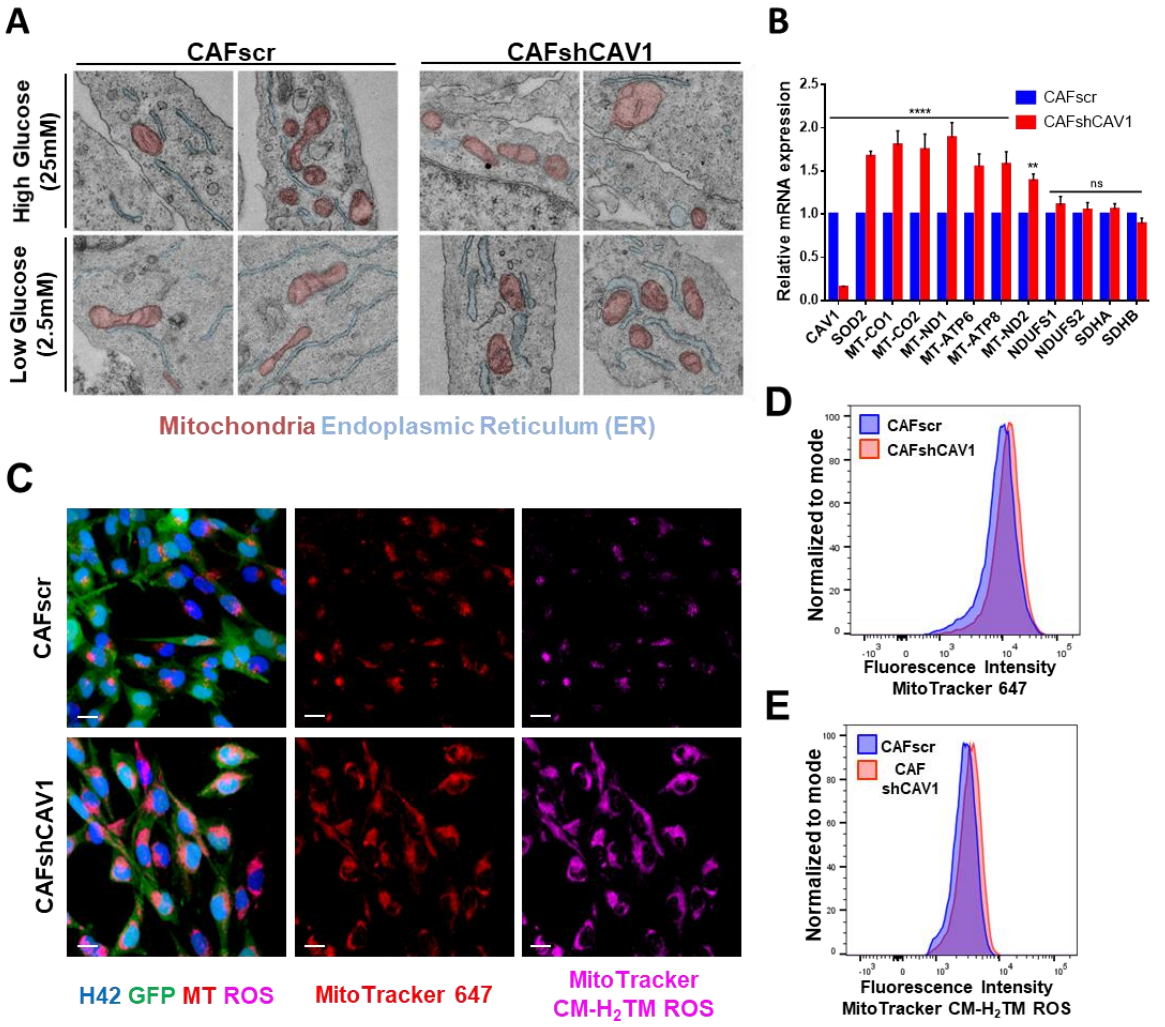

Figure 28. CAFshCAV1 fibroblasts show dilated ER structures and increased mitochondrial mass and ROS production. (A) False-colored electron microscopy section of CAFs cultured in high and low glucose DMEM. CAFshCAV1 fibroblasts show aberrant mitochondrial architecture (light red) and dilated ER (light blue). **(B)** RNASeq gene expression validation by qPCR (see Fig. 27C). Significant upregulation of mitochondrial genome-encoded (MT) OXPHOS genes and *SOD2*, a mitochondrial-derived ROS processing enzyme, are shown. Expression levels of *NDUFS1*, *NDUFS2*, *SDHA* and *SDHB*, genes part of the mitochondrial OXPHOS machinery, but codified by the nuclear genome, remain unchanged. Data are presented as mean ± SEM relative to CAFscr CTRL; n=6, *P<0.05, **P<0.01, ***P<0.001, ****P<0.0001, (Two-way ANOVA, Bonferroni's multiple comparison test). **(C)** Representative fluorescence microscopy images of GFP^{+} CAFs (in green), stained for nuclei (H33342, in blue), mitochondria (MitoTracker 647, in red) and mitochondria-derived ROS production (MitoTracker CM-H2TM ROS, in magenta). Scale bar: 20µm. **(D and E)** Quantification of mitochondrial content and

mitochondria-derived ROS production in CAFs, respectively, by flow cytometry. Data are presented as representative histograms normalized to mode; n=5.

Intriguingly, the endoplasmic reticulum (ER) was also sensitive to CAV1 downregulation. CAV1 mRNA silencing in CAFs led to apparent dilated ER structures **(Fig. 2SC)**, a higher degree of ER discontinuity, and relative loss of ER-mitochondria communication **(Fig. 28A)**. In agreement with challenged ER homeostasis upon CAV1 knockdown in CAFs, the transcriptome analyses revealed activation of integrated stress response (ISR) signatures, such as the already mentioned eIF2α signaling downregulation **(Fig. 27A)** and the decreased expression of ribosomal protein family genes (RPL & RPS) **(Fig. 27B)**. Accordingly, CAFshCAV1 fibroblasts revealed an increased staining for the transcription factor ATF4, which induces transcription of genes directed by the PERK arm of the UPR[382] **(Fig. 2SD)**, and an upregulation of *bona fide* UPR transcriptional targets such as *CHOP* and *XBP1* **(Fig. 31A).**

Because these conditions of dysregulated mitochondrial metabolism and altered ER organelle homeostasis have been reported to increase proangiogenic and proinflammatory signaling[244,251–255,383–385], the causative relationship between these functional imbalances and the enhanced secretion of proangiogenic factors and inflammatory cytokines in CAFshCAV1 fibroblasts was explored.

3.7 Mitochondrial dysfunction is not the cause of proangiogenic cytokine upregulation

A first approach was to intervene the functional alterations observed for mitochondria upon CAV1 downregulation. Metabolically, loss of CAV1 reduces the efficiency of the mitochondrial respiratory chain, and thus aerobic glycolysis predominates over oxidative phosphorylation (OXPHOS) as a means for energy production[307,317,380].

Taking advantage of this preference for energy production, CAFshCAV1 fibroblasts were forced to use OXPHOS, and thus their dysfunctional mitochondria, by drug treatments with 2-deoxyglucose (2-DG), a glycolysis inhibitor, and dichloroacetic acid (DCA), which shifts glucose catabolism from glycolysis to OXPHOS. Besides manifesting CAFshCAV1 mitochondrial dysfunction characterized by impaired OXPHOS **(Fig. 29A)**, these treatments resulted in the upregulation of *CXCL8, IL1B, IL6,* and *VEGFA*, especially in the case of 2-DG treatments **(Fig. 29B and 29C)**. CAFs cultured in low glucose medium (2.5mM) showed similar results **(Fig. 29D)**.

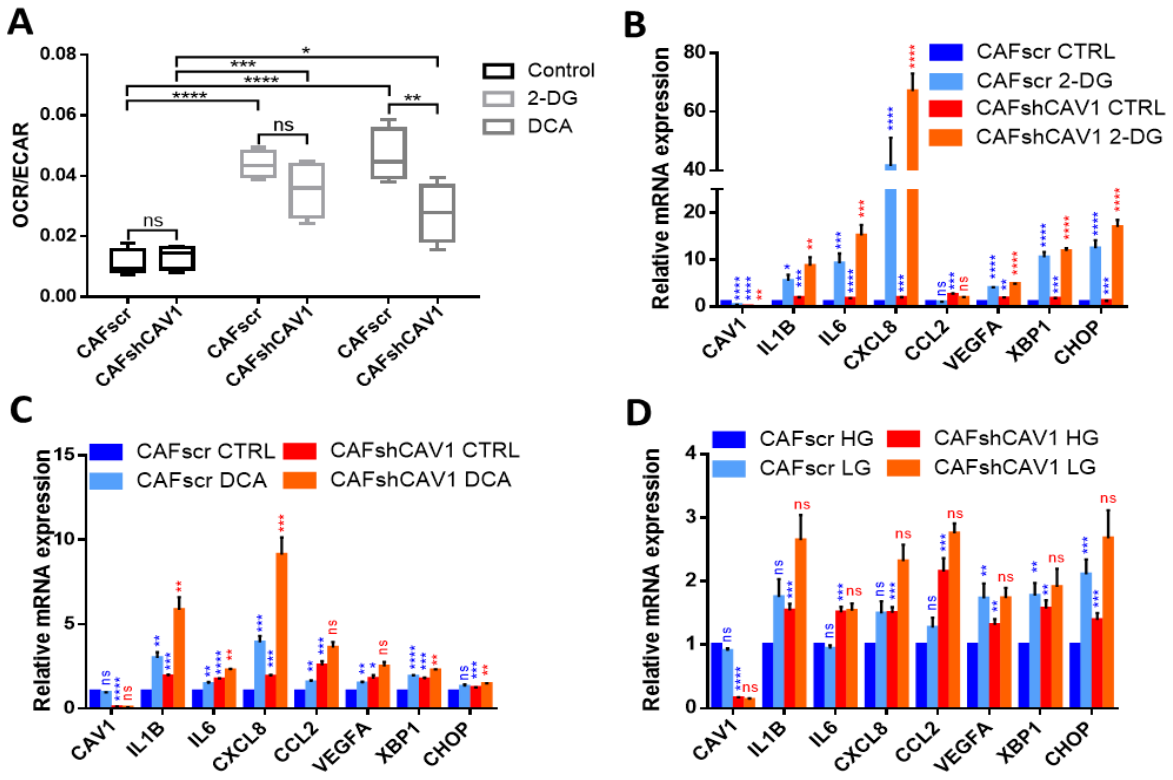

Figure 29. 2-DG and DCA treatments manifest CAFshCAV1 mitochondrial poor OXPHOS performance and increased cytokine production. (A) Seahorse CAF mitochondrial functionality assessment by Oxygen Consumption Rate (OCR, a proxy of mitochondrial oxidative phosphorylation, OXPHOS) and Extracellular Acidification Rate (ECAR, a proxy of glycolytic efficiency) ratio determination. CAFs were treated overnight and during OCR/ECAR determination with either 5mM 2-DG or 25mM DCA, aimed at forcing mitochondrial use for energy production, which showed the poor efficiency of OXPHOS (low OCR/ECAR ratio) in CAFshCAV1 fibroblasts. OCR/ECAR ratios are presented as boxplots (Min to Max values) and are representative of 3 independent experiments; n=6 wells/condition, *P<0.05, **P<0.01, ***P<0.001, ****P<0.0001, (Two-way ANOVA, Tukey's multiple comparison test). **(B,C, and D)** qPCR expression analysis of *CAV1*, cytokines (*IL1B, IL6, CXCL8, CCL2* and *VEGFA*) and ER stress markers (*CHOP* and *XBP1*) from CAFs cultured in either **(D)** high (25mM) or low (2.5mM) glucose DMEM or treated with **(C)** 25mM DCA or **(B)** 5mM 2-DG**.** For qPCR gene expression analysis data are presented as mean ± SEM relative to CAFscr CTRL; n=5, *P<0.05, **P<0.01, ***P<0.001, ****P<0.0001, Significance for comparisons against CAFscr CTRL (vehicle) is depicted in blue, and for CAFshCAV1 CTRL (vehicle) in red (Multiple t-test comparisons, with Holm-Sidak multiple comparison correction).

CAV1 deficiency is associated with reduced cholesterol transport[316] and cholesterol accumulation in mitochondrial membranes, driving mitochondrial dysfunction and aerobic glycolysis[307,317]. This cholesterol accumulation has been reported to prevent the activity of mitochondrial glutathione/2-oxoglutarate antiporters, thus lowering the pool of this ROS-quenching agent (glutathione) in the mitochondria[386,387].

This CAFshCAV1 cellular model also exhibited increased intracellular cholesterol levels (data not shown), as well as elevated ROS **(Fig. 28C and 28E)**. CAF cells were thus exposed to

(i) an inhibitor of endogenous cholesterol synthesis (lovastatin), to curb intracellular free cholesterol accumulation; and (ii) the antioxidant glutathione (GSH), in an attempt to revert mitochondrial dysfunctionality **(Fig. 30)**.

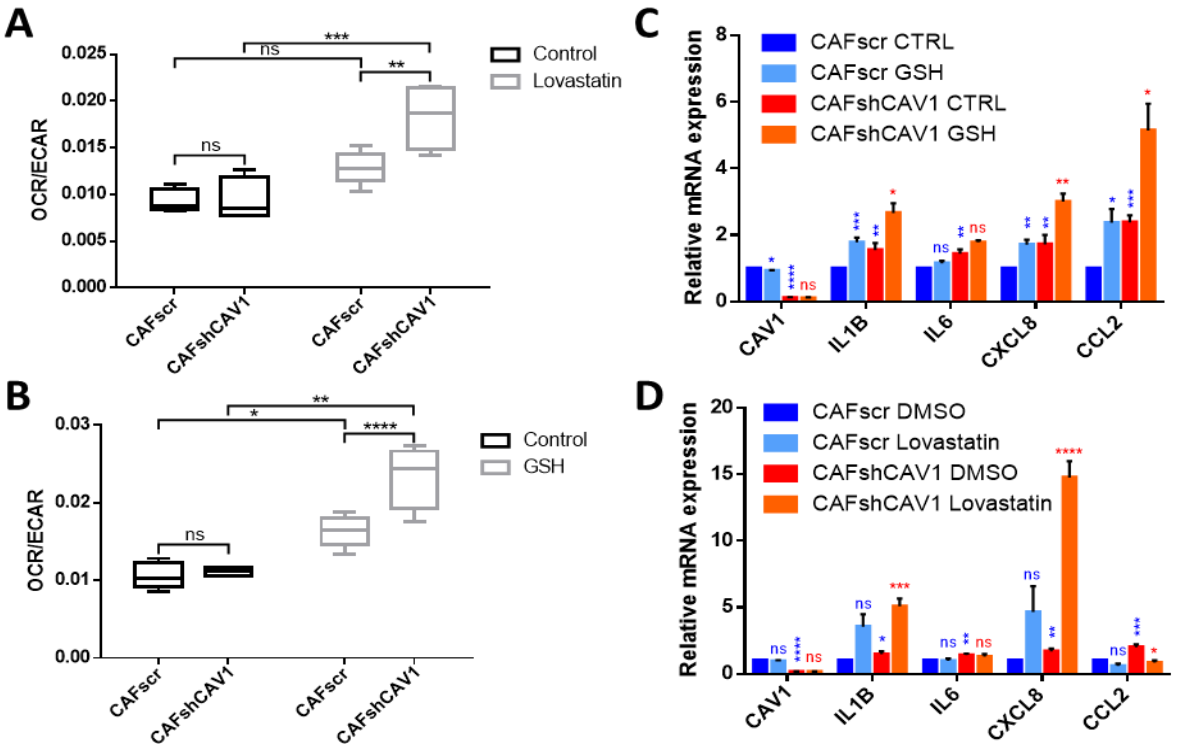

Figure 30. Partial mitochondrial function restoration does not reverse cytokine production. (A and B) Seahorse CAF mitochondrial functionality assessment by OCR/ECAR ratio determination. CAFs were treated overnight and during OCR/ECAR determination with: **(A)** 25µM Lovastatin and **(B)** 5mM GSH, aimed at restoring mitochondrial functionality, which resulted in an increased OCR/ECAR ratio for CAFshCAV1 versus CAFscr fibroblasts, both as a result of increased OXPHOS efficiency and the higher mitochondrial content found in CAFshCAV1. OCR/ECAR ratios are presented as boxplots (Min to Max values) and are representative of 3 independent experiments; n=6 wells/condition, *P<0.05, **P<0.01, ***P<0.001, ****P<0.0001, (Two-way ANOVA, Tukey's multiple comparison test). **(C and D)** qPCR expression analysis of CAV1 and cytokines (*IL1B, IL6, CXCL8, CCL2* and *VEGFA*) from CAFs treated with **(C)** 25µM Lovastatin or **(D)** 5mM Glutathione (GSH). For qPCR gene expression analysis data are presented as mean ± SEM relative to CAFscr CTRL; n=5, *P<0.05, **P<0.01, ***P<0.001, ****P<0.0001, Significance for comparisons against CAFscr CTRL (vehicle) is depicted in blue, and for CAFshCAV1 CTRL (vehicle) in red (Multiple t-test comparisons, with Holm-Sidak multiple comparison correction).

None of these treatments, despite being capable of alleviating intrinsic mitochondrial dysfunction, as assessed by OXPHOS efficiency **(Fig. 30A and 30B)**, were capable of curbing the expression of proangiogenic and proinflammatory cytokines, in fact, a moderate increase in their expression was observed for CAV1-deficient cells **(Fig. 30C and 30D)**. Treatment with an exogenous, fully cell permeant ethyl-ester GSH derivative (GSH-EE), showed similar results in terms of cytokine upregulation (data not shown). Thus, it was interpreted that the

proangiogenic secretory profile displayed by CAFshCAV1 fibroblasts was unlikely to directly derive from a compromised mitochondrial performance.

3.8 Endoplasmic reticulum (ER) stress induction links CAV1 downregulation and proangiogenic cytokine production

Next, the impact on proangiogenic paracrine signaling of CAFs of either inducing ER stress (and the consequent UPR response), using ER stressors such as Thapsigargin or Tunicamycin, or specifically disrupting acting branches of the adaptive UPR response (PERK and IRE1) was tested.

First, CAFs were exposed to either Thapsigargin or Tunicamycin, which, either by inhibiting the sarcoplasmic/endoplasmic reticulum Ca2+-ATPase (SERCA) and autophagosome-lysosome fusion, or by blocking protein glycosylation, respectively, lead to the accumulation of unfolded proteins and activation of ER stress/UPR[388]. Importantly, exposure to ER stressors not only upregulated the expression of proangiogenic factors such as *IL6*, *CXCL8*, and *VEGFA* (along with bona fide ER stress markers such as *XBP1* and *CHOP*), but also downregulated CAV1 expression, both at the transcriptional and protein levels **(Fig. 31A and 31B)**. A slight downregulation of *IL1B* and *CCL2* upon Thapsigargin treatment was also observed **(Fig. 31A)**.

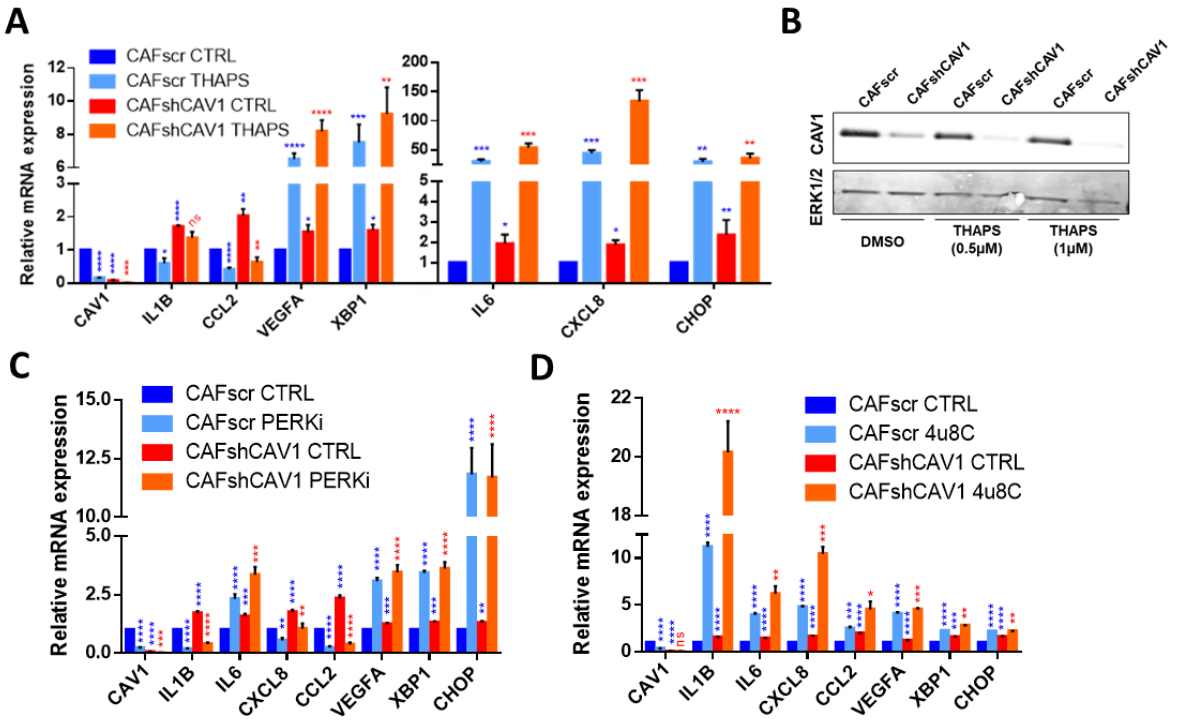

Figure 31. Endoplasmic reticulum (ER) stress induction links CAV1 downregulation and proangiogenic cytokine production (A, C, and D) qPCR expression analysis of CAV1, cytokines (*IL1B, IL6, CXCL8, CCL2* and *VEGFA*) and ER stress markers (*CHOP* and *XBP1*) from CAFs treated for 24h with*:* **(*A*)** 1μM Thapsigargin, an ER stress inducer, **(*C*)** 10μM GSK2606414, a PERK inhibitor, or

(*D*) 5 μM 4μ8C, an IRE1α inhibitor. **(I)** CAV1 Western Blot analysis of CAFs treated for 24h with Thapsigargin. Note the decreased CAV1 protein levels upon treatment. ERK1/2 is used as loading control. For qPCR gene expression analysis data are presented as mean ± SEM relative to CAFscr CTRL; n=5, *P<0.05, **P<0.01, ***P<0.001, ****P<0.0001, Significance for comparisons against CAFscr CTRL (vehicle) is depicted in blue, and for CAFshCAV1 CTRL (vehicle) in red (Multiple t-test comparisons, with Holm-Sidak multiple comparison correction).

Then these analyses were extended to treatments specifically abrogating not ER functional impairment, but its downstream adaptive UPR signaling. Thus, the impact of shutting down two of the key UPR signaling branches, PERK and IRE1α, on cytokine production was evaluated **(Fig. 31C and 31D)**.

While exposure of CAFs to GSK2606414, a PERK inhibitor (PERKi)[256], led to a significant downregulation of the proangiogenic/proinflammatory *CXCL8* cytokine transcript **(Fig. 31C)**, treatment with 4μ8C, an IRE1α inhibitor, markedly upregulated the expression of this gene **(Fig. 31D)**. These complementary results point to a PERK driven axis as an inducer of the expression of IL-8 cytokine upon CAV1 downregulation and ER stress activation; a role that is further enhanced, as a compensatory effect, upon IRE1α UPR axis inhibition. Although *CCL2* and *IL1B* expression follow the same pattern, the same conclusion could not be reached given that ER stress induction with Thapsigargin also results in their downregulation **(Fig. 31A)**.

Even though *VEGFA* and *IL6* are markedly upregulated upon ER stress induction with Thapsigargin **(Fig. 31A)** neither PERK nor IRE1α UPR axis inhibition resulted in the downregulation of any of the two genes **(Fig. 31C and 31D)**. Interestingly, CAV1 downregulation and *XBP1*/*CHOP* (ER stress markers) upregulation were also apparent upon drug-mediated inhibition of both PERK and IRE1α UPR axes **(Fig. 31C and 31D)**.

Taken together these results, regarding the expression of the aforementioned genes under ER induction and PERK or IRE1α inhibition, showcase the redundant and compensatory roles that alternative UPR signaling axes activate when one of them is inhibited. Still, the PERK UPR axis, upon CAV1 downregulation (and subsequent ER stress activation), poses as a plausible responsible for IL-8 upregulation; a proangiogenic cytokine that is key for the observed phenotype of dysfunctional vasculature and increased aggressiveness phenotype observed in sCAV1low tumors (see below).

In addition, a relationship between CAV1 levels an ER stress was established, since CAV1 downregulation activates ER stress (and the subsequent UPR response) and *vice versa,* ER stress induction promotes CAV1 downregulation both at the transcriptional and protein level. Supporting this data, a small pilot screening where different drugs were tested in an attempt to regulate CAV1 levels in pancreatic CAFs offered proteasome inhibitors (bortezomib and

MG-262), considered indirect activators of ER stress[389], as positive hits for downregulation of CAV1 **(Fig. S3)**.

3.9 Low stromal CAV1 levels in breast tumor xenografts are associated with poor prognosis and aggressive metastatic cancer

Besides angiogenesis, hypoxic conditions can also promote tumor aggressiveness[46,73,280–284] and lymphangiogenesis[370,371], the formation of new lymphatic vessels. Not only these vessels constitute efficient conduits for breast cancer cell dissemination[13–15] but lymphangiogenesis is also considered a plausible promoter of breast cancer metastasis[15,390].

Given that low CAV1 stromal levels result in increased tumor hypoxia, a metastasis-promoting factor, and new lymphatic vessel formation was observed in hypoxic areas **(Fig. 22B)**, the survival, relative rate of metastatic dissemination and subsequent thriving of cancer cells were analyzed in mice bearing low or high stromal CAV1 tumors.

To assess metastatic potential, disease progression was followed up after surgical resection of the primary tumor. A first intriguing observation was that mice bearing sCAV1low tumors exhibited significantly lower survival rates, as 50% of this mice group died 2.5 months post-mastectomy, while survival of mice that had been injected only breast cancer cells (MDA-MB-436) or a combination of cancer cells and CAFscr fibroblasts remained unaffected for the duration of the experiment **(Fig. 32A)**. These observations strongly suggested that in this experimental system, low stromal CAV1 expression was associated with worse progression of the disease after removal of primary tumors, presumably because of differential metastatic potential.

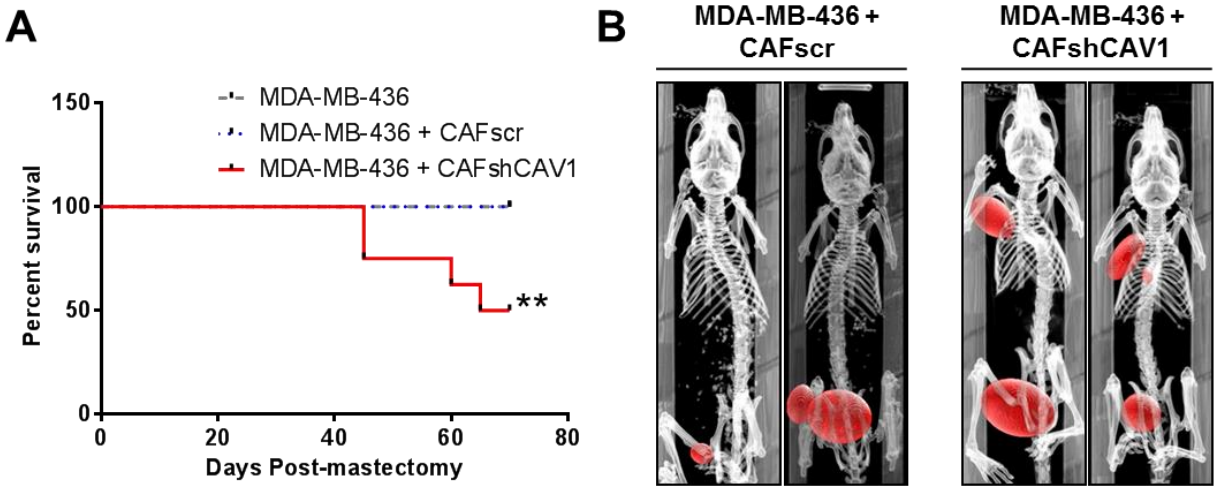

Figure 32. Low stromal Cav1 levels in breast primary tumor are associated with poor prognosis and aggressive metastatic cancer (A) Kaplan-Meier survival curve illustrating post-mastectomy progression-free survival in mice inoculated pre-mastectomy either with tumor cells only (MDA-MB-436), tumor cells plus control fibroblasts (436 + CAFscr, sCAV1high) or tumor cells plus fibroblasts with low

levels of CAV1 (436 + CAFshCAV1, sCAV1low). **P<0.01, log-rank (Mantel-Cox) test; n=8 mice/group from 2 independent experiments. **(B)** Representative 3-D tumor renderings (in red) from mice PET-CT studies performed 2 months post-mastectomy. Recurrent tumors after mastectomy can be observed in the mammary fat pad on both groups, while axillary lymph node and lung metastasis are only detectable in the group with low stromal CAV1 (sCAV1low, MDA-MB-436 + CAFshCAV1).

In order to study breast cancer cell dissemination in a non-invasive manner, 60 days post-mastectomy PET-CT studies of mice using radiolabeled glucose were carried out. As a consequence of cancer cell metastatic dissemination, secondary tumors, also apparent by visual inspection, formed in the lymph nodes located below the upper limbs of mice, a typical site for early metastasis in breast cancer[13–15,390] **(Fig. 32B)**. During necropsy, and posterior histological analysis, the presence of metastases at axillary lymph nodes was evaluated and showed a significantly higher occurrence in the case of mice that bore a sCAV1low primary tumor **(Fig. 33C)**.

Importantly, mice that carried a sCAV1low primary tumor before mastectomy showed a higher maximum glucose uptake in recurrent tumors **(Fig. 33E)**, as well as PET-CT detectable lung metastatic foci **(Fig. 32B)**, both indicative of increased tumor aggressiveness.

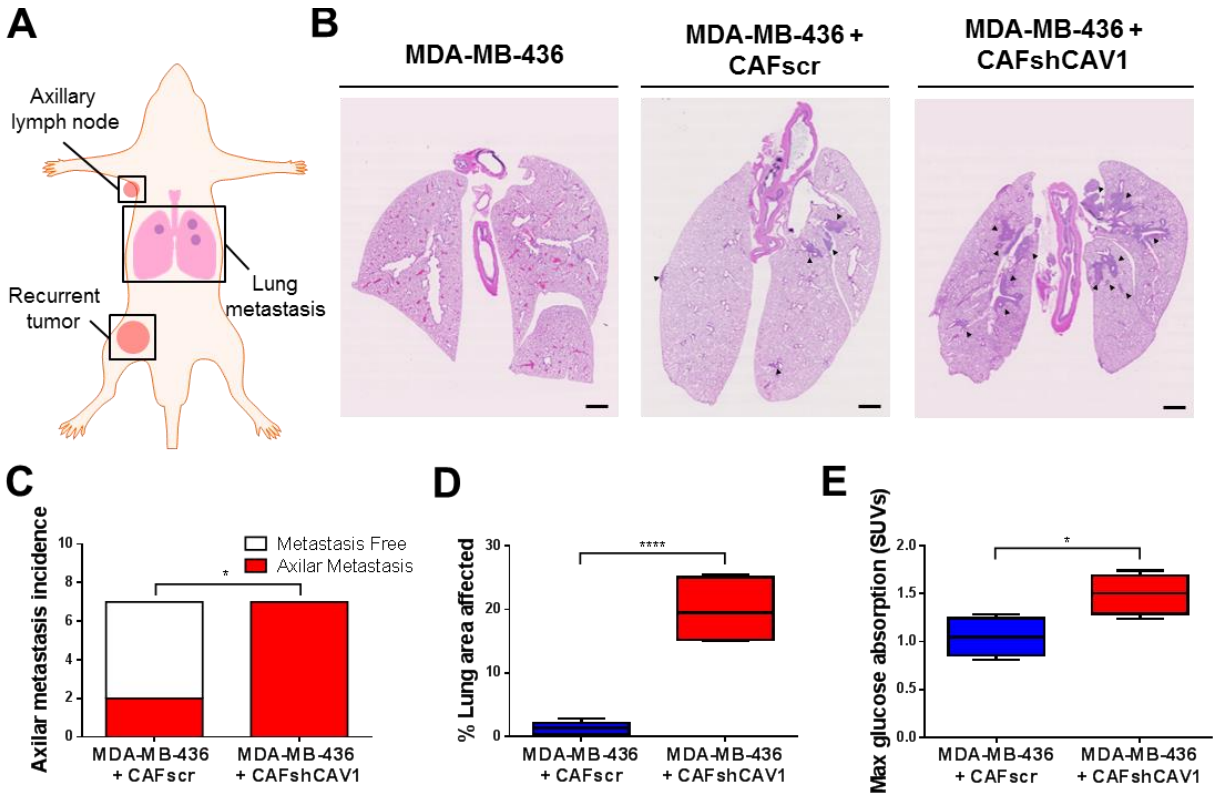

Figure 33. (A) Mouse diagram showing areas analyzed post-mastectomy to evaluate metastatic burden and aggressiveness. **(B)** Representative images of H&E-stained lung sections harvested 2.5 months post-mastectomy. Metastatic lesions appear as dark purple regions, in contrast to the rest of the lung tissue, due to an accumulation of cancer hematoxylin-stained cell nuclei (black arrows). Mice bearing

only tumor cells show no lung metastasis while the presence of both tumor cells and Cancer-Associated fibroblasts give rise to lung metastasis, with greater extent (~ 15-fold) in the case of sCAV1low tumors. Scale bar: 1mm. **(C)** Axillary lymph node tumor metastasis incidence evaluated (by PET-CT and necropsy analysis) 60 days post-mastectomy. *P<0.05; n=7 mice from 2 independent experiments. (Contingency analysis: Two-sided Fisher's exact test). **(D)** Lung area affected by metastatic tumor cells at 2.5 months post-mastectomy (see Fig. 6D). ****P<0.0001. Data are presented as mean ± SEM; n=8/CAFscr group and n=4/CAFshCAV1 group (rest of individuals could not be quantified due to mice death as shown in Fig. 6A). **(E)** Maximum levels of glucose absorption in recurrent tumors obtained from PET-CT studies performed 2 months post-mastectomy (see Figure 33B). Analysis shows an increased absorption in the recurrent tumors derived from more aggressive TCs + CAFshCAV1 xenografts. Data are presented as mean ± SEM; n=4, *P<0.05. Statistical significance was calculated by Two-tailed unpaired t-test when two experimental conditions were compared unless stated otherwise.

Since PET-CT studies are not able to detect lung micro metastases unless these lesions reach a certain size, H&E staining of the lungs of these mice was performed in order to determine the post-mastectomy metastatic burden. A significant increase in lung areas affected by metastatic lesions in mice that pre-mastectomy bore low CAV1 stromal tumors was detected. Metastasis in lungs of mice bearing tumor xenografts composed exclusively of cancer cells was not observed **(Fig. 33B and 33D)**.

In summary, sCAV1low tumors showed an enhanced growth and dissemination of lung and lymph node metastasis that translated into lower survival. Taken as a whole, these results pointed to an increased aggressiveness of sCAV1low tumors.

4. DISCUSSION

4. DISCUSSION

Efforts in breast cancer research have recently shifted from the understanding of cancer cell transformation to the study of the complex cross-talk between cancer cells and the stroma/tumor microenvironment (TME)[45–48], of which Cancer-Associated Fibroblasts (CAFs) constitute a major share[73,75,128]. Furthermore, breast cancer clinical outcome is strongly related to stromal characteristics and markers[58,59,108–111]. Among these markers, downregulation of CAV1 in CAFs has been associated with changes in tumor growth and prognosis with varied results[303,308,323], thus further work is needed to justify the potential prognostic use of stromal CAV1.

Here it is shown how selectively downregulating CAV1 in stromal CAFs generates a defective tumor vasculature in TNBC mouse xenografts. According to the presented results, this work proposes that such dysfunctional network in sCAV1low tumors, and the subsequent increased tumor hypoxia therein: (i) favors malignancy and increased metastasis via the lymphatic system and (ii) sustains the imbalance among pro- and anti-angiogenic cues, further aggravating the aberrant angiogenic process.

In addition, this work establishes a positive feedback loop relationship between CAV1 downregulation and induction of endoplasmic reticulum (ER) stress, which results in the exacerbated proangiogenic signaling deemed responsible for the formation of the non-functional tumor vasculature in the first place. Among these proangiogenic cues, upregulated both in CAFshCAV1 fibroblasts and corresponding sCAV1low tumors, IL-8 poses as a pivotal factor in inducing the observed aberrant tumor vasculature and enhanced metastasis phenotype.

These results, however, do not exclude the implication of CAFs-derived metabolites in the proangiogenic phenotype, or the influence of IL-8 secretion in neutrophil recruitment and later promotion of angiogenesis.

Nevertheless, the reported observations provide an alternate mechanism for the increased aggressiveness previously reported in low stromal CAV1 breast tumors[89,90,331–334,391,392], a phenotype that has been explained thus far by changes in the metabolism of the cancer microenvironment[87,88], and a new model for the loss of CAV1 expression in CAFs, a question that remained a puzzle[128,323].

4.1 Decreased functionality of tumor vasculature in the context of low stromal CAV1: effects in tumor growth and hypoxia

Here, it is shown how breast tumor xenografts expressing low stromal levels of CAV1 (sCAV1low) display a two-step growth curve. Initially, these tumors grow faster than their high

stromal CAV1 counterparts, a behavior fitting previous studies that associate a loss of stromal CAV1 with a metabolic shift favoring cancer cell growth and viability[87,88]. These metabolic changes associated with CAV1 downregulation in CAFs include: (i) an increased production of lactate and pyruvate due to mitochondrial dysfunction, termed Reverse Warburg effect[87], and (ii) an increased generation of recycled free amino acids, fatty acids and nucleotides, a product of autophagy promotion[393]. In this previously referenced model, adjacent cancer cells would directly utilize these energy metabolites and recycled building blocks generated by stromal CAFs to sustain growth. Moreover, the same growth encouraging behavior by CAFshCAV1 fibroblasts on TNBC cell lines is recapitulated *in vitro* as supported by the here presented co-cultures assays.

While these changes in CAF metabolism explain the *in vitro* behavior of tumor cells and the initial stages of tumor onset, where short distance diffusion of these metabolites is possible, it does not take into account changes in angiogenesis, the formation of new blood vessels, a process that shapes tumor behavior in terms of growth, metabolic reprogramming and aggressiveness[46,74,138,145,259]. Besides, cancer cell growth in sCAV1low xenografts is stalled at later stages and does not reach the exponential growth phase characteristic of neovascularization, a process known as the angiogenic switch[140]. As a consequence, sCAV1low tumors are significantly smaller than their sCAV1high stromal counterparts.

Even though a trend for smaller size in sCAV1low tumor remains, further growth of these xenografts abolishes significant size differences. This is a plausible consequence of an adaptive response of cancer cells to the increased hypoxic conditions[394] present in sCAV1low tumors, mediated by a metabolic reprogramming where glycolytic enzymes are upregulated[73,74], or a possible overgrowth of the tumor stromal compartment in response to hypoxia[73,372].

Surprisingly, blood vessel density was higher in sCAV1low tumors. In line with this observation, unbiased RNASeq and proteome profiler analysis of xenograft lysates showed an enhanced and dysregulated proangiogenic signaling in these tumors. Consistent with these findings, the mammary stromal compartment in Cav1-knockout mice shows dramatically increased vascularization[395].

Functionality assessment of tumor vasculature, in terms of perfusion and permeability, shed light on the apparent contradiction between the profuse vascularization of sCAV1low tumors and their lack of thriving at later tumor growth stages. sCAV1low tumor blood vessels were not properly perfused and showed signs of increased permeability, characteristics of an inefficient vascular network. In accordance with this data, a previous study showed that Lewis lung

carcinoma (LLC) tumors implanted in Cav1 −/− mice display increased angiogenesis and tumor vascular permeability[396].

These abnormal tumor vascular networks arise as a consequence of the imbalance between proangiogenic and antiangiogenic molecules[145–147], a condition that the present study shows to be aggravated in both sCAV1low TNBC xenografts and CAFshCAV1 fibroblasts. The resulting structurally aberrant and dysfunctional tumor vascular networks, in turn, promote tumor hypoxia[152], which further aggravates the imbalance in the production of pro- and anti-angiogenic factors. This translates into the generation of a hypoxic/faulty angiogenesis self-sustained positive feedback loop, where dysfunctional tumor vascularization and consequent hypoxia feed on one another[152].

4.2 Role of CAFshCAV1 fibroblasts in aggravating dysfunctional tumor angiogenesis

In line with the increased density of blood vessels present in sCAV1low tumors, transcriptional profiling of CAFshCAV1 fibroblasts also showed a marked upregulated proangiogenic signature. Among other upregulated proangiogenic factors such as *VEGFA*, this profile showed upregulated (both at the transcript and protein levels) *IL6* and *CXCL8*, cytokines that have been demonstrated to stimulate defective angiogenesis via *VEGFA* upregulation[195,397], the increment of endothelial permeability[194] and promotion of faulty pericyte coverage[193].

Since angiogenesis is governed by the interaction of many cues, further study will be required to characterize the contribution of each CAFshCAV1-produced factor in the observed phenotype. Still, a key role of the proangiogenic cytokine *CXCL8*/IL-8[194–196] in the observed vascular dysfunction phenotype present in sCAV1low tumors can be proposed based on: (i) the levels of expression of *CXCL8,* being the highest upregulated cytokine among proangiogenic factors in both CAFshCAV1 fibroblasts and sCAV1low tumors, (ii) the role IL-8 plays in dysfunctional tumor angiogenesis, and (iii) the association of high expression levels of *CXCL8*/IL-8 (both stromal and in circulation) with poor prognosis in breast cancer patients (see below).

CAFshCAV1 fibroblasts do not only display a proangiogenic expression profile, but they are also capable of inducing enhanced sprout formation and increased endothelial cell proliferation in *in vitro* co-culture and conditioned medium experiments, respectively. Altogether these results point to a regulatory role of CAFshCAV1 fibroblasts in increased angiogenesis mediated by secreted factors.

In addition, CAFs are major biosynthetic sources of ECM structural and remodelling proteins, which can modulate the relative availability of angiogenic growth factors by sequestration. By producing ECM-degrading enzymes (i.e. MMPs), CAFs influence in the release of such latent

angiogenic factors (bFGF, VEGF-A, TGF-β), rendering them bioavailable to their receptors on endothelial cells[47,72,86].

Differential protease expression in sCAV1low tumors, as compared to sCAV1hogh tumors, would thus constitute a factor influencing the capillary network formation, however transcriptional profiling by RNASeq and later qPCR validation (of both *in vivo* tumor xenografts and *in vitro* CAFs) showed no differences in expression levels of MMPs associated with regulation of the angiogenic process, such as MMP-2, 9, and 14[202,232]. Besides differential protease expression, modification of ECM mechanical properties by CAFs have also been linked with angiogenesis[242]. In this scenario, the observed increased collagen deposition and fibrosis in sCAV1low tumors could offer a stiffer environment linked to enhanced angiogenesis.

Apart from the balance between pro- and anti-angiogenic cues, endothelial cell metabolism has recently been put forward as a key regulator of angiogenesis[222,223]. In this regard, another conceivable CAFshCAV1-derived factor influencing the observed proangiogenic phenotype would be the distinctive metabolite secretion profile these fibroblasts resulting from a rewiring of their mitochondrial metabolism[87,307,317,380]; downregulation of CAV1 has been shown to result in increased lactate production and secretion, a metabolite that in turn promotes angiogenesis[363,398].

Still, the following question arises: is this imbalance between pro- and anti-angiogenic factors secreted by CAFshCAV1 fibroblasts continuously controlling the tumor angiogenesis process? Looking at the here presented evidence we can envision a situation in which loss or downregulation of CAV1 in the tumor stroma, through the promotion of CAFshCAV1-derived exacerbated proangiogenic signaling, primes and triggers the formation of an inefficient vascular network, which in turn results in increased hypoxia and thus gives rise to a positive feedback loop. In this loop, low intratumoral oxygen concentration would further aggravate the proangiogenic factor imbalance responsible for the generation of the non-functional vasculature in the first place, by sustaining the proangiogenic signaling characteristically activated upon hypoxia[151–155]. Thus, temporal modulation of stromal CAV1 expression at different stages may have a differential impact on tumor progression.

4.3 Interleukin-8 in tumor angiogenesis and metastasis: a direct cause-effect relationship?

The *in vitro* endothelial sprouting and proliferation assays presented in this work point to a direct regulatory role of CAF-derived secreted factors in angiogenesis. Among the upregulated proangiogenic factors expressed by CAFshCAV1, IL-8 has been characterized as a potent proangiogenic effector and inducer of vascular permeability[194–196,399,400], including in the context of breast cancer, where its downregulation results in reduced blood vessel density[401].

Even though the NSG mouse model system used in this work is severely immunodeficient, lacking mature B, T and NK cells[62]; defective monocytes and fully-functional neutrophils constitute most of the remaining mouse immune cells detectable in peripheral blood[402,403]. On this subject, IL-8 constitutes a potent chemotactic effector over neutrophil recruitment[365,366], an immune cell type that is linked with the induction of angiogenesis when recruited into the tumor[230,234,404]. With this information in mind, one could argue that besides the direct effect IL-8 has over endothelial cells during angiogenesis, neutrophil recruitment, caused by IL-8 upregulation in CAFshCAV1 fibroblasts and derived sCAV1low tumors, could also play a role in the observed exacerbated proangiogenic phenotype, a possibility unexplored in this work.

Concerning tumor metastasis, IL-8 has also been shown to be key in the maintenance of breast cancer stem cells (CSCs)[367,368,399], an important tumor subpopulation that has recently been linked with tumor initiation, metastasis, and disease recurrence.

In this regard, future IL-8 inhibition *in vivo* experiments in sCAV1low/sCAV1high xenografts, either using IL-8-blocking monoclonal antibodies or CXCR1/2 (IL-8 receptors) antagonists, would help to find if the upregulation of this cytokine in sCAV1low tumor xenografts is linked with the observed increased aggressiveness in this particular tumor xenografts. The proposed inhibition studies would also help to rule out which of the above-mentioned phenomena (dysfunctional angiogenesis, neutrophil recruitment and/or CSCs maintenance), caused by IL-8 upregulation, is behind the aggressive phenotype of sCAV1low tumor xenografts.

Given its reported potent proangiogenic effect and its upregulation in the more aggressive and aberrantly vascularized sCAV1low tumors, IL-8 constitutes a potential inhibition target for vascular normalization.

On one hand, one could anticipate that treatment of sCAV1low tumors, which express high levels of IL-8, with IL-8 inhibitors could result in vascular normalization, increased tumor oxygenation, and thus lower metastasis incidence. Supporting the association of increased IL-8 levels and the more aggressive phenotype observed in the here reported sCAV1low tumor xenografts, (i) increased levels of circulating IL-8 have been linked with poor prognosis and enhanced tumor cell dissemination in human patients[392,405] and (ii) elevated stromal IL-8 expression is part of a gene signature predicting poor prognosis in breast cancer patients[58].

On the other hand, IL-8 inhibitor treatment of the less-aggressive sCAV1high tumors (where IL-8 is not upregulated) could cause an impairment of tumor blood vessel functionality, which would promote increased rates of metastases as a consequence of the raised hypoxic conditions. This relationship between hypoxia and increased tumor aggressiveness is discussed in the next section.

4.4 Hypoxia, fibrosis and poor prognosis in sCAV1low tumors

Concomitant with hypoxia, an increased modification and deposition of extracellular matrix (ECM), in accordance with altered transcriptome signatures, could also be observed in sCAV1low tumors. This could be a consequence of hypoxic conditions[372] or an independent, intrinsic secondary effect caused by downregulation of CAV1, given its antifibrotic role[406].

Hypoxia and aggressive tumor phenotype[73,269,280–283] are not only linked by fibrosis, a condition associated with therapy-resistant and metastatic breast tumors[121,407], but also by the role hypoxic conditions play in: (i) maintenance of the cancer stem cell (CSC) phenotype required to generate secondary tumors[408], (ii) premetastatic niche formation[409], (iii) cancer cell motility[410], (iv) local tissue invasion, and (v) the generation of lymphatic vessels[153,371,411], which constitute a common conduit for breast cancer cell dissemination and metastasis[13–15]. As a general process, hypoxia contributes to cancer cell escape by providing an aggressive selection pressure for resilient stem-like tumor cells that subsequently migrate away from the primary tumor[46].

In the here described *in vivo* experiments it is shown that stromal downregulation of CAV1 in TNBC xenografts results in lower survival rates, higher incidence of axillary lymph node metastasis and increased lung area affected by metastasis, suggesting that, in line with previous studies[331,334], low stromal CAV1 TNBC tumors are more aggressive. Previous studies support a link between loss of Caveolin-1 (CAV1) in CAFs with poor clinical outcomes in breast cancer in terms of decreased survival, early tumor recurrence, lymph node metastasis and resistance to tamoxifen[89,90,331–334]. Similar clinical values of decreased stromal CAV1 levels have also been found in gastric cancer[412,413], prostate cancer[414,415] ,and malignant melanoma[416]. Conversely, it has been suggested that stromal CAV1 expression is a negative prognostic indicator in breast cancer correlating with increased cancer dissemination[101]; however, this study was focused in local tissue invasiveness via remodeling of the stromal ECM rather than the usual lymphatic metastasis of breast cancer.

Such is the importance of lymphatic dissemination of breast cancer in the clinical setting that one of the most critical steps in staging a newly diagnosed patient with breast cancer is determining if cancer has spread to the regional lymph nodes[15,417]. On this subject, since cancer cell presence in regional mammary “sentinel” lymph nodes is considered to be a strong predictor of recurrence and survival[13,15], specific techniques for detecting nodal involvement and the extension of lymphatic dissemination have been developed (**Sentinel lymph node mapping**)[418].

In this regard, lymphatic propagation has been described as the preferred way for breast cancer metastatic dissemination[13–15]. First, cancer cells derived from the primary tumor site

would invade the regional “sentinel” lymph nodes followed by spreading to distal nodes. At this point, nodal metastatic cells can use either lymphatic or blood vessels for subsequent lymphogenous or hematogenous dissemination, respectively[14,15,390].

The results presented in this work suggest that initial cancer dissemination in our xenograft mouse model occurs preferentially via lymphatic vasculature, given that the first structures found affected after mastectomy, in the luciferase (data not shown) and PET-CT metastases studies, were the axillary lymph nodes. Supporting this hypothesis, further progression of the disease resulted in the invasion of the mediastinal ganglia and the lung, whose apex is right next to the subclavian vein where the lymphatic thoracic duct and the venous system communicate[419], as observed during histological analysis.

This lymphatic network would constitute the escape route of cancer cells from a harsh hypoxic environment that keeps aggravating as a consequence of a dysfunctional vasculature - hypoxia - proangiogenic signaling imbalance loop. In addition, the increased interstitial fluid pressure present in solid tumors, caused by vascular dysfunction and worsened by fibrosis, all of them features aggravated in sCAV1low tumors, could also be a factor facilitating tumor cell escape from the primary tumor, as in an attempt to achieve homeostasis that interstitial fluid would be released through the lymphatic system[15].

Effective transport of cancer cells through the lymphatic system ends up entering the thoracic duct, from where these cells have access to venous blood[15]. In addition, recent studies report an alternative hybrid route for breast cancer cell dissemination in mice via invasion of local blood vessels within a node[14,420].Once breast cancer cells enter the blood circulation they elicit the establishment of metastatic lesions in the lungs, liver, brain and bones. In the case of basal-like breast cancers (BLBCs), a classification under which most TNBCs are included[40,41], the preferred metastatic sites are brain, lung and distant lymph nodes, and to a significantly lesser degree liver and bone[16]. Thus, our experimental xenograft model, using genetically modified CAFs to dissect stromal CAV1 function, recapitulated such natural metastatic tropism, as preferred target organs for metastasis were lung and distal lymph nodes, and with rare exceptions, the liver.

Direct hematogenous and gradual lymphogenous dissemination routes are not mutually excluding, in this regard the enhanced permeability of low stromal CAV1 tumor vasculature could also constitute a facilitating factor for tumor cell intravasation and subsequent metastasis[205,229,313].

As already mentioned, cytokines secreted by CAFs present in the tumor stroma, such as CCL2[421] and IL-8[368,399], have also been shown to increase breast cancer stem cells (CSCs) which promotes metastasis. While hypoxia remains as a major candidate driving force, the

upregulation of these cytokines in CAFshCAV1 fibroblasts could also exert an intrinsic influence on the observed phenotype of increased aggressiveness in sCAV1low tumors.

Different studies have attempted to explain the increased aggressiveness of sCAV1low tumors by virtue of two non-mutually-excluding models: a "Reverse Warburg effect"[87] and the "autophagic tumor stroma"[422] models, whereby loss of CAV1 in CAFs results in the production of metabolites and recycled products used by cancer cells. While these models explain the impact on cancer cell growth and survival, the connection to increased aggressiveness and metastasis is not so clear. Furthermore, although CAFshCAV1 fibroblasts displayed upregulation of autophagy markers, (*DRAM1*, *CTSB* and *BNIP3*) **(Fig. S4A)**, as already described elsewhere[393], conclusive proof of an active autophagy flux[423] in our CAF cellular model was not found as both p62/SQSTM1 accumulation and LC3-II/LC3-I ratio, common active autophagy flux monitoring methods, showed no differences between CAFscr and CAFshCAV1 fibroblasts **(Fig. S4B)**.

Complementary to the "Reverse Warburg effect" model, the current work suggests increased hypoxic conditions in low stromal CAV1 breast tumors as: (i) a factor governing the increased aggressiveness and metastasis in these cancers and (ii) the link sustaining the positive feedback loop among dysfunctional vasculature and imbalanced proangiogenic signaling.

4.5 Endoplasmic reticulum (ER) stress: A missing link between CAV1 downregulation and increased proangiogenic/proinflammatory cytokine production

Previous studies have reported a transcriptional upregulation of *IL1B*, *IL6*, *CXCL8*, *VEGFA* and *TGF-β* in Cav1-knockout mouse mammary stromal fibroblasts[395,424]. Bioinformatic analysis predicted these and other target genes to be regulated by HIF1A (Hypoxia Inducible Factor 1 Alpha) and NFκB (Nuclear Factor kappa-light-chain-enhancer of activated B cells) transcription factors[378], predicted hits that have also been observed in our RNASeq data analysis derived from CAFscr and CAFshCAV1 fibroblasts.

4.5.1 Mitochondrial dysfunction, NFκB and HIF1A activation are not responsible for increased cytokine production in CAFshCAV1 fibroblasts

A potential underlying molecular link between the transcriptional upregulation of proinflammatory/proangiogenic cytokines and mitochondrial dysfunction observed in CAFshCAV1 fibroblasts was explored on the basis of the previously described causative role of damaged mitochondria as sources for inflammation and oxidative stress[383–385].

Oxidative stress and the induction of autophagy can act as pro-activation cues for NFκB signalling[425,426], a transcription factor already predicted to drive the production of those cytokines. This hypothesis was further supported by our initial observations: (i) mitochondria in CAFshCAV1 fibroblasts show both an increased ROS production and a dysfunctional

phenotype, and (ii) forced induction of mitochondrial OXPHOS usage by CAFs, (via 2-DG, DCA and low glucose treatments) leads to further upregulation of cytokine expression, especially in the case of dysfunctional mitochondria-bearing CAFshCAV1 fibroblasts. These findings harmonized with previous studies reporting a lower efficiency of the OXPHOS system in mitochondria derived from Cav1-knockout animals[317,380,381].

However, partially restoring mitochondrial functionality, either by limiting endogenous cholesterol accumulation (lovastatin) or administering exogenous ROS quenchers (GSH and GSH-EE), resulted in a modest increase in cytokine production, ruling out compromised mitochondrial performance as a direct cause for increased cytokine production in CAFshCAV1 cells.

Active autophagic flux in CAFscr and CAFshCAV1 fibroblasts, as another pro-activation cue for NFκB, was evaluated and, as already mentioned, there were no significant differences in this cellular model **(Fig. S4A and S4B)**. Moreover, although activation of NFκB and HIF1A have been demonstrated to induce CAV1 downregulation[393,427], neither NFκB nuclear localization **(Fig. S4C, S4D and S4E)** nor HI1FA expression **(Fig. S4F)** were significantly increased in CAFshCAV1 cells in the present study. Our negative results regarding 2-DG treatment of CAFs as a differential cause for NFκB activation allowed to rule out a potential connection between the observed upregulation of cytokine production and NFκB activation; while 2-DG treatment causes a surge in the studied cytokines expression, NFκB nuclear localization remained unaffected **(Fig. S4D and S4E)**.

Taken together these observations support the interpretation that both mitochondrial dysfunction and NFκB/HIF1A activation can be discarded as major driving causes for cytokine upregulation observed in CAFshCAV1 fibroblasts. Still, given the documented links between these processes and CAV1-dependent cell homeostasis, it will be interesting in the future to assess their contribution under specific conditions, such as concomitant abrogation of UPR signaling (see below).

4.5.2 ER stress activation in CAFshCAV1 fibroblast: pledging guilty for increased proangiogenic/proinflammatory cytokine production

Besides mitochondria, another critical organelle that is emerging as a major determinant in the field of angiogenesis is the endoplasmic reticulum (ER)[244]. Under stress conditions (such as during hypoxia or nutrient deprivation), the endoplasmic reticulum, as a cellular sensor of metabolic imbalance, is able to modulate the formation of new blood vessels to alleviate these stressors[244]. Moreover, CAV1 downregulation and induction of ER stress have been recently linked[428–430].

Originally described as a consequence of misfolded protein accumulation, “ER stress” refers to any disequilibrium between ER performance of functional capacity, and the functional demand imposed by a given cell state. Eukaryotes have evolved complex signaling networks, collectively termed UPR, to monitor parameters affecting ER integrity and function and elicit adaptive functional programs[244,376,377,431,432].

Lipid imbalances and physical properties of the ER membrane are conditions inherently capable of triggering robust UPR signaling, too[433]. However, these specialized signaling systems are also sensitive to cues such as nutrient deprivation and hypoxia[244,250,251], because the ER is an organelle onto which key limiting steps for lipid metabolism, red/ox regulation, calcium and energy homeostasis converge. For this same reason, the UPR does not only regulate “ER-specific” functions but also feeds into broad cell homeostatic programs, including metabolic regulation, inflammation, and proangiogenic signaling[244,376,377,431,432]. Thus, UPR signaling contributes to an ever-growing number of physiological and physiopathological processes, including tumor biology[431,432] and angiogenesis[244].

Interestingly, both 2-DG and low glucose, treatments aimed at inducing OXPHOS usage and under which cytokine production was upregulated in CAFs, are also documented used inducers of ER stress[388].

In order to further investigate if ER stress could be responsible for the increased cytokine production in CAFshCAV1 fibroblasts, commonly used markers of ER stress activation[434] were evaluated in these cells. Among these markers: (i) Ultrastructural examination of the ER by electron microscopy, (ii) *CHOP* and *XBP1* transcript upregulation, (iii) increased *XBP1* splicing and ATF4 staining; in conjunction with unbiased transcriptome profiling assays (RNASeq) pointed to the activation of ER stress and subsequent UPR upon downregulation of CAV1 in CAFs.

Importantly, treatment of CAFs with direct ER stress inducers (Thapsigargin and Tunicamycin) resulted in a marked increase in the production of *IL6*, *CXCL8* and *VEGFA*. Similarly, using genome-wide microarrays[247], other groups have reported upregulation of *CXCL8* and *VEGFA*, as well as other proangiogenic mediators, following experimental *in vitro* induction of ER stress with Thapsigargin. Moreover, human breast carcinoma cell lines respond to nutrient deprivation and ER stress also by upregulating *CXCL8* and *VEGFA*[435]. Furthermore, induction of many of these proangiogenic factors was of similar magnitude or even greater following ER stress than in hypoxic or in aglycemic conditions.

Treatments aimed at specifically abrogating UPR axes downstream of ER stress offered an insight into the pathways responsible for the upregulation of IL-8/*CXCL8*, a potential key cytokine for the observed aberrant tumor vasculature phenotype, in CAFshCAV1 fibroblasts.

Given the increased ATF4 staining **(Fig. S2D)**, *CHOP* upregulation and downregulation of cap-dependent translation (eIF2α-dependent) observed in CAFshCAV1 fibroblasts, the PERK axis of the UPR is clearly activated. In this regard, PERK inhibition resulted in the downregulation of *CXCL8*, pointing to a scenario in which ER stress induction, as a consequence of CAV1 downregulation, and via the PERK-eIF2α-ATF4 axis, would control the expression of this cytokine. Supporting this finding, ATF4 has been described to modulate *CXCL8* expression[249] and the PERK-eIF2α-ATF4 axis activation has been reported to confer a survival advantage to hypoxic tumors[251], probably via angiogenesis induction. On the other hand, IRE1α inhibition, markedly upregulated the expression of *CXCL8,* probably via a compensatory effect of the PERK pathway.

Even though *VEGFA* and *IL6* are markedly upregulated upon ER stress induction, neither PERK nor IRE1α UPR axis inhibition resulted in the downregulation of any of these two genes. In the same way as IRE1α inhibition elicits a compensatory response for *CXCL8* expression via alternative UPR axes activation, this could be the case for *VEGFA* and *IL6*, since these genes are upregulated in response to both PERK and IRE1α axes[248,254,255,436]. Lack of CHOP inhibition upon PERKi treatment could be explained by the shutdown of PERK-driven negative feedback loops (required to reverse CHOP expression), or by parallel ISR pathways[437] (feeding on CHOP upregulation) that could be engaged by the inhibition of PERK.

Although *IL1B* and *CCL2* follow the same expression patterns that *CXCL8* upon IRE1α and PERK inhibition, exogenous ER induction favors their downregulation, thus further studies will be required to unveil the regulatory pathways of these two cytokines upregulated in CAFshCAV1 fibroblasts.

The sum of these results regarding the expression of the aforementioned genes under ER induction and PERK or IRE1α inhibition, showcase the high redundancy and reciprocal compensation regulating UPR signaling. Nonetheless, the PERK-eIF2α-ATF4 pathway is proposed as a predominant, essential branch of the UPR driving IL-8 upregulation upon CAV1 downregulation.

4.5.3 ER stress and CAV1 downregulation: a self-sustaining loop

Previous hypothesis for the source of CAV1 downregulation in stromal CAFs include[128,323]: (i) activation of oncogenes (HRas, V-Abl and Bcr-Abl) or inactivation of tumor suppress genes (p53)[438], (ii) activation of the TGF-β signaling pathway, similar to the activation of fibroblasts in wound healing[439], and (iii) oxidative stress generated by tumor cells, which may downregulate CAV1 in the surrounding stroma via HIF1A and NFκB activation[422,427].

The current work offers an alternative explanation for decreased stromal levels of CAV1 observed in patients with aggressive breast cancer; it shows how ER stress induction derives

in a notable downregulation of CAV1 mRNA, which translates into a decrease of CAV1 protein levels, although not as immediate given the high stability of this membrane protein[440]. Data supporting this claim is not limited to the CAV1 downregulation observed in CAFs when using canonical inducers of ER stress (Thapsigargin, Tunicamycin, 2-Deoxyglucose and low glucose treatments)[388], it is also based on the decreased CAV1 levels detected upon proteasome inhibitor treatments (indirect ER stress inducers)[389] performed in an unbiased drug screening **(Fig. S3)**.

In line with this hypothesis, CAV1 has previously been reported to be reduced in an ER-stress dependent manner in endothelial cells[429,430] and its overexpression has been also shown to rescue Thapsigargin-induced ER stress[428]. In addition, CAV1 is synthesized in the rough endoplasmic reticulum (RER) as an integral membrane protein[303], so perturbations in this organelle could directly affect CAV1 production.

As a side note, tamoxifen, an estrogen receptor modulator used in breast cancer treatment[23,24], also constituted a positive hit for downregulation of CAV1 in CAFs. This phenomenon could be behind the tamoxifen-resistance associated with low stromal CAV1 breast cancers[333].

On the other hand, this work also shows how CAV1 silencing results in ER stress activation. Supporting this data, CAV1 downregulation, via Sirtuin1 deletion and miR-204 upregulation, has also been recently reported to induce ER stress[441]. Moreover, CAV1 is key in the formation of junctional complexes coupling the plasma membrane with ER for correct calcium (Ca^{2+}) signalling[315], thus perturbations in Ca^{2+} levels upon CAV1 downregulation could constitute an inducer of ER stress, given the importance of Ca^{2+} homeostasis for ER functionality.

Furthermore, since CAV1 and caveolae are also involved in cholesterol transport[316,317], and their downregulation or elimination results in altered cholesterol homeostasis, this could generate lipid composition changes in the ER membrane inducing a stress response. Still linking both aberrant calcium signaling and altered ER membrane lipid composition to ER stress induction would require further experimental work.

Since drug-induced ER stress results in CAV1 downregulation, and this work also shows how CAV1 silencing results in ER stress activation, a positive feedback loop between CAV1 loss and ER stress activation can be proposed. Also, this loop could be a major component of the altered behavior of nutrient-deprived tumors (and thus TME), driving an aggressive phenotype and higher propensity to metastasize. As such, CAV1 levels would constitute a useful marker to consider intervention of these pathways to modulate tumor progression.

4.6 Proposed model and future perspectives

Cancer and stromal cells face hypoxic and nutrient deficiency conditions during tumor growth. The ER, as a cellular sensor of metabolic imbalance, activates a stress response as an initial adaptation to these conditions[244–247,376,431,432]. Based on our evidence, ER stress activation could provide a new explanation for a self-sustained circuit leading to CAV1 downregulation in CAFs, a question that remained unsolved[128,323].

In this model, ER stress activation in CAFs, as a result of CAV1 downregulation promotes an exacerbated proangiogenic signaling that results in the formation of an impaired vascular network accompanied by the consequent hypoxia **(Fig. 34A)**. These increased hypoxic conditions do not only further aggravate the proangiogenic and ER stress imbalances, they are proposed as the reason behind increased aggressiveness observed in sCAV1low tumors **(Fig. 34B)**.

The imbalance between pro- and anti-angiogenic cues found in tumors, a condition that the present study shows to be aggravated in sCAV1low TNBC xenografts **(Fig. 19)**, is responsible for the formation of structurally aberrant and dysfunctional tumor vascular networks[155] **(Fig. 18, 20 and 21)**. This situation, in turn, aggravates tumor hypoxia[152] and promotes a general increase in aggressiveness[46,73,282–284], traits also displayed by the described sCAV1low tumors **(Fig. 22, 23, 32 and 33)**.

A recent concept in antiangiogenic therapy is that of vascular normalization[146,285], where instead of aiming at a complete elimination of the tumor vasculature (vascular regression), treatments intent to restore the balance among pro- and anti-angiogenic signals in an attempt to recover blood vessel functionality[266,286]. Although this approach of improving tumor irrigation might sounds counterintuitive, it has been shown to reduce aggressiveness and improve drug delivery.

In the scenario presented in this work, the balance in low stromal CAV1 tumors is tilted to the side of proangiogenic factor production. Among this pool of proangiogenic factors, IL-8 was shown to be highly enriched, both in low stromal CAV1 xenograft lysates **(Fig. 19B and 19D)** and CAFshCAV1 fibroblasts **(Fig. 25A, B, and D)**. In an attempt to normalize and restore vascular functionality in low stromal CAV1 tumors, and thus observe a potential decrease in the aggressive tumor phenotype showed by these tumors, this work proposes administration of IL-8 inhibitors to mice during primary tumor growth. As already mentioned, one could anticipate that IL-8 inhibition in sCAV1high xenografts, where IL-8 expression levels are not upregulated, could provoke a reduction in tumor blood vessel functionality leading to an increased metastatic behavior.

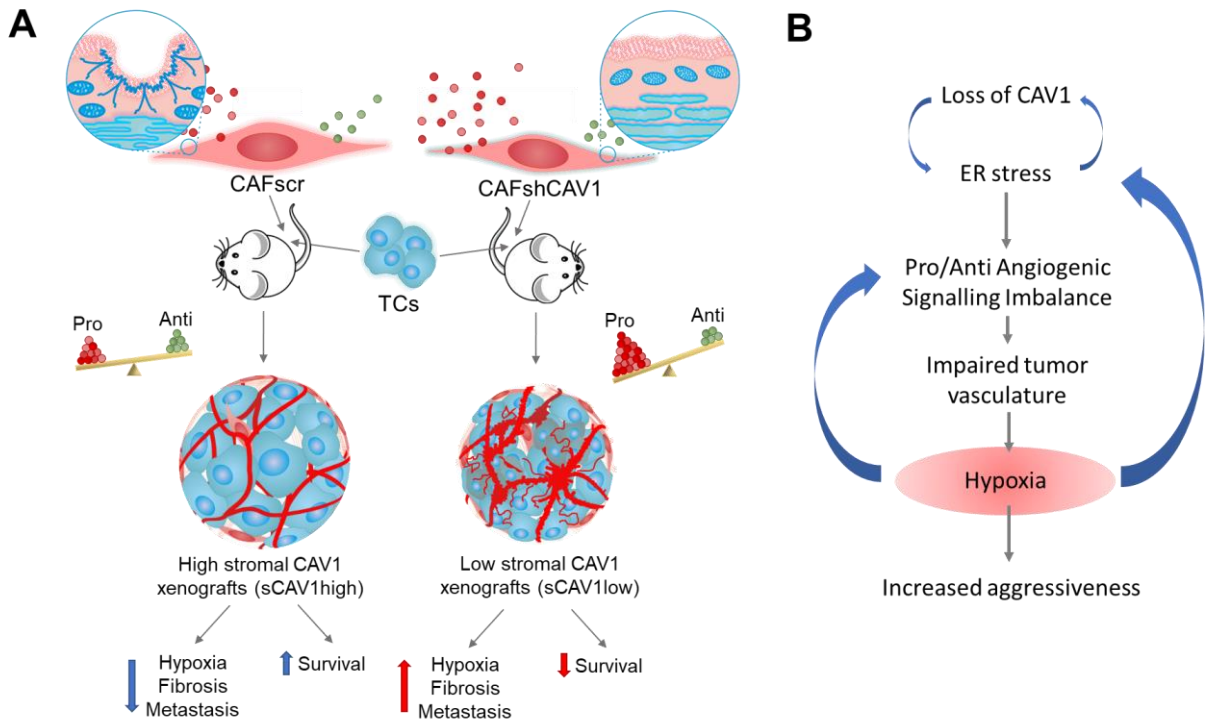

Figure 34. Proposed model for increased aggressiveness in low stromal CAV1 (sCAV1low) xenografts (A) Upon CAV1 downregulation in CAFshCAV1 fibroblasts, an aberrant proangiogenic signaling ensues derived from the activated ER stress. The imbalance in the production of pro- and anti-angiogenic cues, derived from these CAFshCAV1 fibroblasts present in xenografts (low stromal CAV1 xenografts), leads to the formation of an aberrantly dense and dysfunctional tumor vasculature. This blood vessel dysfunctionality results in increased intratumoral hypoxia, which promotes fibrosis and tumor aggressiveness. Insets of CAFs depict CAV1 in the membrane, mitochondria and the ER in blue. Red/green spheres represent pro- and anti-angiogenic cues (respectively). Darkest red spheres represent IL-8. **(B)** CAV1 downregulation and induction of ER stress in CAFs constitutes a positive feedback loop that is responsible for activating an exacerbated production of proangiogenic factors. This imbalance, in turn, primes the formation of an impaired tumor vasculature that promotes intratumoral hypoxia and derives in increased tumor aggressiveness. Hypoxia then constitutes a self-sustaining factor via further unbalancing pro- and anti-angiogenic cues and maintaining the ER stress induction – CAV1 downregulation loop.

These anticipated results concerning IL-8 inhibition lead to two important observations: A first one concerning the concept of vascular regression versus vascular normalization in antiangiogenic therapy, whereby either too strong an inhibition, or the inhibition (and thus dysregulation) of an otherwise normal (non-upregulated) proangiogenic factor, results in decreased tumor vasculature functionality and a more aggressive tumor phenotype[264–268], as proposed for sCAV1high tumors. This study advocates for the latter, where a restoration of the imbalance presented by the cues governing angiogenesis in low stromal CAV1 xenografts could result in vascular normalization and a less belligerent tumor.

Such differential effects of IL-8 inhibition in high or low stromal CAV1 tumors leads to a second observation, bringing to the spotlight the importance of correctly stratifying patients in accordance to well-defined predictive markers for treatment response. The present study propones low CAV1 stromal and high IL-8 tumor expression levels as: (i) markers for poor prognosis of breast cancer (TNBC in this case), as a growing body of evidence has already reported[89,90,331–334,391,392], and (ii) possible predictive markers for treatment response to IL-8 inhibition. Still, standardized techniques for stromal CAV1 detection in patient biopsies and further animal studies will be needed to validate the proposed theoretical predictive value before translating it into a clinical setting.

From a therapeutic point of view, normalizing aberrant angiogenesis in cancer needs new avenues of exploration given the relative inefficacy of present anti-angiogenic therapies which largely depend on ligand neutralization and perturbation of classic angiogenic signaling pathways[182,266,267]. In this regard, this newly proposed ER stress - IL-8 axis in low stromal CAV1 TNBC tumors presents itself as a potential target for ameliorating the delivery of chemotherapeutic drugs and immune cells to tumor masses through vessel normalization, and for curbing stress-induced aggressive behavior leading to metastasis. Moreover, ER stress signaling itself is amenable for pharmacological intervention- combinatorial approaches may be devised additionally including this novel opportunity for fine-tuning tumor biology and architecture.

Finally, and in a more general sense, this study, in line with a recent tendency[45,46,183], suggests that modulating the extracellular environment that surrounds and infiltrates tumors may provide an additional opportunity for therapeutic intervention in hard to treat cancers such as TNBC.

5. CONCLUSIONS / CONCLUSIONES

5.1 CONCLUSIONS

- Presence of Cancer-Associated Fibroblasts (CAFs) in Triple Negative Breast Cancer (TNBC) cell line-derived xenografts promotes angiogenesis.

- sCAV1low tumors, derived from co-injection of TNBC cancer cells with CAFshCAV1 fibroblasts, where Caveolin-1 (CAV1) has been depleted, display an aberrantly high blood vessel density when compared to their sCAV1high counterparts.

- Despite the increased vascular network density, tumor blood vessel functionality in low stromal CAV1 xenografts is impaired, showing poor perfusion and increased leakiness.

- The dysfunctional vasculature present in sCAV1low tumors results in increased tumor hypoxia, which correlates with poor survival and enhanced axillary lymph node and lung metastasis.

- Downregulation of CAV1 activates endoplasmic reticulum (ER) stress, and *vice versa* ER stress induction promotes CAV1 downregulation, thus forming a positive feedback loop.

- Increased ER stress in CAFs, in this case, provoked by CAV1 downregulation, causes an exacerbated proangiogenic phenotype. In particular, upregulation of the proangiogenic Interleukin-8 (IL-8) derives from the activation of the PERK axis of the Unfolded Protein Response (UPR) activated upon ER stress.

5.2 CONCLUSIONES

- La inclusión de fibroblastos estromales asociados al tumor (CAFs, *Cancer-Associated Fibroblasts,* por sus siglas en inglés) en xenoinjertos de células tumorales de cáncer de mama triple negativo (TN) resulta en el incremento de la formación de nuevos vasos sanguíneos en los tumores resultantes (angiogénesis).

- Los tumores con bajos niveles de Caveolina-1 (CAV1) estromal que surgen fruto de la co-inyección de líneas tumorales TN y CAFs dónde CAV1 ha sido silenciada, presentan una mayor densidad de vasos sanguíneos en comparación con aquellos tumores con niveles estromales altos de CAV1.

- A pesar de poseer una red vascular más densa, los tumores con bajos niveles estromales de CAV1 sufren problemas de irrigación ya que sus capilares presentan bajos niveles de perfusión y un incremento de la permeabilidad, lo que se traduce en una funcionalidad reducida.

- Estos problemas de irrigación presentes en los tumores con bajos niveles de CAV1 en el estroma provocan un aumento de la hipoxia intratumoral, un fenómeno que correlaciona con un incremento en la agresividad de dichos tumores (baja supervivencia, incremento de metástasis en nodo linfático axilar y pulmones).

- El silenciamiento de CAV1 activa una respuesta de estrés en el retículo endoplasmático (ER, *Endoplasmic Reticulum*, por sus siglas en inglés), y viceversa*,* la inducción de estrés reticular promueve una bajada en los niveles de CAV1, estableciéndose un círculo vicioso de retroalimentación positiva.

- El incremento del estrés reticular en CAFs, en este caso provocado por el silenciamiento de CAV1, genera un incremento en la producción de factores proangiogénicos en dichos fibroblastos. En particular, el aumento de la expresión y secreción de la citoquina proangiogénica Interleucina-8 (IL-8) se deriva de la estimulación de la vía PERK (vía de la UPR, *Unfolded Protein Response*, activada en respuesta a estrés reticular).

6. BIBLIOGRAPHY

BIBLIOGRAPHY

1. Harbeck, N., Gnant, M. & Thomssen, C. Breast Cancer Is Our Global Responsibility. *Breast Care (Basel).* **10,** 360 (2015).
2. Ferlay, J. *et al.* Cancer incidence and mortality worldwide: Sources, methods and major patterns in GLOBOCAN 2012. *Int. J. Cancer* **136,** E359–E386 (2015).
3. Galceran, J. *et al.* Cancer incidence in Spain, 2015. *Clin. Transl. Oncol.* **19,** 799–825 (2017).
4. Grayson, M. Breast cancer. *Nature* **485,** S49–S49 (2012).
5. Maxmen, A. The hard facts. *Nature* **485,** S50-1 (2012).
6. Lobbezoo, D. J. A. *et al.* Prognosis of metastatic breast cancer: are there differences between patients with de novo and recurrent metastatic breast cancer? *Br. J. Cancer* **112,** 1445–1451 (2015).
7. Gadi, V. K. & Davidson, N. E. Practical Approach to Triple-Negative Breast Cancer. *J. Oncol. Pract.* **13,** 293–300 (2017).
8. Bianchini, G., Balko, J. M., Mayer, I. A., Sanders, M. E. & Gianni, L. Triple-negative breast cancer: challenges and opportunities of a heterogeneous disease. *Nat. Rev. Clin. Oncol.* **13,** 674–690 (2016).
9. Tobon, H. & Salazar, H. Ultrastructure of the Human Mammary Gland. II. Postpartum Lactogenesis. *J. Clin. Endocrinol. Metab.* **40,** 834–844 (1975).
10. Zucca-Matthes, G., Urban, C. & Vallejo, A. Anatomy of the nipple and breast ducts. *Gland Surg.* **5,** 32–6 (2016).
11. Portschy, P. R., Marmor, S., Nzara, R., Virnig, B. A. & Tuttle, T. M. Trends in Incidence and Management of Lobular Carcinoma In Situ: A Population-Based Analysis. *Ann. Surg. Oncol.* **20,** 3240–3246 (2013).
12. Kerlikowske, K. Epidemiology of ductal carcinoma in situ. *J. Natl. Cancer Inst. Monogr.* **2010,** 139–41 (2010).
13. Nathanson, S. D., Kwon, D., Kapke, A., Alford, S. H. & Chitale, D. The Role of Lymph Node Metastasis in the Systemic Dissemination of Breast Cancer. *Ann. Surg. Oncol.* **16,** 3396–3405 (2009).
14. Brown, M. *et al.* Lymph node blood vessels provide exit routes for metastatic tumor cell dissemination in mice. *Science (80-.).* **359,** 1408–1411 (2018).
15. Rahman, M. & Mohammed, S. Breast cancer metastasis and the lymphatic system. *Oncol. Lett.* **10,** 1233–1239 (2015).
16. Kennecke, H. *et al.* Metastatic Behavior of Breast Cancer Subtypes. *J. Clin. Oncol.* **28,** 3271–3277 (2010).
17. Galimberti, V., Monti, S. & Mastropasqua, M. G. DCIS and LCIS are confusing and outdated terms. They should be abandoned in favor of ductal intraepithelial neoplasia (DIN) and lobular intraepithelial neoplasia (LIN). *The Breast* **22,** 431–435 (2013).
18. Pravettoni, G. *et al.* Eliminating 'ductal carcinoma in situ' and 'lobular carcinoma in situ' (DCIS and LCIS) terminology in clinical breast practice: The cognitive psychology point of view. *The Breast* **25,** 82–85 (2016).
19. Weigelt, B., Geyer, F. C. & Reis-Filho, J. S. Histological types of breast cancer: How special are they? *Mol. Oncol.* **4,** 192–208 (2010).
20. Polyak, K. Heterogeneity in breast cancer. *J. Clin. Invest.* **121,** 3786–3788 (2011).

21. Barnard, M. E., Boeke, C. E. & Tamimi, R. M. Established breast cancer risk factors and risk of intrinsic tumor subtypes. *Biochim. Biophys. Acta - Rev. Cancer* **1856,** 73–85 (2015).

22. Giordano, S. H. *et al.* Systemic therapy for patients with advanced human epidermal growth factor receptor 2-positive breast cancer: American Society of Clinical Oncology clinical practice guideline. *J. Clin. Oncol.* **32,** 2078–99 (2014).

23. Burstein, H. J. *et al.* Adjuvant Endocrine Therapy for Women With Hormone Receptor-Positive Breast Cancer: American Society of Clinical Oncology Clinical Practice Guideline Update on Ovarian Suppression. *J. Clin. Oncol.* **34,** 1689–701 (2016).

24. Rugo, H. S. *et al.* Endocrine Therapy for Hormone Receptor-Positive Metastatic Breast Cancer: American Society of Clinical Oncology Guideline. *J. Clin. Oncol.* **34,** 3069–103 (2016).

25. Perou, C. M. *et al.* Molecular portraits of human breast tumours. *Nature* **406,** 747–752 (2000).

26. Sørlie, T. *et al.* Gene expression patterns of breast carcinomas distinguish tumor subclasses with clinical implications. *Proc. Natl. Acad. Sci.* **98,** 10869–10874 (2001).

27. Hu, Z. *et al.* The molecular portraits of breast tumors are conserved across microarray platforms. *BMC Genomics* **7,** 96 (2006).

28. Parker, J. S. *et al.* Supervised risk predictor of breast cancer based on intrinsic subtypes. *J. Clin. Oncol.* **27,** 1160–7 (2009).

29. Dowsett, M. *et al.* Comparison of PAM50 Risk of Recurrence Score With Oncotype DX and IHC4 for Predicting Risk of Distant Recurrence After Endocrine Therapy. *J. Clin. Oncol.* **31,** 2783–2790 (2013).

30. Gnant, M. *et al.* Predicting distant recurrence in receptor-positive breast cancer patients with limited clinicopathological risk: using the PAM50 Risk of Recurrence score in 1478 postmenopausal patients of the ABCSG-8 trial treated with adjuvant endocrine therapy alone. *Ann. Oncol.* **25,** 339–345 (2014).

31. Sestak, I. *et al.* Comparison of the Performance of 6 Prognostic Signatures for Estrogen Receptor–Positive Breast Cancer. *JAMA Oncol.* **4,** 545 (2018).

32. Iwamoto, T. & Pusztai, L. Predicting prognosis of breast cancer with gene signatures: are we lost in a sea of data? *Genome Med.* **2,** 81 (2010).

33. Reis-Filho, J. S., Weigelt, B., Fumagalli, D. & Sotiriou, C. Molecular profiling: moving away from tumor philately. *Sci. Transl. Med.* **2,** 47ps43 (2010).

34. Sotiriou, C. & Pusztai, L. Gene-Expression Signatures in Breast Cancer. *N. Engl. J. Med.* **360,** 790–800 (2009).

35. Troester, M. A. *et al.* Racial Differences in PAM50 Subtypes in the Carolina Breast Cancer Study. *JNCI J. Natl. Cancer Inst.* **110,** 176–182 (2018).

36. Brenton, J. D., Carey, L. A., Ahmed, A. A. & Caldas, C. Molecular Classification and Molecular Forecasting of Breast Cancer: Ready for Clinical Application? *J. Clin. Oncol.* **23,** 7350–7360 (2005).

37. Murria, R. *et al.* Immunohistochemical, genetic and epigenetic profiles of hereditary and triple negative breast cancers. Relevance in personalized medicine. *Am. J. Cancer Res.* **5,** 2330–43 (2015).

38. Weigelt, B. & Reis-Filho, J. S. Histological and molecular types of breast cancer: is there a unifying taxonomy? *Nat. Rev. Clin. Oncol.* **6,** 718–730 (2009).

39. Foulkes, W. D., Smith, I. E. & Reis-Filho, J. S. Triple-Negative Breast Cancer. *N. Engl.*

J. Med. **363,** 1938–1948 (2010).

40. Lehmann, B. D. & Pietenpol, J. A. Identification and use of biomarkers in treatment strategies for triple-negative breast cancer subtypes. *J. Pathol.* **232,** 142–150 (2014).

41. Lehmann, B. D. *et al.* Identification of human triple-negative breast cancer subtypes and preclinical models for selection of targeted therapies. *J. Clin. Invest.* **121,** 2750–2767 (2011).

42. Bertucci, F. *et al.* Gene Expression Profiling Shows Medullary Breast Cancer Is a Subgroup of Basal Breast Cancers. *Cancer Res.* **66,** 4636–4644 (2006).

43. Adams, S. *et al.* Phase 2 study of pembrolizumab as first-line therapy for PD-L1–positive metastatic triple-negative breast cancer (mTNBC): Preliminary data from KEYNOTE-086 cohort B. *J. Clin. Oncol.* **35,** 1088 (2017).

44. Bonotto, M. *et al.* Measures of Outcome in Metastatic Breast Cancer: Insights From a Real-World Scenario. *Oncologist* **19,** 608–615 (2014).

45. Hanahan, D. & Coussens, L. M. Accessories to the Crime: Functions of Cells Recruited to the Tumor Microenvironment. *Cancer Cell* **21,** 309–322 (2012).

46. Quail, D. F. & Joyce, J. A. Microenvironmental regulation of tumor progression and metastasis. *Nat. Med.* **19,** 1423–1437 (2013).

47. Pietras, K. & Östman, A. Hallmarks of cancer: Interactions with the tumor stroma. *Exp. Cell Res.* **316,** 1324–1331 (2010).

48. Ronnov-Jessen, L., Petersen, O. W. & Bissell, M. J. Cellular changes involved in conversion of normal to malignant breast: importance of the stromal reaction. *Physiol. Rev.* **76,** 69–125 (1996).

49. Stewart, T., Tsai, S. C., Grayson, H., Henderson, R. & Opelz, G. Incidence of de-novo breast cancer in women chronically immunosuppressed after organ transplantation. *Lancet (London, England)* **346,** 796–8 (1995).

50. Lindau, D., Gielen, P., Kroesen, M., Wesseling, P. & Adema, G. J. The immunosuppressive tumour network: myeloid-derived suppressor cells, regulatory T cells and natural killer T cells. *Immunology* **138,** 105–115 (2013).

51. Shiao, S. L., Ganesan, A. P., Rugo, H. S. & Coussens, L. M. Immune microenvironments in solid tumors: new targets for therapy. *Genes Dev.* **25,** 2559–2572 (2011).

52. Grivennikov, S. I., Greten, F. R. & Karin, M. Immunity, Inflammation, and Cancer. *Cell* **140,** 883–899 (2010).

53. Balkwill, F. & Mantovani, A. Inflammation and cancer: back to Virchow? *Lancet* **357,** 539–545 (2001).

54. Barcellos-Hoff, M. H., Lyden, D. & Wang, T. C. The evolution of the cancer niche during multistage carcinogenesis. *Nat. Rev. Cancer* **13,** 511–518 (2013).

55. Flier, J. S., Underhill, L. H. & Dvorak, H. F. Tumors: Wounds That Do Not Heal. *N. Engl. J. Med.* **315,** 1650–1659 (1986).

56. De Palma, M. & Hanahan, D. The biology of personalized cancer medicine: Facing individual complexities underlying hallmark capabilities. *Mol. Oncol.* **6,** 111–127 (2012).

57. Hanahan, D. Rethinking the war on cancer. *Lancet* **383,** 558–563 (2014).

58. Finak, G. *et al.* Stromal gene expression predicts clinical outcome in breast cancer. *Nat. Med.* **14,** 518–527 (2008).

59. Farmer, P. *et al.* A stroma-related gene signature predicts resistance to neoadjuvant chemotherapy in breast cancer. *Nat. Med.* **15,** 68–74 (2009).

60. Winslow, S., Leandersson, K., Edsjö, A. & Larsson, C. Prognostic stromal gene signatures in breast cancer. *Breast Cancer Res.* **17,** 23 (2015).

61. Wennmalm, K., Östman, A. & Bergh, J. Stromal signature identifies basal breast cancers. *Nat. Med.* **15,** 237–238 (2009).

62. Shultz, L. D. *et al.* Multiple defects in innate and adaptive immunologic function in NOD/LtSz-scid mice. *J. Immunol.* **154,** 180–91 (1995).

63. Mazzoni, A. *et al.* Myeloid suppressor lines inhibit T cell responses by an NO-dependent mechanism. *J. Immunol.* **168,** 689–95 (2002).

64. Liu, C. *et al.* Expansion of spleen myeloid suppressor cells represses NK cell cytotoxicity in tumor-bearing host. *Blood* **109,** 4336–4342 (2007).

65. Gabrilovich, D. I., Velders, M. P., Sotomayor, E. M. & Kast, W. M. Mechanism of immune dysfunction in cancer mediated by immature Gr-1+ myeloid cells. *J. Immunol.* **166,** 5398–406 (2001).

66. von Boehmer, H. & Daniel, C. Therapeutic opportunities for manipulating TReg cells in autoimmunity and cancer. *Nat. Rev. Drug Discov.* **12,** 51–63 (2013).

67. Whiteside, T. L., Schuler, P. & Schilling, B. Induced and natural regulatory T cells in human cancer. *Expert Opin. Biol. Ther.* **12,** 1383–1397 (2012).

68. Bates, G. J. *et al.* Quantification of Regulatory T Cells Enables the Identification of High-Risk Breast Cancer Patients and Those at Risk of Late Relapse. *J. Clin. Oncol.* **24,** 5373–5380 (2006).

69. Zacharakis, N. *et al.* Immune recognition of somatic mutations leading to complete durable regression in metastatic breast cancer. *Nat. Med.* **24,** 724–730 (2018).

70. Jenkins, R. W., Barbie, D. A. & Flaherty, K. T. Mechanisms of resistance to immune checkpoint inhibitors. *Br. J. Cancer* **118,** 9–16 (2018).

71. Goswami, S. *et al.* Macrophages Promote the Invasion of Breast Carcinoma Cells via a Colony-Stimulating Factor-1/Epidermal Growth Factor Paracrine Loop. *Cancer Res.* **65,** 5278–5283 (2005).

72. Kalluri, R. & Zeisberg, M. Fibroblasts in cancer. *Nat. Rev. Cancer* **6,** 392–401 (2006).

73. Petrova, V., Annicchiarico-Petruzzelli, M., Melino, G. & Amelio, I. The hypoxic tumour microenvironment. *Oncogenesis* **7,** 10 (2018).

74. Hanahan, D. & Weinberg, R. A. Hallmarks of cancer: the next generation. *Cell* **144,** 646–74 (2011).

75. Kalluri, R. The biology and function of fibroblasts in cancer. *Nat. Rev. Cancer* **16,** 582–598 (2016).

76. Tao, L., Huang, G., Song, H., Chen, Y. & Chen, L. Cancer associated fibroblasts: An essential role in the tumor microenvironment. *Oncol. Lett.* **14,** 2611–2620 (2017).

77. Orimo, A. *et al.* Stromal Fibroblasts Present in Invasive Human Breast Carcinomas Promote Tumor Growth and Angiogenesis through Elevated SDF-1/CXCL12 Secretion. *Cell* **121,** 335–348 (2005).

78. Elenbaas, B. & Weinberg, R. A. Heterotypic Signaling between Epithelial Tumor Cells and Fibroblasts in Carcinoma Formation. *Exp. Cell Res.* **264,** 169–184 (2001).

79. Raz, Y. & Erez, N. An inflammatory vicious cycle: Fibroblasts and immune cell recruitment in cancer. *Exp. Cell Res.* **319,** 1596–1603 (2013).

80. Avgustinova, A. *et al.* Tumour cell-derived Wnt7a recruits and activates fibroblasts to promote tumour aggressiveness. *Nat. Commun.* **7,** 10305 (2016).

81. Micallef, L. *et al.* The myofibroblast, multiple origins for major roles in normal and pathological tissue repair. *Fibrogenesis Tissue Repair* **5,** S5 (2012).

82. Marsh, T., Pietras, K. & McAllister, S. S. Fibroblasts as architects of cancer pathogenesis. *Biochim. Biophys. Acta - Mol. Basis Dis.* **1832,** 1070–1078 (2013).

83. Tyan, S.-W. *et al.* Breast Cancer Cells Induce Cancer-Associated Fibroblasts to Secrete Hepatocyte Growth Factor to Enhance Breast Tumorigenesis. *PLoS One* **6,** e15313 (2011).

84. Cirri, P. & Chiarugi, P. Cancer associated fibroblasts: the dark side of the coin. *Am. J. Cancer Res.* **1,** 482–497 (2011).

85. Erez, N., Truitt, M., Olson, P., Hanahan, D. & Hanahan, D. Cancer-Associated Fibroblasts Are Activated in Incipient Neoplasia to Orchestrate Tumor-Promoting Inflammation in an NF-κB-Dependent Manner. *Cancer Cell* **17,** 135–147 (2010).

86. Räsänen, K. & Vaheri, A. Activation of fibroblasts in cancer stroma. *Exp. Cell Res.* **316,** 2713–2722 (2010).

87. Pavlides, S. *et al.* The reverse Warburg effect: Aerobic glycolysis in cancer associated fibroblasts and the tumor stroma. *Cell Cycle* **8,** 3984–4001 (2009).

88. Martinez-Outschoorn, U. E. *et al.* Oxidative stress in cancer associated fibroblasts drives tumor-stroma co-evolution: A new paradigm for understanding tumor metabolism, the field effect and genomic instability in cancer cells. *Cell Cycle* **9,** 3256–76 (2010).

89. Sloan, E. K. *et al.* Stromal cell expression of caveolin-1 predicts outcome in breast cancer. *Am. J. Pathol.* **174,** 2035–43 (2009).

90. Witkiewicz, A. K. *et al.* An absence of stromal caveolin-1 expression predicts early tumor recurrence and poor clinical outcome in human breast cancers. *Am. J. Pathol.* **174,** 2023–34 (2009).

91. Stover, D. G., Bierie, B. & Moses, H. L. A delicate balance: TGF-β and the tumor microenvironment. *J. Cell. Biochem.* **101,** 851–861 (2007).

92. Felipe Lima, J., Nofech-Mozes, S., Bayani, J. & Bartlett, J. M. S. EMT in Breast Carcinoma-A Review. *J. Clin. Med.* **5,** (2016).

93. Mani, S. A. *et al.* The Epithelial-Mesenchymal Transition Generates Cells with Properties of Stem Cells. *Cell* **133,** 704–715 (2008).

94. Chaffer, C. L. & Weinberg, R. A. A Perspective on Cancer Cell Metastasis. *Science (80-.).* **331,** 1559–1564 (2011).

95. Yu, Y. *et al.* Cancer-associated fibroblasts induce epithelial–mesenchymal transition of breast cancer cells through paracrine TGF-β signalling. *Br. J. Cancer* **110,** 724–732 (2014).

96. Ho-Yen, C. M., Jones, J. L. & Kermorgant, S. The clinical and functional significance of c-Met in breast cancer: a review. *Breast Cancer Res.* **17,** 52 (2015).

97. Erdogan, B. *et al.* Cancer-associated fibroblasts promote directional cancer cell migration by aligning fibronectin. *J. Cell Biol.* **216,** 3799–3816 (2017).

98. Calvo, F. *et al.* Mechanotransduction and YAP-dependent matrix remodelling is required for the generation and maintenance of cancer-associated fibroblasts. *Nat. Cell Biol.* **15,** 637–646 (2013).

99. Gaggioli, C. *et al.* Fibroblast-led collective invasion of carcinoma cells with differing roles for RhoGTPases in leading and following cells. *Nat Cell Biol* **9,** 1392–1400 (2007).

100. Albrengues, J. *et al.* Epigenetic switch drives the conversion of fibroblasts into proinvasive cancer-associated fibroblasts. *Nat. Commun.* **6,** 10204 (2015).

101. Goetz, J. G. *et al.* Biomechanical remodeling of the microenvironment by stromal caveolin-1 favors tumor invasion and metastasis. *Cell* **146,** 148–163 (2011).

102. Stuelten, C. H. *et al.* Breast cancer cells induce stromal fibroblasts to express MMP-9 via secretion of TNF-alpha and TGF-beta. *J. Cell Sci.* **118,** 2143–53 (2005).

103. Levental, K. R. *et al.* Matrix crosslinking forces tumor progression by enhancing integrin signaling. *Cell* **139,** 891–906 (2009).

104. Boire, A. *et al.* PAR1 Is a Matrix Metalloprotease-1 Receptor that Promotes Invasion and Tumorigenesis of Breast Cancer Cells. *Cell* **120,** 303–313 (2005).

105. Sternlicht, M. D. *et al.* The stromal proteinase MMP3/stromelysin-1 promotes mammary carcinogenesis. *Cell* **98,** 137–46 (1999).

106. Wyckoff, J. B. *et al.* Direct Visualization of Macrophage-Assisted Tumor Cell Intravasation in Mammary Tumors. *Cancer Res.* **67,** 2649–2656 (2007).

107. Gocheva, V. *et al.* IL-4 induces cathepsin protease activity in tumor-associated macrophages to promote cancer growth and invasion. *Genes Dev.* **24,** 241–55 (2010).

108. Bergamaschi, A. *et al.* Extracellular matrix signature identifies breast cancer subgroups with different clinical outcome. *J. Pathol.* **214,** 357–367 (2008).

109. Sung, H. *et al.* Breast cancer risk factors and mammographic density among high-risk women in urban China. *npj Breast Cancer* **4,** 3 (2018).

110. Boyd, N. F. *et al.* Breast tissue composition and susceptibility to breast cancer. *J. Natl. Cancer Inst.* **102,** 1224–37 (2010).

111. Peres, J. Understanding Breast Density and Breast Cancer Risk. *JNCI J. Natl. Cancer Inst.* **104,** 1345–1346 (2012).

112. Ratajczak-Wielgomas, K. *et al.* Periostin expression in cancer-associated fibroblasts of invasive ductal breast carcinoma. *Oncol. Rep.* **36,** 2745–2754 (2016).

113. Ruan, K., Bao, S. & Ouyang, G. The multifaceted role of periostin in tumorigenesis. *Cell. Mol. Life Sci.* **66,** 2219–2230 (2009).

114. Morishita, R. *et al.* Role of periostin in cancer progression and metastasis: Inhibition of breast cancer progression and metastasis by anti-periostin antibody in a murine model. *Int. J. Mol. Med.* **28,** 181–6 (2011).

115. Chiquet-Ehrismann, R., Mackie, E. J., Pearson, C. A. & Sakakura, T. Tenascin: an extracellular matrix protein involved in tissue interactions during fetal development and oncogenesis. *Cell* **47,** 131–9 (1986).

116. Mackie, E. J. *et al.* Tenascin is a stromal marker for epithelial malignancy in the mammary gland. *Proc. Natl. Acad. Sci. U. S. A.* **84,** 4621–5 (1987).

117. Munson, J. M. & Shieh, A. C. Interstitial fluid flow in cancer: implications for disease progression and treatment. *Cancer Manag. Res.* **6,** 317–28 (2014).

118. Olive, K. P. *et al.* Inhibition of Hedgehog Signaling Enhances Delivery of Chemotherapy in a Mouse Model of Pancreatic Cancer. *Science (80-.).* **324,** 1457–1461 (2009).

119. Kano, M. R. *et al.* Improvement of cancer-targeting therapy, using nanocarriers for intractable solid tumors by inhibition of TGF-beta signaling. *Proc. Natl. Acad. Sci.* **104,** 3460–3465 (2007).

120. Pietras, K. *et al.* Inhibition of platelet-derived growth factor receptors reduces interstitial hypertension and increases transcapillary transport in tumors. *Cancer Res.* **61,** 2929–34 (2001).

121. Takai, K., Le, A., Weaver, V. M. & Werb, Z. Targeting the cancer-associated fibroblasts

as a treatment in triple-negative breast cancer. *Oncotarget* **7,** 82889–82901 (2016).

122. Virchow, R. *Die Cellularpathologie in ihrer Begründung auf physiologische und pathologische Gewebelehre : zwanzig Vorlesungen, gehalten während der Monate Februar, März und April 1858 in Pathologischen Institute zu Berlin*. (Verlag von August Hirschwald ..., 1858).

123. Tarin, D. & Croft, C. B. Ultrastructural features of wound healing in mouse skin. *J. Anat.* **105,** 189–90 (1969).

124. Tarin, D. & Croft, C. B. Ultrastructural studies of wound healing in mouse skin. II. Dermo-epidermal interrelationships. *J. Anat.* **106,** 79–91 (1970).

125. Darby, I. A., Laverdet, B., Bonté, F. & Desmoulière, A. Fibroblasts and myofibroblasts in wound healing. *Clin. Cosmet. Investig. Dermatol.* **7,** 301–11 (2014).

126. Rønnov-Jessen, L. & Petersen, O. W. Induction of alpha-smooth muscle actin by transforming growth factor-beta 1 in quiescent human breast gland fibroblasts. Implications for myofibroblast generation in breast neoplasia. *Lab. Invest.* **68,** 696–707 (1993).

127. Tomasek, J. J., Gabbiani, G., Hinz, B., Chaponnier, C. & Brown, R. A. Myofibroblasts and mechano-regulation of connective tissue remodelling. *Nat. Rev. Mol. Cell Biol.* **3,** 349–363 (2002).

128. Mao, Y., Keller, E. T., Garfield, D. H., Shen, K. & Wang, J. Stromal cells in tumor microenvironment and breast cancer. *Cancer Metastasis Rev.* **32,** 303–15 (2013).

129. Quante, M. *et al.* Bone Marrow-Derived Myofibroblasts Contribute to the Mesenchymal Stem Cell Niche and Promote Tumor Growth. *Cancer Cell* **19,** 257–272 (2011).

130. Zeisberg, E. M., Potenta, S., Xie, L., Zeisberg, M. & Kalluri, R. Discovery of Endothelial to Mesenchymal Transition as a Source for Carcinoma-Associated Fibroblasts. *Cancer Res.* **67,** 10123–10128 (2007).

131. Petersen, O. W. *et al.* Epithelial to Mesenchymal Transition in Human Breast Cancer Can Provide a Nonmalignant Stroma. *Am. J. Pathol.* **162,** 391–402 (2003).

132. Scheel, C. & Weinberg, R. A. Cancer stem cells and epithelial–mesenchymal transition: Concepts and molecular links. *Semin. Cancer Biol.* **22,** 396–403 (2012).

133. Chang, H. Y. *et al.* Diversity, topographic differentiation, and positional memory in human fibroblasts. *Proc. Natl. Acad. Sci. U. S. A.* **99,** 12877–82 (2002).

134. Lu, N. *et al.* The human alpha11 integrin promoter drives fibroblast-restricted expression in vivo and is regulated by TGF-beta1 in a Smad- and Sp1-dependent manner. *Matrix Biol* **29,** 166–176 (2010).

135. Zeisberg, E. M. & Zeisberg, M. The role of promoter hypermethylation in fibroblast activation and fibrogenesis. *J. Pathol.* **229,** 264–273 (2013).

136. Allinen, M. *et al.* Molecular characterization of the tumor microenvironment in breast cancer. *Cancer Cell* **6,** 17–32 (2004).

137. Hu, M. *et al.* Distinct epigenetic changes in the stromal cells of breast cancers. *Nat. Genet.* **37,** 899–905 (2005).

138. Folkman, J. Tumor Angiogenesis: Therapeutic Implications. *N. Engl. J. Med.* **285,** 1182–1186 (1971).

139. Folkman, J. & Hanahan, D. Switch to the angiogenic phenotype during tumorigenesis. *Princess Takamatsu Symp.* **22,** 339–47 (1991).

140. Folkman, J., Watson, K., Ingber, D. & Hanahan, D. Induction of angiogenesis during the transition from hyperplasia to neoplasia. *Nature* **339,** 58–61 (1989).

141. Bluff, J. E. *et al.* Angiogenesis is associated with the onset of hyperplasia in human ductal breast disease. *Br. J. Cancer* **101,** 666–72 (2009).

142. Welti, J., Loges, S., Dimmeler, S. & Carmeliet, P. Recent molecular discoveries in angiogenesis and antiangiogenic therapies in cancer. *J. Clin. Invest.* **123,** 3190–3200 (2013).

143. Olfert, I. M., Baum, O., Hellsten, Y. & Egginton, S. Advances and challenges in skeletal muscle angiogenesis. *Am. J. Physiol. Heart Circ. Physiol.* **310,** H326-36 (2016).

144. Carmeliet, P. & Jain, R. K. Molecular mechanisms and clinical applications of angiogenesis. *Nature* **473,** 298–307 (2011).

145. Bergers, G. & Benjamin, L. E. Tumorigenesis and the angiogenic switch. *Nat. Rev. Cancer* **3,** 401–410 (2003).

146. Goel, S., Wong, A. H.-K. & Jain, R. K. Vascular normalization as a therapeutic strategy for malignant and nonmalignant disease. *Cold Spring Harb. Perspect. Med.* **2,** a006486 (2012).

147. Reinacher-Schick, A., Pohl, M. & Schmiegel, W. Drug Insight: antiangiogenic therapies for gastrointestinal cancers—focus on monoclonal antibodies. *Nat. Clin. Pract. Gastroenterol. Hepatol.* **5,** 250–267 (2008).

148. Morikawa, S. *et al.* Abnormalities in Pericytes on Blood Vessels and Endothelial Sprouts in Tumors. *Am. J. Pathol.* **160,** 985–1000 (2002).

149. Baluk, P., Morikawa, S., Haskell, A., Mancuso, M. & McDonald, D. M. Abnormalities of Basement Membrane on Blood Vessels and Endothelial Sprouts in Tumors. *Am. J. Pathol.* **163,** 1801–1815 (2003).

150. Potente, M., Gerhardt, H. & Carmeliet, P. Basic and Therapeutic Aspects of Angiogenesis. *Cell* **146,** 873–887 (2011).

151. Liao, D. & Johnson, R. S. Hypoxia: A key regulator of angiogenesis in cancer. *Cancer Metastasis Rev.* **26,** 281–290 (2007).

152. Muz, B., de la Puente, P., Azab, F. & Azab, A. K. The role of hypoxia in cancer progression, angiogenesis, metastasis, and resistance to therapy. *Hypoxia* **3,** 83 (2015).

153. Semenza, G. L. Cancer-stromal cell interactions mediated by hypoxia-inducible factors promote angiogenesis, lymphangiogenesis, and metastasis. *Oncogene* **32,** 4057–63 (2013).

154. Kugeratski, F. G. The secretome of hypoxic mammary cancer-associated fibroblasts unveils pro-angiogenic factors. (2017).

155. LaGory, E. L. & Giaccia, A. J. The ever-expanding role of HIF in tumour and stromal biology. *Nat. Cell Biol.* **18,** 356–365 (2016).

156. Caduff, J. H., Fischer, L. C. & Burri, P. H. Scanning electron microscope study of the developing microvasculature in the postnatal rat lung. *Anat. Rec.* **216,** 154–164 (1986).

157. Crivellato, E., Nico, B., Vacca, A. & Ribatti, D. B-cell non-Hodgkin's lymphomas express heterogeneous patterns of neovascularization. *Haematologica* **88,** 671–8 (2003).

158. Paku, S. *et al.* A New Mechanism for Pillar Formation during Tumor-Induced Intussusceptive Angiogenesis: Inverse Sprouting. *Am. J. Pathol.* **179,** 1573–1585 (2011).

159. Hlushchuk, R. *et al.* Tumor recovery by angiogenic switch from sprouting to intussusceptive angiogenesis after treatment with PTK787/ZK222584 or ionizing radiation. *Am. J. Pathol.* **173,** 1173–85 (2008).

160. Ribatti, D. *et al.* Microvascular density, vascular endothelial growth factor

immunoreactivity in tumor cells, vessel diameter and intussusceptive microvascular growth in primary melanoma. *Oncol. Rep.* **14,** 81–4 (2005).

161. Donnem, T. *et al.* Vessel co-option in primary human tumors and metastases: an obstacle to effective anti-angiogenic treatment? *Cancer Med.* **2,** 427–36 (2013).

162. Coelho, A. L. *et al.* Angiogenesis in NSCLC: is vessel co-option the trunk that sustains the branches? *Oncotarget* **8,** 39795–39804 (2017).

163. Küsters, B. *et al.* Vascular endothelial growth factor-A(165) induces progression of melanoma brain metastases without induction of sprouting angiogenesis. *Cancer Res.* **62,** 341–5 (2002).

164. Bridgeman, V. L. *et al.* Vessel co-option is common in human lung metastases and mediates resistance to anti-angiogenic therapy in preclinical lung metastasis models. *J. Pathol.* **241,** 362–374 (2017).

165. Vermeulen, P. B. *et al.* Liver metastases from colorectal adenocarcinomas grow in three patterns with different angiogenesis and desmoplasia. *J. Pathol.* **195,** 336–342 (2001).

166. Stessels, F. *et al.* Breast adenocarcinoma liver metastases, in contrast to colorectal cancer liver metastases, display a non-angiogenic growth pattern that preserves the stroma and lacks hypoxia. *Br. J. Cancer* **90,** 1429–36 (2004).

167. Budde, M. D., Gold, E., Jordan, E. K., Smith-Brown, M. & Frank, J. A. Phase contrast MRI is an early marker of micrometastatic breast cancer development in the rat brain. *NMR Biomed.* **25,** 726–36 (2012).

168. Asahara, T. *et al.* Bone marrow origin of endothelial progenitor cells responsible for postnatal vasculogenesis in physiological and pathological neovascularization. *Circ. Res.* **85,** 221–8 (1999).

169. Marçola, M. & Rodrigues, C. E. Endothelial progenitor cells in tumor angiogenesis: another brick in the wall. *Stem Cells Int.* **2015,** 832649 (2015).

170. Liekens, S., Schols, D. & Hatse, S. CXCL12-CXCR4 axis in angiogenesis, metastasis and stem cell mobilization. *Curr. Pharm. Des.* **16,** 3903–20 (2010).

171. Ceradini, D. J. *et al.* Progenitor cell trafficking is regulated by hypoxic gradients through HIF-1 induction of SDF-1. *Nat. Med.* **10,** 858–864 (2004).

172. Heissig, B. *et al.* Recruitment of stem and progenitor cells from the bone marrow niche requires MMP-9 mediated release of kit-ligand. *Cell* **109,** 625–37 (2002).

173. Maniotis, A. J. *et al.* Vascular Channel Formation by Human Melanoma Cells in Vivo and in Vitro: Vasculogenic Mimicry. *Am. J. Pathol.* **155,** 739–752 (1999).

174. Wang, R. *et al.* Glioblastoma stem-like cells give rise to tumour endothelium. *Nature* **468,** 829–833 (2010).

175. Folkins, C. *et al.* Glioma tumor stem-like cells promote tumor angiogenesis and vasculogenesis via vascular endothelial growth factor and stromal-derived factor 1. *Cancer Res.* **69,** 7243–51 (2009).

176. Cheng, L. *et al.* Glioblastoma Stem Cells Generate Vascular Pericytes to Support Vessel Function and Tumor Growth. *Cell* **153,** 139–152 (2013).

177. Ferrara, N. & Henzel, W. J. Pituitary follicular cells secrete a novel heparin-binding growth factor specific for vascular endothelial cells. *Biochem. Biophys. Res. Commun.* **161,** 851–858 (1989).

178. Senger, D. R. *et al.* Tumor cells secrete a vascular permeability factor that promotes accumulation of ascites fluid. *Science* **219,** 983–5 (1983).

179. Lobov, I. B. *et al.* Delta-like ligand 4 (Dll4) is induced by VEGF as a negative regulator

of angiogenic sprouting. *Proc. Natl. Acad. Sci.* **104,** 3219–3224 (2007).

180. Harrington, L. S. *et al.* Regulation of multiple angiogenic pathways by Dll4 and Notch in human umbilical vein endothelial cells. *Microvasc. Res.* **75,** 144–154 (2008).

181. Nagy, J. A. *et al.* Permeability properties of tumor surrogate blood vessels induced by VEGF-A. *Lab. Investig.* **86,** 767–780 (2006).

182. Ronca, R., Benkheil, M., Mitola, S., Struyf, S. & Liekens, S. Tumor angiogenesis revisited: Regulators and clinical implications. *Med. Res. Rev.* **37,** 1231–1274 (2017).

183. De Palma, M., Biziato, D. & Petrova, T. V. Microenvironmental regulation of tumour angiogenesis. *Nat. Rev. Cancer* **17,** 457–474 (2017).

184. Benedito, R. *et al.* Notch-dependent VEGFR3 upregulation allows angiogenesis without VEGF–VEGFR2 signalling. *Nature* **484,** 110–114 (2012).

185. Noguera-Troise, I. *et al.* Blockade of Dll4 inhibits tumour growth by promoting non-productive angiogenesis. *Nature* **444,** 1032–1037 (2006).

186. Xue, Y. *et al.* PDGF-BB modulates hematopoiesis and tumor angiogenesis by inducing erythropoietin production in stromal cells. *Nat. Med.* **18,** 100–110 (2012).

187. Pardali, E. & ten Dijke, P. Transforming growth factor-beta signaling and tumor angiogenesis. *Front. Biosci. (Landmark Ed.* **14,** 4848–61 (2009).

188. Seo, H.-R. *et al.* Intrinsic FGF2 and FGF5 promotes angiogenesis of human aortic endothelial cells in 3D microfluidic angiogenesis system. *Sci. Rep.* **6,** 28832 (2016).

189. Korc, M. & Friesel, R. E. The role of fibroblast growth factors in tumor growth. *Curr. Cancer Drug Targets* **9,** 639–51 (2009).

190. Sullivan, L. A. & Brekken, R. A. The VEGF family in cancer and antibody-based strategies for their inhibition. *MAbs* **2,** 165–75 (2010).

191. Kobayashi, H., DeBusk, L. M. & Lin, P. C. in *Antiangiogenic Agents in Cancer Therapy* 171–187 (Humana Press, 2008). doi:10.1007/978-1-59745-184-0_10

192. Voronov, E. *et al.* IL-1 is required for tumor invasiveness and angiogenesis. *Proc. Natl. Acad. Sci. U. S. A.* **100,** 2645–50 (2003).

193. Gopinathan, G. *et al.* Interleukin-6 Stimulates Defective Angiogenesis. *Cancer Res* **75,** 3098–3107 (2015).

194. Petreaca, M. L., Yao, M., Liu, Y., DeFea, K. & Martins-Green, M. Transactivation of Vascular Endothelial Growth Factor Receptor-2 by Interleukin-8 (IL-8/CXCL8) Is Required for IL-8/CXCL8-induced Endothelial Permeability. *Mol. Biol. Cell* **18,** 5014–5023 (2007).

195. Martin, D., Galisteo, R. & Gutkind, J. S. CXCL8/IL8 Stimulates Vascular Endothelial Growth Factor (VEGF) Expression and the Autocrine Activation of VEGFR2 in Endothelial Cells by Activating NFκB through the CBM (Carma3/Bcl10/Malt1) Complex. *J. Biol. Chem.* **284,** 6038–6042 (2009).

196. Matsuo, Y. *et al.* CXCL8/IL-8 and CXCL12/SDF-1alpha co-operatively promote invasiveness and angiogenesis in pancreatic cancer. *Int J Cancer* **124,** 853–861 (2009).

197. Niu, J., Azfer, A., Zhelyabovska, O., Fatma, S. & Kolattukudy, P. E. Monocyte Chemotactic Protein (MCP)-1 Promotes Angiogenesis via a Novel Transcription Factor, MCP-1-induced Protein (MCPIP). *J. Biol. Chem.* **283,** 14542–14551 (2008).

198. Ma, J. *et al.* MCP-1 mediates TGF-beta-induced angiogenesis by stimulating vascular smooth muscle cell migration. *Blood* **109,** 987–94 (2007).

199. Zhang, M. *et al.* CXCL12 enhances angiogenesis through CXCR7 activation in human

umbilical vein endothelial cells. *Sci. Rep.* **7,** 8289 (2017).

200. Tseng, D., Vasquez-Medrano, D. A. & Brown, J. M. Targeting SDF-1/CXCR4 to inhibit tumour vasculature for treatment of glioblastomas. *Br. J. Cancer* **104,** 1805–1809 (2011).

201. Campbell, N. E. *et al.* Extracellular matrix proteins and tumor angiogenesis. *J. Oncol.* **2010,** 586905 (2010).

202. Arroyo, A. G. & Iruela-Arispe, M. L. Extracellular matrix, inflammation, and the angiogenic response. *Cardiovasc. Res.* **86,** 226–235 (2010).

203. Lakshmikanthan, S. *et al.* Rap1 promotes VEGFR2 activation and angiogenesis by a mechanism involving integrin v 3. *Blood* **118,** 2015–2026 (2011).

204. Mahabeleshwar, G. H., Feng, W., Reddy, K., Plow, E. F. & Byzova, T. V. Mechanisms of integrin-vascular endothelial growth factor receptor cross-activation in angiogenesis. *Circ. Res.* **101,** 570–80 (2007).

205. Egeblad, M., Rasch, M. G. & Weaver, V. M. Dynamic interplay between the collagen scaffold and tumor evolution. *Curr. Opin. Cell Biol.* **22,** 697–706 (2010).

206. Bonnans, C., Chou, J. & Werb, Z. Remodelling the extracellular matrix in development and disease. *Nat. Rev. Mol. Cell Biol.* **15,** 786–801 (2014).

207. Shao, R. *et al.* Acquired expression of periostin by human breast cancers promotes tumor angiogenesis through up-regulation of vascular endothelial growth factor receptor 2 expression. *Mol. Cell. Biol.* **24,** 3992–4003 (2004).

208. Van Obberghen-Schilling, E. *et al.* Fibronectin and tenascin-C: accomplices in vascular morphogenesis during development and tumor growth. *Int. J. Dev. Biol.* **55,** 511–525 (2011).

209. Klenotic, P. A., Zhang, C. & Lin, Z. Emerging roles of CCN proteins in vascular development and pathology. *J. Cell Commun. Signal.* **10,** 251–257 (2016).

210. Brown, L. F. *et al.* Vascular stroma formation in carcinoma in situ, invasive carcinoma, and metastatic carcinoma of the breast. *Clin. Cancer Res.* **5,** 1041–56 (1999).

211. Rivera, L. B., Bradshaw, A. D. & Brekken, R. A. The regulatory function of SPARC in vascular biology. *Cell. Mol. Life Sci.* **68,** 3165–3173 (2011).

212. Lawler, P. R. & Lawler, J. Molecular Basis for the Regulation of Angiogenesis by Thrombospondin-1 and -2. *Cold Spring Harb. Perspect. Med.* **2,** a006627–a006627 (2012).

213. Rothhammer, T., Bataille, F., Spruss, T., Eissner, G. & Bosserhoff, A.-K. Functional implication of BMP4 expression on angiogenesis in malignant melanoma. *Oncogene* **26,** 4158–4170 (2007).

214. Stabile, H. *et al.* Bone morphogenic protein antagonist Drm/gremlin is a novel proangiogenic factor. *Blood* **109,** 1834–1840 (2007).

215. David, L., Feige, J.-J. & Bailly, S. Emerging role of bone morphogenetic proteins in angiogenesis. *Cytokine Growth Factor Rev.* **20,** 203–212 (2009).

216. Mehlen, P., Delloye-Bourgeois, C. & Chédotal, A. Novel roles for Slits and netrins: axon guidance cues as anticancer targets? *Nat. Rev. Cancer* **11,** 188–197 (2011).

217. Tamagnone, L. Emerging Role of Semaphorins as Major Regulatory Signals and Potential Therapeutic Targets in Cancer. *Cancer Cell* **22,** 145–152 (2012).

218. Larson, J., Schomberg, S., Schroeder, W. & Carpenter, T. C. Endothelial EphA receptor stimulation increases lung vascular permeability. *Am. J. Physiol. Lung Cell. Mol. Physiol.* **295,** L431-9 (2008).

219. Pasquale, E. B. Eph-Ephrin Bidirectional Signaling in Physiology and Disease. *Cell* **133,** 38–52 (2008).

220. Wang, S. & Olson, E. N. AngiomiRs--key regulators of angiogenesis. *Curr. Opin. Genet. Dev.* **19,** 205–11 (2009).

221. Wang, W., Zhang, E. & Lin, C. MicroRNAs in tumor angiogenesis. *Life Sci.* **136,** 28–35 (2015).

222. Eelen, G., de Zeeuw, P., Simons, M. & Carmeliet, P. Endothelial Cell Metabolism in Normal and Diseased Vasculature. *Circ. Res.* **116,** 1231–1244 (2015).

223. Potente, M. & Carmeliet, P. The Link Between Angiogenesis and Endothelial Metabolism. *Annu. Rev. Physiol.* **79,** 43–66 (2017).

224. Schoors, S. *et al.* Partial and Transient Reduction of Glycolysis by PFKFB3 Blockade Reduces Pathological Angiogenesis. *Cell Metab.* **19,** 37–48 (2014).

225. De Bock, K. *et al.* Role of PFKFB3-Driven Glycolysis in Vessel Sprouting. *Cell* **154,** 651–663 (2013).

226. Leek, R. D. *et al.* Association of macrophage infiltration with angiogenesis and prognosis in invasive breast carcinoma. *Cancer Res.* **56,** 4625–9 (1996).

227. Clear, A. J. *et al.* Increased angiogenic sprouting in poor prognosis FL is associated with elevated numbers of CD163+ macrophages within the immediate sprouting microenvironment. *Blood* **115,** 5053–6 (2010).

228. Koh, Y. W., Park, C.-S., Yoon, D. H., Suh, C. & Huh, J. CD163 Expression Was Associated with Angiogenesis and Shortened Survival in Patients with Uniformly Treated Classical Hodgkin Lymphoma. *PLoS One* **9,** e87066 (2014).

229. Harney, A. S. *et al.* Real-Time Imaging Reveals Local, Transient Vascular Permeability, and Tumor Cell Intravasation Stimulated by TIE2hi Macrophage-Derived VEGFA. *Cancer Discov.* **5,** 932–943 (2015).

230. Murdoch, C., Muthana, M., Coffelt, S. B. & Lewis, C. E. The role of myeloid cells in the promotion of tumour angiogenesis. *Nat. Rev. Cancer* **8,** 618–631 (2008).

231. Baer, C., Squadrito, M. L., Iruela-Arispe, M. L. & De Palma, M. Reciprocal interactions between endothelial cells and macrophages in angiogenic vascular niches. *Exp. Cell Res.* **319,** 1626–1634 (2013).

232. Kessenbrock, K., Plaks, V. & Werb, Z. Matrix Metalloproteinases: Regulators of the Tumor Microenvironment. *Cell* **141,** 52–67 (2010).

233. Mazzieri, R. *et al.* Targeting the ANG2/TIE2 Axis Inhibits Tumor Growth and Metastasis by Impairing Angiogenesis and Disabling Rebounds of Proangiogenic Myeloid Cells. *Cancer Cell* **19,** 512–526 (2011).

234. Coffelt, S. B., Wellenstein, M. D. & de Visser, K. E. Neutrophils in cancer: neutral no more. *Nat. Rev. Cancer* **16,** 431–446 (2016).

235. Kujawski, M. *et al.* Stat3 mediates myeloid cell–dependent tumor angiogenesis in mice. *J. Clin. Invest.* **118,** 3367–3377 (2008).

236. Sabrkhany, S., Griffioen, A. W. & oude Egbrink, M. G. A. The role of blood platelets in tumor angiogenesis. *Biochim. Biophys. Acta - Rev. Cancer* **1815,** 189–196 (2011).

237. Sharma, D., Brummel-Ziedins, K. E., Bouchard, B. A. & Holmes, C. E. Platelets in Tumor Progression: A Host Factor That Offers Multiple Potential Targets in the Treatment of Cancer. *J. Cell. Physiol.* **229,** 1005–1015 (2014).

238. Egeblad, M., Nakasone, E. S. & Werb, Z. Tumors as organs: complex tissues that interface with the entire organism. *Dev. Cell* **18,** 884–901 (2010).

239. Orimo, A. & Weinberg, R. A. Stromal fibroblasts in cancer: a novel tumor-promoting cell type. *Cell Cycle* **5,** 1597–1601 (2006).

240. Fukumura, D. *et al.* Tumor induction of VEGF promoter activity in stromal cells. *Cell* **94,** 715–25 (1998).

241. Crawford, Y. *et al.* PDGF-C Mediates the Angiogenic and Tumorigenic Properties of Fibroblasts Associated with Tumors Refractory to Anti-VEGF Treatment. *Cancer Cell* **15,** 21–34 (2009).

242. Sewell-Loftin, M. K. *et al.* Cancer-associated fibroblasts support vascular growth through mechanical force. *Sci. Rep.* **7,** 12574 (2017).

243. Ke, Q. & Costa, M. Hypoxia-Inducible Factor-1 (HIF-1). *Mol. Pharmacol.* **70,** 1469–1480 (2006).

244. Binet, F. & Sapieha, P. ER Stress and Angiogenesis. *Cell Metab.* **22,** 560–575 (2015).

245. Deng, Y. *et al.* The Xbp1s/GalE axis links ER stress to postprandial hepatic metabolism. *J. Clin. Invest.* **123,** 455–468 (2013).

246. Binet, F. *et al.* Neuronal ER Stress Impedes Myeloid-Cell-Induced Vascular Regeneration through IRE1α Degradation of Netrin-1. *Cell Metab.* **17,** 353–371 (2013).

247. Pereira, E. R., Liao, N., Neale, G. A. & Hendershot, L. M. Transcriptional and Post-Transcriptional Regulation of Proangiogenic Factors by the Unfolded Protein Response. *PLoS One* **5,** e12521 (2010).

248. Ghosh, R. *et al.* Transcriptional Regulation of VEGF-A by the Unfolded Protein Response Pathway. *PLoS One* **5,** e9575 (2010).

249. Gargalovic, P. S. *et al.* Identification of inflammatory gene modules based on variations of human endothelial cell responses to oxidized lipids. *Proc. Natl. Acad. Sci. U. S. A.* **103,** 12741–6 (2006).

250. Pereira, E. R., Frudd, K., Awad, W. & Hendershot, L. M. Endoplasmic Reticulum (ER) Stress and Hypoxia Response Pathways Interact to Potentiate Hypoxia-inducible Factor 1 (HIF-1) Transcriptional Activity on Targets Like Vascular Endothelial Growth Factor (VEGF). *J. Biol. Chem.* **289,** 3352–3364 (2014).

251. Fels, D. R. & Koumenis, C. The PERK/eIF2α/ATF4 module of the UPR in hypoxia resistance and tumor growth. *Cancer Biol. Ther.* **5,** 723–728 (2006).

252. Blais, J. D. *et al.* Perk-dependent translational regulation promotes tumor cell adaptation and angiogenesis in response to hypoxic stress. *Mol. Cell. Biol.* **26,** 9517–32 (2006).

253. Gupta, S., McGrath, B. & Cavener, D. R. PERK Regulates the Proliferation and Development of Insulin-Secreting Beta-Cell Tumors in the Endocrine Pancreas of Mice. *PLoS One* **4,** e8008 (2009).

254. Drogat, B. *et al.* IRE1 signaling is essential for ischemia-induced vascular endothelial growth factor-A expression and contributes to angiogenesis and tumor growth in vivo. *Cancer Res.* **67,** 6700–7 (2007).

255. Auf, G. *et al.* Inositol-requiring enzyme 1alpha is a key regulator of angiogenesis and invasion in malignant glioma. *Proc. Natl. Acad. Sci. U. S. A.* **107,** 15553–8 (2010).

256. Axten, J. M. *et al.* Discovery of GSK2656157: An Optimized PERK Inhibitor Selected for Preclinical Development. *ACS Med. Chem. Lett.* **4,** 964–968 (2013).

257. Atkins, C. *et al.* Characterization of a novel PERK kinase inhibitor with antitumor and antiangiogenic activity. *Cancer Res.* **73,** 1993–2002 (2013).

258. Chen, X. *et al.* XBP1 promotes triple-negative breast cancer by controlling the HIF1α pathway. *Nature* **508,** 103–107 (2014).

259. Hillen, F. & Griffioen, A. W. Tumour vascularization: sprouting angiogenesis and beyond. *Cancer Metastasis Rev.* **26,** 489–502 (2007).

260. Boere, I. A., Hamberg, P. & Sleijfer, S. It takes two to tango: Combinations of conventional cytotoxics with compounds targeting the vascular endothelial growth factorâ€“vascular endothelial growth factor receptor pathway in patients with solid malignancies. *Cancer Sci.* **101,** 7–15 (2010).

261. Zirlik, K. & Duyster, J. Anti-Angiogenics: Current Situation and Future Perspectives. *Oncol. Res. Treat.* **41,** 166–171 (2018).

262. Weis, S. M. & Cheresh, D. A. Tumor angiogenesis: molecular pathways and therapeutic targets. *Nat. Med.* **17,** 1359–1370 (2011).

263. Gampenrieder, S. P., Westphal, T. & Greil, R. Antiangiogenic therapy in breast cancer. *Memo* **10,** 194–201 (2017).

264. Bergers, G. & Hanahan, D. Modes of resistance to anti-angiogenic therapy. *Nat. Rev. Cancer* **8,** 592–603 (2008).

265. Gacche, R. N. Compensatory angiogenesis and tumor refractoriness. *Oncogenesis* **4,** e153–e153 (2015).

266. Ferrara, N. & Adamis, A. P. Ten years of anti-vascular endothelial growth factor therapy. *Nat. Rev. Drug Discov.* **15,** 385–403 (2016).

267. Vasudev, N. S. & Reynolds, A. R. Anti-angiogenic therapy for cancer: current progress, unresolved questions and future directions. *Angiogenesis* **17,** 471–494 (2014).

268. Ebos, J. M. L. & Kerbel, R. S. Antiangiogenic therapy: impact on invasion, disease progression and metastasis. *Nat. Rev. Clin. Oncol.* **8,** 210–221 (2011).

269. Conley, S. J. *et al.* Antiangiogenic agents increase breast cancer stem cells via the generation of tumor hypoxia. *Proc. Natl. Acad. Sci.* **109,** 2784–2789 (2012).

270. Loges, S., Schmidt, T. & Carmeliet, P. Mechanisms of Resistance to Anti-Angiogenic Therapy and Development of Third-Generation Anti-Angiogenic Drug Candidates. *Genes Cancer* **1,** 12–25 (2010).

271. Hu, Y.-L. *et al.* Hypoxia-Induced Autophagy Promotes Tumor Cell Survival and Adaptation to Antiangiogenic Treatment in Glioblastoma. *Cancer Res.* **72,** 1773–1783 (2012).

272. Bensaad, K. *et al.* Fatty Acid Uptake and Lipid Storage Induced by HIF-1α Contribute to Cell Growth and Survival after Hypoxia-Reoxygenation. *Cell Rep.* **9,** 349–365 (2014).

273. Pisarsky, L. *et al.* Targeting Metabolic Symbiosis to Overcome Resistance to Anti-angiogenic Therapy. *Cell Rep.* **15,** 1161–1174 (2016).

274. Fischer, C. *et al.* Anti-PlGF Inhibits Growth of VEGF(R)-Inhibitor-Resistant Tumors without Affecting Healthy Vessels. *Cell* **131,** 463–475 (2007).

275. Scholz, A. *et al.* Endothelial cell-derived angiopoietin-2 is a therapeutic target in treatment-naive and bevacizumab-resistant glioblastoma. *EMBO Mol. Med.* **8,** 39–57 (2016).

276. Huang, D. *et al.* Interleukin-8 mediates resistance to antiangiogenic agent sunitinib in renal cell carcinoma. *Cancer Res.* **70,** 1063–71 (2010).

277. Rigamonti, N. *et al.* Role of Angiopoietin-2 in Adaptive Tumor Resistance to VEGF Signaling Blockade. *Cell Rep.* **8,** 696–706 (2014).

278. Gabrusiewicz, K. *et al.* Anti-vascular endothelial growth factor therapy-induced glioma invasion is associated with accumulation of Tie2-expressing monocytes. *Oncotarget* **5,** 2208–20 (2014).

279. Liang, W. & Ferrara, N. The Complex Role of Neutrophils in Tumor Angiogenesis and Metastasis. *Cancer Immunol. Res.* **4,** 83–91 (2016).

280. Rohwer, N. & Cramer, T. Hypoxia-mediated drug resistance: Novel insights on the functional interaction of HIFs and cell death pathways. *Drug Resist. Updat.* **14,** 191–201 (2011).

281. Marie-Egyptienne, D. T., Lohse, I. & Hill, R. P. Cancer stem cells, the epithelial to mesenchymal transition (EMT) and radioresistance: Potential role of hypoxia. *Cancer Lett.* **341,** 63–72 (2013).

282. Gilkes, D. M. & Semenza, G. L. Role of hypoxia-inducible factors in breast cancer metastasis. *Future Oncol.* **9,** 1623–36 (2013).

283. Vaupel, P. Hypoxia and Aggressive Tumor Phenotype: Implications for Therapy and Prognosis. *Oncologist* **13,** 21–26 (2008).

284. Semenza, G. L. The hypoxic tumor microenvironment: A driving force for breast cancer progression. *Biochim. Biophys. Acta - Mol. Cell Res.* **1863,** 382–391 (2016).

285. Jain, R. K. Normalization of Tumor Vasculature: An Emerging Concept in Antiangiogenic Therapy. *Science (80-.).* **307,** 58–62 (2005).

286. Carmeliet, P. & Jain, R. K. Principles and mechanisms of vessel normalization for cancer and other angiogenic diseases. *Nat. Rev. Drug Discov.* **10,** 417–427 (2011).

287. Navarro, P. *et al.* Targeting Tumor Mitochondrial Metabolism Overcomes Resistance to Antiangiogenics. *Cell Rep.* **15,** 2705–2718 (2016).

288. Huang, Y., Stylianopoulos, T., Duda, D. G., Fukumura, D. & Jain, R. K. Benefits of Vascular Normalization Are Dose and Time Dependent--Letter. *Cancer Res.* **73,** 7144–7146 (2013).

289. Dumont, R. A. *et al.* Noninvasive imaging of alphaVbeta3 function as a predictor of the antimigratory and antiproliferative effects of dasatinib. *Cancer Res.* **69,** 3173–9 (2009).

290. Vakoc, B. J. *et al.* Three-dimensional microscopy of the tumor microenvironment in vivo using optical frequency domain imaging. *Nat. Med.* **15,** 1219–1223 (2009).

291. Nagengast, W. B. *et al.* VEGF-PET Imaging Is a Noninvasive Biomarker Showing Differential Changes in the Tumor during Sunitinib Treatment. *Cancer Res.* **71,** 143–153 (2011).

292. Jain, R. K. *et al.* Biomarkers of response and resistance to antiangiogenic therapy. *Nat. Rev. Clin. Oncol.* **6,** 327–338 (2009).

293. Rodriguez-Pascual, J. & Cubillo, A. Dynamic Biomarkers of Response to Antiangiogenic Therapies in Colorectal Cancer: A Review. *Curr. Pharmacogenomics Person. Med.* **15,** 81–85 (2017).

294. Migneco, G. *et al.* Glycolytic cancer associated fibroblasts promote breast cancer tumor growth, without a measurable increase in angiogenesis: Evidence for stromal-epithelial metabolic coupling. *Cell Cycle* **9,** 2412–2422 (2010).

295. Fra, A. M., Williamson, E., Simons, K. & Parton, R. G. De novo formation of caveolae in lymphocytes by expression of VIP21-caveolin. *Proc. Natl. Acad. Sci. U. S. A.* **92,** 8655–9 (1995).

296. Drab, M. *et al.* Loss of Caveolae, Vascular Dysfunction, and Pulmonary Defects in Caveolin-1 Gene-Disrupted Mice. *Science (80-.).* **293,** 2449–2452 (2001).

297. Walser, P. J. *et al.* Constitutive Formation of Caveolae in a Bacterium. *Cell* **150,** 752–763 (2012).

298. Hill, M. M. *et al.* PTRF-Cavin, a Conserved Cytoplasmic Protein Required for Caveola

Formation and Function. *Cell* **132,** 113–124 (2008).

299. Liu, L. *et al.* Deletion of Cavin/PTRF Causes Global Loss of Caveolae, Dyslipidemia, and Glucose Intolerance. *Cell Metab.* **8,** 310–317 (2008).

300. Palade, G. E. Fine structure of blood capillaries. *J. Appl. Phys.* 1424 (1953).

301. Yamada, E. The fine structure of the gall bladder epithelium of the mouse. *J. Biophys. Biochem. Cytol.* **1,** 445–58 (1955).

302. Parat, M.-O., Anand-Apte, B. & Fox, P. L. Differential caveolin-1 polarization in endothelial cells during migration in two and three dimensions. *Mol. Biol. Cell* **14,** 3156–68 (2003).

303. Parton, R. G. & del Pozo, M. A. Caveolae as plasma membrane sensors, protectors and organizers. *Nat Rev Mol Cell Biol* **14,** 98–112 (2013).

304. Sotgia, F. *et al.* Caveolin-1 and Cancer Metabolism in the Tumor Microenvironment: Markers, Models, and Mechanisms. *Annu. Rev. Pathol. Mech. Dis.* **7,** 423–467 (2012).

305. Millán, J. *et al.* Lymphocyte transcellular migration occurs through recruitment of endothelial ICAM-1 to caveola- and F-actin-rich domains. *Nat. Cell Biol.* **8,** 113–123 (2006).

306. Head, B. P. *et al.* Loss of Caveolin-1 Accelerates Neurodegeneration and Aging. *PLoS One* **5,** e15697 (2010).

307. Fernandez-Rojo, M. A. *et al.* Caveolin-1 orchestrates the balance between glucose and lipid-dependent energy metabolism: implications for liver regeneration. *Hepatology* **55,** 1574–1584 (2012).

308. Martinez-Outschoorn, U. E., Sotgia, F. & Lisanti, M. P. Caveolae and signalling in cancer. *Nat. Rev. Cancer* **15,** 225–237 (2015).

309. Hancock, J. F. *et al.* Dominant-negative caveolin inhibits H-Ras function by disrupting cholesterol-rich plasma membrane domains. *Nat. Cell Biol.* **1,** 98–105 (1999).

310. Li, S., Couet, J. & Lisanti, M. P. Src tyrosine kinases, Galpha subunits, and H-Ras share a common membrane-anchored scaffolding protein, caveolin. Caveolin binding negatively regulates the auto-activation of Src tyrosine kinases. *J. Biol. Chem.* **271,** 29182–90 (1996).

311. Gottlieb-Abraham, E. *et al.* Src-mediated caveolin-1 phosphorylation affects the targeting of active Src to specific membrane sites. *Mol. Biol. Cell* **24,** 3881–95 (2013).

312. Mineo, C. & Shaul, P. W. in *Advances in experimental medicine and biology* **729,** 51–62 (2012).

313. Gratton, J.-P. *et al.* Selective inhibition of tumor microvascular permeability by cavtratin blocks tumor progression in mice. *Cancer Cell* **4,** 31–39 (2003).

314. Morais, C., Ebrahem, Q., Anand-Apte, B. & Parat, M.-O. Altered angiogenesis in caveolin-1 gene-deficient mice is restored by ablation of endothelial nitric oxide synthase. *Am. J. Pathol.* **180,** 1702–14 (2012).

315. Pani, B. *et al.* Activation of TRPC1 by STIM1 in ER-PM microdomains involves release of the channel from its scaffold caveolin-1. *Proc. Natl. Acad. Sci. U. S. A.* **106,** 20087–92 (2009).

316. Frank, P. G. *et al.* Caveolin-1 and regulation of cellular cholesterol homeostasis. *Am. J. Physiol. Circ. Physiol.* **291,** H677–H686 (2006).

317. Bosch, M. *et al.* Caveolin-1 deficiency causes cholesterol-dependent mitochondrial dysfunction and apoptotic susceptibility. *Curr. Biol.* **21,** 681–686 (2011).

318. Furuchi, T. & Anderson, R. G. Cholesterol depletion of caveolae causes hyperactivation of extracellular signal-related kinase (ERK). *J. Biol. Chem.* **273,** 21099–104 (1998).

319. Fielding, C. J., Bist, A. & Fielding, P. E. Caveolin mRNA levels are up-regulated by free cholesterol and down-regulated by oxysterols in fibroblast monolayers. *Proc. Natl. Acad. Sci. U. S. A.* **94,** 3753–8 (1997).

320. Murata, M. *et al.* VIP21/caveolin is a cholesterol-binding protein. *Proc. Natl. Acad. Sci. U. S. A.* **92,** 10339–43 (1995).

321. Frühbeck, G., López, M. & Diéguez, C. Role of caveolins in body weight and insulin resistance regulation. *Trends Endocrinol. Metab.* **18,** 177–182 (2007).

322. Sargiacomo, M. *et al.* Oligomeric structure of caveolin: implications for caveolae membrane organization. *Proc. Natl. Acad. Sci. U. S. A.* **92,** 9407–11 (1995).

323. Chen, D. & Che, G. Value of caveolin-1 in cancer progression and prognosis: Emphasis on cancer-associated fibroblasts, human cancer cells and mechanism of caveolin-1 expression (Review). *Oncol Lett* **8,** 1409–1421 (2014).

324. Hoop, C. L., Sivanandam, V. N., Kodali, R., Srnec, M. N. & van der Wel, P. C. A. Structural characterization of the caveolin scaffolding domain in association with cholesterol-rich membranes. *Biochemistry* **51,** 90–9 (2012).

325. Nassoy, P. & Lamaze, C. Stressing caveolae new role in cell mechanics. *Trends Cell Biol.* **22,** 381–389 (2012).

326. Lee, S. W., Reimer, C. L., Oh, P., Campbell, D. B. & Schnitzer, J. E. Tumor cell growth inhibition by caveolin re-expression in human breast cancer cells. *Oncogene* **16,** 1391–1397 (1998).

327. Capozza, F. *et al.* Absence of Caveolin-1 Sensitizes Mouse Skin to Carcinogen-Induced Epidermal Hyperplasia and Tumor Formation. *Am. J. Pathol.* **162,** 2029–2039 (2003).

328. Cerezo, A. *et al.* The Absence of Caveolin-1 Increases Proliferation and Anchorage-Independent Growth by a Rac-Dependent, Erk-Independent Mechanism. *Mol. Cell. Biol.* **29,** 5046–5059 (2009).

329. Yang, G., Timme, T. L., Frolov, A., Wheeler, T. M. & Thompson, T. C. Combined c-Myc and Caveolin-1 Expression in Human Prostate Carcinoma Predicts Prostate Carcinoma Progression. *Cancer* (2005). doi:10.1002/cncr.20905

330. Felicetti, F. *et al.* Caveolin-1 tumor-promoting role in human melanoma. *Int. J. Cancer* **125,** 1514–1522 (2009).

331. Witkiewicz, A. K. *et al.* Loss of stromal caveolin-1 expression predicts poor clinical outcome in triple negative and basal-like breast cancers. *Cancer Biol. Ther.* **10,** 135–43 (2010).

332. Simpkins, S. A., Hanby, A. M., Holliday, D. L. & Speirs, V. Clinical and functional significance of loss of caveolin-1 expression in breast cancer-associated fibroblasts. *J. Pathol.* **227,** 490–498 (2012).

333. El-Gendi, S. M., Mostafa, M. F. & El-Gendi, A. M. Stromal Caveolin-1 Expression in Breast Carcinoma. Correlation with Early Tumor Recurrence and Clinical Outcome. *Pathol. Oncol. Res.* **18,** 459–469 (2012).

334. Yeong, J. *et al.* Caveolin-1 expression as a prognostic marker in triple negative breast cancers of Asian women. *J. Clin. Pathol.* **71,** 161–167 (2018).

335. Martin-Padura, I. *et al.* The White Adipose Tissue Used in Lipotransfer Procedures Is a Rich Reservoir of CD34+ Progenitors Able to Promote Cancer Progression. *Cancer Res.* **72,** 325–334 (2012).

336. Gkontra, P. *et al.* Deciphering microvascular changes after myocardial infarction through 3D fully automated image analysis. *Sci. Rep.* **8,** 1854 (2018).

337. Buades, A., Coll, B. & Morel, J.-M. A Non-Local Algorithm for Image Denoising. in *2005 IEEE Computer Society Conference on Computer Vision and Pattern Recognition (CVPR'05)* **2,** 60–65 (IEEE, 2005).

338. Frangi, A. F., Niessen, W. J., Vincken, K. L. & Viergever, M. A. in 130–137 (Springer, Berlin, Heidelberg, 1998). doi:10.1007/BFb0056195

339. Otsu, N. A Threshold Selection Method from Gray-Level Histograms. *IEEE Trans. Syst. Man. Cybern.* **9,** 62–66 (1979).

340. Ahrens, J., Geveci, B. & Law, C. *ParaView: An End-User Tool for Large Data Visualization*. *Visualization Handbook* (2005).

341. Loening, A. M. & Gambhir, S. S. AMIDE: a free software tool for multimodality medical image analysis. *Mol. Imaging* **2,** 131–7 (2003).

342. Andrews, S. FastQC: A Quality Control tool for High Throughput Sequence Data. (2010). Available at: http://www.bioinformatics.babraham.ac.uk/projects/fastqc/. (Accessed: 3rd May 2018)

343. Martin, M. Cutadapt removes adapter sequences from high-throughput sequencing reads. *EMBnet.journal* **17,** 10 (2011).

344. Li, B. & Dewey, C. N. RSEM: accurate transcript quantification from RNA-Seq data with or without a reference genome. *BMC Bioinformatics* **12,** 323 (2011).

345. Robinson, M. D., McCarthy, D. J. & Smyth, G. K. edgeR: a Bioconductor package for differential expression analysis of digital gene expression data. *Bioinformatics* **26,** 139–140 (2010).

346. Kuleshov, M. V. *et al.* Enrichr: a comprehensive gene set enrichment analysis web server 2016 update. *Nucleic Acids Res.* **44,** W90–W97 (2016).

347. Nakatsu, M. N. *et al.* VEGF121 and VEGF165 Regulate Blood Vessel Diameter Through Vascular Endothelial Growth Factor Receptor 2 in an in vitro Angiogenesis Model. *Lab. Investig.* **83,** 1873–1885 (2003).

348. Erfle, H. *et al.* Reverse transfection on cell arrays for high content screening microscopy. *Nat Protoc* **2,** 392–399 (2007).

349. Jimenez-Carretero, D. *et al.* Tox_(R)CNN: Deep Learning-Based Nuclei Profiling tool For Drug Toxicity Screening. *bioRxiv* 334557 (2018). doi:10.1101/334557

350. Morton, J. & Snider, T. A. Guidelines for collection and processing of lungs from aged mice for histological studies. *Pathobiol. Aging Age Relat. Dis.* **7,** 1313676 (2017).

351. Lowe, D. G. Distinctive Image Features from Scale-Invariant Keypoints. *Int. J. Comput. Vis.* **60,** 91–110 (2004).

352. Sternberg & R., S. Biomedical Image Processing. *Computer (Long. Beach. Calif).* **16,** 22–34 (1983).

353. Ruifrok, A. C. & Johnston, D. A. Quantification of histochemical staining by color deconvolution. *Anal. Quant. Cytol. Histol.* **23,** 291–9 (2001).

354. Chaudhury, K. N., Sage, D. & Unser, M. Fast $O(1)$ Bilateral Filtering Using Trigonometric Range Kernels. *IEEE Trans. Image Process.* **20,** 3376–3382 (2011).

355. Wilkinson, M. H. F. (Michael H. F. . & Schut, F. *Digital image analysis of microbes : imaging, morphometry, fluorometry, and motility techniques and applications*. (Wiley, 1998).

356. Roerdink, J. B. T. M. & Meijster, A. The Watershed Transform: Definitions, Algorithms and Parallelization Strategies. *Fundam. Inf.* **41,** 187–228 (2000).

357. Kim, J. H. *et al.* High cleavage efficiency of a 2A peptide derived from porcine teschovirus-1 in human cell lines, zebrafish and mice. *PLoS One* **6,** e18556 (2011).

358. Mezzanotte, L. *et al.* Sensitive Dual Color In Vivo Bioluminescence Imaging Using a New Red Codon Optimized Firefly Luciferase and a Green Click Beetle Luciferase. *PLoS One* **6,** e19277 (2011).

359. Zhang, W. M. *et al.* Analysis of the human integrin alpha11 gene (ITGA11) and its promoter. *Matrix Biol* **21,** 513–523 (2002).

360. Stegmeier, F., Hu, G., Rickles, R. J., Hannon, G. J. & Elledge, S. J. A lentiviral microRNA-based system for single-copy polymerase II-regulated RNA interference in mammalian cells. *Proc. Natl. Acad. Sci. U. S. A.* **102,** 13212–7 (2005).

361. Strutz, F. *et al.* Identification and characterization of a fibroblast marker: FSP1. *J Cell Biol* **130,** 393–405 (1995).

362. Hanahan, D. & Weinberg, R. A. The hallmarks of cancer. *Cell* **100,** 57–70 (2000).

363. Vegran, F., Boidot, R., Michiels, C., Sonveaux, P. & Feron, O. Lactate Influx through the Endothelial Cell Monocarboxylate Transporter MCT1 Supports an NF- B/IL-8 Pathway that Drives Tumor Angiogenesis. *Cancer Res.* **71,** 2550–2560 (2011).

364. Azenshtein, E. *et al.* The angiogenic factors CXCL8 and VEGF in breast cancer: regulation by an array of pro-malignancy factors. *Cancer Lett* **217,** 73–86 (2005).

365. Hammond, M. E. *et al.* IL-8 induces neutrophil chemotaxis predominantly via type I IL-8 receptors. *J. Immunol.* **155,** 1428–33 (1995).

366. Singer, M. & Sansonetti, P. J. IL-8 is a key chemokine regulating neutrophil recruitment in a new mouse model of Shigella-induced colitis. *J. Immunol.* **173,** 4197–206 (2004).

367. Singh, J. K., Simões, B. M., Howell, S. J., Farnie, G. & Clarke, R. B. Recent advances reveal IL-8 signaling as a potential key to targeting breast cancer stem cells. *Breast Cancer Res.* **15,** 210 (2013).

368. Chen, L. *et al.* The IL-8/CXCR1 axis is associated with cancer stem cell-like properties and correlates with clinical prognosis in human pancreatic cancer cases. *Sci. Rep.* **4,** 5911 (2015).

369. Aguilera, K. Y. & Brekken, R. A. Hypoxia Studies with Pimonidazolein vivo. *Bio-protocol* **4,** (2014).

370. Mikhaylova, M. *et al.* Hypoxia Increases Breast Cancer Cell-Induced Lymphatic Endothelial Cell Migration. *Neoplasia* **10,** 380–IN5 (2008).

371. Morfoisse, F., Renaud, E., Hantelys, F., Prats, A.-C. & Garmy-Susini, B. Role of hypoxia and vascular endothelial growth factors in lymphangiogenesis. *Mol. Cell. Oncol.* **2,** e1024821 (2015).

372. Lokmic, Z., Musyoka, J., Hewitson, T. D. & Darby, I. A. in *International review of cell and molecular biology* **296,** 139–185 (2012).

373. Pickup, M. W., Mouw, J. K. & Weaver, V. M. The extracellular matrix modulates the hallmarks of cancer. *EMBO Rep.* **15,** 1243–53 (2014).

374. Newman, A. C., Nakatsu, M. N., Chou, W., Gershon, P. D. & Hughes, C. C. W. The requirement for fibroblasts in angiogenesis: fibroblast-derived matrix proteins are essential for endothelial cell lumen formation. *Mol. Biol. Cell* **22,** 3791–800 (2011).

375. Welch-Reardon, K. M. *et al.* Angiogenic sprouting is regulated by endothelial cell expression of Slug. *J. Cell Sci.* **127,** 2017–28 (2014).

376. Hotamisligil, G. S. Endoplasmic Reticulum Stress and the Inflammatory Basis of Metabolic Disease. *Cell* **140,** 900–917 (2010).

377. Shin, S. & Argon, Y. Stressed-Out Endoplasmic Reticulum Inflames the Mitochondria. *Immunity* **43,** 409–11 (2015).

378. Pavlides, S. *et al.* Loss of stromal caveolin-1 leads to oxidative stress, mimics hypoxia and drives inflammation in the tumor microenvironment, conferring the 'reverse Warburg effect': A transcriptional informatics analysis with validation. *Cell Cycle* **9,** 2201–2219 (2010).

379. Sala-Vila, A. *et al.* Interplay between hepatic mitochondria-associated membranes, lipid metabolism and caveolin-1 in mice. *Sci. Rep.* **6,** 27351 (2016).

380. Wernstedt Asterholm, I., Mundy, D. I., Weng, J., Anderson, R. G. W. & Scherer, P. E. Altered Mitochondrial Function and Metabolic Inflexibility Associated with Loss of Caveolin-1. *Cell Metab.* **15,** 171–185 (2012).

381. Fernandez-Rojo, M. A. & Ramm, G. A. Caveolin-1 Function in Liver Physiology and Disease. *Trends Mol. Med.* **22,** 889–904 (2016).

382. Fusakio, M. E. *et al.* Transcription factor ATF4 directs basal and stress-induced gene expression in the unfolded protein response and cholesterol metabolism in the liver. *Mol. Biol. Cell* **27,** 1536–51 (2016).

383. Naik, E. & Dixit, V. M. Mitochondrial reactive oxygen species drive proinflammatory cytokine production. *J. Exp. Med.* **208,** 417–20 (2011).

384. Lin, J., Ke, Y., Li, Z., Zhong, Q. & Li, R. The secretion of proinflammatory cytokines and chemokines in stimulated fibroblast-like synoviocytes of osteoarthritis. *Osteoarthr. Cartil.* **20,** S240 (2012).

385. Mills, E. L., Kelly, B. & O'Neill, L. A. J. Mitochondria are the powerhouses of immunity. *Nat. Immunol.* **18,** 488–498 (2017).

386. Mari, M., Morales, A., Colell, A., Garcia-Ruiz, C. & Fernandez-Checa, J. C. Mitochondrial glutathione, a key survival antioxidant. *Antioxid Redox Signal* **11,** 2685–2700 (2009).

387. Ribas, V., Garci-a-Ruiz, C. & Fernandez-Checa, J. C. Glutathione and mitochondria. *Front. Pharmacol.* **5,** 151 (2014).

388. Oslowski, C. M. & Urano, F. Measuring ER stress and the unfolded protein response using mammalian tissue culture system. *Methods Enzymol.* **490,** 71–92 (2011).

389. Obeng, E. A. *et al.* Proteasome inhibitors induce a terminal unfolded protein response in multiple myeloma cells. *Blood* **107,** 4907–16 (2006).

390. Ran, S., Volk, L., Hall, K. & Flister, M. J. Lymphangiogenesis and lymphatic metastasis in breast cancer. *Pathophysiology* **17,** 229–251 (2010).

391. Fang, Q. I. *et al.* Increased CXCL8 Expression Is Negatively Correlated with the Overall Survival of Patients with ER-Negative Breast Cancer. *Anticancer Res.* **37,** 4845–4852 (2017).

392. Milovanovic, J., Todorovic-Rakovic, N. & Abu Rabi, Z. The prognostic role of interleukin-8 (IL-8) and matrix metalloproteinases -2 and -9 in lymph node-negative untreated breast cancer patients. *J. BUON.* **18,** 866–73 (2013).

393. Martinez-Outschoorn, U. E. *et al.* Autophagy in cancer associated fibroblasts promotes tumor cell survival. *Cell Cycle* **9,** 3515–3533 (2010).

394. Hubbi, M. E. & Semenza, G. L. Regulation of cell proliferation by hypoxia-inducible factors. *Am. J. Physiol. Cell Physiol.* **309,** C775-82 (2015).

395. Sotgia, F. *et al.* Caveolin-1−/− Null Mammary Stromal Fibroblasts Share Characteristics with Human Breast Cancer-Associated Fibroblasts. *Am. J. Pathol.* **174,** 746–761 (2009).

396. Lin, M. I., Yu, J., Murata, T. & Sessa, W. C. Caveolin-1-Deficient Mice Have Increased Tumor Microvascular Permeability, Angiogenesis, and Growth. *Cancer Res.* **67,** 2849–2856 (2007).

397. Huang, S.-P. *et al.* Interleukin-6 Increases Vascular Endothelial Growth Factor and Angiogenesis in Gastric Carcinoma. *J. Biomed. Sci.* **11,** 517–527 (2004).

398. Sonveaux, P. *et al.* Targeting the Lactate Transporter MCT1 in Endothelial Cells Inhibits Lactate-Induced HIF-1 Activation and Tumor Angiogenesis. *PLoS One* **7,** e33418 (2012).

399. Liu, Q. *et al.* The CXCL8-CXCR1/2 pathways in cancer. *Cytokine Growth Factor Rev.* **31,** 61–71 (2016).

400. Sparmann, A. & Bar-Sagi, D. Ras-induced interleukin-8 expression plays a critical role in tumor growth and angiogenesis. *Cancer Cell* **6,** 447–458 (2004).

401. Yao, C. *et al.* Interleukin-8 modulates growth and invasiveness of estrogen receptor-negative breast cancer cells. *Int. J. Cancer* **121,** 1949–1957 (2007).

402. Ishikawa, F. *et al.* Development of functional human blood and immune systems in NOD/SCID/IL2 receptor chainnull mice. *Blood* **106,** 1565–1573 (2005).

403. Shultz, L. D. *et al.* Human lymphoid and myeloid cell development in NOD/LtSz-scid IL2R gamma null mice engrafted with mobilized human hemopoietic stem cells. *J. Immunol.* **174,** 6477–89 (2005).

404. Tazzyman, S., Niaz, H. & Murdoch, C. Neutrophil-mediated tumour angiogenesis: subversion of immune responses to promote tumour growth. *Semin. Cancer Biol.* **23,** 149–58 (2013).

405. Benoy, I. H. *et al.* Increased serum interleukin-8 in patients with early and metastatic breast cancer correlates with early dissemination and survival. *Clin. Cancer Res.* **10,** 7157–62 (2004).

406. Gvaramia, D., Blaauboer, M. E., Hanemaaijer, R. & Everts, V. Role of caveolin-1 in fibrotic diseases. *Matrix Biol.* **32,** 307–315 (2013).

407. Loeffler, M., Krüger, J. A., Niethammer, A. G. & Reisfeld, R. A. Targeting tumor-associated fibroblasts improves cancer chemotherapy by increasing intratumoral drug uptake. *J. Clin. Invest.* **116,** 1955–1962 (2006).

408. Zhang, C. *et al.* Hypoxia induces the breast cancer stem cell phenotype by HIF-dependent and ALKBH5-mediated m^6A-demethylation of NANOG mRNA. *Proc. Natl. Acad. Sci. U. S. A.* **113,** E2047-56 (2016).

409. Wong, C. C.-L. *et al.* Hypoxia-inducible factor 1 is a master regulator of breast cancer metastatic niche formation. *Proc. Natl. Acad. Sci. U. S. A.* **108,** 16369–74 (2011).

410. VanHook, A. M. Hypoxia-induced plasticity in cancer cell migration. *Sci. Signal.* **10,** eaan0467 (2017).

411. Ji, R.-C. Hypoxia and lymphangiogenesis in tumor microenvironment and metastasis. *Cancer Lett.* **346,** 6–16 (2014).

412. Zhao, X. *et al.* Caveolin-1 Expression Level in Cancer Associated Fibroblasts Predicts Outcome in Gastric Cancer. *PLoS One* **8,** e59102 (2013).

413. He, Y. *et al.* Quantum Dots-Based Immunofluorescent Imaging of Stromal Fibroblasts Caveolin-1 and Light Chain 3B Expression and Identification of Their Clinical Significance in Human Gastric Cancer. *Int. J. Mol. Sci.* **13,** 13764–13780 (2012).

414. Di Vizio, D. *et al.* An absence of stromal caveolin-1 is associated with advanced prostate cancer, metastatic disease spread and epithelial Akt activation. *Cell Cycle* **8,** 2420–2424 (2009).

415. Ayala, G. *et al.* Loss of caveolin-1 in prostate cancer stroma correlates with reduced relapse-free survival and is functionally relevant to tumour progression. *J. Pathol.* **231,** 77–87 (2013).

416. Wu, K. N. *et al.* Loss of stromal caveolin-1 expression in malignant melanoma metastases predicts poor survival. *Cell Cycle* **10,** 4250–4255 (2011).

417. Edge, S. B. & Compton, C. C. The American Joint Committee on Cancer: the 7th Edition of the AJCC Cancer Staging Manual and the Future of TNM. *Ann. Surg. Oncol.* **17,** 1471–1474 (2010).

418. Park, C. *et al.* Internal Mammary Sentinel Lymph Node Mapping for Invasive Breast Cancer: Implications for Staging and Treatment. *Breast J.* **11,** 29–33 (2005).

419. Shao, L., Takeda, K., Kato, S., Mori, S. & Kodama, T. Communication between lymphatic and venous systems in mice. *J. Immunol. Methods* **424,** 100–105 (2015).

420. Pereira, E. R. *et al.* Lymph node metastases can invade local blood vessels, exit the node, and colonize distant organs in mice. *Science* **359,** 1403–1407 (2018).

421. Tsuyada, A. *et al.* CCL2 Mediates Cross-talk between Cancer Cells and Stromal Fibroblasts That Regulates Breast Cancer Stem Cells. *Cancer Res.* **72,** 2768–2779 (2012).

422. Martinez-Outschoorn, U. E. *et al.* The autophagic tumor stroma model of cancer or 'battery-operated tumor growth'. *Cell Cycle* **9,** 4297–4306 (2010).

423. Shi, Y. *et al.* Critical role of CAV1/caveolin-1 in cell stress responses in human breast cancer cells via modulation of lysosomal function and autophagy. *Autophagy* **11,** 769–784 (2015).

424. Martinez-Outschoorn, U. E. *et al.* Cytokine production and inflammation drive autophagy in the tumor microenvironment. *Cell Cycle* **10,** 1784–1793 (2011).

425. Song, C. *et al.* Oxidative stress-mediated NFkappaB phosphorylation upregulates p62/SQSTM1 and promotes retinal pigmented epithelial cell survival through increased autophagy. *PLoS One* **12,** e0171940 (2017).

426. Criollo, A. *et al.* Autophagy is required for the activation of NFkappaB. *Cell Cycle* **11,** 194–199 (2012).

427. Chiavarina, B. *et al.* HIF1-alpha functions as a tumor promoter in cancer associated fibroblasts, and as a tumor suppressor in breast cancer cells: Autophagy drives compartment-specific oncogenesis. *Cell Cycle* **9,** 3534–51 (2010).

428. Li, L., Ren, C. H., Tahir, S. A., Ren, C. & Thompson, T. C. Caveolin-1 maintains activated Akt in prostate cancer cells through scaffolding domain binding site interactions with and inhibition of serine/threonine protein phosphatases PP1 and PP2A. *Mol. Cell. Biol.* **23,** 9389–404 (2003).

429. Fork, C., Hitzel, J., Nichols, B. J., Tikkanen, R. & Brandes, R. P. Flotillin-1 facilitates toll-like receptor 3 signaling in human endothelial cells. *Basic Res. Cardiol.* **109,** 439 (2014).

430. Kassan, M. *et al.* MicroRNA-204 promotes vascular endoplasmic reticulum stress and endothelial dysfunction by targeting Sirtuin1. *Sci. Rep.* **7,** 9308 (2017).

431. Urra, H., Dufey, E., Avril, T., Chevet, E. & Hetz, C. Endoplasmic Reticulum Stress and the Hallmarks of Cancer. *Trends in Cancer* **2,** 252–262 (2016).

432. Obacz, J. *et al.* Regulation of tumor-stroma interactions by the unfolded protein

response. *FEBS J.* (2017). doi:10.1111/febs.14359

433. Volmer, R. & Ron, D. Lipid-dependent regulation of the unfolded protein response. *Curr. Opin. Cell Biol.* **33,** 67–73 (2015).

434. Corazzari, M., Gagliardi, M., Fimia, G. M. & Piacentini, M. Endoplasmic Reticulum Stress, Unfolded Protein Response, and Cancer Cell Fate. *Front. Oncol.* **7,** 78 (2017).

435. Marjon, P. L., Bobrovnikova-Marjon, E. V & Abcouwer, S. F. Expression of the pro-angiogenic factors vascular endothelial growth factor and interleukin-8/CXCL8 by human breast carcinomas is responsive to nutrient deprivation and endoplasmic reticulum stress. *Mol. Cancer* **3,** 4 (2004).

436. Wang, Y. *et al.* The unfolded protein response induces the angiogenic switch in human tumor cells through the PERK/ATF4 pathway. *Cancer Res.* **72,** 5396–406 (2012).

437. Taniuchi, S., Miyake, M., Tsugawa, K., Oyadomari, M. & Oyadomari, S. Integrated stress response of vertebrates is regulated by four eIF2α kinases. *Sci. Rep.* **6,** 32886 (2016).

438. Anita Bist, ‡, Christopher J. Fielding, ‡,§ and & Phoebe E. Fielding*, ‡,ǁ. p53 Regulates Caveolin Gene Transcription, Cell Cholesterol, and Growth by a Novel Mechanism†. (2000). doi:10.1021/BI991721H

439. Sanders, Y. Y. *et al.* SMAD-independent down-regulation of caveolin-1 by TGF-β: effects on proliferation and survival of myofibroblasts. *PLoS One* **10,** e0116995 (2015).

440. Han, B., Copeland, C. A., Tiwari, A. & Kenworthy, A. K. Assembly and Turnover of Caveolae: What Do We Really Know? *Front. cell Dev. Biol.* **4,** 68 (2016).

441. Kassan, M. *et al.* Sirtuin1 protects endothelial Caveolin-1 expression and preserves endothelial function via suppressing miR-204 and endoplasmic reticulum stress. *Sci. Rep.* **7,** 42265 (2017).

7. SUPPLEMENTAL MATERIAL

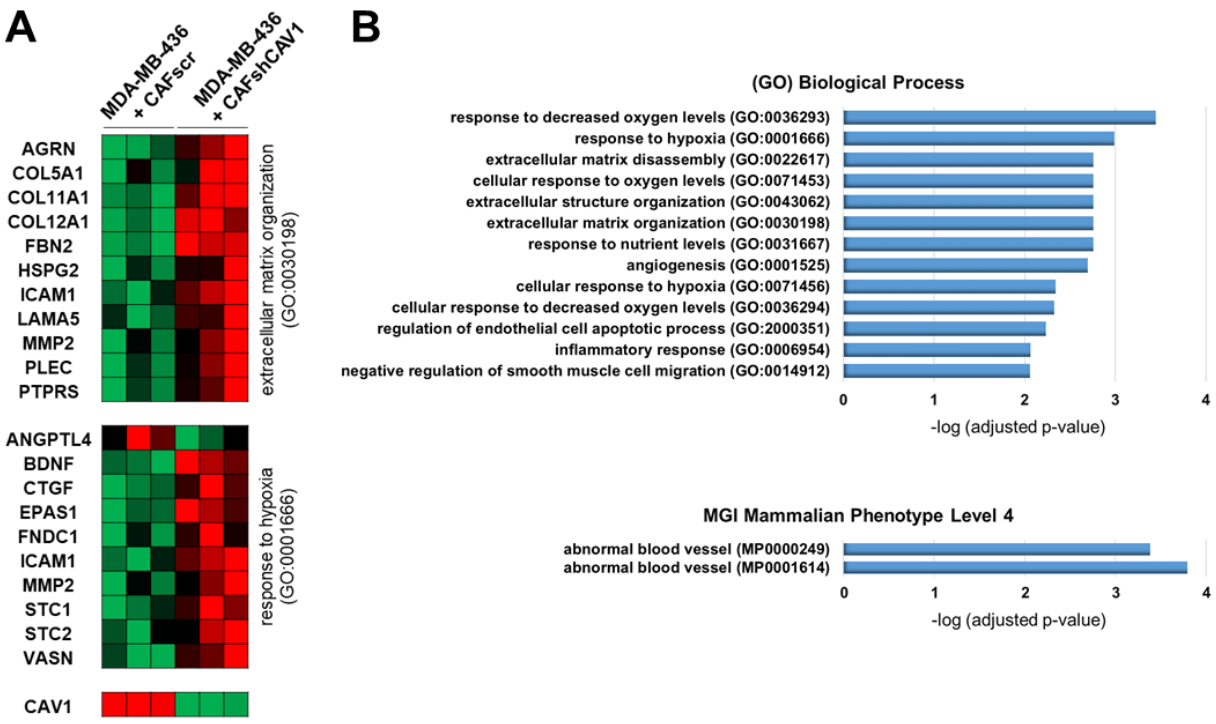

Figure S1. Prolonging tumor primary growth results in enriched hypoxia and fibrosis gene expression signatures in low stromal CAV1 (sCAV1low) tumors. (A) RNASeq-derived gene expression profile heatmaps of primary tumor xenograft lysates showing a significant upregulation of genes related to extracellular matrix organization and hypoxia in sCAV1low tumors resected 40 days post cell injection in the mammary fat pad. n=3/group. In gene expression heatmap red denotes increased gene expression while green corresponds to downregulation. **(B)** Gene enrichment analysis of differentially expressed genes in sCAV1low tumors resected 40 days post cell injection in the mammary fat pad. Analysis was performed with with Enrichr web tool, it shows top hits in Gene Ontology (GO) of Biological Process and MGI Mammalian Phenotype scored by P-value. Note the enrichment in biological processes related to response of low oxygen levels (hypoxia). Significance is represented as –log (P-value).

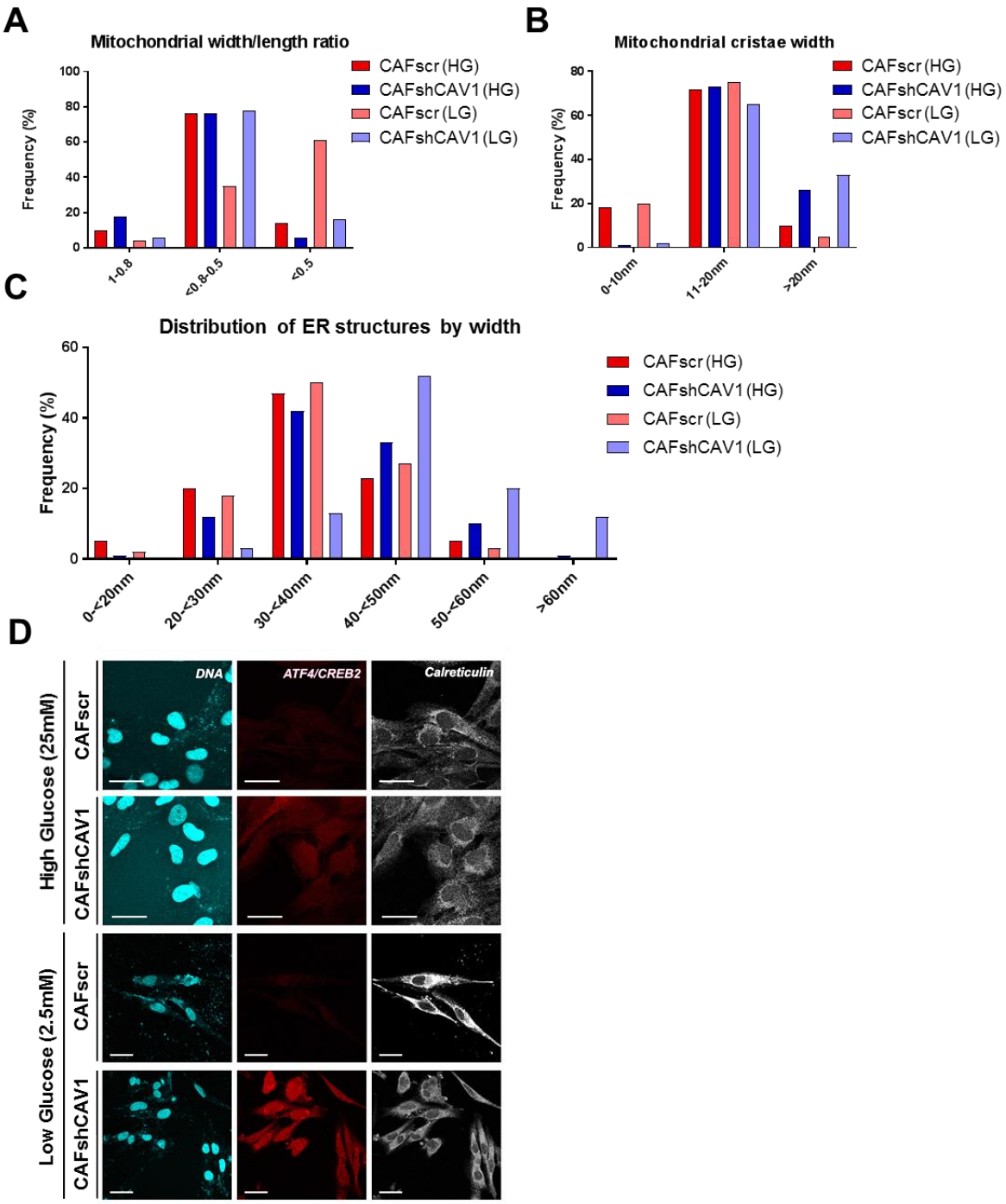

Figure S2. ER stress-related organelle morphological traits and UPR-derived transcription factor nuclear localization are enriched in CAFshCAV1 fibroblasts. (A, B, and D) Quantification of **(A and B)** mitochondrial, and **(C)** endoplasmic reticulum structural features associated with disfunctionality and ISR activation. Features, such as ER and mitochondrial cristae engrossment become more apparent under ER stress inducing low glucose (LG) cell culture conditions. **(D)** Representative fluorescence microscopy images of CAFs grown in HG or LG DMEM, stained for nuclei (H33342, in cyan), endoplasmic reticulum (Calreticulin, in white) and ATF4/CREB2 transcription factor from PERK axis of the UPR (MitoTracker CM-H2TM ROS, in red). In basal HG conditions, according with UPR PERK axis activation, CAFshCAV1 fibroblasts show increased staining of ATF4, a situation that becomes clearer under the ER stress, and thus UPR, inducing LG condition. Scale bar: 20µm.

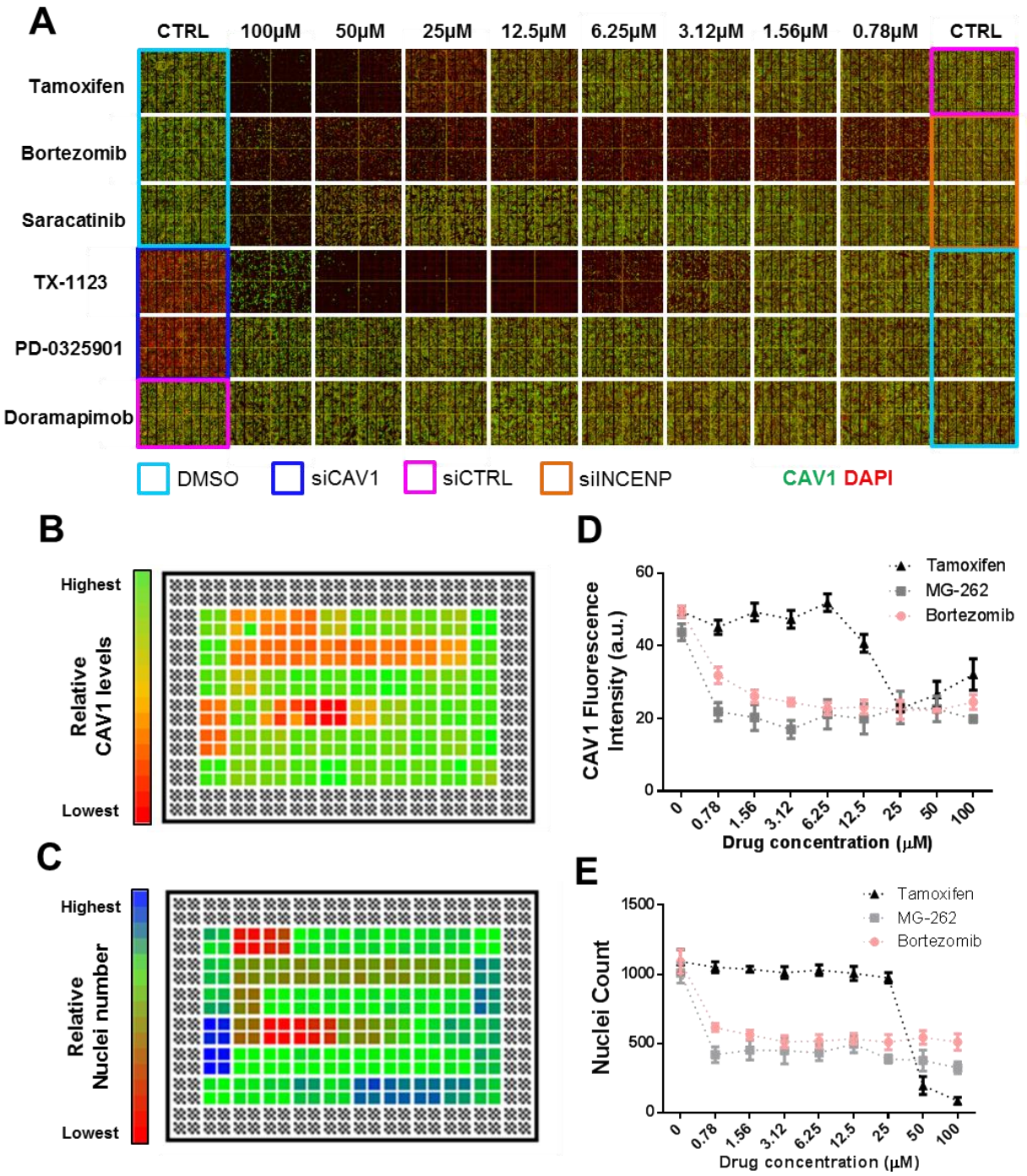

Figure S3. High Content Screening of drugs regulating CAV1 levels in pancreatic CAFs. (A) Whole 384-well plate fluorescence microscopy image reconstruction. Each grid cell corresponds to 4 merged wells (20 images each) treated with the same experimental condition. Pancreatic CAFs were seeded and treated for 24h with serial dilutions of different predicted DMSO-dissolved CAV1 regulators. Afterwards, cells were fixed and stained for CAV1 (in green) and nuclei (DAPI, in red). As a control for the staining process a number of wells were pre-coated before cell-seeding with CAV1 siRNA (dark blue), siINCENP (which generates multinucleated cells and serves as a control for the siRNA delivery, in orange) and a non-targeting siRNA control. DMSO was the control vehicle (light blue). **(B and C)** Heatmap representation of (B) CAV1 cytoplasmic fluorescence intensity and (C) nuclei number, respectively. **(D and E)** Quantification of (D) CAV1 fluorescence intensity and (E) nuclei numbers.

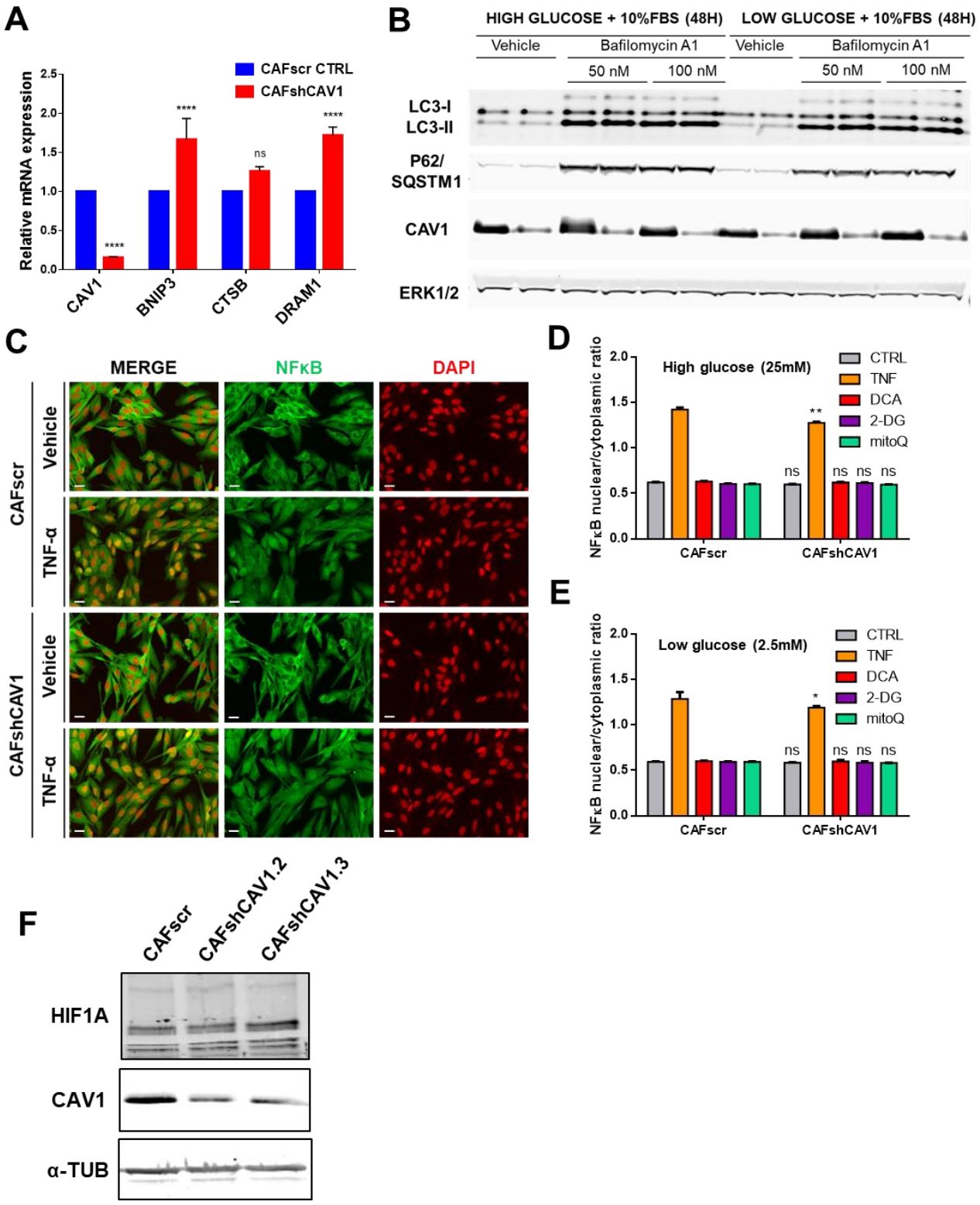

Figure S4. Autophagy, NFκB and HIF1A signalling are not upregulated in CAFshCAV1 fibroblasts. (A) qPCR expression analysis of CAV1, mitophagy (BNIP3) and autophagy (CTSB,DRAM1) markers in primary breast CAFs. **(B)** Western Blot analysis of CAFs cultured in High (25mM) or Low (2.5mM) glucose DMEM for 48h. Bafilomycin A1 is an inhibitor of the late phase of autophagy, which allows the study of active autophagy flux by preventing the degradation of LC3 and p62, common autophagy markers. Both in basal and BafA1 treated conditions CAFs show no difference

in LC3-II/LC3-I ratio or p62 accumulation. Data are representative of 4 independent experiments. **(C)** Representative CAFs fibroblast immunofluorescence depicting NFκB staining (in green) and total cell nuclei number (red, DAPI staining). CAFs cells were grown in the presence of TNF-α (as a positive control treatment for NFκB nuclear translocation)**,** and other treatments capable of inducing cytokine upregulation (2-DG, DCA) or quenchig mitochondrial ROS (mitoQ) in either high (HG) or low (LG) DMEM (HG images are shown). Observe nuclear localization of NFκB upon TNF treatment and the absence of differences in the untreated CAFs. See Fig. S4D and S4E. Scale bar: 20 μm **(D and E)** Quantification of NFκB nuclear/cytoplasmic intensity. Data is representative od 3 independent experiments. (Two-way ANOVA, Bonferroni's multiple comparison test). Besides upon TNF treatments no significant differences are observed among CAFscr and CAFshCAV1 fibroblasts. **(F)** Western Blot analysis of CAFs cultured in low (2.5mM) glucose DMEM for 7 days. No differences were observed in HIF1A levels. For qPCR gene expression analysis data are presented as mean ± SEM relative to CAFscr CTRL; n=5, *P<0.05, **P<0.01, ***P<0.001, ****P<0.0001, Significance for comparisons against CAFscr CTRL (vehicle) is depicted in blue, and for CAFshCAV1 CTRL (vehicle) in red. (Multiple t-test comparisons, with Holm-Sidak multiple comparison correction).

A

Panther 2016 Enrichr

Index	Name	P-value	Adjusted p-value	Z-score	Combined score
1	Integrin signalling pathway_Homo sapiens_P00034	0.01422	0.2300	-1.69	2.48
2	Axon guidance mediated by Slit/Robo_Homo sapiens_P00008	0.004372	0.1661	-1.07	1.92
3	Cholesterol biosynthesis_Homo sapiens_P00014	0.01816	0.2300	-0.41	0.60
4	Endothelin signaling pathway_Homo sapiens_P00019	0.1332	0.7546	-1.24	0.35
5	Histamine H1 receptor mediated signaling pathway_Homo sapiens_P04385	0.07556	0.7178	-1.03	0.34
6	Inflammation mediated by chemokine and cytokine signaling pathway_Homo sapiens_P00031	0.2038	0.7546	-1.12	0.32
7	Axon guidance mediated by netrin_Homo sapiens_P00009	0.09524	0.7238	-0.90	0.29
8	VEGF signaling pathway_Homo sapiens_P00056	0.2332	0.7546	-0.89	0.25
9	Apoptosis signaling pathway_Homo sapiens_P00006	0.2454	0.7546	-0.78	0.22
10	Ubiquitin proteasome pathway_Homo sapiens_P00060	0.1670	0.7546	-0.71	0.20

B

KEGG 2016 Enrichr

Index	Name	P-value	Adjusted p-value	Z-score	Combined score
1	Fatty acid metabolism_Homo sapiens_hsa01212	0.00001697	0.001595	-1.83	11.82
2	ECM-receptor interaction_Homo sapiens_hsa04512	0.000008477	0.001594	-1.71	11.03
3	Influenza A_Homo sapiens_hsa05164	0.0004700	0.02114	-1.89	7.30
4	Fatty acid biosynthesis_Homo sapiens_hsa00061	0.0001025	0.006421	-1.34	6.75
5	Hematopoietic cell lineage_Homo sapiens_hsa04640	0.0005622	0.02114	-1.67	6.44
6	Focal adhesion_Homo sapiens_hsa04510	0.001348	0.03621	-1.77	5.88
7	Axon guidance_Homo sapiens_hsa04360	0.0009741	0.03052	-1.65	5.75
8	Toxoplasmosis_Homo sapiens_hsa05145	0.002799	0.05847	-1.71	4.85
9	Small cell lung cancer_Homo sapiens_hsa05222	0.002632	0.05847	-1.67	4.73
10	PI3K-Akt signaling pathway_Homo sapiens_hsa04151	0.006962	0.09349	-1.73	4.10

Figure S5. Signaling pathways upregulated in CAFshCAV1 fibroblasts. (A and B) Gene enrichment analysis performed in Panther and KEGG cell signaling pathway databases, respectively, via Enrichr web tool. TOP10 hits are shown.

A

Panther 2016 Enrichr

Index	Name	P-value	Adjusted p-value	Z-score	Combined score
1	Toll receptor signaling pathway_Homo sapiens_P00054	0.0002048	0.008600	-1.39	11.82
2	Glycolysis_Homo sapiens_P00024	0.0001615	0.008600	-1.29	11.28
3	Apoptosis signaling pathway_Homo sapiens_P00006	0.0009466	0.02650	-1.49	10.40
4	Integrin signalling pathway_Homo sapiens_P00034	0.003749	0.05249	-1.30	7.28
5	CCKR signaling map ST_Homo sapiens_P06959	0.02890	0.2100	-0.85	3.00
6	B cell activation_Homo sapiens_P00010	0.03000	0.2100	-0.50	1.75
7	Interleukin signaling pathway_Homo sapiens_P00036	0.03781	0.2268	-0.36	1.17
8	Fructose galactose metabolism_Homo sapiens_P02744	0.001265	0.02656	-0.17	1.13
9	Huntington disease_Homo sapiens_P00029	0.06426	0.3191	-0.21	0.57
10	Axon guidance mediated by netrin_Homo sapiens_P00009	0.01941	0.1631	-0.13	0.52

B

KEGG 2016 Enrichr

Index	Name	P-value	Adjusted p-value	Z-score	Combined score
1	TNF signaling pathway_Homo sapiens_hsa04668	4.083e-8	0.00001074	-1.91	21.91
2	Legionellosis_Homo sapiens_hsa05134	9.424e-8	0.00001239	-1.88	21.22
3	Herpes simplex infection_Homo sapiens_hsa05168	0.000004658	0.0004084	-1.73	13.50
4	Pathways in cancer_Homo sapiens_hsa05200	0.0003620	0.01214	-1.98	8.72
5	Influenza A_Homo sapiens_hsa05164	0.0001815	0.009547	-1.87	8.68
6	NF-kappa B signaling pathway_Homo sapiens_hsa04064	0.0001589	0.009547	-1.68	7.82
7	Osteoclast differentiation_Homo sapiens_hsa04380	0.0004055	0.01214	-1.71	7.54
8	Hepatitis C_Homo sapiens_hsa05160	0.0004423	0.01214	-1.66	7.31
9	Chagas disease (American trypanosomiasis)_Homo sapiens_hsa05142	0.0005077	0.01214	-1.56	6.89
10	Small cell lung cancer_Homo sapiens_hsa05222	0.0005925	0.01298	-1.54	6.70

Figure S6. Signaling pathways upregulated in low stromal CAV1 (sCAV1low) xenografts. (A and B) Gene enrichment analysis performed in Panther and KEGG cell signaling pathway databases, respectively, via Enrichr web tool. TOP10 hits are shown. Raw data corresponds to low stromal CAV1 tumors mastectomized 30 days post-cell injection in the mice fat-mammary pad.

Table S1. Morphological parameters of tumor xenograft vasculature obtained upon automated image analysis. Related to Figure S2A and S2B. Mean ± SD of all parameters for MDA-MB-436 (TCs), MDA-MB-436 + CAFscr (TCs + CAFscr) and MDA-MB-436 + CAFshCAV1 (TCs + CAFshCAV1) tumors (columns 2 to 4) along with multiple comparisons between the different tumor categories (columns 5 to 7). Up and down-arrows indicate increase and decrease respectively of the parameter value for (i) TCs tumors compared with TCs + CAFscr tumors (column 5), (ii) TCs tumors compared with TCs + CAFshCAV1 tumors (column 6), and (iii) TCs + CAFscr tumors compared with TCs + CAFshCAV1 tumors (column 7). Red (for increase) and blue (for decrease) colors are used to denote that the difference is statistically significant. Data include images from 3 independent experiments; n = 11 whole tumor images/MDA-MB-436 group and n = 31 whole tumor images/MDA-MB-436 + CAF groups, *P<0.05, **P<0.01, ***P<0.001, ****P<0.0001, (One-way ANOVA, Bonferroni's multiple comparison test).

Morphology (Structure-level metrics)	**TCs**	**SCR**	**shCAV1**	**TCs vs SCR**	**TCs vs shCAV1**	**SCR vs shCAV1**
Fractal Dimension	1.76±0.12	1.81±0.15	1.84±0.21	↓	↓	↓
Lacunarity (×10^2)	95.94±1.29	92.12±2.47	90.75±4.84	↑*	↑***	↑
Vascular Volume Density (%)	7.75±1.78	11.35±3.68	14.37±3.84	↓*	↓***	↓**
Vascular Surface area per vascular volume ratio (mm^2/mm^3)	204.65±20.72	222.78±50.68	210.14±31.31	↓	↓	↑
Vascular surface area density (mm^2/mm^3)	15.74±3.19	24.56±8.21	30.42±10.59	↓*	↓***	↓*
Breadth Density (mm^2/mm^3)	126.36±27.46	201.07±70.25	233.94±106.39	↓*	↓**	↓
Euler Characteristic Density ($1/mm^3$)	-705.92±667.9	-2947.4±2720.06	-5240.46±7899.6	↑	↑	↑
Total network length (mm)	237.56±105.78	846.55±442.83	1026.31±437.93	↓***	↓***	↓
Angioarchitecture (Skeleton-based metrics)						
Vascular segment radius (µm)	8.58±1.09	7.98±1.46	8.15±1.18	↑	↑	↓
Vascular segment length (µm)	41.13±11.86	41.4±7.6	40.55±10.6	↓	↑	↑
Vascular segment surface ($µm^2$)	1648.5±634.25	1553.62±495.33	1565.4±553.36	↑	↑	↓
Vascular segment volume ($µm^3$)	5780.59±2498.3	5084.82±2080.56	5205.15±2186.38	↑	↑	↓
Tortuosity (µm/ µm)	1.58±0.1	1.55±0.08	1.53±0.07	↑	↑	↑
Branching nodes (×10^4)[a]	13.11±4.95	12.64±2.97	13.97±5.92	↑	↓	↓
Blind ends/sprouts (×10^4)[a]	0.17±0.18	0.24±0.19	0.38±0.49	↓	↓	↓
Branching nodes[b]	13.11±4.95	12.64±2.97	13.97±5.92	↓	↓	↓
Blind ends/sprouts[b]	4.29±2.48	3.84±1.3	3.96±1.98	↑	↑	↓
Number of bifurcations[b]	11.17±4.17	10.63±2.56	11.62±5.02	↑	↓	↓
Number of trifurcations[b]	1.62±0.69	1.64±0.39	1.91±0.79	↓	↓	↓
Number of higher order connections[b]	0.32±0.14	0.37±0.12	0.44±0.18	↓	↓	↓

[a]Number per mm^3 of tissue
[b]Number per mm vascular length

Table S2. List of primer sequences used for qPCR gene expression analysis. Related to materials & methods section: RNA purification and qPCR analysis. List of primers used for human gene expression analysis.

qPCR SYBR-primers used in human gene expression analysis

Symbol	Acc No	Fwd primer (5'-3')	Rev primer (5'-3')
GAPDH	NM_002046	ATCACCATCTTCCAGGAGCG	CCTGCAAATGAGCCCCAG
ACTB	NM_001101	CACCTTCCAGCAGATGTGGA	AGCATTTGCGGTGGACGATGG
HPRT1	NM_000194	CCTGGCGTCGTGATTAGTGAT	AGACGTTCAGTCCTGTCCATAA
CAV1	NM_001172895	GATCAGTGGGCCTCCAAGG	GCTCACACAATGGCCTCCAT
VEGFA	NM_003376	AGGGCAGAATCATCACGAAGT	AGGGTCTCGATTGGATGGCA
IL1B	NM_000576	TTCGACACATGGGATAACGAGG	TTTTTGCTGTGAGTCCCGGAG
IL6	NM_000600	CCTGAACCTTCCAAAGATGGC	TTCACCAGGCAAGTCTCCTAA
CXCL8	NM_000584	ACTGAGAGTGATTGAGAGTGGAC	AACCCTCTGCACCCAGTTTTC
SDHA	NM_004168	CAGCATGTGTTACCAAGCTG	GGTGTCGTAGAAATGCCACC
SDHB	NM_003000	GACACCAACCTCAATAAGGTCTC	GGCTCAATGGATTTGTACTGTGC
NDUFS1	NM_005006	TGGAAGACAAGAACATTGGGC	GCAAACCTGATGCAGCGAG
NDUFS2	NM_004550	ACCCAAGCAAAGAAACAGCC	AATGAGCTTCTCAGTGCCTC
SOD2	NM_000636	CTGATTTGGACAAGCAGCAA	CTGGACAAACCTCAGCCCTA
MT-CO1	GQ369957	GGCCTGACTGGCATTGTATT	TGGCGTAGGTTTGGTCTAGG
MT-CO2	GQ369957	CCATCCCTACGCATCCTTTAC	GTTTGCTCCACAGATTTCAGAG
MT-ND1	GQ369957	TCCTCTTCTTAACAACATACC	GGTGAAGAGTTTTATGGC
MT-ND2	GQ369957	TCCAGCACCACGACCCTACT	TTCGATAATGGCCCATTTGG
MT-ATP6	GQ369957	CCTTATGAGCGGGCACAG	CAGGGCTATTGGTTGAATGAG
MT-ATP8	GQ369957	CTAAATACTACCGTATGGCCC	GGGCTTTGGTGAGGGAGG
CCL2	NM_002982	CAGCCAGATGCAATCAATGCC	TGGAATCCTGAACCCACTTCT
EDN1	NM_001955	AAGGCAACAGACCGTGAAAAT	CGACCTGGTTTGTCTTAGGTG
THBS1	NM_003246	AGACTCCGCATCGCAAAGG	TCACCACGTTGTTGTCAAGGG
THBS2	NM_003247	GACACGCTGGATCTCACCTAC	GAAGCTGTCTATGAGGTCGCA
CTSB	NM_001908	ACAACGTGGACATGAGCTACT	TCGGTAAACATAACTCTCTGGGG
DRAM1	NM_018370	TCAAATATCACCATTGATTTCTG	GCCACATACGGATGGTCATCTC
BNIP3	NM_004052	GACGGAGTAGCTCCAAGAGC	CTGGTGGAGGTTGTCAGACG
XBP1	NM_001079539	TTACGAGAGAAAACTCATGGC	GGGTCCAAGTTGTCGAATGC
CHOP	NM_001195056	CAGAACCAGCAGAGGTCACA	AGCTGTGCCACTTTCCTTTC
FAP	NM_004460	TGAACGAGTATGTTTGCAGTGG	GGTCTTTGGACAATCCCATGT
FSP1	NM_002961	GATGAGCAACTTGGACAGCAA	CTGGGCTGCTTATCTTGGGAAG
ITGA11(2)	NM_001004439	ACACAGTTTTGACGGCATTTGG	GCAGACAGCAAGCGGTAAA
ITGA11(3)	NM_001004439	GACCTACATGGACATCGTCATTG	ATCTTCGCCATACTGCACAAC
ITGA11(4)	NM_001004439	GCAACGCTGTGATTCTGTGG	AGATGGGCGTGAAGCAGAGG
ITGA11(5)	NM_001004439	GGGCAGATCCAGGTTGGAGT	TCAATGCCAAATGCCGTCCG
ITGA11(6)	NM_001004439	AAGATATGCGGTGGCCGTCC	TCGTTCTTGTTGGTGCCTTCC
MMP2	NM_001127891	CCCACTGCGGTTTTCTCGAAT	CAAAGGGGTATCCATCGCCAT
MMP9	NM_004994	TGTACCGCTATGGTTACACTCG	GGCAGGGACAGTTGCTTCT

Table S3. List of antibodies used for Western Blot and immunofluorescence assays. Related to materials & methods sections: Protein extraction and Western Blot (WB) analysis and immunofluorescence analyses (IF). Table includes: (i) Detected protein, (ii) unique UniProtKB identifier, (iii) antibody descriptions with clone number in between parenthesis ( ) and, for phosphorylated proteins (p-), recognized phosphorylated residues between brackets [ ], (iv) species in which the antibody is produced, (v) producer, (vi) catalog number, (vii) techniques in which the antibody was used, and (viii) recommended dilutions. Abbreviations stand for: mAb (monoclonal antibody) and pAb (polyclonal antibody).

Protein	UniProtID	Antibody	Species	Producer	Cat.No	App.	Dilution
CAV1	Q03135	Caveolin-1 (D46G3) XP®	Rabbit mAb	Cell Signalling	3267S	WB, IF	1:5000, 1:1000
TBA1A	Q71U36	Anti-α-Tubulin (DM1A)	Mouse mAb	Sigma	T9026	WB	1:5000
LC3B	Q9GZQ8	LC3B (D11) XP®	Rabbit mAb	Cell Signalling	3868S	WB	1:1000
P62	Q13501	Anti-p62 / SQSTM1 (C-term)	Guinea Pig pAb	Progen	GP62-C	WB	1:1000
ERK1/2	P27361 / P28482	p44/42 MAPK (Erk1/2) (L34F12)	Mouse mAb	Cell Signalling	4696S	WB	1:2000
PERK	Q9NZJ5	Anti-PERK	Rabbit pAb	Abcam	ab65142	WB	1:1000
p-PERK	Q9NZJ5	Phosp-PERK [Thr980] (16F8)	Rabbit mAb	Cell Signalling	3179S	WB	1:1000
ATF4	P18848	CREB-2 Abody (B-3)	Mouse mAb	Santa Cruz	sc-390063	IF	1:500
Calreticulin	P27797	Anti-Calreticulin	Rabbit pAb	Abcam	ab2907	IF	1:1000
eIF2α	Q9BY44	Anti-EIF2S1/EIF2α	Mouse mAb	Abcam	ab5369	WB	1:1000

p-eIF2α	Q9BY44	Phosp-eIF2α [Ser51] (119A11)	Rabbit mAb	Cell Signalling	3597S	WB	1:1000
CHOP	P35638	CHOP (L63F7)	Mouse mAb	Cell Signalling	2895S	WB	1:1000
CHOP	P35638	GADD 153 Antibody (B-3)	Mouse mAb	Santa Cruz	sc-7351	IF	1:500
CD31	P16284	Anti-PECAM-1 (2H8)	Armenian Hamster mAb	Merck	MAB1398Z	IF	1:250
HIF1A	Q16665	Anti-HIF-1 alpha (EP1215Y)	Rabbit mAb	Abcam	ab51608	IF	1:250
PDGFRB	P09619	PDGFRB (G.290.3)	Mouse mAb	Thermo Fisher	MA5-15143	IF	1:250
LYVE1	Q9Y5Y7	Anti-LYVE1	Rabbit pAb	Abcam	ab14917	IF	1:250
NFκB (p65)	Q04206	Anti-NF-kB p65	Rabbit pAb	Abcam	ab16502	IF	1:1000
ITGA11	Q9UKX5	Human/Mouse Integrin alpha 11 Antibody	Mouse mAb	R&D sys	MAB4235	WB	1:500

Table S4. CAV1-targeting and luciferase expressing bicistronic lentiviral vectors: Cloning primer sequences, synthetic miRNA oligos and lentivirus diagrams. Related to materials & methods section: Lentiviral and retroviral vector generation. (A) List of primers used for cassette amplification. All primers include the corresponding restriction enzyme sites used for cloning on their 5' ends. (B) Chemically synthesized and PAGE purified oligos used to generate miR30-based hairpins. Flanking *XhoI* and *EcoRI* ready available sites are shown in lowercase. Non-targeting and *CAV1*-targeting sequences are marked in bold. (C) Promoter amplification and MCS generation primers (Phos: Phosphorylated 5'). Resulting lentiviral vectors: (D) pLVX-CMV-ChFP2A, (E) pLVX-CMV-ChFP2A-RE8luc, (F) pLVX-CMV-ChFP2A-Puro^R-miR30.scr, (G) pLVX-CMV-Puro^R-miR30.scr, (H) pLVX-MCS-ChFP2A-RE8luc-miR30.scr and (I) pLVX-ITGA11-ChFP2A-RE8luc-miR30.scr. Lentiviral backbone elements (LTR, RRE, cPPT, WPRE and Ψ) are shown in grey, colored boxes correspond to: CherryFP (fluorescent protein), RE8luc (luciferase), Puro^R (puromycin resistance) and miR5'-3' (microRNA flanking sequences). P2A self-cleaving peptide appears in white.

Table S4A. Primers used for lentivirus cassette amplification

Amplified Cassette	Sequence (5' - 3')	Designator
CMV-CherryFP-P2A	5'-ACATCGATGGGAGTTCCGCGTTACATAAC-3'	Forward (A1)
	5'-ACGCGTCCAGAGGTTGATTGTCGACG-3'	Reverse (A2)
PpyRE8 luciferase	5'-GCTTAATTAAGGAGGACGCCAAGAACATC-3'	Forward (L1)
	5'-TAGTTTAAACCTCAGATCTTGCCGCCCTTCTT-3'	Reverse (L2)
Puro^R-miR30.scr	5'-CCTTTAATTAAGGCCACCGAGTACAAGC-3'	Forward (M1)
	5'-CCAGACGCGTCCTAGGTAATACG-3'	Reverse (M2)
CMV-Puro^R-miR30.scr	5'-TACCGGTCATGGCCACCGAGTACAAGC-3'	Forward (M1.1)
	5'-CCAGACGCGTCCTAGGTAATACG-3'	Reverse (M2)
CherryFP-P2A	5'-TAATCGATATGGTGAGCAAGGGCGAGG-3'	Forward (B1)
	5'-TCTAGACCAGAGGTTGATTGTCGACG-3'	Reverse (B2)
miR30.scr backbone	5'-CCCGTTTAAACGTTTGTTTGAATGAGG-3'	Forward (MB1)
	5'-GCCACGCGTAGTGATTTAATTTATACC-3'	Reverse (MB2)

Table S4B. Non-targeting and *CAV1*-targeting synthetic miRNA oligos.

Target	Sequence (5' - 3')
Non-targeting (scr)	5'-tcgagAAGGTATATTGCTGTTGACAGTGAGCG**ATCTCGCTTGGGCGAGAGTAAG**TAGT GAAGCCACAGATGTA**CTTACTCTCGCCCAAGCGAGAG**TGCCTACTGCCTCGg-3'
	5'-aattcCGAGGCAGTAGGCACTCTCGCTTGGGCGAGAGTAAGTACATCTGTGGCTTCAC TACTTACTCTCGCCCAAGCGAGATCGCTCACTGTCAACAGCAATATACCTTc-3'
shCAV1.2	5'-tcgagAAGGTATATTGCTGTTGACAGTGAGCG**CGACGTGGTCAAGATTGACTTT**TAGT GAAGCCACAGATGTA**AAAGTCAATCTTGACCACGTCA**TGCCTACTGCCTCGg-3'
	5'-aattcCGAGGCAGTAGGCATGACGTGGTCAAGATTGACTTTTACATCTGTGGCTTCACT AAAAGTCAATCTTGACCACGTCGCGCTCACTGTCAACAGCAATATACCTTc-3'
shCAV1.3	5'-tcgagAAGGTATATTGCTGTTGACAGTGAGCG**CCCACCTTCACTGTGACGAAAT**TAGT GAAGCCACAGATGTA**ATTTCGTCACAGTGAAGGTGGT**TGCCTACTGCCTCGg-3'
	5'-aattcCGAGGCAGTAGGCAACCACCTTCACTGTGACGAAATTACATCTGTGGCTTCACT AATTTCGTCACAGTGAAGGTGGGCGCTCACTGTCAACAGCAATATACCTTc-3'

shCAV1.4 5'-tcgagAAGGTATATTGCTGTTGACAGTGAGCG**AGCATCAACTTGCAGAAAGAAA**TAGT
GAAGCCACAGATGTA**TTTCTTTCTGCAAGTTGATGCG**TGCCTACTGCCTCGg-3'

5'-aattcCGAGGCAGTAGGCAGGGCAGTTGTACCATGCATTAATACATCTGTGGCTTCAC
TATTAATGCATGGTACAACTGCCTCGCTCACTGTCAACAGCAATATACCTTc-3'

shCAV1.5 5'-tcgagAAGGTATATTGCTGTTGACAGTGAGCG**AGGCAGTTGTACCATGCATTAA**TAGT
GAAGCCACAGATGTA**TTAATGCATGGTACAACTGCCC**TGCCTACTGCCTCGg-3'

5'-aattcCGAGGCAGTAGGCACGCATCAACTTGCAGAAAGAAATACATCTGTGGCTTCAC
TATTTCTTTCTGCAAGTTGATGCTCGCTCACTGTCAACAGCAATATACCTTc-3'

Table S4C. Primers used for ITGA11 promoter amplification and MCS insertion

Amplified Cassette	**Sequence (5' - 3')**	**Designator**
-2123 +25 pITGA11	5'-TAACCGGTGGCACCTGTGAGGACGG-3'	Forward (I1)
	5'-TACATATGGCGGCACGGCGGCTG-3'	Reverse (I2)
MCS oligos		
MCS1	5'- [Phos]CGATACTAGTGGCGCGCCACCGGTCATATGAT-3'	
MCS2	5'- [Phos]CGATCATATGACCGGTGGCGCGCCACTAGTAT-3'	

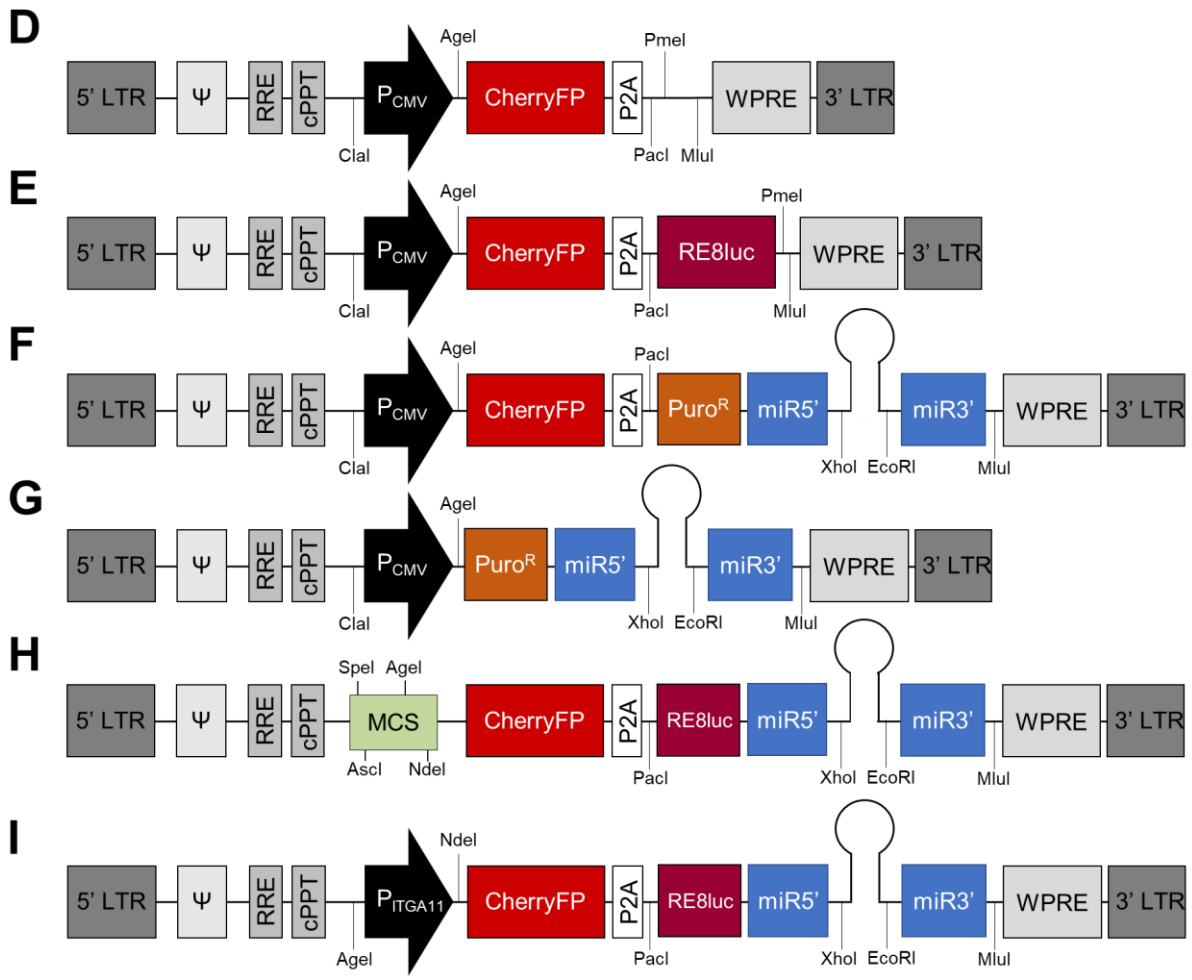

Table S5. RNASeq gene expression analysis data derived from xenografts removed 30 days post-implantation. Gene expression fold-change (FC) is represented as log_2FC and color coded from highest (+ values in red, upregulated in low stromal CAV1 xenografts) to lowest (- values in green, downregulated) values. Benjamini-Hochberg adjusted p-values for multiple comparisons (adj.P.Val).

ID	hgnc_symbol	logFC	adj.P.Val
ENSG00000173432	SAA1	6,45607	9,87E-24
ENSG00000262526		5,88833	0,0001134
ENSG00000156510	HKDC1	5,49874	4,09E-28
ENSG00000179046	TRIML2	5,27855	2,61E-32
ENSG00000268902	CSAG2	5,21808	3,93E-11
ENSG00000215218	UBE2QL1	5,21187	1,66E-14
ENSG00000164438	TLX3	4,92469	9,69E-24
ENSG00000176887	SOX11	4,90901	1,05E-28
ENSG00000160233	LRRC3	4,81849	1,07E-19
ENSG00000163995	ABLIM2	4,71884	2,89E-18
ENSG00000215612	HMX1	4,67313	7,34E-23
ENSG00000142185	TRPM2	4,66139	2,19E-19
ENSG00000147381	MAGEA4	4,64947	1,42E-09
ENSG00000147202	DIAPH2	4,64795	4,59E-20
ENSG00000183570	PCBP3	4,63434	2,93E-20
ENSG00000165810	BTNL9	4,63172	3,57E-14
ENSG00000189190	ZNF600	4,61218	1,48E-13
ENSG00000182195	LDOC1	4,57056	7,69E-12
ENSG00000170837	GPR27	4,56905	4,50E-18
ENSG00000198538	ZNF28	4,5632	4,22E-12
ENSG00000148082	SHC3	4,5333	4,28E-14
ENSG00000175928	LRRN1	4,51483	2,64E-14
ENSG00000148803	FUOM	4,48079	1,58E-22
ENSG00000087510	TFAP2C	4,48008	1,18E-11
ENSG00000162493	PDPN	4,43357	5,02E-14
ENSG00000082397	EPB41L3	4,43113	1,42E-47
ENSG00000229967		4,429	1,69E-20
ENSG00000235961	PNMA6C	4,41333	5,19E-16
ENSG00000163395	IGFN1	4,40006	2,96E-67
ENSG00000197951	ZNF71	4,39976	1,07E-16
ENSG00000074211	PPP2R2C	4,39297	8,97E-39
ENSG00000169436	COL22A1	4,3434	5,58E-18
ENSG00000151640	DPYSL4	4,30879	2,62E-22
ENSG00000170430	MGMT	4,30464	7,26E-23
ENSG00000170571	EMB	4,29395	6,96E-20
ENSG00000151892	GFRA1	4,29034	3,48E-14
ENSG00000197444	OGDHL	4,28886	7,52E-29
ENSG00000182636	NDN	4,27627	1,26E-16
ENSG00000186310	NAP1L3	4,22919	1,54E-14
ENSG00000102109	PCSK1N	4,2273	2,19E-19
ENSG00000145911	N4BP3	4,21273	1,80E-35
ENSG00000224945		4,15583	1,30E-12
ENSG00000213886	UBD	4,15394	1,69E-10
ENSG00000180730	SHISA2	4,14703	2,40E-19
ENSG00000132182	NUP210	4,13071	4,99E-49
ENSG00000121413	ZSCAN18	4,12387	2,08E-20
ENSG00000124260	MAGEA10	4,11305	5,09E-19
ENSG00000163638	ADAMTS9	4,09653	8,20E-14
ENSG00000122133	PAEP	4,06481	7,11E-13
ENSG00000130558	OLFM1	4,0455	5,78E-13
ENSG00000007264	MATK	4,04251	2,92E-15
ENSG00000196632	WNK3	4,02609	7,92E-12
ENSG00000124102	PI3	4,02352	3,20E-16
ENSG00000178573	MAF	4,00245	7,00E-11
ENSG00000105717	PBX4	3,99836	1,30E-09
ENSG00000070159	PTPN3	3,9815	1,18E-16
ENSG00000173110	HSPA6	3,98013	1,76E-41
ENSG00000166391	MOGAT2	3,97823	2,72E-12
ENSG00000131773	KHDRBS3	3,96972	4,82E-16
ENSG00000136856	SLC2A8	3,96295	4,01E-10
ENSG00000259075	POC1B-GALNT4	3,94572	0,0200657

ID	hgnc_symbol	logFC	adj.P.Val
ENSG00000259075	POC1B-GALNT4	3,94572	2,01E-02
ENSG00000136244	IL6	3,89983	1,29E-15
ENSG00000180543	TSPYL5	3,89127	2,09E-16
ENSG00000180190	TDRP	3,88395	4,62E-16
ENSG00000008517	IL32	3,88117	2,35E-52
ENSG00000169429	CXCL8	3,87617	2,89E-18
ENSG00000135116	HRK	3,86492	3,03E-20
ENSG00000268916		3,86438	2,51E-11
ENSG00000258498	DIO3OS	3,85396	2,22E-13
ENSG00000099284	H2AFY2	3,84828	2,09E-24
ENSG00000122378	FAM213A	3,8328	4,38E-30
ENSG00000066735	KIF26A	3,82995	2,94E-14
ENSG00000125730	C3	3,82744	4,72E-31
ENSG00000189223	PAX8-AS1	3,79014	2,68E-29
ENSG00000177614	PGBD5	3,765	4,31E-14
ENSG00000185101	ANO9	3,75098	3,09E-23
ENSG00000160183	TMPRSS3	3,73956	3,85E-08
ENSG00000196387	ZNF140	3,73317	2,67E-09
ENSG00000172247	C1QTNF4	3,73315	2,21E-36
ENSG00000080007	DDX43	3,70179	7,51E-16
ENSG00000178445	GLDC	3,69278	1,94E-18
ENSG00000169418	NPR1	3,68105	3,88E-20
ENSG00000204604	ZNF468	3,6788	2,25E-09
ENSG00000184160	ADRA2C	3,66878	4,79E-19
ENSG00000090339	ICAM1	3,65295	1,12E-50
ENSG00000204179	PTPN20A	3,64801	6,76E-09
ENSG00000185274	WBSCR17	3,64559	9,92E-11
ENSG00000165300	SLITRK5	3,64371	5,49E-18
ENSG00000077522	ACTN2	3,64004	7,07E-16
ENSG00000101210	EEF1A2	3,61976	1,28E-27
ENSG00000126970	ZC4H2	3,59972	7,01E-16
ENSG00000130294	KIF1A	3,59937	1,96E-18
ENSG00000271503	CCL5	3,59868	1,77E-15
ENSG00000162738	VANGL2	3,5978	6,20E-20
ENSG00000164742	ADCY1	3,59201	5,43E-15
ENSG00000163121	NEURL3	3,58942	6,64E-16
ENSG00000165238	WNK2	3,58887	9,30E-12
ENSG00000181143	AP1M1	3,58426	3,38E-14
ENSG00000203326	ZNF525	3,57052	2,71E-10
ENSG00000120149	MSX2	3,5535	3,88E-08
ENSG00000147180	ZNF711	3,54912	2,53E-14
ENSG00000276547	PCDHGB5	3,53333	1,30E-09
ENSG00000130540	SULT4A1	3,52892	1,94E-11
ENSG00000180921	FAM83H	3,49797	5,97E-19
ENSG00000198203	SULT1C2	3,49004	7,39E-21
ENSG00000158106	RHPN1	3,48834	4,85E-24
ENSG00000196458	ZNF605	3,48556	8,52E-10
ENSG00000181218	HIST3H2A	3,45694	6,26E-08
ENSG00000196867	ZFP28	3,44918	9,47E-09
ENSG00000105357	MYH14	3,44476	5,05E-11
ENSG00000176595	KBTBD11	3,42226	1,25E-13
ENSG00000187957	DNER	3,41543	5,97E-10
ENSG00000272620	AFAP1-AS1	3,3905	3,36E-19
ENSG00000154118	JPH3	3,38767	1,48E-12
ENSG00000002933	TMEM176A	3,36068	8,12E-09
ENSG00000124107	SLPI	3,3442	1,52E-12
ENSG00000129354	AP1M2	3,33094	4,26E-19
ENSG00000182463	TSHZ2	3,31517	1,22E-07
ENSG00000121316	PLBD1	3,30886	2,65E-23
ENSG00000102854	MSLN	3,29951	2,17E-14
ENSG00000196730	DAPK1	3,28802	4,45E-09

ID	hgnc_symbol	logFC	adj.P.Val
ENSG00000101187	SLCO4A1	2,5251	1,11E-50
ENSG00000125618	PAX8	2,51877	7,31E-13
ENSG00000177706	FAM20C	2,50785	5,24E-25
ENSG00000233532	LINC00460	2,50118	3,29E-07
ENSG00000154655	L3MBTL4	2,48762	0,0001961
ENSG00000189423	USP32P3	2,47984	1,74E-06
ENSG00000182240	BACE2	2,47176	2,46E-18
ENSG00000261771	DYX1C1-CCPG1	2,47043	0,0185601
ENSG00000160712	IL6R	2,47005	4,90E-12
ENSG00000163520	FBLN2	2,46146	1,10E-21
ENSG00000185291	IL3RA	2,45713	0,0010618
ENSG00000139910	NOVA1	2,45459	1,82E-09
ENSG00000184258	CDR1	2,4513	0,0001209
ENSG00000188385	JAKMIP3	2,45061	2,67E-06
ENSG00000011201	KAL1	2,44404	6,66E-05
ENSG00000167972	ABCA3	2,44018	2,19E-17
ENSG00000187479	C11orf96	2,42524	3,17E-05
ENSG00000163347	CLDN1	2,41216	5,45E-11
ENSG00000182326	C1S	2,40369	3,14E-39
ENSG00000249751	ECSCR	2,37343	2,28E-09
ENSG00000205927	OLIG2	2,36732	0,0005231
ENSG00000101017	CD40	2,35429	8,02E-06
ENSG00000236081	ELFN1-AS1	2,35173	0,0002007
ENSG00000245680	ZNF585B	2,35089	2,32E-05
ENSG00000075618	FSCN1	2,32658	1,72E-32
ENSG00000103037	SETD6	2,31409	2,28E-06
ENSG00000067606	PRKCZ	2,31325	7,65E-11
ENSG00000135549	PKIB	2,3101	5,62E-08
ENSG00000272884		2,30707	0,0001068
ENSG00000134769	DTNA	2,28899	4,95E-10
ENSG00000248871	TNFSF12-TNFSF	2,28239	0,0085105
ENSG00000159403	C1R	2,28218	1,58E-43
ENSG00000163734	CXCL3	2,27009	2,07E-05
ENSG00000273590		2,24702	1,61E-08
ENSG00000205336	GPR56	2,22789	1,59E-06
ENSG00000137726	FXYD6	2,21797	3,43E-07
ENSG00000189337	KAZN	2,21042	7,82E-16
ENSG00000183092	BEGAIN	2,2081	2,15E-12
ENSG00000149582	TMEM25	2,20042	7,16E-06
ENSG00000118503	TNFAIP3	2,18466	4,31E-29
ENSG00000161958	FGF11	2,18416	1,23E-17
ENSG00000166432	ZMAT1	2,18303	9,80E-05
ENSG00000104419	NDRG1	2,17977	6,11E-38
ENSG00000174669	SLC29A2	2,17851	3,86E-15
ENSG00000275216		2,17824	1,19E-11
ENSG00000151883	PARP8	2,17801	2,48E-07
ENSG00000134326	CMPK2	2,17512	1,06E-17
ENSG00000108691	CCL2	2,17391	0,0008947
ENSG00000135127	CCDC64	2,1488	1,15E-05
ENSG00000250899		2,13849	1,92E-08
ENSG00000172183	ISG20	2,13526	3,28E-15
ENSG00000102032	RENBP	2,13408	3,47E-21
ENSG00000198879	SFMBT2	2,13197	0,0002431
ENSG00000140993	TIGD7	2,13196	0,0001453
ENSG00000273259	GAA	2,12397	0,0118809
ENSG00000134321	RSAD2	2,1142	6,43E-13
ENSG00000225138		2,11221	7,75E-27
ENSG00000132470	ITGB4	2,09575	2,04E-22
ENSG00000226051	ZNF503-AS1	2,09394	1,19E-05
ENSG00000120784	ZFP30	2,08628	7,67E-05
ENSG00000025708	TYMP	2,06962	1,20E-19

ID	hgnc_symbol	logFC	adj.P.Val
ENSG00000154639	CXADR	2,0688	1,81E-07
ENSG00000170458	CD14	2,06829	0,0003864
ENSG00000214110	LDHAP4	2,04723	6,66E-05
ENSG00000135083	CCNJL	2,03135	1,22E-05
ENSG00000196781	TLE1	2,02634	3,37E-16
ENSG00000163131	CTSS	2,01203	2,73E-11
ENSG00000198093	ZNF649	2,00322	0,0052294
ENSG00000184985	SORCS2	1,99174	7,63E-11
ENSG00000174990	CA5A	1,99168	5,01E-06
ENSG00000197905	TEAD4	1,98755	1,12E-17
ENSG00000105963	ADAP1	1,98246	0,000192
ENSG00000152977	ZIC1	1,98173	1,31E-06
ENSG00000196967	ZNF585A	1,97959	0,0021731
ENSG00000135119	RNFT2	1,97841	5,89E-09
ENSG00000007516	BAIAP3	1,97298	0,0005208
ENSG00000041353	RAB27B	1,97266	8,27E-06
ENSG00000131127	ZNF141	1,97225	0,0001481
ENSG00000261971		1,96774	3,88E-08
ENSG00000104177	MYEF2	1,96507	6,18E-13
ENSG00000180573	HIST1H2AC	1,94782	1,01E-15
ENSG00000205403	CFI	1,92885	0,0006401
ENSG00000103485	QPRT	1,92682	8,68E-15
ENSG00000185818	NAT8L	1,92228	9,62E-16
ENSG00000223414	LINC00473	1,92154	5,30E-05
ENSG00000260428	SCXB	1,91711	7,74E-08
ENSG00000074181	NOTCH3	1,9138	4,67E-42
ENSG00000057294	PKP2	1,91324	0,0004638
ENSG00000178726	THBD	1,90624	0,0005497
ENSG00000234284	ZNF879	1,90414	7,29E-06
ENSG00000129521	EGLN3	1,88955	9,61E-08
ENSG00000058085	LAMC2	1,87808	0,0001902
ENSG00000150782	IL18	1,87653	8,39E-06
ENSG00000139629	GALNT6	1,86708	2,10E-05
ENSG00000006118	TMEM132A	1,8665	8,43E-39
ENSG00000092969	TGFB2	1,86084	2,08E-20
ENSG00000131650	KREMEN2	1,85951	8,02E-06
ENSG00000021645	NRXN3	1,84335	0,00261
ENSG00000159167	STC1	1,8242	5,75E-05
ENSG00000148655	C10orf11	1,81448	2,11E-06
ENSG00000271781		1,81081	0,002449
ENSG00000272405		1,80968	0,0002899
ENSG00000103381	CPPED1	1,79918	1,37E-05
ENSG00000136944	LMX1B	1,79561	0,0002691
ENSG00000054356	PTPRN	1,79428	1,48E-12
ENSG00000113645	WWC1	1,78473	1,01E-22
ENSG00000235897	TM4SF19-AS1	1,77388	0,0008195
ENSG00000111674	ENO2	1,77218	9,09E-45
ENSG00000106070	GRB10	1,77144	3,61E-11
ENSG00000213996	TM6SF2	1,76855	0,005321
ENSG00000152137	HSPB8	1,76411	6,15E-09
ENSG00000228203	RNF144A-AS1	1,76171	0,0016197
ENSG00000066248	NGEF	1,76073	0,0002129
ENSG00000160781	PAQR6	1,74684	6,66E-05
ENSG00000105696	TMEM59L	1,73742	1,05E-06
ENSG00000125538	IL1B	1,73632	0,0087495
ENSG00000077238	IL4R	1,73377	6,09E-13
ENSG00000007237	GAS7	1,72584	1,91E-08
ENSG00000064042	LIMCH1	1,71832	4,70E-29
ENSG00000084636	COL16A1	1,7166	2,21E-22
ENSG00000115457	IGFBP2	1,70963	4,63E-05
ENSG00000130762	ARHGEF16	1,69384	0,0002014

Table S5. RNASeq gene expression analysis data derived from xenografts removed 30 days post-implantation. Gene expression fold-change (FC) is represented as log_2FC and color coded from highest (+ values in red, upregulated in low stromal CAV1 xenografts) to lowest (- values in green, downregulated) values. Benjamini-Hochberg adjusted p-values for multiple comparisons (adj.P.Val).

ID	hgnc_symbol	logFC	adj.P.Val
ENSG00000130762	ARHGEF16	1,69384	0,0002014
ENSG00000197565	COL4A6	1,6927	0,0125043
ENSG00000105499	PLA2G4C	1,6876	4,79E-06
ENSG00000074370	ATP2A3	1,68645	0,0052668
ENSG00000188818	ZDHHC11	1,67495	1,99E-05
ENSG00000162591	MEGF6	1,6742	8,98E-08
ENSG00000089820	ARHGAP4	1,67069	2,55E-15
ENSG00000121753	BAI2	1,66932	4,50E-14
ENSG00000094963	FMO2	1,65174	0,0006552
ENSG00000099998	GGT5	1,64671	0,00844
ENSG00000049249	TNFRSF9	1,64637	1,93E-07
ENSG00000161551	ZNF577	1,6445	0,0135396
ENSG00000136826	KLF4	1,6419	3,12E-12
ENSG00000184545	DUSP8	1,64022	2,96E-08
ENSG00000022267	FHL1	1,63878	8,14E-13
ENSG00000162086	ZNF75A	1,6386	0,0013452
ENSG00000107968	MAP3K8	1,63675	2,42E-05
ENSG00000143816	WNT9A	1,62305	0,004985
ENSG00000145623	OSMR	1,62255	2,76E-21
ENSG00000204682	CASC10	1,62136	0,0039288
ENSG00000162407	PPAP2B	1,59773	6,12E-08
ENSG00000130600	H19	1,59495	1,20E-23
ENSG00000198157	HMGN5	1,58704	2,11E-05
ENSG00000168398	BDKRB2	1,58376	1,45E-07
ENSG00000135063	FAM189A2	1,56722	0,0054252
ENSG00000115267	IFIH1	1,56362	1,29E-17
ENSG00000177283	FZD8	1,56208	0,0002546
ENSG00000196074	SYCP2	1,56036	0,0044222
ENSG00000154898	CCDC144CP	1,55871	0,0335259
ENSG00000102755	FLT1	1,54905	0,0114907
ENSG00000142408	CACNG8	1,5447	0,0003426
ENSG00000162595	DIRAS3	1,54425	0,0014975
ENSG00000161133	USP41	1,53908	0,0080376
ENSG00000197943	PLCG2	1,5318	2,48E-05
ENSG00000104856	RELB	1,53045	1,50E-19
ENSG00000131459	GFPT2	1,52848	1,88E-13
ENSG00000203883	SOX18	1,52826	0,0065656
ENSG00000163814	CDCP1	1,52742	3,26E-07
ENSG00000136943	CTSV	1,52428	0,0020089
ENSG00000173156	RHOD	1,51798	5,32E-07
ENSG00000233327	USP32P2	1,50837	0,00126
ENSG00000100031	GGT1	1,50259	1,94E-08
ENSG00000154358	OBSCN	1,49644	9,44E-17
ENSG00000197599	CCDC154	1,49345	0,0224408
ENSG00000174939	ASPHD1	1,49066	5,02E-10
ENSG00000130822	PNCK	1,48529	0,0230133
ENSG00000176463	SLCO3A1	1,48418	2,27E-06
ENSG00000139370	SLC15A4	1,47665	7,02E-08
ENSG00000100167	03-sep	1,47647	1,17E-05
ENSG00000112902	SEMA5A	1,47213	3,38E-08
ENSG00000135480	KRT7	1,47116	0,0037628
ENSG00000157766	ACAN	1,46912	0,0027581
ENSG00000137642	SORL1	1,46681	0,0168637
ENSG00000138646	HERC5	1,46172	5,24E-15
ENSG00000147799	ARHGAP39	1,46104	5,82E-09
ENSG00000073060	SCARB1	1,45864	4,07E-16
ENSG00000140479	PCSK6	1,45074	0,0002646
ENSG00000188290	HES4	1,44842	2,19E-19
ENSG00000122863	CHST3	1,44683	5,73E-12
ENSG00000198346	ZNF813	1,44581	0,0082429

ID	hgnc_symbol	logFC	adj.P.Val
ENSG00000146054	TRIM7	1,44578	5,14E-06
ENSG00000136048	DRAM1	1,43703	3,94E-11
ENSG00000261373	VPS9D1-AS1	1,42906	0,0038201
ENSG00000173918	C1QTNF1	1,42584	0,0062235
ENSG00000153233	PTPRR	1,4248	0,0085996
ENSG00000197472	ZNF695	1,42106	0,0049257
ENSG00000171045		1,42067	1,23E-08
ENSG00000163220	S100A9	1,41975	0,0115374
ENSG00000120820	GLT8D2	1,41688	0,0023186
ENSG00000109625	CPZ	1,41686	6,61E-07
ENSG00000165507	C10orf10	1,41554	3,93E-05
ENSG00000162849	KIF26B	1,40994	0,0073296
ENSG00000136295	TTYH3	1,40716	4,51E-23
ENSG00000159753	RLTPR	1,40328	0,033833
ENSG00000119922	IFIT2	1,40135	6,35E-20
ENSG00000240694	PNMA2	1,40101	1,58E-11
ENSG00000133424	LARGE	1,40088	0,0258712
ENSG00000147852	VLDLR	1,40054	1,73E-06
ENSG00000268083		1,3994	0,0267428
ENSG00000223802	CERS1	1,39801	0,0022175
ENSG00000069431	ABCC9	1,3951	2,52E-07
ENSG00000079215	SLC1A3	1,39503	3,28E-05
ENSG00000164181	ELOVL7	1,39234	0,0247219
ENSG00000196557	CACNA1H	1,39183	0,0142252
ENSG00000272031	ANKRD34A	1,38928	0,0025859
ENSG00000187764	SEMA4D	1,38477	0,0005562
ENSG00000228594	C1orf233	1,37814	0,0146482
ENSG00000117013	KCNQ4	1,37495	0,0153828
ENSG00000234449		1,3737	3,88E-07
ENSG00000221890	NPTXR	1,37194	0,0007539
ENSG00000204519	ZNF551	1,3719	0,0031574
ENSG00000247228		1,37001	0,0189923
ENSG00000171224	C10orf35	1,36187	0,0003566
ENSG00000115648	MLPH	1,36174	0,0209151
ENSG00000184489	PTP4A3	1,36161	6,57E-07
ENSG00000106804	C5	1,35842	0,008441
ENSG00000065320	NTN1	1,34907	0,0001134
ENSG00000164342	TLR3	1,34641	0,0111929
ENSG00000273151		1,33876	0,001034
ENSG00000204282	TNRC6C-AS1	1,33543	0,0019189
ENSG00000151067	CACNA1C	1,33428	0,0013259
ENSG00000159733	ZFYVE28	1,32496	5,38E-06
ENSG00000116016	EPAS1	1,32451	3,03E-20
ENSG00000081803	CADPS2	1,3242	0,00407
ENSG00000168685	IL7R	1,32155	3,24E-14
ENSG00000175471	MCTP1	1,3195	0,0225967
ENSG00000178814	OPLAH	1,31786	5,45E-11
ENSG00000148344	PTGES	1,31266	0,0012294
ENSG00000244291	C7orf13	1,30918	0,0022041
ENSG00000139117	CPNE8	1,30883	0,0001082
ENSG00000107719	PALD1	1,30864	0,0015712
ENSG00000166165	CKB	1,30641	1,39E-06
ENSG00000253846	PCDHGA10	1,30564	0,0465621
ENSG00000133687	TMTC1	1,29963	8,75E-05
ENSG00000181790	BAI1	1,29719	0,0191627
ENSG00000179698	KIAA1875	1,29538	4,61E-05
ENSG00000134070	IRAK2	1,2825	8,06E-08
ENSG00000168961	LGALS9	1,28159	0,0169437
ENSG00000158258	CLSTN2	1,27749	0,0445029
ENSG00000064547	LPAR2	1,27691	0,0001139

ID	hgnc_symbol	logFC	adj.P.Val
ENSG00000142303	ADAMTS10	1,27581	0,0042446
ENSG00000099812	MISP	1,27049	0,0294167
ENSG00000141524	TMC6	1,26933	1,86E-10
ENSG00000011105	TSPAN9	1,26848	3,54E-13
ENSG00000260077		1,26503	0,0423128
ENSG00000177989	ODF3B	1,26458	1,04E-05
ENSG00000177570	SAMD12	1,26183	0,0303488
ENSG00000126602	TRAP1	1,25615	7,28E-13
ENSG00000111331	OAS3	1,25128	1,80E-20
ENSG00000138772	ANXA3	1,25017	9,06E-06
ENSG00000188002		1,25	0,0001792
ENSG00000136235	GPNMB	1,24735	1,56E-06
ENSG00000181444	ZNF467	1,24626	0,0002993
ENSG00000087253	LPCAT2	1,24615	0,0382874
ENSG00000077150	NFKB2	1,24591	2,66E-21
ENSG00000169085	C8orf46	1,244	1,15E-05
ENSG00000072071	LPHN1	1,23772	2,36E-08
ENSG00000229644	NAMPTL	1,23614	1,04E-07
ENSG00000107281	NPDC1	1,23552	5,85E-08
ENSG00000197635	DPP4	1,23529	0,0044652
ENSG00000115461	IGFBP5	1,23516	0,0160575
ENSG00000198517	MAFK	1,23345	8,83E-22
ENSG00000147813	NAPRT1	1,22765	1,01E-11
ENSG00000103942	HOMER2	1,22519	0,0150194
ENSG00000056558	TRAF1	1,22156	5,03E-06
ENSG00000172164	SNTB1	1,21733	0,0159874
ENSG00000187955	COL14A1	1,21192	0,0069929
ENSG00000064225	ST3GAL6	1,21094	0,0005046
ENSG00000268903		1,2105	2,75E-05
ENSG00000090530	LEPREL1	1,20996	0,0288424
ENSG00000101493	ZNF516	1,20605	0,0082611
ENSG00000120306	CYSTM1	1,20483	4,16E-05
ENSG00000105464	GRIN2D	1,20472	1,42E-07
ENSG00000119508	NR4A3	1,20154	0,0336943
ENSG00000142494	SLC47A1	1,20093	0,0093421
ENSG00000230257	NFE4	1,20069	3,72E-07
ENSG00000069424	KCNAB2	1,20014	8,36E-10
ENSG00000120129	DUSP1	1,19942	4,46E-19
ENSG00000173227	SYT12	1,19524	0,0027181
ENSG00000173193	PARP14	1,19323	5,26E-19
ENSG00000072832	CRMP1	1,18997	8,52E-10
ENSG00000143452	HORMAD1	1,18896	7,27E-05
ENSG00000272419		1,18887	4,23E-05
ENSG00000147804	SLC39A4	1,18545	4,16E-08
ENSG00000167767	KRT80	1,18306	7,36E-10
ENSG00000164136	IL15	1,18216	0,0006196
ENSG00000183098	GPC6	1,17746	1,63E-05
ENSG00000008513	ST3GAL1	1,17559	1,98E-09
ENSG00000196372	ASB13	1,16842	2,36E-05
ENSG00000048052	HDAC9	1,16725	0,0009654
ENSG00000272016		1,16571	4,77E-05
ENSG00000178531	CTXN1	1,16498	0,0224408
ENSG00000105255	FSD1	1,1649	0,0001725
ENSG00000008394	MGST1	1,16214	2,77E-11
ENSG00000036672	USP2	1,15773	0,0421219
ENSG00000270194		1,15661	0,0496256
ENSG00000146966	DENND2A	1,15287	8,41E-09
ENSG00000158186	MRAS	1,15282	2,79E-05
ENSG00000116985	BMP8B	1,1523	0,0007075
ENSG00000160161	CILP2	1,14661	0,0105538

ID	hgnc_symbol	logFC	adj.P.Val
ENSG00000171223	JUNB	1,14633	1,13E-16
ENSG00000164171	ITGA2	1,14228	0,002143
ENSG00000205885	C1RL-AS1	1,14154	0,0027376
ENSG00000167785	ZNF558	1,14079	9,61E-06
ENSG00000184916	JAG2	1,13802	3,86E-05
ENSG00000107201	DDX58	1,13363	1,62E-09
ENSG00000171298	GAA	1,1336	6,65E-11
ENSG00000172059	KLF11	1,13298	2,24E-06
ENSG00000174672	BRSK2	1,13284	0,013597
ENSG00000146674	IGFBP3	1,13114	5,17E-07
ENSG00000171388	APLN	1,13007	0,0171553
ENSG00000257151	PWAR6	1,12754	0,0426996
ENSG00000105699	LSR	1,1272	1,99E-05
ENSG00000165124	SVEP1	1,126	0,0204603
ENSG00000137628	DDX60	1,12277	1,58E-08
ENSG00000243649	CFB	1,12228	5,11E-10
ENSG00000143382	ADAMTSL4	1,12046	1,10E-09
ENSG00000188283	ZNF383	1,11806	0,0232879
ENSG00000176490	DIRAS1	1,11726	0,0356417
ENSG00000151025	GPR158	1,10842	0,0083122
ENSG00000170365	SMAD1	1,10538	0,0008275
ENSG00000153885	KCTD15	1,1022	1,12E-06
ENSG00000165312	OTUD1	1,09542	1,79E-06
ENSG00000106266	SNX8	1,09457	8,60E-10
ENSG00000144749	LRIG1	1,08875	2,79E-10
ENSG00000277701		1,08484	0,0070857
ENSG00000136002	ARHGEF4	1,08166	0,0164324
ENSG00000139178	C1RL	1,07989	5,18E-10
ENSG00000138944	KIAA1644	1,07814	0,0316279
ENSG00000179832	MROH1	1,06946	3,06E-13
ENSG00000183486	MX2	1,06583	5,03E-06
ENSG00000198796	ALPK2	1,06505	0,001065
ENSG00000102996	MMP15	1,06476	0,019805
ENSG00000125945	ZNF436	1,06098	1,93E-09
ENSG00000113070	HBEGF	1,0572	0,0001068
ENSG00000119917	IFIT3	1,0542	3,19E-09
ENSG00000164638	SLC29A4	1,0526	0,0009089
ENSG00000176406	TTC9	1,04905	0,0180954
ENSG00000158286	RNF207	1,04775	1,42E-05
ENSG00000146592	CREB5	1,04571	0,000485
ENSG00000049769	PPP1R3F	1,03757	0,0175638
ENSG00000196208	GREB1	1,03488	0,0063342
ENSG00000124216	SNAI1	1,03226	0,0377657
ENSG00000196083	IL1RAP	1,03186	0,0004142
ENSG00000110328	GALNT18	1,03015	0,0088157
ENSG00000134363	FST	1,02873	3,15E-08
ENSG00000158769	F11R	1,02832	1,22E-05
ENSG00000121406	ZNF549	1,02286	0,0098482
ENSG00000172893	DHCR7	1,01802	2,30E-10
ENSG00000164855	TMEM184A	1,0177	0,0284719
ENSG00000188827	SLX4	1,01661	0,0002397
ENSG00000111266	DUSP16	1,01524	4,15E-07
ENSG00000149781	FERMT3	1,0094	1,82E-06
ENSG00000174705	SH3PXD2B	1,00937	5,05E-09
ENSG00000123342	MMP19	1,00858	0,0258078
ENSG00000103202	NME4	1,0079	6,17E-13
ENSG00000126603	GLIS2	1,00758	1,16E-06
ENSG00000156587	UBE2L6	1,00658	5,35E-10
ENSG00000161011	SQSTM1	1,0026	1,44E-15
ENSG00000236609	ZNF853	1,00087	0,0039271

Table S5. RNASeq gene expression analysis data derived from xenografts removed 30 days post-implantation. Gene expression fold-change (FC) is represented as log_2FC and color coded from highest (+ values in red, upregulated in low stromal CAV1 xenografts) to lowest (- values in green, downregulated) values. Benjamini-Hochberg adjusted p-values for multiple comparisons (adj.P.Val).

ID	hgnc_symbol	logFC	adj.P.Val
ENSG00000130962	PRRG1	0,99953	0,0048736
ENSG00000185338	SOCS1	0,99887	0,0327104
ENSG00000125965	GDF5	0,99599	0,0134942
ENSG00000135049	AGTPBP1	0,99105	8,45E-05
ENSG00000165655	ZNF503	0,9907	5,86E-08
ENSG00000140450	ARRDC4	0,98954	1,72E-06
ENSG00000213190	MLLT11	0,98617	7,20E-07
ENSG00000216490	IFI30	0,98554	2,48E-05
ENSG00000243509		0,98472	0,0023575
ENSG00000130702	LAMA5	0,97988	1,54E-15
ENSG00000013588	GPRC5A	0,97915	7,24E-13
ENSG00000146072	TNFRSF21	0,97841	1,33E-05
ENSG00000107338	SHB	0,97787	7,20E-07
ENSG00000231584	FAHD2CP	0,97768	0,0359098
ENSG00000204860	FAM201A	0,97583	0,0277855
ENSG00000111335	OAS2	0,97542	3,03E-05
ENSG00000099194	SCD	0,97422	2,90E-16
ENSG00000189067	LITAF	0,96663	3,70E-08
ENSG00000132819	RBM38	0,96618	2,30E-06
ENSG00000230606		0,96349	0,002185
ENSG00000166710	B2M	0,9631	2,35E-16
ENSG00000173511	OR7A10	0,96298	1,41E-11
ENSG00000080503	SMARCA2	0,96069	8,38E-07
ENSG00000166974	MAPRE2	0,96017	1,84E-05
ENSG00000197461	PDGFA	0,95886	4,83E-07
ENSG00000184979	USP18	0,95849	1,31E-06
ENSG00000168672	FAM84B	0,95843	0,0003651
ENSG00000163132	MSX1	0,95615	1,39E-06
ENSG00000182118	FAM89A	0,95597	0,0098538
ENSG00000170873	MTSS1	0,95488	0,0263428
ENSG00000168404	MLKL	0,94464	0,0010544
ENSG00000110446	SLC15A3	0,94394	0,0037111
ENSG00000174938	SEZ6L2	0,94268	1,66E-09
ENSG00000134824	FADS2	0,94023	1,39E-12
ENSG00000234745	HLA-B	0,94009	1,27E-16
ENSG00000137959	IFI44L	0,93725	9,21E-08
ENSG00000258947		0,93724	1,08E-11
ENSG00000277150	F8A3	0,93577	0,000123
ENSG00000171992	SYNPO	0,93434	3,93E-05
ENSG00000132718	SYT11	0,93111	0,0038129
ENSG00000185133	INPP5J	0,93092	0,0462389
ENSG00000138642	HERC6	0,93078	5,42E-06
ENSG00000185745	IFIT1	0,92768	5,38E-06
ENSG00000001617	SEMA3F	0,92691	0,0066295
ENSG00000205903	ZNF316	0,92634	2,58E-12
ENSG00000146083	RNF44	0,92522	5,90E-08
ENSG00000112096	SOD2	0,92298	2,88E-15
ENSG00000136999	NOV	0,92101	0,0027724
ENSG00000161013	MGAT4B	0,91405	2,77E-11
ENSG00000166923	GREM1	0,91375	1,18E-08
ENSG00000146574	CCZ1B	0,91239	6,69E-06
ENSG00000104998	IL27RA	0,91222	0,0263428
ENSG00000165175	MID1IP1	0,91143	1,28E-08
ENSG00000089127	OAS1	0,90739	0,000489
ENSG00000132359	RAP1GAP2	0,90507	8,07E-10
ENSG00000003137	CYP26B1	0,90461	0,0175638
ENSG00000154153	FAM134B	0,90408	0,0461299
ENSG00000117245	KIF17	0,90371	0,0496707
ENSG00000088899		0,90245	4,12E-05
ENSG00000188158	NHS	0,90126	1,59E-05

ID	hgnc_symbol	logFC	adj.P.Val
ENSG00000164535	DAGLB	0,90077	2,72E-08
ENSG00000135736	CCDC102A	0,90049	0,0026837
ENSG00000153815	CMIP	0,89724	1,05E-07
ENSG00000166532	RIMKLB	0,89645	2,18E-07
ENSG00000226742	HSBP1L1	0,89494	0,0175638
ENSG00000095739	BAMBI	0,89455	0,0039709
ENSG00000171813	PWWP2B	0,88703	4,79E-06
ENSG00000103148	NPRL3	0,88548	0,0004004
ENSG00000157601	MX1	0,88373	3,95E-05
ENSG00000171208	NETO2	0,88213	0,0012741
ENSG00000062282	DGAT2	0,87838	0,0065546
ENSG00000140853	NLRC5	0,87725	0,0001137
ENSG00000172216	CEBPB	0,87541	3,81E-09
ENSG00000113739	STC2	0,8753	9,20E-09
ENSG00000160190	SLC37A1	0,87449	0,0257222
ENSG00000164877	MICALL2	0,86288	9,20E-11
ENSG00000128274	A4GALT	0,86012	0,0098052
ENSG00000131378	RFTN1	0,85988	0,0107941
ENSG00000136247	ZDHHC4	0,85859	4,97E-08
ENSG00000105767	CADM4	0,85658	0,0021866
ENSG00000120594	PLXDC2	0,85582	0,0216067
ENSG00000170345	FOS	0,84716	0,0326933
ENSG00000206337	HCP5	0,84527	0,0067294
ENSG00000129757	CDKN1C	0,84155	9,74E-08
ENSG00000149177	PTPRJ	0,84146	6,56E-05
ENSG00000151692	RNF144A	0,83966	0,0001892
ENSG00000159399	HK2	0,83789	2,89E-10
ENSG00000165752	STK32C	0,83592	3,91E-05
ENSG00000103351	CLUAP1	0,8332	0,0013552
ENSG00000176485	PLA2G16	0,83211	0,0034904
ENSG00000101213	PTK6	0,82944	0,0266713
ENSG00000077585	GPR137B	0,82669	0,023286
ENSG00000185686	PRAME	0,82305	2,95E-08
ENSG00000051523	CYBA	0,82043	4,57E-08
ENSG00000134901	KDELC1	0,81952	3,46E-05
ENSG00000090661	CERS4	0,81772	0,0019601
ENSG00000204642	HLA-F	0,81761	3,20E-05
ENSG00000134516	DOCK2	0,8176	0,0302679
ENSG00000059122	FLYWCH1	0,8137	0,0001955
ENSG00000162772	ATF3	0,81271	1,17E-05
ENSG00000139182	CLSTN3	0,81175	1,00E-06
ENSG00000121310	ECHDC2	0,80833	2,66E-05
ENSG00000184254	ALDH1A3	0,80329	0,0042769
ENSG00000178338	ZNF354B	0,80312	0,0158556
ENSG00000138131	LOXL4	0,80212	0,0130218
ENSG00000006740	ARHGAP44	0,79763	0,0437269
ENSG00000250786	SNHG18	0,79744	0,0343591
ENSG00000046604	DSG2	0,79632	1,91E-06
ENSG00000107738	C10orf54	0,7948	0,0045864
ENSG00000125257	ABCC4	0,7921	0,0037501
ENSG00000214357	NEURL1B	0,79201	0,000175
ENSG00000109107	ALDOC	0,79107	0,0009638
ENSG00000143514	TP53BP2	0,78776	2,34E-08
ENSG00000100906	NFKBIA	0,78745	2,41E-09
ENSG00000156515	HK1	0,78639	4,48E-09
ENSG00000133627	ACTR3B	0,7863	0,0299378
ENSG00000187608	ISG15	0,78441	4,12E-05
ENSG00000102858	GPR84	0,78081	6,69E-05
ENSG00000118960	HS1BP3	0,77927	0,000175
ENSG00000196793	ZNF239	0,77909	0,0404514

ID	hgnc_symbol	logFC	adj.P.Val
ENSG00000196793	ZNF239	0,77909	0,0404514
ENSG00000144339	TMEFF2	0,77893	0,0424974
ENSG00000073578	SDHA	0,77782	3,73E-08
ENSG00000145476	CYP4V2	0,77019	0,0004363
ENSG00000100342	APOL1	0,76823	0,0001068
ENSG00000187098	MITF	0,75437	0,0124361
ENSG00000127415	IDUA	0,75349	0,0005072
ENSG00000146067	FAM193B	0,75321	1,09E-07
ENSG00000170525	PFKFB3	0,75095	4,59E-05
ENSG00000129925	TMEM8A	0,75067	9,57E-06
ENSG00000123240	OPTN	0,75024	8,71E-09
ENSG00000104549	SQLE	0,74922	3,51E-07
ENSG00000246705	H2AFJ	0,7476	2,87E-05
ENSG00000138166	DUSP5	0,74471	2,98E-05
ENSG00000242802	AP5Z1	0,74469	1,24E-07
ENSG00000184371	CSF1	0,74386	2,22E-06
ENSG00000106346	USP42	0,74256	0,001545
ENSG00000169131	ZNF354A	0,74238	0,0030361
ENSG00000130066	SAT1	0,74213	1,05E-06
ENSG00000197070	ARRDC1	0,74102	0,0013435
ENSG00000101255	TRIB3	0,73842	0,0002365
ENSG00000160326	SLC2A6	0,73676	0,0002275
ENSG00000125347	IRF1	0,73562	7,21E-05
ENSG00000168890	TMEM150A	0,73548	0,0342699
ENSG00000130193	THEM6	0,73404	0,0021907
ENSG00000173334	TRIB1	0,73387	0,0025981
ENSG00000135766	EGLN1	0,73296	3,76E-08
ENSG00000181381	DDX60L	0,72976	0,0026837
ENSG00000188191	PRKAR1B	0,72919	0,0253499
ENSG00000115380	EFEMP1	0,72828	0,0001057
ENSG00000072786	STK10	0,72622	1,09E-05
ENSG00000125354	06-sep	0,72279	0,0017904
ENSG00000140859	KIFC3	0,72242	8,89E-08
ENSG00000213853	EMP2	0,72162	0,0115531
ENSG00000204261	PSMB8-AS1	0,72002	0,0130258
ENSG00000185022	MAFF	0,71935	1,27E-05
ENSG00000075340	ADD2	0,71772	0,0405177
ENSG00000163568	AIM2	0,71755	0,0403852
ENSG00000145147	SLIT2	0,71612	8,96E-05
ENSG00000163840	DTX3L	0,71511	7,62E-07
ENSG00000197381	ADARB1	0,71443	6,20E-05
ENSG00000163874	ZC3H12A	0,71283	0,0005497
ENSG00000103742	IGDCC4	0,7107	0,0005285
ENSG00000154277	UCHL1	0,70732	0,0002578
ENSG00000206503	HLA-A	0,70552	2,99E-09
ENSG00000112972	HMGCS1	0,70303	1,33E-06
ENSG00000153395	LPCAT1	0,70262	0,0002133
ENSG00000261796	ISY1-RAB43	0,69938	0,0041087
ENSG00000069482	GAL	0,69902	0,0070288
ENSG00000130821	SLC6A8	0,69696	1,45E-07
ENSG00000171823	FBXL14	0,69502	0,0353392
ENSG00000206190	ATP10A	0,69468	0,0216067
ENSG00000163291	PAQR3	0,69427	0,0066622
ENSG00000151552	QDPR	0,69398	0,0015436
ENSG00000184992	BRI3BP	0,69278	0,0026879
ENSG00000090565	RAB11FIP3	0,69075	0,000151
ENSG00000163703	CRELD1	0,69053	0,0019984
ENSG00000181625	SLX1B	0,69036	0,0473806
ENSG00000158023	WDR66	0,68657	0,0385402
ENSG00000107130	NCS1	0,68374	1,41E-06

ID	hgnc_symbol	logFC	adj.P.Val
ENSG00000101680	LAMA1	0,68206	0,0065475
ENSG00000108771	DHX58	0,68006	0,0021752
ENSG00000132481	TRIM47	0,67798	5,22E-05
ENSG00000137767	SQRDL	0,67548	0,0295245
ENSG00000145901	TNIP1	0,67539	1,45E-07
ENSG00000137965	IFI44	0,67482	1,22E-05
ENSG00000172731	LRRC20	0,67291	0,0266941
ENSG00000122884	P4HA1	0,66975	1,42E-06
ENSG00000091622	PITPNM3	0,66678	0,048009
ENSG00000007384	RHBDF1	0,66671	3,25E-05
ENSG00000165806	CASP7	0,66398	0,0038201
ENSG00000164916	FOXK1	0,66323	5,09E-07
ENSG00000162104	ADCY9	0,66233	0,0230358
ENSG00000076706	MCAM	0,66224	0,0003211
ENSG00000263528	IKBKE	0,65817	0,0100538
ENSG00000119280	C1orf198	0,65618	4,38E-05
ENSG00000076944	ZNF14	0,65544	0,0004185
ENSG00000106012	IQCE	0,65213	0,0012294
ENSG00000148339	SLC25A25	0,65097	0,0019751
ENSG00000169826	CSGALNACT2	0,64924	0,0018246
ENSG00000224078	SNHG14	0,64854	0,0026616
ENSG00000169926	KLF13	0,64834	7,48E-05
ENSG00000113269	RNF130	0,64583	0,0002317
ENSG00000134780	DAGLA	0,64519	0,0172627
ENSG00000157827	FMNL2	0,64174	0,0021255
ENSG00000119771	KLHL29	0,64054	0,0122785
ENSG00000116729	WLS	0,63752	0,001052
ENSG00000121281	ADCY7	0,63682	0,0381815
ENSG00000113719	ERGIC1	0,63668	4,65E-05
ENSG00000160447	PKN3	0,6363	6,44E-05
ENSG00000070404	FSTL3	0,6356	3,07E-06
ENSG00000166833	NAV2	0,63452	0,0001087
ENSG00000277586	NEFL	0,63442	0,0314279
ENSG00000197355	UAP1L1	0,63398	1,13E-05
ENSG00000167766	ZNF83	0,63393	0,0074157
ENSG00000068971	PPP2R5B	0,63267	0,0001468
ENSG00000135899	SP110	0,63237	0,0068558
ENSG00000136240	KDELR2	0,62979	1,19E-06
ENSG00000198576	ARC	0,6293	0,0445381
ENSG00000185753	CXorf38	0,62729	0,0004941
ENSG00000130827	PLXNA3	0,62662	6,88E-06
ENSG00000141682	PMAIP1	0,6265	0,0004894
ENSG00000184232	OAF	0,6244	0,0078997
ENSG00000153066	TXNDC11	0,62289	0,0046242
ENSG00000178764	ZHX2	0,62205	0,0082272
ENSG00000170558	CDH2	0,62195	0,0026733
ENSG00000166825	ANPEP	0,62079	8,97E-05
ENSG00000184557	SOCS3	0,61822	0,0002432
ENSG00000132840	BHMT2	0,61607	0,0096665
ENSG00000175416	CLTB	0,61589	0,0006203
ENSG00000140443	IGF1R	0,61256	0,001421
ENSG00000167508	MVD	0,61185	0,0004638
ENSG00000078403	MLLT10	0,61167	0,0040473
ENSG00000186812	ZNF397	0,61053	0,0337048
ENSG00000168016	TRANK1	0,6097	0,0127703
ENSG00000002822	MAD1L1	0,60937	0,0001681
ENSG00000187243	MAGED4B	0,60901	8,02E-06
ENSG00000152582	SPEF2	0,60878	0,0330965
ENSG00000126709	IFI6	0,60831	0,0042578
ENSG00000167779	IGFBP6	0,60654	0,0005208

Table S5. RNASeq gene expression analysis data derived from xenografts removed 30 days post-implantation. Gene expression fold-change (FC) is represented as log_2FC and color coded from highest (+ values in red, upregulated in low stromal CAV1 xenografts) to lowest (- values in green, downregulated) values. Benjamini-Hochberg adjusted p-values for multiple comparisons (adj.P.Val).

ID	hgnc_symbol	logFC	adj.P.Val
ENSG00000136193	SCRN1	0,60589	3,20E-05
ENSG00000185842	DNAH14	0,6021	0,0341458
ENSG00000159110	IFNAR2	0,60204	0,0197215
ENSG00000086289	EPDR1	0,59423	0,0255569
ENSG00000089486	CDIP1	0,5937	0,0358412
ENSG00000139146	FAM60A	0,59237	0,0001134
ENSG00000185885	IFITM1	0,59103	0,0260345
ENSG00000103187	COTL1	0,58867	2,07E-05
ENSG00000102024	PLS3	0,5885	0,0001725
ENSG00000178685	PARP10	0,58742	4,20E-05
ENSG00000188549	C15orf52	0,58726	0,0006192
ENSG00000227671	MIR3916	0,58597	0,0098529
ENSG00000167994	RAB3IL1	0,58561	0,0338037
ENSG00000136238	RAC1	0,58307	3,48E-06
ENSG00000109790	KLHL5	0,58194	0,0172185
ENSG00000132635	PCED1A	0,58159	0,0001377
ENSG00000130787	HIP1R	0,58158	0,0085498
ENSG00000124006	OBSL1	0,57895	0,0002594
ENSG00000059378	PARP12	0,57838	7,04E-05
ENSG00000196562	SULF2	0,5779	0,0024946
ENSG00000138496	PARP9	0,57698	0,0009993
ENSG00000105939	ZC3HAV1	0,57644	5,23E-05
ENSG00000136854	STXBP1	0,57605	0,0053218
ENSG00000168394	TAP1	0,57563	2,47E-05
ENSG00000132109	TRIM21	0,57556	0,0164691
ENSG00000128739	SNRPN	0,57547	0,0002958
ENSG00000167632	TRAPPC9	0,57536	0,0047358
ENSG00000105835	NAMPT	0,57526	4,52E-06
ENSG00000143878	RHOB	0,57443	8,79E-06
ENSG00000103326	CAPN15	0,57334	0,0004638
ENSG00000185880	TRIM69	0,5731	0,0087495
ENSG00000011275	RNF216	0,57291	6,52E-05
ENSG00000146587	RBAK	0,57169	0,0046183
ENSG00000164631	ZNF12	0,56793	0,005648
ENSG00000145604	SKP2	0,56663	0,0003664
ENSG00000108797	CNTNAP1	0,56642	4,93E-05
ENSG00000186350	RXRA	0,56613	0,0001551
ENSG00000196204	RNF216P1	0,56591	0,0015927
ENSG00000145390	USP53	0,56544	0,0347206
ENSG00000105137	SYDE1	0,56385	0,0001504
ENSG00000130589	HELZ2	0,5607	0,0013347
ENSG00000157193	LRP8	0,56006	0,0354511
ENSG00000188070	C11orf95	0,55948	0,0025307
ENSG00000034053	APBA2	0,55641	0,0247257
ENSG00000164970	FAM219A	0,55545	0,0014611
ENSG00000122674	CCZ1	0,55373	8,89E-05
ENSG00000111057	KRT18	0,55257	2,93E-05
ENSG00000074527	NTN4	0,55246	0,0316279
ENSG00000130779	CLIP1	0,55232	0,0018437
ENSG00000163661	PTX3	0,55055	0,0193114
ENSG00000113240	CLK4	0,54906	0,025868
ENSG00000111684	LPCAT3	0,54799	0,0012488
ENSG00000151693	ASAP2	0,54574	0,0303488
ENSG00000179526	SHARPIN	0,54525	7,36E-05
ENSG00000134352	IL6ST	0,54341	0,0017117
ENSG00000125485	DDX31	0,54309	0,0022786
ENSG00000198753	PLXNB3	0,54253	0,0054252
ENSG00000186193	SAPCD2	0,54185	0,0142125
ENSG00000132510	KDM6B	0,54134	0,0002298
ENSG00000196776	CD47	0,541	0,0001442

ID	hgnc_symbol	logFC	adj.P.Val
ENSG00000167996	FTH1	0,54089	3,84E-06
ENSG00000104522	TSTA3	0,54061	0,0001019
ENSG00000143641	GALNT2	0,54004	9,86E-05
ENSG00000142949	PTPRF	0,53987	0,0013732
ENSG00000008256	CYTH3	0,5383	0,0012065
ENSG00000224389	C4B	0,53829	0,0251209
ENSG00000149485	FADS1	0,53672	0,0002177
ENSG00000165832	TRUB1	0,53564	0,0244014
ENSG00000159128	IFNGR2	0,53469	0,0001876
ENSG00000226210		0,53104	0,0266161
ENSG00000182871	COL18A1	0,53006	0,0015436
ENSG00000080819	CPOX	0,52855	0,0116264
ENSG00000119950	MXI1	0,52805	0,0311107
ENSG00000120549	KIAA1217	0,52713	0,0229645
ENSG00000063587	ZNF275	0,52549	0,0041659
ENSG00000213445	SIPA1	0,5253	0,0006441
ENSG00000178397	FAM220A	0,52523	0,0197235
ENSG00000111752	PHC1	0,5251	0,0003136
ENSG00000154640	BTG3	0,52496	0,0002133
ENSG00000113569	NUP155	0,52438	0,0018278
ENSG00000060138	YBX3	0,52361	7,36E-05
ENSG00000142733	MAP3K6	0,52009	0,0069389
ENSG00000185033	SEMA4B	0,51994	0,0013259
ENSG00000169398	PTK2	0,51958	0,0001082
ENSG00000184216	IRAK1	0,51771	0,0004185
ENSG00000116675	DNAJC6	0,51767	0,0462389
ENSG00000178719	GRINA	0,51728	4,78E-05
ENSG00000142089	IFITM3	0,51588	0,0021069
ENSG00000140044	JDP2	0,51369	0,0411488
ENSG00000039560	RAI14	0,51259	0,0002364
ENSG00000134897	BIVM	0,51239	0,0076454
ENSG00000132530	XAF1	0,51233	0,0253804
ENSG00000275993		0,51157	0,0011004
ENSG00000159674	SPON2	0,51113	0,0002673
ENSG00000162522	KIAA1522	0,50918	0,0146404
ENSG00000166123	GPT2	0,50702	0,0145212
ENSG00000158470	B4GALT5	0,50585	0,0031266
ENSG00000128335	APOL2	0,50424	0,0066703
ENSG00000130640	TUBGCP2	0,50397	0,0001744
ENSG00000025039	RRAGD	0,50347	0,0341941
ENSG00000118200	CAMSAP2	0,50131	0,0222035
ENSG00000162073	PAQR4	0,50058	0,0344294
ENSG00000171552	BCL2L1	0,49985	0,0005726
ENSG00000118900	UBN1	0,49914	0,0095808
ENSG00000185187	SIGIRR	0,49909	0,0285822
ENSG00000197226	TBC1D9B	0,49855	0,0015139
ENSG00000050748	MAPK9	0,49804	0,0043214
ENSG00000105270	CLIP3	0,49745	0,0048907
ENSG00000197603	C5orf42	0,49745	0,0369759
ENSG00000068079	IFI35	0,49655	0,0336943
ENSG00000157181	C1orf27	0,49519	0,0130543
ENSG00000204264	PSMB8	0,49475	0,0008211
ENSG00000198355	PIM3	0,4941	0,001383
ENSG00000168056	LTBP3	0,49409	0,0005208
ENSG00000102572	STK24	0,4938	0,0004249
ENSG00000064932	SBNO2	0,49362	0,0006722
ENSG00000105339	DENND3	0,49259	0,0384953
ENSG00000205726	ITSN1	0,49215	0,0078376
ENSG00000175130	MARCKSL1	0,49174	0,0006204
ENSG00000102178	UBL4A	0,49133	0,0038201

ID	hgnc_symbol	logFC	adj.P.Val
ENSG00000038532	CLEC16A	0,49121	0,0420661
ENSG00000147383	NSDHL	0,48865	0,008088
ENSG00000135821	GLUL	0,48685	0,0001886
ENSG00000171608	PIK3CD	0,48668	0,0037362
ENSG00000115756	HPCAL1	0,48484	0,0014657
ENSG00000161010	C5orf45	0,48472	0,001084
ENSG00000168884	TNIP2	0,48287	0,0009142
ENSG00000136770	DNAJC1	0,48284	0,020997
ENSG00000143774	GUK1	0,48274	0,0002265
ENSG00000121486	TRMT1L	0,48206	0,0271447
ENSG00000120885	CLU	0,47957	0,0258078
ENSG00000138685	FGF2	0,4788	0,002333
ENSG00000163545	NUAK2	0,47879	0,0122494
ENSG00000142192	APP	0,47874	0,0001792
ENSG00000176171	BNIP3	0,47752	0,0085004
ENSG00000120539	MASTL	0,47712	0,0157119
ENSG00000155545	MIER3	0,4764	0,0300156
ENSG00000176788	BASP1	0,47592	0,0015937
ENSG00000167987	VPS37C	0,47484	0,0168101
ENSG00000221968	FADS3	0,47465	0,0008843
ENSG00000119729	RHOQ	0,47455	0,0025369
ENSG00000122515	ZMIZ2	0,47452	0,00189
ENSG00000086232	EIF2AK1	0,47403	0,0005208
ENSG00000131149	GSE1	0,47371	0,0256556
ENSG00000074855	ANO8	0,4728	0,0175638
ENSG00000145214	DGKQ	0,4721	0,0347809
ENSG00000111676	ATN1	0,47103	0,0008032
ENSG00000079459	FDFT1	0,46975	0,0010839
ENSG00000104518	GSDMD	0,46892	0,0010769
ENSG00000069399	BCL3	0,46833	0,0095293
ENSG00000187953	PMS2CL	0,46801	0,0372063
ENSG00000182095	TNRC18	0,46741	0,0008401
ENSG00000002549	LAP3	0,46731	0,0008956
ENSG00000196422	PPP1R26	0,46661	0,0043264
ENSG00000203879	GDI1	0,46657	0,0006021
ENSG00000168724	DNAJC21	0,4662	0,0030318
ENSG00000146576	C7orf26	0,46502	0,0295834
ENSG00000180104	EXOC3	0,46216	0,0037715
ENSG00000160948	VPS28	0,46079	0,0012853
ENSG00000229807	XIST	0,46064	0,0010115
ENSG00000116984	MTR	0,45987	0,0028249
ENSG00000080608	KIAA0020	0,45941	0,0161229
ENSG00000160439	RDH13	0,45758	0,04839
ENSG00000184428	TOP1MT	0,45745	0,0040803
ENSG00000235655	H3F3AP4	0,45606	0,0498142
ENSG00000188735	TMEM120B	0,45406	0,0060816
ENSG00000185340	GAS2L1	0,45181	0,0057239
ENSG00000215021	PHB2	0,45173	0,0009638
ENSG00000173153	ESRRA	0,44923	0,0044219
ENSG00000196954	CASP4	0,4488	0,0436436
ENSG00000277203	F8A1	0,44842	0,0070288
ENSG00000103260	METRN	0,44718	0,0139996
ENSG00000134899	ERCC5	0,44698	0,0045188
ENSG00000157954	WIPI2	0,44633	0,0020733
ENSG00000150938	CRIM1	0,44484	0,0046837
ENSG00000100979	PLTP	0,44414	0,0057162
ENSG00000144746	ARL6IP5	0,44366	0,0026391
ENSG00000117139	KDM5B	0,44324	0,0090826
ENSG00000249915	PDCD6	0,44149	0,006242
ENSG00000148143	ZNF462	0,4408	0,0324137

ID	hgnc_symbol	logFC	adj.P.Val
ENSG00000122958	VPS26A	0,44062	0,0033761
ENSG00000131652	THOC6	0,44053	0,0410371
ENSG00000160972	PPP1R16A	0,44036	0,0138798
ENSG00000182325	FBXL6	0,44017	0,0091885
ENSG00000134900	TPP2	0,4401	0,0041433
ENSG00000152684	PELO	0,43767	0,0336616
ENSG00000116133	DHCR24	0,43635	0,0230968
ENSG00000134371	CDC73	0,43604	0,0213227
ENSG00000176454	LPCAT4	0,43582	0,007829
ENSG00000106305	AIMP2	0,43492	0,0165252
ENSG00000175309	PHYKPL	0,43354	0,0258078
ENSG00000152518	ZFP36L2	0,43331	0,0081318
ENSG00000153339	TRAPPC8	0,4328	0,0398679
ENSG00000145247	OCIAD2	0,43153	0,0317243
ENSG00000116962	NID1	0,43098	0,004676
ENSG00000127022	CANX	0,42986	0,0078623
ENSG00000122729	ACO1	0,42956	0,0130543
ENSG00000080822	CLDND1	0,42925	0,0057972
ENSG00000119537	KDSR	0,42696	0,0223987
ENSG00000067064	IDI1	0,42687	0,0263652
ENSG00000113552	GNPDA1	0,4266	0,0087439
ENSG00000113300	CNOT6	0,42619	0,0243788
ENSG00000160753	RUSC1	0,42594	0,0028281
ENSG00000108828	VAT1	0,42581	0,0036366
ENSG00000099290	FAM21A	0,42426	0,012075
ENSG00000166444	ST5	0,42259	0,005932
ENSG00000164880	INTS1	0,42199	0,0085004
ENSG00000110697	PITPNM1	0,42183	0,027132
ENSG00000103126	AXIN1	0,42113	0,0244681
ENSG00000166900	STX3	0,4201	0,0410293
ENSG00000188313	PLSCR1	0,41983	0,0341458
ENSG00000126746	ZNF384	0,41965	0,0053203
ENSG00000092010	PSME1	0,41775	0,0026995
ENSG00000167693	NXN	0,41751	0,0098837
ENSG00000106392	C1GALT1	0,41624	0,0439566
ENSG00000148730	EIF4EBP2	0,41361	0,0038201
ENSG00000136758	YME1L1	0,41185	0,0125154
ENSG00000140105	WARS	0,40804	0,0119396
ENSG00000138413	IDH1	0,40672	0,0160447
ENSG00000111321	MIF4GD	0,40611	0,0054452
ENSG00000109501	WFS1	0,40425	0,044553
ENSG00000134109	EDEM1	0,4039	0,0119701
ENSG00000060982	BCAT1	0,40378	0,035148
ENSG00000037474	NSUN2	0,40369	0,0297204
ENSG00000052802	MSMO1	0,40298	0,0134796
ENSG00000135052	GOLM1	0,40193	0,007829
ENSG00000109736	MFSD10	0,40135	0,0091678
ENSG00000161714	PLCD3	0,40114	0,0145852
ENSG00000186480	INSIG1	0,40078	0,0057833
ENSG00000113460	BRIX1	0,40012	0,0153828
ENSG00000052126	PLEKHA5	0,39959	0,0455973
ENSG00000151929	BAG3	0,39939	0,0073233
ENSG00000109787	KLF3	0,39782	0,0244681
ENSG00000148400	NOTCH1	0,39745	0,0241576
ENSG00000184470	TXNRD2	0,39662	0,0127161
ENSG00000048828	FAM120A	0,39656	0,0082611
ENSG00000147454	SLC25A37	0,39592	0,0069618
ENSG00000180182	MED14	0,39581	0,022801
ENSG00000122705	CLTA	0,39519	0,0085498
ENSG00000146066	HIGD2A	0,39385	0,0125994

Table S5. RNASeq gene expression analysis data derived from xenografts removed 30 days post-implantation. Gene expression fold-change (FC) is represented as log_2FC and color coded from highest (+ values in red, upregulated in low stromal CAV1 xenografts) to lowest (- values in green, downregulated) values. Benjamini-Hochberg adjusted p-values for multiple comparisons (adj.P.Val).

ID	hgnc_symbol	logFC	adj.P.Val
ENSG00000136205	TNS3	0,39142	0,0160447
ENSG00000118707	TGIF2	0,38971	0,0341941
ENSG00000221869	CEBPD	0,3897	0,0123075
ENSG00000169213	RAB3B	0,38904	0,0374146
ENSG00000148824	MTG1	0,38765	0,0190932
ENSG00000221963	APOL6	0,38694	0,0454494
ENSG00000116679	IVNS1ABP	0,38537	0,0090826
ENSG00000127527	SPATA22	0,38535	0,019647
ENSG00000087074	PPP1R15A	0,38362	0,0186831
ENSG00000087460	GNAS	0,38319	0,00448
ENSG00000161021	MAML1	0,38308	0,0329701
ENSG00000006625	GGCT	0,38223	0,0273907
ENSG00000110536	PTPMT1	0,38198	0,0320734
ENSG00000135968	GCC2	0,38134	0,0308238
ENSG00000198853	RUSC2	0,38071	0,0384068
ENSG00000029993	HMGB3	0,37985	0,0161229
ENSG00000172661	FAM21C	0,37858	0,0320734
ENSG00000130560	UBAC1	0,37742	0,0339457
ENSG00000160949	TONSL	0,37742	0,0230358
ENSG00000134874	DZIP1	0,37723	0,0195636
ENSG00000189043	NDUFA4	0,37488	0,0205344
ENSG00000112941	PAPD7	0,3745	0,0319678
ENSG00000204525	HLA-C	0,37403	0,0099182
ENSG00000079332	SAR1A	0,37304	0,0175542
ENSG00000164466	SFXN1	0,37178	0,0377852
ENSG00000168653	NDUFS5	0,36938	0,0466268
ENSG00000071894	CPSF1	0,36756	0,0157119
ENSG00000014164	ZC3H3	0,36742	0,0306798
ENSG00000139197	PEX5	0,36735	0,0447911
ENSG00000164713	BRI3	0,36699	0,0153126
ENSG00000114354	TFG	0,36587	0,0125899
ENSG00000198546	ZNF511	0,36387	0,0282137
ENSG00000160932	LY6E	0,36319	0,0258712
ENSG00000112977	DAP	0,36227	0,0185601
ENSG00000185567	AHNAK2	0,36029	0,0461299
ENSG00000157778	PSMG3	0,35888	0,0433163
ENSG00000175137	SH3BP5L	0,35664	0,0392601
ENSG00000116977	LGALS8	0,35551	0,0303488
ENSG00000127191	TRAF2	0,3553	0,0348246
ENSG00000265972	TXNIP	0,35527	0,0158002
ENSG00000179091	CYC1	0,35484	0,0241713
ENSG00000127526	SLC35E1	0,35462	0,0394795
ENSG00000108861	DUSP3	0,35353	0,0258712
ENSG00000172638	EFEMP2	0,35252	0,0230133
ENSG00000153147	SMARCA5	0,35208	0,0445217
ENSG00000213699	SLC35F6	0,35102	0,0443063
ENSG00000105058	FAM32A	0,34821	0,0337627
ENSG00000197724	PHF2	0,3472	0,0312041
ENSG00000168159	RNF187	0,34683	0,0408324
ENSG00000197746	PSAP	0,34525	0,0273907
ENSG00000165637	VDAC2	0,34034	0,0306959
ENSG00000068323	TFE3	0,34009	0,0462389
ENSG00000149115	TNKS1BP1	0,33809	0,0266941
ENSG00000204628	GNB2L1	0,3373	0,0255569
ENSG00000115073	ACTR1B	0,33715	0,044766
ENSG00000198910	L1CAM	0,33701	0,0310776
ENSG00000198959	TGM2	0,33409	0,0376631
ENSG00000134884	ARGLU1	0,33194	0,0486857
ENSG00000185122	HSF1	0,33053	0,0375565
ENSG00000089693	MLF2	0,33003	0,0403863

ID	hgnc_symbol	logFC	adj.P.Val
ENSG00000231925	TAPBP	0,32675	0,0323659
ENSG00000143256	PFDN2	0,32228	0,0482065
ENSG00000143384	MCL1	0,32176	0,0319558
ENSG00000148110	HIATL1	0,32008	0,0472217
ENSG00000102144	PGK1	0,31975	0,0497471
ENSG00000143761	ARF1	0,31966	0,0317254
ENSG00000120694	HSPH1	0,3166	0,0404222
ENSG00000198840	MT-ND3	0,31628	0,0358553
ENSG00000111669	TPI1	0,30704	0,0463323
ENSG00000198888	MT-ND1	0,30233	0,0438799
ENSG00000108821	COL1A1	-0,2869	0,0313563
ENSG00000108424	KPNB1	-0,2919	0,0468806
ENSG00000100097	LGALS1	-0,3058	0,0424974
ENSG00000204231	RXRB	-0,3065	0,0462389
ENSG00000164924	YWHAZ	-0,3098	0,0315146
ENSG00000099250	NRP1	-0,3098	0,0471064
ENSG00000117632	STMN1	-0,3111	0,0388567
ENSG00000124614	RPS10	-0,3114	0,0325912
ENSG00000184009	ACTG1	-0,313	0,0355777
ENSG00000239672	NME1	-0,3133	0,0480185
ENSG00000002586	CD99	-0,3137	0,0495798
ENSG00000137309	HMGA1	-0,3157	0,0330965
ENSG00000049618	ARID1B	-0,3159	0,0410371
ENSG00000163348	PYGO2	-0,3162	0,0428539
ENSG00000106683	LIMK1	-0,3176	0,0372272
ENSG00000143545	RAB13	-0,3178	0,0394948
ENSG00000167601	AXL	-0,3179	0,0336011
ENSG00000176890	TYMS	-0,318	0,044738
ENSG00000244038	DDOST	-0,3183	0,0383602
ENSG00000204392	LSM2	-0,3187	0,0488793
ENSG00000154845	PPP4R1	-0,3188	0,0382874
ENSG00000105810	CDK6	-0,3195	0,0344093
ENSG00000143624	INTS3	-0,3204	0,0345262
ENSG00000156482	RPL30	-0,3217	0,0230358
ENSG00000120708	TGFBI	-0,3222	0,049137
ENSG00000160299	PCNT	-0,3226	0,0408995
ENSG00000214736	TOMM6	-0,3228	0,0386998
ENSG00000147526	TACC1	-0,3246	0,0398679
ENSG00000196704	AMZ2	-0,3259	0,0354212
ENSG00000180340	FZD2	-0,3261	0,0443272
ENSG00000073969	NSF	-0,328	0,0408744
ENSG00000196367	TRRAP	-0,3295	0,0388567
ENSG00000128791	TWSG1	-0,33	0,043198
ENSG00000101335	MYL9	-0,3303	0,0335259
ENSG00000105771	SMG9	-0,3312	0,0415452
ENSG00000180901	KCTD2	-0,3314	0,048815
ENSG00000164687	FABP5	-0,3316	0,0263652
ENSG00000017797	RALBP1	-0,3384	0,0230968
ENSG00000122335	SERAC1	-0,3384	0,0409646
ENSG00000122406	RPL5	-0,3384	0,0166418
ENSG00000186575	NF2	-0,3385	0,0299602
ENSG00000166025	AMOTL1	-0,3385	0,0409646
ENSG00000168386	FILIP1L	-0,3394	0,0482139
ENSG00000124788	ATXN1	-0,3402	0,0448683
ENSG00000112297	AIM1	-0,3409	0,0273907
ENSG00000264364	DYNLL2	-0,3413	0,0281305
ENSG00000049239	H6PD	-0,3434	0,0301635
ENSG00000005156	LIG3	-0,3435	0,0341458
ENSG00000111696	NT5DC3	-0,3441	0,0360962
ENSG00000105341	DDHD2	-0,3448	0,0456545

ID	hgnc_symbol	logFC	adj.P.Val
ENSG00000162627	SNX7	-0,346	0,0377657
ENSG00000162408	NOL9	-0,3466	0,0410293
ENSG00000108799	EZH1	-0,3467	0,0367636
ENSG00000072121	ZFYVE26	-0,3471	0,0413875
ENSG00000149639	SOGA1	-0,3476	0,0227612
ENSG00000125686	MED1	-0,3477	0,0344262
ENSG00000198467	TPM2	-0,348	0,0137662
ENSG00000164109	MAD2L1	-0,3485	0,0334589
ENSG00000121957	GPSM2	-0,3499	0,0320734
ENSG00000152661	GJA1	-0,3502	0,0244681
ENSG00000243678	NME1-NME2	-0,3509	0,0119701
ENSG00000259040	BLOC1S5-TXNDC	-0,3517	0,0374146
ENSG00000173171	MTX1	-0,3525	0,0161229
ENSG00000198830	HMGN2	-0,3532	0,0085004
ENSG00000142676	RPL11	-0,3535	0,0090337
ENSG00000198198	SZT2	-0,3539	0,0325313
ENSG00000090006	LTBP4	-0,3542	0,0496088
ENSG00000119865	CNRIP1	-0,3544	0,0499983
ENSG00000068097	HEATR6	-0,3556	0,0323659
ENSG00000165678	GHITM	-0,3566	0,0192881
ENSG00000142669	SH3BGRL3	-0,3572	0,0229157
ENSG00000137818	RPLP1	-0,3579	0,0146404
ENSG00000151176	PLBD2	-0,3586	0,0344294
ENSG00000065135	GNAI3	-0,359	0,0144166
ENSG00000112144	ICK	-0,3591	0,0205386
ENSG00000002834	LASP1	-0,3592	0,0123264
ENSG00000172057	ORMDL3	-0,3607	0,0303149
ENSG00000173207	CKS1B	-0,3609	0,0146166
ENSG00000099622	CIRBP	-0,3611	0,0183439
ENSG00000188643	S100A16	-0,3612	0,0269044
ENSG00000062716	VMP1	-0,3616	0,0273907
ENSG00000113657	DPYSL3	-0,3623	0,0243944
ENSG00000224877	C17orf89	-0,3625	0,0485956
ENSG00000163297	ANTXR2	-0,3627	0,0152966
ENSG00000143621	ILF2	-0,3631	0,0085004
ENSG00000138092	CENPO	-0,3643	0,0160447
ENSG00000136451	VEZF1	-0,3654	0,0154369
ENSG00000269905		-0,3679	0,0341324
ENSG00000256053	APOPT1	-0,368	0,0250775
ENSG00000063601	MTMR1	-0,3681	0,0344093
ENSG00000134222	PSRC1	-0,3695	0,0331968
ENSG00000067225	PKM	-0,3705	0,0245239
ENSG00000116251	RPL22	-0,3711	0,0065192
ENSG00000213246	SUPT4H1	-0,373	0,0165252
ENSG00000163359	COL6A3	-0,3742	0,0086615
ENSG00000111348	ARHGDIB	-0,376	0,0311304
ENSG00000083168	KAT6A	-0,3774	0,0303149
ENSG00000154229	PRKCA	-0,3804	0,0116335
ENSG00000110315	RNF141	-0,3813	0,0432063
ENSG00000080823	MOK	-0,3819	0,0116481
ENSG00000270069	MIR222HG	-0,3869	0,0232741
ENSG00000123689	G0S2	-0,3884	0,0421859
ENSG00000213178		-0,3885	0,0084369
ENSG00000146476	C6orf211	-0,3889	0,0197737
ENSG00000154734	ADAMTS1	-0,3907	0,0173139
ENSG00000085719	CPNE3	-0,391	0,0054656
ENSG00000073050	FOXH1	-0,3919	0,0276638
ENSG00000219481	NBPF1	-0,3919	0,0403147
ENSG00000177106	EPS8L2	-0,3919	0,0353795
ENSG00000214114	MYCBP	-0,3937	0,0330965

ID	hgnc_symbol	logFC	adj.P.Val
ENSG00000104381	GDAP1	-0,3947	0,0344093
ENSG00000173546	CSPG4	-0,3958	0,0112475
ENSG00000117155	SSX2IP	-0,397	0,0303488
ENSG00000009307	CSDE1	-0,3972	0,0070288
ENSG00000135919	SERPINE2	-0,3984	0,0213227
ENSG00000105989	WNT2	-0,3997	0,0423378
ENSG00000134986	NREP	-0,3998	0,0216305
ENSG00000115414	FN1	-0,4025	0,0011436
ENSG00000168077	SCARA3	-0,4031	0,0282379
ENSG00000128510	CPA4	-0,4038	0,0144166
ENSG00000117543	DPH5	-0,4047	0,0142252
ENSG00000100106	TRIOBP	-0,4075	0,0219366
ENSG00000170921	TANC2	-0,4078	0,0071503
ENSG00000148180	GSN	-0,4084	0,0063643
ENSG00000177954	RPS27	-0,4101	0,001533
ENSG00000197457	STMN3	-0,4105	0,0168561
ENSG00000168785	TSPAN5	-0,4108	0,0303151
ENSG00000049245	VAMP3	-0,4128	0,0029839
ENSG00000182158	CREB3L2	-0,4171	0,0164324
ENSG00000120318	ARAP3	-0,4175	0,008036
ENSG00000137962	ARHGAP29	-0,4208	0,0026806
ENSG00000049192	ADAMTS6	-0,4217	0,0065475
ENSG00000134802	SLC43A3	-0,4242	0,0192724
ENSG00000166173	LARP6	-0,4247	0,0074157
ENSG00000041988	THAP3	-0,4253	0,0225967
ENSG00000115232	ITGA4	-0,4275	0,0139178
ENSG00000006453	BAIAP2L1	-0,4296	0,0073543
ENSG00000101000	PROCR	-0,4318	0,0265579
ENSG00000269821	KCNQ1OT1	-0,4323	0,029637
ENSG00000264112		-0,4324	0,0026837
ENSG00000141576	RNF157	-0,433	0,0067294
ENSG00000137831	UACA	-0,4339	0,0078376
ENSG00000204410	MSH5	-0,4355	0,0071272
ENSG00000213523	SRA1	-0,4369	0,0244397
ENSG00000148175	STOM	-0,4392	0,0133297
ENSG00000116670	MAD2L2	-0,4419	0,0082611
ENSG00000178031	ADAMTSL1	-0,4428	0,0023503
ENSG00000079931	MOXD1	-0,444	0,0021685
ENSG00000223749	MIR503HG	-0,4442	0,0057902
ENSG00000160007	ARHGAP35	-0,4484	0,0017147
ENSG00000137337	MDC1	-0,4485	0,0007078
ENSG00000144681	STAC	-0,4517	0,0191669
ENSG00000159164	SV2A	-0,4518	0,0016661
ENSG00000001461	NIPAL3	-0,4528	0,0074488
ENSG00000145715	RASA1	-0,4571	0,0015139
ENSG00000169946	ZFPM2	-0,4573	0,0131812
ENSG00000166813	KIF7	-0,4577	0,02022
ENSG00000167549	CORO6	-0,4578	0,0178917
ENSG00000197956	S100A6	-0,4584	0,000155
ENSG00000223865	HLA-DPB1	-0,4616	0,0131403
ENSG00000184838	PRR16	-0,4618	0,0358687
ENSG00000127481	UBR4	-0,4631	0,0061526
ENSG00000142621	FHAD1	-0,4632	0,0018246
ENSG00000197535	MYO5A	-0,4656	0,0045415
ENSG00000105048	TNNT1	-0,4675	0,0085684
ENSG00000161992	PRR35	-0,4694	0,004288
ENSG00000090539	CHRD	-0,47	0,010038
ENSG00000149948	HMGA2	-0,4716	0,0060538
ENSG00000125726	CD70	-0,4736	0,0266078
ENSG00000231607	DLEU2	-0,4749	0,048714

Table S5. RNASeq gene expression analysis data derived from xenografts removed 30 days post-implantation. Gene expression fold-change (FC) is represented as log_2FC and color coded from highest (+ values in red, upregulated in low stromal CAV1 xenografts) to lowest (- values in green, downregulated) values. Benjamini-Hochberg adjusted p-values for multiple comparisons (adj.P.Val).

ID	hgnc_symbol	logFC	adj.P.Val
ENSG00000144057	ST6GAL2	-0,477	0,0329659
ENSG00000171953	ATPAF2	-0,4884	0,0325912
ENSG00000140403	DNAJA4	-0,4893	0,0022367
ENSG00000167074	TEF	-0,4912	0,0459255
ENSG00000004139	SARM1	-0,4928	0,0019499
ENSG00000170989	S1PR1	-0,495	0,0230148
ENSG00000164318	EGFLAM	-0,496	0,0202246
ENSG00000236824	BCYRN1	-0,4972	0,0071272
ENSG00000189171	S100A13	-0,4984	0,0001169
ENSG00000197594	ENPP1	-0,5018	0,0001718
ENSG00000133816	MICAL2	-0,5073	0,0006441
ENSG00000145431	PDGFC	-0,5075	0,0077018
ENSG00000128656	CHN1	-0,5208	0,0024668
ENSG00000085117	CD82	-0,5233	0,0005227
ENSG00000271529	CICP14	-0,5246	0,0219123
ENSG00000110429	FBXO3	-0,526	0,0130258
ENSG00000228696	ARL17B	-0,5294	0,044738
ENSG00000075826	SEC31B	-0,531	0,0498277
ENSG00000117152	RGS4	-0,5482	0,0043646
ENSG00000159184	HOXB13	-0,5504	0,048815
ENSG00000205670	SMIM11	-0,5534	0,0154369
ENSG00000109452	INPP4B	-0,5598	0,0401071
ENSG00000220842		-0,566	0,0008166
ENSG00000110092	CCND1	-0,5778	4,35E-06
ENSG00000179163	FUCA1	-0,5867	0,0075778
ENSG00000112619	PRPH2	-0,5895	0,0049328
ENSG00000196754	S100A2	-0,5903	3,46E-05
ENSG00000154736	ADAMTS5	-0,595	0,0001066
ENSG00000131477	RAMP2	-0,5971	0,02983
ENSG00000165072	MAMDC2	-0,5987	0,0036436
ENSG00000213366	GSTM2	-0,61	0,0002909
ENSG00000243302		-0,6114	0,0085498
ENSG00000162511	LAPTM5	-0,6181	0,0145798
ENSG00000173530	TNFRSF10D	-0,6222	0,0001406
ENSG00000188452	CERKL	-0,6264	0,0026391
ENSG00000198768	APCDD1L	-0,6419	7,49E-06
ENSG00000170961	HAS2	-0,6441	0,0002397
ENSG00000259207	ITGB3	-0,6495	0,0420191
ENSG00000266086		-0,6534	0,044738
ENSG00000213058		-0,6762	0,0019381
ENSG00000231290	APCDD1L-AS1	-0,6859	0,0003866
ENSG00000185532	PRKG1	-0,6875	0,0232562
ENSG00000179546	HTR1D	-0,7273	0,0223987
ENSG00000164707	SLC13A4	-0,7395	0,0247219
ENSG00000154096	THY1	-0,7793	1,88E-07
ENSG00000268173		-0,7849	0,0039524
ENSG00000242588		-0,8325	0,005011
ENSG00000178809	TRIM73	-0,8371	0,0182798
ENSG00000224114		-0,862	0,0194207
ENSG00000259024	TVP23C-CDRT4	-0,9252	0,0025704
ENSG00000172927	MYEOV	-0,9425	7,70E-08
ENSG00000228981		-0,9749	0,0004288
ENSG00000235373		-1,0456	0,0237084
ENSG00000267645	POLR2J2	-1,1161	0,0016371
ENSG00000145681	HAPLN1	-1,3615	0,0024627
ENSG00000203394		-1,3895	0,0002521
ENSG00000231822		-1,4499	0,0360759
ENSG00000277125		-1,6354	0,0242954
ENSG00000254870	ATP6V1G2-DDX3	-1,8678	1,81E-09
ENSG00000257594	GALNT4	-2,3427	0,0154369

ID	hgnc_symbol	logFC	adj.P.Val
ENSG00000105974	CAV1	-2,487	3,81E-114
ENSG00000260892		-3,0167	1,11E-05
ENSG00000261684		-3,3788	0,0049622
ENSG00000254721		-3,5463	2,46E-06
ENSG00000270316	C10orf32-ASMT	-5,1226	0,0008211

Table S6. RNASeq gene expression analysis data derived from xenografts removed 40 days post-implantation. Gene expression fold-change (FC) is represented as log_2FC and color coded from highest (+ values in red, upregulated in low stromal CAV1 xenografts) to lowest (- values in green, downregulated) values. Benjamini-Hochberg adjusted p-values for multiple comparisons (adj.P.Val).

ID	hgnc_symbol	logFC	adj.P.Val
ENSG00000148346	LCN2	2,045596	0,028336
ENSG00000255152	MSH5-SAPCD1	2,002525	0,033337
ENSG00000108342	CSF3	1,964561	0,001048
ENSG00000163739	CXCL1	1,470155	0,013832
ENSG00000125538	IL1B	1,455739	0,000352
ENSG00000060718	COL11A1	1,448327	3,82E-09
ENSG00000136244	IL6	1,295209	0,004125
ENSG00000135312	HTR1B	1,168583	0,025829
ENSG00000173432	SAA1	1,146104	0,001047
ENSG00000144802	NFKBIZ	1,050571	0,03291
ENSG00000173918	C1QTNF1	1,044405	0,044886
ENSG00000124102	PI3	0,989606	0,022427
ENSG00000169429	CXCL8	0,948367	0,054528
ENSG00000118523	CTGF	0,9375	1,65E-07
ENSG00000183889		0,927572	5,45E-05
ENSG00000183458		0,91949	0,004409
ENSG00000139874	SSTR1	0,9072	0,022427
ENSG00000111799	COL12A1	0,858208	2,41E-10
ENSG00000159167	STC1	0,84278	0,00147
ENSG00000117525	F3	0,842685	0,025829
ENSG00000143631	FLG	0,83654	0,000414
ENSG00000184985	SORCS2	0,826184	0,016685
ENSG00000255103	KIAA0754	0,802871	0,04268
ENSG00000179304	FAM156B	0,775241	0,042317
ENSG00000164694	FNDC1	0,775123	0,020368
ENSG00000008710	PKD1	0,772642	0,000257
ENSG00000196159	FAT4	0,762888	0,032713
ENSG00000176697	BDNF	0,761505	0,000629
ENSG00000178860	MSC	0,744839	0,009464
ENSG00000101825	MXRA5	0,721959	0,029447
ENSG00000139970	RTN1	0,700681	0,013244
ENSG00000132510	KDM6B	0,698922	0,025672
ENSG00000171951	SCG2	0,671467	0,029138
ENSG00000121005	CRISPLD1	0,657991	0,001882
ENSG00000131149	GSE1	0,652473	0,011765
ENSG00000113739	STC2	0,652137	0,007128
ENSG00000064042	LIMCH1	0,646735	0,000908
ENSG00000123384	LRP1	0,645181	0,000616
ENSG00000145147	SLIT2	0,64103	0,000464
ENSG00000164362	TERT	0,635454	0,018996
ENSG00000159399	HK2	0,614746	0,013244
ENSG00000105429	MEGF8	0,603989	0,022427
ENSG00000130164	LDLR	0,602011	0,000104
ENSG00000146674	IGFBP3	0,597894	0,032569
ENSG00000145934	TENM2	0,592991	0,006376
ENSG00000116016	EPAS1	0,584937	0,000908
ENSG00000138829	FBN2	0,583432	4,68E-05
ENSG00000108797	CNTNAP1	0,569804	0,006507
ENSG00000174807	CD248	0,568304	0,029138
ENSG00000008513	ST3GAL1	0,562145	0,0094
ENSG00000233369		0,560353	0,005203
ENSG00000243649	CFB	0,558849	0,006376
ENSG00000164951	PDP1	0,556529	0,012035

ID	hgnc_symbol	logFC	adj.P.Val
ENSG00000087245	MMP2	0,551171	0,023226
ENSG00000182095	TNRC18	0,550441	0,005876
ENSG00000138166	DUSP5	0,543542	0,00703
ENSG00000117569	PTBP2	0,542261	0,022427
ENSG00000090339	ICAM1	0,542155	0,012035
ENSG00000185567	AHNAK2	0,536339	0,020896
ENSG00000188157	AGRN	0,534647	0,001519
ENSG00000166833	NAV2	0,531536	0,03291
ENSG00000072310	SREBF1	0,531396	0,009464
ENSG00000140937	CDH11	0,526859	0,011765
ENSG00000168140	VASN	0,526535	0,016947
ENSG00000130702	LAMA5	0,517342	0,011765
ENSG00000112972	HMGCS1	0,512876	0,007025
ENSG00000142798	HSPG2	0,510781	0,023473
ENSG00000125730	C3	0,502682	0,030217
ENSG00000132182	NUP210	0,501293	0,028336
ENSG00000231925	TAPBP	0,495883	0,005876
ENSG00000167548	KMT2D	0,492876	0,025102
ENSG00000108175	ZMIZ1	0,489382	0,019813
ENSG00000127603	MACF1	0,482384	0,01148
ENSG00000006118	TMEM132A	0,47764	0,021264
ENSG00000105426	PTPRS	0,477303	0,04965
ENSG00000130635	COL5A1	0,470606	0,036631
ENSG00000178209	PLEC	0,466412	0,01148
ENSG00000148411	NACC2	0,455201	0,025102
ENSG00000164916	FOXK1	0,454515	0,022427
ENSG00000082805	ERC1	0,452872	0,052174
ENSG00000166825	ANPEP	0,446466	0,022427
ENSG00000116604	MEF2D	0,414583	0,025829
ENSG00000169710	FASN	0,408844	0,022427
ENSG00000196924	FLNA	0,346515	0,000772
ENSG00000049245	VAMP3	-0,48163	0,006376
ENSG00000165678	GHITM	-0,50637	0,006376
ENSG00000166592	RRAD	-0,59142	0,01506
ENSG00000125726	CD70	-0,60244	0,001194
ENSG00000079257	LXN	-0,61127	0,047382
ENSG00000224578	HNRNPA1P48	-0,63534	0,018385
ENSG00000278619	MRM1	-0,63842	0,036631
ENSG00000130600	H19	-0,81287	1,91E-08
ENSG00000215784	FAM72D	-0,92466	0,011765
ENSG00000004799	PDK4	-1,15946	0,030217
ENSG00000213145	CRIP1	-1,21443	0,000672
ENSG00000167772	ANGPTL4	-1,56635	2,23E-05
ENSG00000180389	ATP5EP2	-1,68601	0,022829
ENSG00000105974	CAV1	-3,04018	1,8E-152
ENSG00000234648		-5,1131	3,35E-11

Table S7. RNASeq gene expression analysis data derived from *in vitro* 3D collagen-cultured CAFs. Gene expression fold-change (FC) is represented as log_2FC and color coded from highest (positive values in red, upregulated in CAFshCAV1 fibroblasts) to lowest (negative values in green, downregulated) values. Benjamini-Hochberg adjusted p-values for multiple comparisons (adj.P.Val).

ID	hgnc_symbol	logFC	adj.P.Val
ENSG00000232220	AC008440.2	8,23094	7,217E-13
ENSG00000226964	RHEBP2	7,96869	1,191E-10
ENSG00000185641	AC034236.1	7,90483	3,253E-09
ENSG00000269972	AC004542.1	7,66733	3,343E-09
ENSG00000173678	SPDYE2B	4,94491	5,004E-05
ENSG00000274615	AC233968.1	3,35893	4,242E-07
ENSG00000236552	RPL13AP5	3,27341	0,0021948
ENSG00000261052	SULT1A3	3,19128	0,0006393
ENSG00000169203		3,14353	3,129E-05
ENSG00000253816		2,49421	0,004115
ENSG00000277125		2,45126	0,0016727
ENSG00000196167	COLCA1	2,19359	0,0319548
ENSG00000180229	HERC2P3	1,90438	0,0351876
ENSG00000196205	EEF1A1P5	1,81226	5,151E-07
ENSG00000270276	HIST2H4A	1,47339	0,0067682
ENSG00000265590		1,42063	0,0402787
ENSG00000181625	SLX1B	1,24007	0,0110788
ENSG00000101670	LIPG	1,05241	0,03394
ENSG00000254996	ANKHD1-EIF4EB	1,02101	0,0021661
ENSG00000152092	ASTN1	1,01984	0,035955
ENSG00000169429	CXCL8	0,99876	0,0022509
ENSG00000156463	SH3RF2	0,87588	0,0279154
ENSG00000269547		0,86361	0,0183794
ENSG00000198910	L1CAM	0,83847	1,379E-36
ENSG00000125730	C3	0,7798	9,169E-39
ENSG00000065320	NTN1	0,77173	0,0057951
ENSG00000157601	MX1	0,75286	0,0001082
ENSG00000072657	TRHDE	0,70376	0,0002118
ENSG00000012171	SEMA3B	0,68862	0,0286696
ENSG00000185567	AHNAK2	0,68769	1,752E-08
ENSG00000272398	CD24	0,66555	0,0274359
ENSG00000163131	CTSS	0,64642	0,0382972
ENSG00000138944	KIAA1644	0,64062	0,0244026
ENSG00000244257	PKD1P1	0,6356	0,0329383
ENSG00000243649	CFB	0,62732	1,239E-09
ENSG00000115041	KCNIP3	0,60567	0,04168
ENSG00000111335	OAS2	0,59333	0,0034906
ENSG00000275993		0,59125	0,0017387
ENSG00000138623	SEMA7A	0,58692	4,305E-08
ENSG00000261796	ISY1-RAB43	0,58335	0,0380798
ENSG00000225630	MTND2P28	0,57618	4,189E-05
ENSG00000114270	COL7A1	0,5753	4,724E-06
ENSG00000136040	PLXNC1	0,57478	0,00023
ENSG00000100342	APOL1	0,56492	0,0020056
ENSG00000072310	SREBF1	0,55849	5,604E-18
ENSG00000144802	NFKBIZ	0,55684	1,999E-05
ENSG00000100867	DHRS2	0,5543	0,0003644
ENSG00000099194	SCD	0,55222	4,204E-29
ENSG00000130589	HELZ2	0,55163	3,62E-12
ENSG00000187720	THSD4	0,55101	1,326E-06
ENSG00000157193	LRP8	0,5449	0,0025174
ENSG00000125538	IL1B	0,54416	0,0446641
ENSG00000137767	SQRDL	0,54095	0,0340547
ENSG00000165029	ABCA1	0,53673	5,879E-08
ENSG00000158258	CLSTN2	0,52649	0,0031555
ENSG00000111331	OAS3	0,51703	0,021075
ENSG00000198888	MT-ND1	0,51115	1,351E-12
ENSG00000108691	CCL2	0,50044	0,0161777
ENSG00000168398	BDKRB2	0,48959	5,324E-06
ENSG00000128606	LRRC17	0,4875	0,0039806
ENSG00000130702	LAMA5	0,48366	7,088E-08

ID	hgnc_symbol	logFC	adj.P.Val
ENSG00000185745	IFIT1	0,48278	0,0031127
ENSG00000245532	NEAT1	0,48093	4,595E-12
ENSG00000110888	CAPRIN2	0,48071	0,0157469
ENSG00000117569	PTBP2	0,47438	0,0001139
ENSG00000198712	MT-CO2	0,47132	5,069E-14
ENSG00000198763	MT-ND2	0,4671	4,023E-10
ENSG00000262246	CORO7	0,46691	0,0304064
ENSG00000214548	MEG3	0,46426	0,0016603
ENSG00000102359	SRPX2	0,46322	0,0179964
ENSG00000049249	TNFRSF9	0,46201	0,0006514
ENSG00000248527	MTATP6P1	0,45752	1,615E-07
ENSG00000123358	NR4A1	0,45367	0,04168
ENSG00000186480	INSIG1	0,43984	8,423E-15
ENSG00000198804	MT-CO1	0,43563	1,031E-07
ENSG00000104332	SFRP1	0,42718	6,704E-16
ENSG00000176973	KPNA2	0,42658	0,0289955
ENSG00000050344	NFE2L3	0,42446	0,015626
ENSG00000126709	IFI6	0,42341	9,475E-06
ENSG00000076554	TPD52	0,42216	0,0245767
ENSG00000183722	LHFP	0,42211	0,002372
ENSG00000169213	RAB3B	0,42182	5,395E-05
ENSG00000184371	CSF1	0,42146	9,375E-11
ENSG00000130164	LDLR	0,42099	6,332E-14
ENSG00000210082	MT-RNR2	0,419	1,207E-16
ENSG00000041982	TNC	0,41536	8,742E-12
ENSG00000096433	ITPR3	0,41203	3,177E-10
ENSG00000137965	IFI44	0,40769	0,0207954
ENSG00000170558	CDH2	0,40516	0,0246263
ENSG00000198727	MT-CYB	0,40345	3,929E-07
ENSG00000204580	DDR1	0,40217	5,776E-12
ENSG00000212907	MT-ND4L	0,40189	2,807E-05
ENSG00000167191	GPRC5B	0,39882	0,0286696
ENSG00000198938	MT-CO3	0,39807	7,413E-11
ENSG00000138496	PARP9	0,39804	0,0184978
ENSG00000111674	ENO2	0,3971	0,0004288
ENSG00000166833	NAV2	0,39304	9,35E-06
ENSG00000049130	KITLG	0,3929	0,0227626
ENSG00000198695	MT-ND6	0,39263	0,0026423
ENSG00000075213	SEMA3A	0,39161	0,0018134
ENSG00000147100	SLC16A2	0,39026	2,234E-06
ENSG00000147459	DOCK5	0,3897	0,0001058
ENSG00000188158	NHS	0,38208	0,0050756
ENSG00000132561	MATN2	0,37757	2,629E-08
ENSG00000171310	CHST11	0,37736	0,0376443
ENSG00000163975	MFI2	0,37517	0,0002291
ENSG00000198899	MT-ATP6	0,37232	0,0002287
ENSG00000228253	MT-ATP8	0,3719	0,0010848
ENSG00000138166	DUSP5	0,36965	0,0167936
ENSG00000032389	TSSC1	0,36675	0,0310641
ENSG00000198886	MT-ND4	0,35694	0,0002837
ENSG00000237975	FLG-AS1	0,3568	0,0249215
ENSG00000177409	SAMD9L	0,35383	0,0144006
ENSG00000144681	STAC	0,35276	0,023027
ENSG00000135905	DOCK10	0,35258	0,0026423
ENSG00000041353	RAB27B	0,35	0,0218139
ENSG00000165288	BRWD3	0,34765	0,0431162
ENSG00000176170	SPHK1	0,34628	0,0447515
ENSG00000138193	PLCE1	0,34338	0,030053
ENSG00000145147	SLIT2	0,3416	0,0018089
ENSG00000198786	MT-ND5	0,33752	0,0015489
ENSG00000198840	MT-ND3	0,33645	3,469E-07

ID	hgnc_symbol	logFC	adj.P.Val
ENSG00000006625	GGCT	0,33559	0,0139116
ENSG00000151914	DST	0,33373	1,57E-06
ENSG00000119917	IFIT3	0,32854	0,0174358
ENSG00000125398	SOX9	0,32743	4,187E-07
ENSG00000213066	FGFR1OP	0,32537	0,0029905
ENSG00000146376	ARHGAP18	0,32057	0,0119896
ENSG00000145555	MYO10	0,31926	0,0004643
ENSG00000185813	PCYT2	0,31341	0,0263757
ENSG00000119139	TJP2	0,31201	0,0003821
ENSG00000006118	TMEM132A	0,31046	0,0079032
ENSG00000211459	MT-RNR1	0,30903	1,82E-06
ENSG00000115107	STEAP3	0,3072	0,0455936
ENSG00000077152	UBE2T	0,30675	0,0099472
ENSG00000174136	RGMB	0,30549	0,0005229
ENSG00000198604	BAZ1A	0,3051	0,0002414
ENSG00000185947	ZNF267	0,30398	0,008898
ENSG00000112096	SOD2	0,30193	3,37E-08
ENSG00000171608	PIK3CD	0,30166	0,0099466
ENSG00000101347	SAMHD1	0,29891	0,0005325
ENSG00000008710	PKD1	0,29788	0,0004398
ENSG00000180447	GAS1	0,29724	0,0293885
ENSG00000170776	AKAP13	0,29707	2,234E-06
ENSG00000138778	CENPE	0,29703	0,0346485
ENSG00000120875	DUSP4	0,29582	0,0139539
ENSG00000173705	SUSD5	0,29541	0,0162623
ENSG00000163820	FYCO1	0,29133	0,0025174
ENSG00000166797	FAM96A	0,28942	0,0198118
ENSG00000136048	DRAM1	0,28844	1,126E-05
ENSG00000177706	FAM20C	0,28655	0,0001225
ENSG00000164171	ITGA2	0,28482	0,0125715
ENSG00000139880	CDH24	0,28449	0,0293885
ENSG00000278540	ACACA	0,28449	1,321E-05
ENSG00000108797	CNTNAP1	0,28203	0,0047499
ENSG00000197321	SVIL	0,28184	0,04168
ENSG00000172216	CEBPB	0,28023	0,0048092
ENSG00000159167	STC1	0,27648	0,0307308
ENSG00000109756	RAPGEF2	0,27445	0,0286696
ENSG00000011021	CLCN6	0,27197	0,0119896
ENSG00000169710	FASN	0,27151	1,272E-06
ENSG00000115295	CLIP4	0,27092	0,0231069
ENSG00000031691	CENPQ	0,27045	0,0283891
ENSG00000134824	FADS2	0,26967	0,0008062
ENSG00000111670	GNPTAB	0,26839	0,0021441
ENSG00000112769	LAMA4	0,26782	0,0012816
ENSG00000166471	TMEM41B	0,26686	0,0164967
ENSG00000163840	DTX3L	0,26443	0,0029727
ENSG00000177542	SLC25A22	0,26331	0,045211
ENSG00000146373	RNF217	0,26094	0,021075
ENSG00000143631	FLG	0,25776	0,0050241
ENSG00000033867	SLC4A7	0,25731	0,0020389
ENSG00000161091	MFSD12	0,257	0,0106283
ENSG00000138182	KIF20B	0,2559	0,0018937
ENSG00000163597	SNHG16	0,25351	0,0004143
ENSG00000123983	ACSL3	0,25175	0,0003821
ENSG00000148730	EIF4EBP2	0,25109	0,0001801
ENSG00000067064	IDI1	0,25028	0,0151613
ENSG00000168077	SCARA3	0,24869	0,0096021
ENSG00000164465	DCBLD1	0,24724	0,0088939
ENSG00000136235	GPNMB	0,24626	0,0170382
ENSG00000109046	WSB1	0,24511	0,0491125
ENSG00000144674	GOLGA4	0,24398	0,002742

ID	hgnc_symbol	logFC	adj.P.Val
ENSG00000197045	GMFB	0,24394	0,0002641
ENSG00000109066	TMEM104	0,24249	0,0064921
ENSG00000164823	OSGIN2	0,24235	0,0357298
ENSG00000128591	FLNC	0,2411	0,0005603
ENSG00000165055	METTL2B	0,24048	0,0271632
ENSG00000131711	MAP1B	0,24022	0,0001714
ENSG00000072274	TFRC	0,23918	2,724E-05
ENSG00000050165	DKK3	0,23906	0,0094551
ENSG00000157483	MYO1E	0,23846	0,0010709
ENSG00000068366	ACSL4	0,2382	0,0001979
ENSG00000168461	RAB31	0,23797	0,0011538
ENSG00000054654	SYNE2	0,2368	0,0226169
ENSG00000156671	SAMD8	0,23604	0,0119896
ENSG00000163297	ANTXR2	0,23595	0,0034906
ENSG00000169855	ROBO1	0,23585	0,0142293
ENSG00000196937	FAM3C	0,234	0,0002039
ENSG00000196776	CD47	0,2331	0,0137888
ENSG00000127914	AKAP9	0,23296	0,0045286
ENSG00000171055	FEZ2	0,23191	0,0349465
ENSG00000123240	OPTN	0,23076	0,0165538
ENSG00000068912	ERLEC1	0,2305	0,0074038
ENSG00000121060	TRIM25	0,23047	0,0019453
ENSG00000049323	LTBP1	0,22884	0,0006993
ENSG00000173821	RNF213	0,22725	0,0012745
ENSG00000035862	TIMP2	0,22265	0,0001234
ENSG00000188643	S100A16	0,22251	0,0014813
ENSG00000039560	RAI14	0,22242	0,0255511
ENSG00000112972	HMGCS1	0,2219	0,0321356
ENSG00000109787	KLF3	0,22151	0,0479161
ENSG00000101745	ANKRD12	0,2203	0,013153
ENSG00000160285	LSS	0,21917	0,0138255
ENSG00000162576	MXRA8	0,21886	0,0023849
ENSG00000113083	LOX	0,2188	0,0012805
ENSG00000058668	ATP2B4	0,21828	0,0108965
ENSG00000149485	FADS1	0,21749	0,0012816
ENSG00000091409	ITGA6	0,21599	0,0026423
ENSG00000006576	PHTF2	0,21326	0,0068553
ENSG00000239264	TXNDC5	0,21286	0,0090958
ENSG00000152332	UHMK1	0,21061	0,0017561
ENSG00000142156	COL6A1	0,20829	0,0019847
ENSG00000141458	NPC1	0,20656	0,0200808
ENSG00000110841	PPFIBP1	0,20529	0,0217095
ENSG00000176658	MYO1D	0,20292	0,035955
ENSG00000003436	TFPI	0,20184	0,0035621
ENSG00000163565	IFI16	0,20055	0,0238458
ENSG00000145623	OSMR	0,20011	0,0249215
ENSG00000105576	TNPO2	0,19916	0,0321356
ENSG00000170385	SLC30A1	0,19905	0,0388403
ENSG00000148848	ADAM12	0,19851	0,0187369
ENSG00000146676	PURB	0,19722	0,0104196
ENSG00000130779	CLIP1	0,19628	0,0247746
ENSG00000173230	GOLGB1	0,19611	0,0249215
ENSG00000100815	TRIP11	0,19455	0,0147922
ENSG00000164951	PDP1	0,19408	0,0081194
ENSG00000231925	TAPBP	0,193	0,0048355
ENSG00000117519	CNN3	0,19272	0,0064433
ENSG00000117298	ECE1	0,18955	0,0080874
ENSG00000082641	NFE2L1	0,18936	0,0080874
ENSG00000117724	CENPF	0,18921	0,0287396
ENSG00000181704	YIPF6	0,18883	0,0460754
ENSG00000224531	SMIM13	0,18877	0,031493

Table S7. RNASeq gene expression analysis data derived from *in vitro* 3D collagen-cultured CAFs. Gene expression fold-change (FC) is represented as log_2FC and color coded from highest (positive values in red, upregulated in CAFshCAV1 fibroblasts) to lowest (negative values in green, downregulated) values. Benjamini-Hochberg adjusted p-values for multiple comparisons (adj.P.Val).

ID	hgnc_symbol	logFC	adj.P.Val
ENSG00000137177	KIF13A	0,18866	0,0174358
ENSG00000100997	ABHD12	0,1857	0,0128471
ENSG00000188042	ARL4C	0,18504	0,0363349
ENSG00000090889	KIF4A	0,18376	0,0474999
ENSG00000131016	AKAP12	0,18337	0,0099472
ENSG00000157106	SMG1	0,18072	0,0286696
ENSG00000055332	EIF2AK2	0,18033	0,021685
ENSG00000151893	CACUL1	0,17982	0,0351876
ENSG00000116133	DHCR24	0,17973	0,0184396
ENSG00000071054	MAP4K4	0,17924	0,0146752
ENSG00000164733	CTSB	0,17617	0,0050937
ENSG00000135862	LAMC1	0,17607	0,0118003
ENSG00000107957	SH3PXD2A	0,17593	0,0249215
ENSG00000158270	COLEC12	0,1751	0,0185072
ENSG00000108854	SMURF2	0,1744	0,0361327
ENSG00000213625	LEPROT	0,17304	0,0418916
ENSG00000184743	ATL3	0,16874	0,0473037
ENSG00000162909	CAPN2	0,16711	0,0167816
ENSG00000057019	DCBLD2	0,16536	0,0298666
ENSG00000108179	PPIF	0,16385	0,047034
ENSG00000132824	SERINC3	0,16201	0,0355241
ENSG00000116260	QSOX1	0,1609	0,0434901
ENSG00000188157	AGRN	0,16056	0,0418916
ENSG00000156535	CD109	0,15416	0,0344345
ENSG00000128595	CALU	0,15105	0,033799
ENSG00000120708	TGFBI	0,14592	0,043977
ENSG00000105193	RPS16	-0,1428	0,0490083
ENSG00000063177	RPL18	-0,1439	0,0445537
ENSG00000148303	RPL7A	-0,1442	0,0440839
ENSG00000198431	GML	-0,1524	0,0343167
ENSG00000139926	FRMD6	-0,1549	0,0282103
ENSG00000142534	RPS11	-0,155	0,0227626
ENSG00000204388	HSPA1B	-0,1555	0,0263265
ENSG00000110880	CORO1C	-0,1587	0,0255511
ENSG00000089157	RPLP0	-0,1621	0,0198664
ENSG00000169100	SLC25A6	-0,1648	0,0191721
ENSG00000140988	RPS2	-0,1661	0,0109154
ENSG00000142871	CYR61	-0,167	0,0267385
ENSG00000135677	GNS	-0,1679	0,0135152
ENSG00000184900	SUMO3	-0,1684	0,0293885
ENSG00000111817	DSE	-0,1689	0,0198118
ENSG00000147475	ERLIN2	-0,1692	0,0324185
ENSG00000128510	CPA4	-0,1698	0,0221317
ENSG00000162430	SEPN1	-0,1709	0,0325975
ENSG00000163430	FSTL1	-0,1715	0,0070879
ENSG00000197958	RPL12	-0,1717	0,0102571
ENSG00000186340	THBS2	-0,1718	0,0199249
ENSG00000083845	RPS5	-0,1719	0,0221337
ENSG00000183688	FAM101B	-0,173	0,0347705
ENSG00000241343	RPL36A	-0,1751	0,0231069
ENSG00000124813	RUNX2	-0,1752	0,0191344
ENSG00000197702	PARVA	-0,1762	0,0351876
ENSG00000196313	POM121	-0,1775	0,0447515
ENSG00000213741	RPS29	-0,178	0,0200808
ENSG00000106723	SPIN1	-0,179	0,0321592
ENSG00000101290	CDS2	-0,1793	0,0427825
ENSG00000150347	ARID5B	-0,1797	0,021685
ENSG00000063245	EPN1	-0,1798	0,0227768
ENSG00000149257	SERPINH1	-0,1803	0,0090958
ENSG00000058063	ATP11B	-0,1807	0,0351876
ENSG00000119408	NEK6	-0,1811	0,0240563

ID	hgnc_symbol	logFC	adj.P.Val
ENSG00000158941	CCAR2	-0,1817	0,0308082
ENSG00000234851		-0,1827	0,0129579
ENSG00000011304	PTBP1	-0,1829	0,008898
ENSG00000227097		-0,184	0,0460754
ENSG00000197594	ENPP1	-0,1856	0,0103869
ENSG00000167996	FTH1	-0,1863	0,0036263
ENSG00000177600	RPLP2	-0,1871	0,0031127
ENSG00000019549	SNAI2	-0,1875	0,015626
ENSG00000171150	SOCS5	-0,1894	0,047995
ENSG00000079805	MUCL1	-0,1895	0,0162332
ENSG00000175970	UNC119B	-0,1898	0,0452733
ENSG00000119402	FBXW2	-0,1914	0,023027
ENSG00000136937	NCBP1	-0,1939	0,0293885
ENSG00000156639	ZFAND3	-0,1943	0,008296
ENSG00000108821	COL1A1	-0,1943	0,0119896
ENSG00000162521	RBBP4	-0,1951	0,0045141
ENSG00000204217	BMPR2	-0,1992	0,0227626
ENSG00000082781	ITGB5	-0,2008	0,002742
ENSG00000087245	MMP2	-0,2026	0,0049268
ENSG00000135372	NAT10	-0,2045	0,0064332
ENSG00000114062	UBE3A	-0,205	0,006169
ENSG00000106211	HSPB1	-0,2062	0,003805
ENSG00000187498	COL4A1	-0,2095	0,019487
ENSG00000101335	MYL9	-0,2098	0,0021689
ENSG00000138061	CYP1B1	-0,2113	0,0009146
ENSG00000147457	CHMP7	-0,2123	0,0379649
ENSG00000136153	LMO7	-0,2138	0,0031855
ENSG00000143970	ASXL2	-0,2152	0,0366105
ENSG00000124766	SOX4	-0,2165	0,021685
ENSG00000204262	COL5A2	-0,218	0,0002576
ENSG00000092964	DPYSL2	-0,2183	0,0069572
ENSG00000185122	HSF1	-0,2215	0,0249215
ENSG00000129474	AJUBA	-0,224	0,0031127
ENSG00000095261	PSMD5	-0,2248	0,0185032
ENSG00000115380	EFEMP1	-0,2251	0,0010841
ENSG00000125753	VASP	-0,2254	0,0256721
ENSG00000164741	DLC1	-0,226	0,000594
ENSG00000177954	RPS27	-0,2274	0,0031492
ENSG00000104823	ECH1	-0,2296	0,0293885
ENSG00000198833	UBE2J1	-0,23	0,0034935
ENSG00000012232	EXTL3	-0,2318	0,0019472
ENSG00000137809	FLRT1	-0,2337	0,0008864
ENSG00000137818	RPLP1	-0,2347	2,497E-05
ENSG00000114251	WNT5A	-0,2357	0,0012849
ENSG00000144283	PKP4	-0,2383	0,0184931
ENSG00000177700	POLR2L	-0,2389	0,0011988
ENSG00000159267	HLCS	-0,2399	0,0501182
ENSG00000163171	CDC42EP3	-0,2399	0,0005303
ENSG00000156052	GNAQ	-0,2408	0,0018004
ENSG00000006042	TMEM98	-0,2423	0,0227626
ENSG00000105137	SYDE1	-0,2432	0,0227626
ENSG00000204389	HSPA1A	-0,2437	0,0002142
ENSG00000162889	MAPKAPK2	-0,2449	0,0007489
ENSG00000153904	DDAH1	-0,2484	0,0005303
ENSG00000167513	CDT1	-0,2494	0,0156067
ENSG00000162734	PEA15	-0,2511	5,317E-05
ENSG00000131389	SLC6A6	-0,2513	0,0038883
ENSG00000197457	STMN3	-0,2534	0,005984
ENSG00000089006	SNX5	-0,254	0,0018004
ENSG00000139329	LUM	-0,2549	0,0015396
ENSG00000084444	KIAA1467	-0,2555	0,0465882

ID	hgnc_symbol	logFC	adj.P.Val
ENSG00000141424	SLC39A6	-0,2562	0,0049507
ENSG00000206418	RAB12	-0,2571	0,0069572
ENSG00000160953	MUM1	-0,2572	0,0358537
ENSG00000258232		-0,2603	0,004194
ENSG00000133243	BTBD2	-0,2608	0,0033862
ENSG00000168255	POLR2J3	-0,2643	0,0200808
ENSG00000113721	PDGFRB	-0,2644	0,0079932
ENSG00000101911	PRPS2	-0,2649	0,0006565
ENSG00000111711	GOLT1B	-0,2671	0,0104936
ENSG00000049245	VAMP3	-0,2683	0,0001223
ENSG00000168916	ZNF608	-0,2687	0,04168
ENSG00000063438	AHRR	-0,2697	0,0045781
ENSG00000243927	MRPS6	-0,2716	0,0298548
ENSG00000111799	COL12A1	-0,2716	1,326E-06
ENSG00000156531	PHF6	-0,2724	0,000594
ENSG00000164442	CITED2	-0,2756	5,8E-07
ENSG00000105220	GPI	-0,2777	8,241E-07
ENSG00000047644	WWC3	-0,2782	3,025E-05
ENSG00000138069	RAB1A	-0,2786	2,875E-05
ENSG00000163659	TIPARP	-0,2795	0,0128471
ENSG00000091986	CCDC80	-0,2797	0,000101
ENSG00000168778	TCTN2	-0,2833	0,0231484
ENSG00000269888		-0,2839	0,0361193
ENSG00000064393	HIPK2	-0,2864	2,023E-06
ENSG00000155760	FZD7	-0,2889	1,904E-05
ENSG00000166224	SGPL1	-0,2923	0,0011538
ENSG00000137075	RNF38	-0,2976	0,0168259
ENSG00000233369		-0,2978	4,441E-05
ENSG00000106683	LIMK1	-0,2983	3,411E-06
ENSG00000157045	NTAN1	-0,3008	0,0002288
ENSG00000154222	CC2D1B	-0,3086	0,002264
ENSG00000100335	MIEF1	-0,3102	7,463E-06
ENSG00000088367	EPB41L1	-0,3141	0,0069572
ENSG00000111412	C12orf49	-0,3192	0,0017147
ENSG00000162980	ARL5A	-0,3196	0,0002641
ENSG00000115758	ODC1	-0,3204	3,462E-06
ENSG00000005075	POLR2J	-0,321	0,0017147
ENSG00000101079	NDRG3	-0,3221	0,0044175
ENSG00000169439	SDC2	-0,3221	2,036E-05
ENSG00000234127	TRIM26	-0,3225	8,461E-06
ENSG00000167693	NXN	-0,3238	3,639E-05
ENSG00000106484	MEST	-0,3248	2,891E-09
ENSG00000166402	TUB	-0,3272	0,0014635
ENSG00000106554	CHCHD3	-0,3282	7,193E-07
ENSG00000074219	TEAD2	-0,3286	0,0194613
ENSG00000110492	MDK	-0,3311	1,442E-08
ENSG00000123689	G0S2	-0,3335	0,0380798
ENSG00000166340	TPP1	-0,3339	6,765E-08
ENSG00000103888	CEMIP	-0,3352	9,063E-05
ENSG00000076770	MBNL3	-0,3357	0,0380798
ENSG00000116954	RRAGC	-0,3455	5,483E-05
ENSG00000137801	THBS1	-0,3472	5,344E-11
ENSG00000143341	HMCN1	-0,3489	0,0186761
ENSG00000182492	BGN	-0,3547	0,0035342
ENSG00000165449	SLC16A9	-0,3578	0,0053141
ENSG00000153721	CNKSR3	-0,3586	8,412E-06
ENSG00000167244	IGF2	-0,3586	0,0286696
ENSG00000145919	BOD1	-0,3595	2,428E-05
ENSG00000163935	SFMBT1	-0,362	0,0021745
ENSG00000106052	TAX1BP1	-0,3649	5,89E-09
ENSG00000099622	CIRBP	-0,3695	1,17E-05

ID	hgnc_symbol	logFC	adj.P.Val
ENSG00000013619	MAMLD1	-0,3716	0,043977
ENSG00000205250	E2F4	-0,3739	0,0029571
ENSG00000185722	ANKFY1	-0,3758	1,837E-09
ENSG00000151292	CSNK1G3	-0,3799	4,532E-05
ENSG00000090470	PDCD7	-0,3806	0,0003185
ENSG00000128714	HOXD13	-0,3823	0,03394
ENSG00000158987	RAPGEF6	-0,387	0,0004306
ENSG00000056998	GYG2	-0,3875	0,0149889
ENSG00000165655	ZNF503	-0,3933	0,0006565
ENSG00000101224	CDC25B	-0,406	8,52E-11
ENSG00000151702	FLI1	-0,4081	0,0226585
ENSG00000198959	TGM2	-0,4299	1,11E-10
ENSG00000169071	ROR2	-0,4342	0,0001738
ENSG00000038427	VCAN	-0,4358	7,018E-14
ENSG00000184838	PRR16	-0,4373	8,2E-07
ENSG00000168685	IL7R	-0,4394	1,155E-08
ENSG00000164761	TNFRSF11B	-0,4446	0,0154846
ENSG00000085719	CPNE3	-0,4538	4,161E-17
ENSG00000162692	VCAM1	-0,4559	0,0293885
ENSG00000113732	ATP6V0E1	-0,4574	4,307E-10
ENSG00000117152	RGS4	-0,4606	6,746E-05
ENSG00000134986	NREP	-0,4635	8,763E-16
ENSG00000135097	MSI1	-0,4665	0,0161777
ENSG00000074621	SLC24A1	-0,486	0,0073043
ENSG00000179387	ELMOD2	-0,4939	2,851E-07
ENSG00000166923	GREM1	-0,5064	1,911E-25
ENSG00000139211	AMIGO2	-0,5227	4,313E-09
ENSG00000011465	DCN	-0,5299	5,395E-05
ENSG00000152049	KCNE4	-0,5379	0,0090445
ENSG00000106771	TMEM245	-0,539	6,357E-22
ENSG00000137337	MDC1	-0,5487	2,125E-21
ENSG00000104067	TJP1	-0,551	1,161E-12
ENSG00000079102	RUNX1T1	-0,5569	0,0031555
ENSG00000128656	CHN1	-0,5594	1,419E-05
ENSG00000184232	OAF	-0,5833	0,0030497
ENSG00000154736	ADAMTS5	-0,5987	9,71E-17
ENSG00000172260	NEGR1	-0,5995	0,0019438
ENSG00000149948	HMGA2	-0,6078	1,469E-06
ENSG00000165678	GHITM	-0,637	2,999E-30
ENSG00000143473	KCNH1	-0,6512	0,0001558
ENSG00000172780	RAB43	-0,6623	0,0050201
ENSG00000152377	SPOCK1	-0,7318	3,003E-47
ENSG00000140299	BNIP2	-0,8122	2,999E-30
ENSG00000002834	LASP1	-0,8261	9,964E-56
ENSG00000122694	GLIPR2	-0,8982	0,0006766
ENSG00000269378	ITGB1P1	-0,9737	0,0302535
ENSG00000230409	TCEA1P2	-0,9777	0,007253
ENSG00000142178	SIK1	-1,026	0,0293726
ENSG00000235174	RPL39P3	-1,084	3,291E-06
ENSG00000170667	RASA4B	-1,2985	2,428E-05
ENSG00000259040	BLOC1S5-TXNDC	-1,4775	2,619E-63
ENSG00000167774		-1,5282	0,0341707
ENSG00000242852	ZNF709	-2,0062	0,0168495
ENSG00000259952		-2,0332	0,0003031
ENSG00000274570		-2,1424	0,0231484
ENSG00000229927	RHEBP1	-2,2732	0,0293885
ENSG00000271894		-2,2806	0,0293885
ENSG00000277971		-2,6263	0,0180433
ENSG00000270136	MINOS1-NBL1	-2,8708	6,858E-12
ENSG00000105974	CAV1	-2,8903	0
ENSG00000258757		-3,2297	0,0005325

8. APPENDIX

Curriculum Vitae

Alberto Díez
PhD student & biotechnologist

Work

2017 — **PhD visiting student**
Centre for Molecular Inflammation Research (CEMIR, NTNU), Trondheim, Norway

Autophagy Lab, Geir Bjørkøy . PhD. lab, EMBO Short-term fellowship (starting June 2017)
Skills: Flow cytometry, mitochondrial respiration and autophagy functional assays

2014 — **PhD student**
Centro Nacional de Investigaciones Cardiovasculares (CNIC), Spain

Integrin Signalling Lab, Miguel Ángel del Pozo MD. PhD. lab, "la Caixa" PhD fellowship (starting May 2014)
Skills: siRNA & Drug High Content Screening (HCS) assay tuning, Image analysis, Interdisciplinary research, Xenograft mouse models, RNASeq analysis

2013 — **CNIC Master Student + Research Technician**
Centro Nacional de Investigaciones Cardiovasculares (CNIC), Spain

Integrin Signalling Lab, Miguel Ángel del Pozo MD. PhD. lab, 2012 CNIC Master fellowship + Research Contract (17 months)
Skills: Viral Vector design & generation, Confocal Microscopy, Genome Editing (ZnFinger nuclease & CRISPR/Cas9), qPCR

2012 — **Visiting Graduate Student**
University of California San Diego (UCSD), CA

Cellular and Molecular Medicine (CMM), Marilyn G. Farquhar PhD. lab, Goya Mundus Grant (4 months)
Skills: Protein purification, Western Blot, Pull-down assays, Eukaryotic cell culture, Viral vectors handling & generation

2011 — **Visiting Undergraduate Student**
Centro Nacional de Biotecnología (CNB), Spain

Bacterial Engineering for Biomedical Applications, Luis Ángel Fernández PhD. lab, Erasmus placement (4months)
Skills: Gene cloning, PCR, Bacterial cell culture, bacterial genome modification

Information

Name	Alberto Díez Sánchez
Born	2nd December 1989
Age	28
Nationality	Spanish
Languages	Spanish, English, French
Phone	+34 635 240 540
Email	adiez.biotech@gmail.com

Skills

Laboratory

Molecular Biology	●●●●○
Cell Culture	●●●●○
High Content Screening	●●●●○
Confocal Microscopy	●●●○○
Animal experimentation	●●●○○

Software

DNA editing (Lasergene)	●●●●●
Image Analysis (Fiji, Acapella...)	●●●●○
Statistics (GraphPad)	●●●●○
Bioinformatics	●●●○○
Microsoft Office	●●●○○

Day-to-day skills

Oral communication	●●●●●
Process automation	●●●●○
Proposal writing	●●●●○
Design	●●●○○
Team management	●●●○○

Sandgata 24B, H407, 7012 Trondheim, Norway. Tel +34 635 240 540
adiez.biotech@gmail.com ; adiez@cnic.es

Curriculum Vitae

Alberto Díez
PhD student & biotechnologist

Education

2012 - **PhD Student (CNIC - UAM)**
Universidad Autónoma de Madrid, Madrid, Spain

Studying the role of stromal fibroblasts in cancer progression & angiogenesis using both *in vitro* & *in vivo* assays , High Content Screening campaigns, gene editing and Next Generation Sequencing techniques.
In progress

2012-13 **Master in Biomolecular Medicine (UAM)**
Universidad Autónoma de Madrid, Madrid, Spain

1 year specialization in the frontier between basic and clinical research, focused in Cell Signaling & Cardiovascular disease
Grade: 3.86 GPA

2007-12 **BS in Biotechnology (UFV) + MBA in Management of Biotech companies**
Universidad Francisco de Vitoria, Madrid, Spain

5-year degree including Human Physiology, Biochemistry, Genetics, Molecular Biology, Virology, Bioinformatics & Omics with laboratory hands-on.
Grade: 3.84 GPA

2010-11 **Bachelor of Science in Biotechnology (AIT)**
Athlone Institute of Technology, Athlone, Ireland

Obtained the degree after 1 year of study abroad during my Erasmus leave, mainly focused on hands-on lab techniques.
Grade: Distinction w/First Class Honors

Funding

Grants
EMBO Short-Term fellowship (2017)
"La Caixa" 2014 PhD in Spanish Universities (2014 - 2018)
CNIC 2012 Master Program (CNIC, 2012 - 2013)
Goya Mundus 2012 Grant (UPC/EMES, Summer 2012)
UFV Scholarship for students with Excellent Academic Performance (UFV, 2007 - 2012)

Awards
AIT Student of the Year in BSc in Biotechnology (AIT, Oct 2011)
Madrid Academic Excellence Scholarship (EMES, 2010 - 2011)

References

Miguel Ángel del Pozo, MD, PhD
Principal Investigator

Centro Nacional de Investigaciones Cardiovasculares (CNIC)
Melchor Fernández Almagro 5, 28027 Madrid (Spain)

T +34 661 43 14 74
E madelpozo@cnic.es

Mehul Shah, MD, PhD
Associate Director Medical Affairs

Actelion
5000 Shoreline Ct Suite 200, South San Francisco, CA 94080

T +1 (914) 646-8090
E mehul.shah@actelion.com

Luis Ángel Fernández, PhD
Principal Investigator

Centro Nacional de Biotecnología (CNB)
Darwin 3, 28049 Madrid (Spain)

T +34 91 585 4854
E lafdez@cnb.csic.es

Courses

- **Course on Microscopy and Advanced Applications** (Zeiss, 2014)
- **Animal Experimentation Function A** (Charles River Laboratories, 2015)
- **Open Water Diver** (PADI, 2011)
- **Become a web developer from scratch** (Udemy, in progress)

Sandgata 24B, H407, 7012 Trondheim, Norway. Tel +34 635 240 540
adiez.biotech@gmail.com ; adiez@cnic.es

Curriculum Vitae

Alberto Díez
PhD student & biotechnologist

Projects

Drug screening targeting Cav1 in pancreatic stromal fibroblasts

Collaboration with Experimental Therapeutics + Gastrointestinal Cancer at CNIO (Spanish National Cancer Research Center)

Designed a small 50 drug screening with various doses and successfully found 3 approved drugs capable of decreasing Cav1 levels.
Coordinated a team of image analysis engineers and high content technicians.

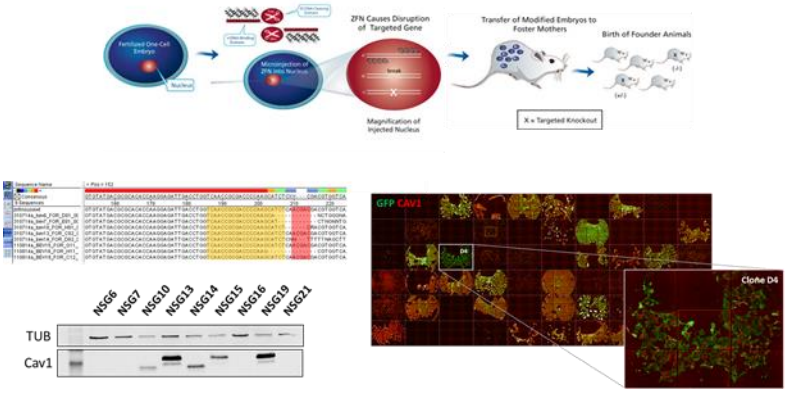

Genome editing of Cav1 in NSG mice & various cell lines

Collaboration with Transgenics Unit at CNIC

An NSG Cav1 KO mice colony has been established using ZnFinger mediated genome editing in record time.
Deletion of Cav1 gene in cell lines with an improved version (designed and modified by myself) of the commercial ZnFinger plasmid provided by Sigma increasing the efficiency of the procedure and decreasing the workload.

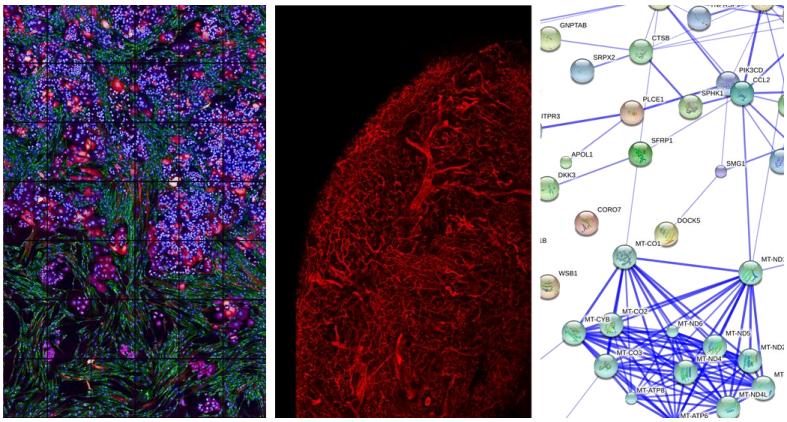

Role of Cav1 levels in stromal fibroblasts in angiogenesis, tumor hypoxia & disease progression

PhD Project at CNIC

I am using a combination of HCS assays, transcriptomics and animal models to unveil the effect of the absence of Cav1 in the stroma of breast cancer tumors, particularly in tumor angiogenesis, hypoxia and metastasis (Work in progress)

Sandgata 24B, H407, 7012 Trondheim, Norway. Tel +34 635 240 540
adiez.biotech@gmail.com ; adiez@cnic.es